UNIVERSITÄT HAMBURG

Fakultät für Mathematik, Informatik und Naturwissenschaften

Fachbereich Biologie

Prof. Dr. Stefan Hoth

UNIVERSITÄTSKLINIKUM HAMBURG-EPPENDORF

Klinik für Pädiatrische Hämatologie und Onkologie

Prof. Dr. med. Stefan Rutkowski

FORSCHUNGSINSTITUT KINDERKREBS-ZENTRUM HAMBURG

AG Schüller

Prof. Dr. med. Ulrich Schüller

Biological and molecular characterization of the cellular origins and progression of atypical teratoid/rhabdoid tumors (AT/RT)

Dissertation

zur Erlangung des Doktorgrades Dr. rer. nat. / PhD

an der Fakultät für Mathematik, Informatik und Naturwissenschaften der Universität Hamburg.

vorgelegt von:

Lea Altendorf

aus Lüneburg

Hamburg 2025

Erste/r Gutachter/in: Prof. Dr. rer. nat. Wolfgang Streit

Zweite/r Gutachter/in: Prof. Dr. med. Ulrich Schüller

Datum der Disputation: 14.10.2025

Publication 1

Aim of publication 1

The goal of this work was to characterize histopathological and molecular differences of 26 paired primary and recurrent atypical teratoid/rhabdoid tumors (AT/RT) to identify mechanisms of disease progression and recurrence. We collected primary-recurrence pairs of all DNA methylation subtypes and performed histological examination, DNA methylation analyses, and gene expression profiling using bulk RNA sequencing (bulk RNAseq) data. In addition, we determined chromosomal copy-number variations (CNVs) based on the DNA methylation data. The results showed that global DNA methylation patterns were similar between primary tumors and paired recurrences. CNV analysis demonstrated an enhanced chromosome 1q gain and chromosome 10 loss in AT/RT-SHH recurrences as well as differentially expressed cancer-associated genes, which should be considered as new promising therapeutic targets.

Contribution to publication 1

This study was mainly planned by Prof. Dr. med. Ulrich Schüller, Prof. Dr. med. Pascal Johann, Prof. Dr. med. Michael Frühwald and me. As a shared first author, I performed the collection and quantification of the immunohistochemistry (IHC). In addition, DNA methylation data for most of the cases were generated in our lab, and all bioinformatic analysis were done by me. This also included the identification and characterization of CNVs. Furthermore, I performed bioinformatic analysis of the bulk RNAseq data. I wrote the first draft of the manuscript, which was thoroughly reviewed by Prof. Dr. med. Pascal Johann, who is the second shared first author, Prof. Dr. med. Ulrich Schüller, and Prof. Dr. med. Frühwald. Additionally, the figures were designed and interpreted by me. After finalizing the manuscript, I integrated the feedback of the co-authors. Processing of the reviewer comments after submission was shared equally between Prof. Dr. med. Pascal Johann and me.

First reviewer: Prof. Dr. rer. nat. Wolfgang Streit

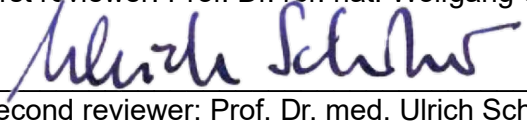

Second reviewer: Prof. Dr. med. Ulrich Schüller

Publication 2

Aim of publication 2

The second publication attempted to identify the cellular origins of AT/RT-SMARCA4, including the generation of a mouse model. So far, the cellular origin is completely unknown, and no *Smarca4*-deficient mouse model has developed any tumors. We generated *P0-Cre::Smarca4*$^{fl/fl}$ mice because previously, a *P0-Cre*-driven *Smarcb1* knockout led to RT-like tumor development. In addition, we generated *Smarca4-p.R1189*$^{*+/-}$ mice because this point mutation was previously identified in the germline of a family suffering from AT/RT-SMARCA4. Finally, *P0-Cre::Smarca4*$^{fl/wt}$ and *Smarca4-p.R1189*$^{*+/-}$ mice were crossed. None of these mice developed any tumors, and therefore, we assume that loss of *Smarca4* must occur earlier or AT/RT-SMARCA4 originate from a different cell type. Nevertheless, the mice developed impaired peripheral nerve sheaths, resulting in paralysis of the limbs.

Contribution to publication 2

This work was done together with Dr. med. Sina Neyazi, who mainly planned the project together with Prof. Dr. med. Ulrich Schüller and who generated these mice. I joined the monitoring of the mice, which also included sacrificing the mice after reaching a moderate level of neurological symptoms. Within this work, I collected survival and weight data and prepared the brains, muscles, and nerves for IHC. Furthermore, I analysed the IHC data and performed the quantification of our results. I wrote the first draft of the manuscript, which was critically reviewed by Dr. med. Sina Neyazi and Prof. Dr. med. Ulrich Schüller. In addition, I designed the figures. The integration of co-author feedback was performed by me, and the reviewer comments were addressed by Dr. med. Sina Neyazi and me.

First reviewer: Prof. Dr. rer. nat. Wolfgang Streit

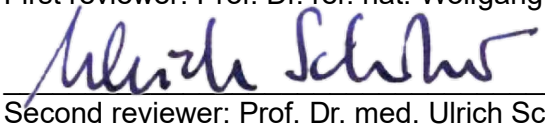

Second reviewer: Prof. Dr. med. Ulrich Schüller

Unpublished manuscript 1

Aim of manuscript 1

This study is a continuation of publication 1. Here, we generated single-nucleus RNA sequencing (snRNAseq) data of eight AT/RT primary-recurrence pairs. We performed clustering analysis and investigated the tumor cells and the tumor microenvironment (TME) separately. For the TME, we performed differential abundance testing of the different cell types, which revealed enrichment of *CD1A*$^{+}$ *CD207*$^{+}$ dendritic cells (DC) in AT/RT recurrences. Using the tumor cells, we investigated the cancer cell states and identified probable therapy-resistant cells for AT/RT-MYC, which were further characterized by differentially expressed genes and pathways. Our findings were validated *in vitro*. We observed increased partial epithelial-mesenchymal transition (pEMT) in AT/RT-MYC recurrences, and therapy-resistant cells were characterized by altered extracellular matrix (ECM) remodeling, among others. Expression of these was correlated with inferior survival.

Contribution to manuscript 1

I designed the study together with Prof. Dr. med. Ulrich Schüller. I collected the samples for the snRNAseq protocol, which was then performed by the Kerl group of the University Hospital Münster. The entire bioinformatic analysis was performed by me. This included preprocessing, filtering, normalization, and alignment to the human genome, as well as performing the integration and clustering analyses. I established the *CIBERSORT* algorithm, performed differential gene expression analysis, and assigned the cancer cell states. Additionally, I established the cell culture and treatment of AT/RT cell lines, including the determination of adequate inhibitor concentrations. The cell culture was then handed over to Vanessa Thaden. Finally, I collected bulk RNAseq data with matching survival data, mainly with the help of Prof. Dr. med. Martin Hasselblatt, Prof. Dr. med. Michael Frühwald and Prof. Dr. med. Pascal Johann. The survival analyses were performed by me. I wrote the manuscript and designed all figures, which were reviewed by Prof. Dr. med. Ulrich Schüller. This manuscript was submitted to *Neuro-Oncology* on the 6th of June, 2025, and is currently under review.

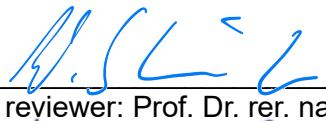

First reviewer: Prof. Dr. rer. nat. Wolfgang Streit

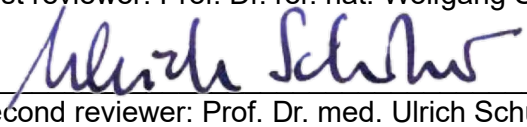

Second reviewer: Prof. Dr. med. Ulrich Schüller

Unpublished manuscript 2

Aim of manuscript 2

The second unpublished manuscript deals once more with the cellular origins of AT/RT. Here, we investigated the cellular origin of AT/RT-TYR. The goal was to determine cell type signatures of these tumors, which might give indications regarding the cell of origin. We examined numerous AT/RT biopsies and observed intermingled choroid plexus (CP) tissue in 35% of all investigated AT/RT-TYR, which was predominant for this subtype. As AT/RT-TYR mainly occur in the fourth ventricle, we hypothesize that precursors of the CP of the fourth ventricle could be the cellular origin. We then investigated CP marker expression using histology and bulk RNAseq data, which was again enriched in AT/RT-TYR. Furthermore, we performed *CIBERSORT* analysis to find similarities to cell types of the developing human cerebellum, which resulted in the highest similarity to CP. SnRNAseq analyses revealed the occurrence of healthy CP cells, which clustered in proximity to the AT/RT-TYR tumor cells. Finally, we generated *Foxj1-cre::Smarcb1*$^{fl/fl}$ mice, whose CP was characterized by large, atypical, monociliary cells and a gene expression profile similar to human AT/RT-TYR.

Contribution to manuscript 2

This study was planned by Prof. Dr. med. Ulrich Schüller, Prof. Dr. med. Martin Hasselblatt and me. At first, I collected the biopsies of all AT/RT DNA methylation subtypes and investigated them for the occurrence of CP. I examined all IHC stainings. In addition, I integrated and analysed the bulkRNA seq data of the AT/RT and additional central nervous system (CNS) tumors. *CIBERSORT* analysis was performed by me. The snRNAseq data were generated by the Kerl group in Münster. I performed all bioinformatic analyses as described for the unpublished manuscript 1. All mice experiments were performed by me, including the planning, breeding, monitoring, sacrificing, preparation of the brains and CPs, IHC quantification, and generation of the bulk RNAseq data. Finally, I designed all figures and wrote the manuscript draft. This manuscript will be submitted when the results of *Foxj1-cre::Smarcb1*$^{fl/fl}$*::p53*$^{fl/fl}$ mice are integrated.

First reviewer: Prof. Dr. rer. nat. Wolfgang Streit

Second reviewer: Prof. Dr. med. Ulrich Schüller

Table of contents

Publication 1 2
Aim of publication 1 2
Contribution to publication 1 2
Publication 2 3
Aim of publication 2 3
Contribution to publication 2 3
Unpublished manuscript 1 4
Aim of manuscript 1 4
Contribution to manuscript 1 4
Unpublished manuscript 2 5
Aim of manuscript 2 5
Contribution to manuscript 2 5
1. Introduction 8
1.1 Brain development and embryonal brain tumors 8
1.2 Epidemiology and symptoms of malignant rhabdoid tumors 9
1.3 Current standard-of-care therapy for AT/RT 10
1.4 Genetics of AT/RT – *SMARCB1* and *SMARCA4* mutations and the role of the switch/sucrose non-fermentable (SWI/SNF) complex 10
1.5 AT/RT DNA methylation subtypes and clinical characteristics 12
1.6 Histopathology and diagnosis of AT/RT 15
1.7 Cellular origins of AT/RT 16
1.8 AT/RT mouse models 16
1.9 Tumor progression, recurrence, and therapy resistance 18
1.10 Aim of this work 19
2. Publication 1 22
3. Publication 2 47
4. Unpublished manuscript 1 53
5. Unpublished manuscript 2 88
6. Discussion 124
7. Abstract 140
8. Zusammenfassung 141
9. Abbreviations 143
10. References 146
11. List of publications 165

11.1 First-authorships 165
11.2 Co-authorships 165
11.3 Submitted manuscripts 166
11.4 Manuscript drafts 167
12. Danksagung 168
13. Eidesstattliche Versicherung 169

1. Introduction

1.1 Brain development and embryonal brain tumors

The brain is one of the most important organs of all vertebrates. As being part of the CNS, next to the spinal cord, it is critically involved in the processing of sensory and motoric information (Eilbert 2014; Pessoa et al. 2019). Human brain development, including cell fate and tissue shape, requires complex embryonal developmental processes. This includes mechanical changes in cell and tissue shapes as well as gene expression changes for cell fate decisions. Embryonal development was mainly studied in mice because humans and mice share fundamental developmental processes (Shahbazi 2020). After a series of cell divisions that follow upon fertilization, a pluripotent blastocyst arises at embryonal day 3 (E3) in mice and E4 in humans, which further develops into epiblasts and hypoblasts at E4 in mice and E6 in humans (Shahbazi 2020). During subsequent gastrulation, three germ layers develop: Ectoderm, endoderm, and mesoderm (mice E6.5 and human E13-E20; Shahbazi 2020; Stiles and Jernigan 2010). These layers give rise to different cell types. The nervous system, including the brain and spinal cord, arises from the ectoderm (Kiecker et al. 2016). At first, the ectoderm forms the neural tube during a process called neurulation. The neural plate is formed by thickening of the ectoderm (Sadler 2005). At the border of the neural plate, the neural crest arises (Mayor and Theveneau 2013). After that, the neural plate receives stimuli starting the formation of the neural tube (mice E8.5-E10 and human E20-E27). The neural crest cells become migratory and develop into different cell types (Sadler 2005; Zohn and Sarkar 2008; Stiles and Jernigan 2010; Shahbazi 2020). Afterwards, the neural tube develops into three primary vesicles: The prosencephalon (forebrain), the mesencephalon (midbrain), and the rhombencephalon (hindbrain; mice E9.5 and human E28; Kiecker et al. 2016; Shahbazi 2020). Further developmental signals lead to the differentiation of five secondary vesicles (mice E10.5 and human E49; Stiles and Jernigan 2010). On the one hand, this includes the subdivision of the prosencephalon into the telencephalon (anterior), which gives rise to the ganglionic eminence, further developing into interneurons and basal ganglia (Encha-Razavi and Sonigo 2003), and the cerebral hemispheres. On the other hand, the diencephalon (caudal) gives rise to the thalamic and hypothalamic brain regions. The mesencephalon most likely develops into the cerebral aqueduct. The rhombencephalon is also subdivided into the myelencephalon (posterior), developing into the medulla oblongata, and the metencephalon (anterior), which gives rise to the cerebellum (Stiles and Jernigan 2010). Overall, the rhombencephalon is divided into the rhombomeres 0-11 (r0-r11; Guthrie and Lumsden 1991). r0 and r1 develop into the cerebellum, whereas r2-r11 develop into different nerves (Leto et al. 2016; van Essen et al. 2020; Krumlauf and Wilkinson 2021). r0 is also called isthmus and is involved in the

stabilization of the midbrain-hindbrain boundary (Leto et al. 2016). In addition, r0 and r1 form the upper rhombic lip (URL; mice E12.5 and human E49), which gives rise to excitatory neuronal progenitors, which further develop into deep cerebellar nuclei, granule cells, and unipolar brush cells (UBC; Leto et al. 2016; van Essen et al. 2020; Consalez et al. 2021). The remaining rhombomeres form the ventricular zone (VZ; mice E12.5 and human E49), which is involved in the lining of the cerebellum, including the fourth ventricle. The VZ is characterized by inhibitory neuronal progenitors, which develop into Purkinje cells and astrocytes (Leto et al. 2016; van Essen et al. 2020). The choroid plexus (CP) of the fourth ventricle is supposed to start to arise from r1 at E9.5 in mice (E46 in humans; Müller and O'Rahilly 1990), and is formed at the dorsal midline (Cheng et al. 2012; Kompaníková and Bryja 2022). CP progenitors from r1 proliferate and develop into epithelial cells, which extend into an epithelial tissue bundle, characterized by a cobblestone-like pattern – the CP (Kaiser et al. 2021; Dani et al. 2021). It is responsible for the production and transport of the cerebrospinal fluid, which is regulated by multiple cilia. These are short hair-like extensions of the cell membrane, which are formed during a process called ciliogenesis (Narita and Takeda 2015; Mao et al. 2025).

Abnormalities in brain development can not only result in developmental disorders, but are also associated with pediatric brain tumors. These are supposed to arise during embryonal brain development, because such tumors occur very early in life. Genes that are involved in fundamental developmental processes can also be involved in the development of pediatric brain tumors when they are deregulated. Most of these genes are also associated with tumor predisposition syndromes, which means that the respective genes are already mutated in the germline (Bruschi et al. 2021). One of these embryonal brain tumors is the atypical teratoid/rhabdoid tumor (AT/RT; Kamenova et al. 2023; Tulla et al. 2015).

1.2 Epidemiology and symptoms of malignant rhabdoid tumors

Malignant rhabdoid tumors (MRT) are highly aggressive pediatric tumors which can be divided into further subtypes regarding their localizations. Extracranial malignant rhabdoid tumors (eMRT) arise in the soft tissue (Tsuneyoshi et al. 1985) or as rhabdoid tumors of the kidney (RTK; Haas et al. 1981). These tumors make up about 35% of all MRT, but the majority of these tumors (~65%) occur in the CNS, which are called AT/RT (Rorke et al. 1996). eMRT can often be removed by gross total resection, which leads to a significantly better survival than for AT/RT (Nemes et al. 2021; Nemes et al. 2022). AT/RT have a very poor prognosis, being a WHO grade 4 embryonal CNS tumor, which is the worst stage that includes highly malignant tumors and is characterized by a significantly shortened survival (Louis et al. 2021). AT/RT patients have a median overall survival (OS) of 17 months, depending on risk groups (Frühwald et al. 2020; Upadhyaya et al. 2021). Patients show symptoms like headache, vomiting,

lethargy, ataxia, macrocephaly, and hemi- or paraplegia. The form of the symptoms depends on the tumor localization and size (Rorke et al. 1996; Hasselblatt et al. 2011; Arnhold et al. 2016; Bookhout et al. 2018).

Overall, AT/RT are very rare and make up 1-2% of all pediatric brain tumors (Richardson et al. 2018), with incidences between 0.3 and 0.6 per 100,000 patients in the first year of life and between 0.03 and 0.26 per 100,000 patients in the fifth until ninth year of life (Ostrom et al. 2014; Louis et al. 2021; Ostrom et al. 2022). But nevertheless, they are the most common malignant CNS tumors in children younger than one year of age (Ginn and Gajjar 2012; Richardson et al. 2018). Multiple rhabdoid tumors (RT) at different localizations occur in 6% of the patients (Frühwald et al. 2016; Frühwald et al. 2020), and distant metastases can be found in 20-30% (Oka and Scheithauer 1999; Frühwald et al. 2020; Gastberger et al. 2023). In the majority of cases, the tumors progress or recur after a very short time, and only a few patients are still alive five years following diagnosis of a recurrence (Carey et al. 2022; Steinbügl et al. 2022).

1.3 Current standard-of-care therapy for AT/RT

The standard-of-care therapy for AT/RT includes surgery, aiming for maximal safe resection, and conventional or high-dose chemotherapy. Conventional chemotherapy uses a combination of drugs that target proliferating cells and inhibit their cell division using different mechanisms of inhibition, which increases the effectiveness. These are applied in repetitive cycles to allow the normal tissue to recover (Cavalcanti and Soares 2021; Letai and de The 2024). High-dose chemotherapy includes the application of higher doses of conventional chemotherapeutics (Petersdorf and Livingston 1994; Lafay-Cousin and Dufour 2022). Radiotherapy is not recommended for children younger than three years and is only applied in single cases (Gastberger et al. 2023). Targeted therapies for AT/RT are lacking, but due to the high toxicity of conventional and high-dose chemotherapy, they are urgently needed (Cavalcanti and Soares 2021). As AT/RT are rare, international therapy guidelines are limited. There are two registries, including a larger cohort of AT/RT patients:

The Canadian Paediatric Brain Tumor Consortium (CBTC) by Lucie Lafay-Cousin includes 50 patients, who were treated using maximal safe tumor resection and either conventional therapy, anthracycline-based chemotherapy, or high-dose chemotherapy. Radiotherapy was applied for half of the patients (Lafay-Cousin et al. 2012).

The European Rhabdoid Registry (EU-RHAB) registry by Prof. Dr. med. Frühwald includes 143 patients that were treated using maximal safe tumor resection and anthracycline-based chemotherapy with either nine or six alternating courses of 2× or 3× DOX (doxorubicin, intra-

ventricular methotrexate), ICE (ifosfamide, carboplatinum, etoposide, intra-ventricular methotrexate), and VCA (vincristine, cyclophosphamide, actinomycin-D, intra-ventricular methotrexate). Mostly, a subsequent high-dose chemotherapy (carboplatinum or thiotepa) was applied. Radiotherapy was not used for patients younger than 18 months (Benesch et al. 2014; Seeringer et al. 2014; Frühwald et al. 2016).

1.4 Genetics of AT/RT – *SMARCB1* and *SMARCA4* mutations and the role of the switch/sucrose non-fermentable (SWI/SNF) complex

The underlying genetic causes of AT/RT are *SMARCB1* mutations in 95% of the cases (Biegel et al. 1999) and in very rare cases, *SMARCA4* is mutated instead (0.5-2%; Schneppenheim et al. 2010; Hasselblatt et al. 2014; Holdhof et al. 2020a). These mutations are potentially present in the germline of the patients. On the one hand, *SMARCB1* germline mutations occur in about 30% of the patients on average, who then suffer from the rhabdoid tumor predisposition syndrome 1 (RTPS1; OMIM #609322; Foulkes et al. 2017; Sredni and Tomita 2015). On the other hand, *SMARCA4* germline mutations are highly frequent (73%) and affected patients suffer from the rhabdoid tumor predisposition syndrome 2 (RTPS2; OMIM #613325; Foulkes et al. 2017; Sredni and Tomita 2015).

Both SMARCB1 and SMARCA4 are part of the SWI/SNF complex, which is an ATP-dependent chromatin remodeling complex (Figure 1). Human DNA is condensed into nucleosomes, which are wrapped around an octamer of histones. These nucleosomes are further condensed into chromatin, whose structure is dynamic. Only the opened state called euchromatin is accessible for proteins like transcription factors (TF) or DNA repair (McGinty and Tan 2015; Clapier et al. 2017). These structural changes of the chromatin are catalyzed by ATP-dependent chromatin remodeling complexes like the SWI/SNF complex through ATP hydrolysis, resulting in nucleosome repositioning and editing. Therefore, the SWI/SNF complex is responsible for the DNA accessibility and regulation of gene expression (Wilson and Roberts 2011). It was originally identified in yeast as being involved in sucrose fermentation as well as in switching the mating type (Stern et al. 1984; Neigeborn and Carlson 1984). In humans, it is a complex of 2 MDa, which is comprised of 15 subunits that are encoded by 29 genes, including *SMARCB1* and *SMARCA4* (Phelan et al. 1999). The exact composition of the SWI/SNF complex, in mammals mostly called BAF complex, changes during neural development as shown in embryonic stem cells. The embryonic-stem-cell-BAF (esBAF) complex is required for maintaining pluripotency, self-renewal, and proliferation in embryonic stem cells (Ho et al. 2011). The neural progenitor BAF (npBAF) complex is present in neural progenitors, and the neuronal BAF (nBAF) complex in post-mitotic neurons. npBAF is involved in the proliferation of neuronal stem cells and inhibits their differentiation, whereas nBAF plays a role in the

dendritic and neuronal morphogenesis (Staahl et al. 2013). Nevertheless, SMARCB1 and SMARCA4 are retained in all forms. Overall, this shows that distinct gene expression profiles of the SWI/SNF complex can be found in different cell types and that the SWI/SNF complex is active in diverse cell types. It is required for adequate neurogenesis and gliogenesis (Tuoc et al. 2017; Braun et al. 2021).

SMARCB1 encodes one of the three core subunits of the SWI/SNF complex, next to *SMARCC1* and *SMARCC2*. It is known to be a tumor suppressor and plays a role in cell cycle progression and epigenetic regulation (Kadoch et al. 2013). In addition, *SMARCB1* is involved in the Wnt signaling pathway, which is a signal transduction pathway involved in carcinogenesis and embryonic development. The inhibition of retinoblastoma target genes like *E2F* factors and *CCND1*, which are upregulated in AT/RT, is also *SMARCB1*-driven (Kalimuthu and Chetty 2016; Wang et al. 2017a).

Each SWI/SNF complex subunit contains an ATPase, SMARCA2 or SMARCA4. Therefore, SMARCA4 has one of the most important functions (Wang et al. 1996). Additionally, it is known to be critically involved in the embryonal development of the CNS, as shown in different mouse models (see section 1.8). *SMARCA4* mutations are the second most frequent mutations associated with tumor development in humans. Based on *in vitro* studies, it is considered as a tumor suppressor (Kadoch et al. 2013).

As being involved in chromatin remodeling, DNA repair (Lans et al. 2012), immune response (Cui et al. 2004), and cell cycle control (Hah et al. 2010), mutations in the SWI/SNF complex play an important role in developmental disorders and tumorigenesis (Bögershausen and Wollnik 2018).

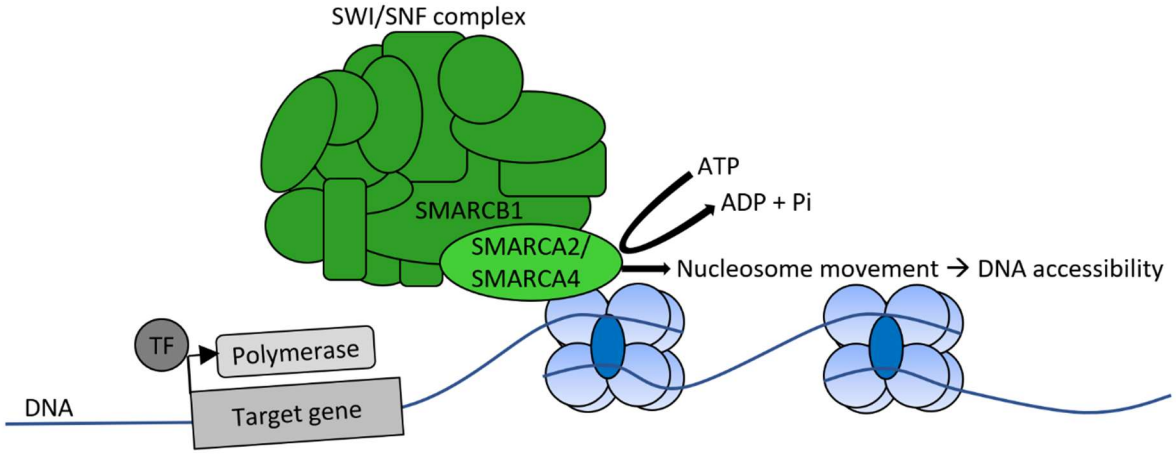

Figure 1: ATP-dependent chromatin remodeling performed by the SWI/SNF complex. The SWI/SNF complex consists of 15 subunits, with SMARCB1 as one of the three core subunits. Each subunit contains and ATPase, SMARCA2 or SMARCA4, which performs ATP hydrolysis by binding to nucleosomes, resulting in nucleosome movement and editing. This induces changes in the DNA accessibility, which allows TF to bind accessible DNA regions, leading to respective gene expression. Modified after Bögershausen and Wollnik 2018.

1.5 AT/RT DNA methylation subtypes and clinical characteristics

AT/RT can be further divided into different molecular subtypes based on their DNA methylation profiles, which are AT/RT-SHH, AT/RT-TYR, and AT/RT-MYC for *SMARCB1*-deficient cases (Johann et al. 2016; Torchia et al. 2016; Ho et al. 2020). Patients suffering from tumors with *SMARCA4* mutations form their own subtype: AT/RT-SMARCA4 (Holdhof et al. 2020a; Figure 2).

The majority of the tumors belong to AT/RT-SHH (41%). Sex distributions are balanced, with a slight male predominance (54-55%), and the median age of disease onset of patients belonging to this subtype is 20 months. These tumors mostly occur in the cerebrum, which is known as supratentorial localization (65-67%), and rarely in the cerebellum, which is known as infratentorial localization (35-37%). The *SMARCB1* mutations are mainly point mutations or focal deletions, and in 41% of the patients, the mutation is already present in the germline (Holdhof et al. 2020a; Ho et al. 2020). This subtype is further characterized by an upregulation of the Sonic Hedgehog (SHH) and NOTCH pathways, both required for embryonic cell differentiation, as well as neurogenesis pathways, and the subtype-specific genes *GLI2*, *PTCH2*, *BOC*, *ASCL1*, *CBL*, *HES1*, and *FOXK1* (Johann et al. 2016; Ho et al. 2020). As AT/RT-SHH is the most heterogenous subtype, it is further divided into AT/RT-SHH-1A, AT/RT-SHH-1B, and AT/RT-SHH-2 based on their DNA methylation profiles. Both AT/RT-SHH-1A and AT/RT-SHH-1B occur mainly supratentorial (88% and 85%, respectively), but most AT/RT-SHH-2 are located infratentorial. In addition, age differences are observed, with AT/RT-SHH-1B comprising the oldest patients (median age 107 months; Federico et al. 2022).

About 34% of the tumors belong to AT/RT-TYR. The sex distribution of the patients is comparable to AT/RT-SHH (55-57% male). The median age of disease onset is 12 months, and the majority of these tumors are located infratentorially (75-78%), the remaining tumors occur supratentorially (22-25%). AT/RT-TYR are characterized by entire loss of chromosome 22. Furthermore, *SMARCB1* germline mutations are found in 27% of the patients (Holdhof et al. 2020a; Ho et al. 2020). Subtype-specific enriched pathways are melanogenesis, BMP signaling, which includes the expression of growth factors and cytokines, Wnt signaling, and ciliogenesis. Related upregulated genes are *TYR*, *MITF*, and *CCND1*. In addition, mesenchymal genes like *OTX2*, *LMX1A*, and *BMP4* are overexpressed in this subtype (Johann et al. 2016; Ho et al. 2020).

AT/RT-MYC tumors make up about 23% of the cases. The sex distribution is similar to AT/RT-SHH and AT/RT-TYR (52-54% male). The patients exhibiting this subtype are relatively old, with a median age of 27 months. Furthermore, these are the only tumors that can occur in the spinal cord (12%), but half the tumors are again located supratentorially and 38% infratentorially. AT/RT-MYC usually exhibit broad deletions of chromosome 22, including

SMARCB1, however, germline mutations are very rare (7%; Holdhof et al. 2020a; Ho et al. 2020). Signature genes are involved in the ECM, including collagens, and *HOX* genes are also enriched. Additional upregulated genes in AT/RT-MYC are *MYC* and *REST* (Johann et al. 2016; Ho et al. 2020).

Very rare tumors present *SMARCA4* mutations that are characterized by point mutations or focal deletions. These cases belong to AT/RT-SMARCA4 (0.5-2%), whose patients show a male predominance (70%). The patients are the youngest compared to the other subtypes, with a median age of 3 months. Also, these tumors are mainly located supratentorially (67%). A special characteristic is the high frequency of germline mutations (73%). Subtype-specific enriched genes are *EPHA5*, *ROCK1*, and *FGF10* (Holdhof et al. 2020a).

The AT/RT DNA methylation subtypes also differ in their outcomes. The worst prognosis is known for AT/RT-SMARCA4. AT/RT-SMARCA4 is associated with global hypomethylation, which in turn is associated with a poor prognosis in different cancer entities (Sive et al. 2016; Notaro et al. 2016). In addition, the patients are very young, and therefore, radiotherapy can not be applied in most cases. The best prognosis is observed for AT/RT-TYR, a globally hypermethylated tumor, especially if the patients are older than 12 months. Frühwald et al. defined different risk groups, with age <1 year and non-TYR signature as high risk (five-year OS = 0%), <1 year and AT/RT-TYR or ≥1 year and non-TYR as intermediate risk (five-year OS = 32.5 ± 8.7%), and ≥1 year and AT/RT-TYR as standard risk (five-year OS = 71.5 ± 12.2%; Frühwald et al. 2020). Federico et al. reported the best survival for AT/RT-SHH-1B, which include the oldest patients (Federico et al. 2022).

In summary, the AT/RT DNA methylation subtypes differ regarding their clinical characteristics and gene expression profiles. Different localizations suppose distinct cellular origins, and the subtypes should be considered for the development of novel treatments.

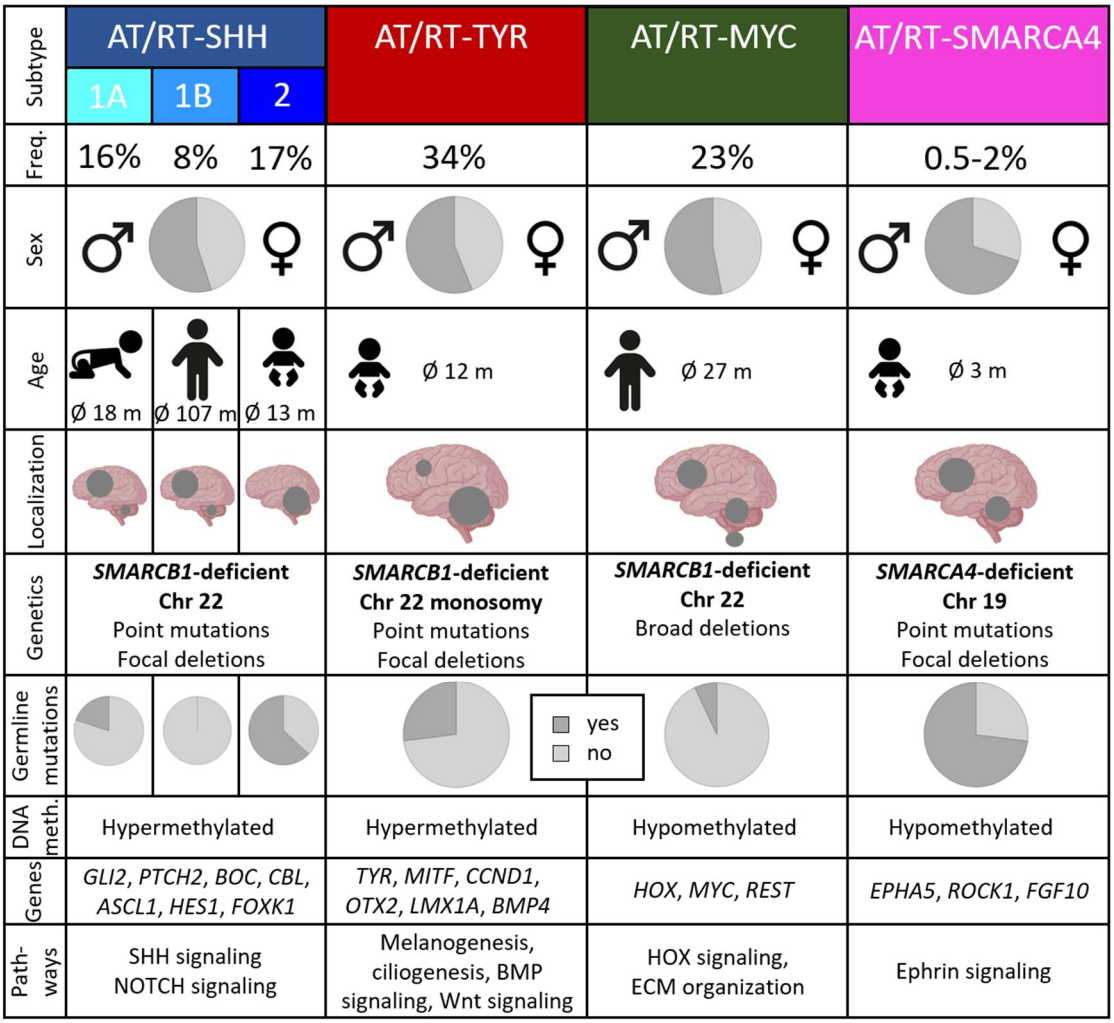

Figure 2: AT/RT DNA methylation subtypes with clinical and molecular characteristics. Three major *SMARCB1*-deficient subtypes have been identified based on DNA methylation profiling: AT/RT-SHH (blue) with the subgroups AT/RT-SHH-1A, -1B, and -2, AT/RT-TYR (red), and AT/RT-MYC (green). *SMARCA4*-deficient tumors form their own DNA methylation subtype: AT/RT-SMARCA4 (pink). The subtypes demonstrated differences in frequency, sex and age distribution, tumor localization, mutation type and frequency of germline mutations, as well as in their global DNA methylation and gene expression profiles. Modified after Holdhof et al. 2020a, Ho et al. 2020, and Johann et al. 2016.

1.6 Histopathology and diagnosis of AT/RT

Microscopically, AT/RT are mainly characterized by rhabdoid cells, which can be arranged in nests or sheets. Rhabdoid cells have eccentric nuclei with prominent eosinophilic nucleoli. The chromatin is vesicular, and the cytoplasm is abundant (Biswas et al. 2016; Louis et al. 2021). Additional features are the presence of poorly differentiated small-round-blue cells as well as mesenchymal and epithelial areas, the proportion is also dependent on the DNA methylation subtype. AT/RT-SHH are mainly comprised of small-round-blue cells, ATRT-TYR of epithelial cells, and AT/RT-MYC of mesenchymal and rhabdoid cells (Zin et al. 2021).

Because the tumors are very heterogeneous and despite of the very characteristic rhabdoid cells, AT/RT generally cannot be diagnosed solely by the use of histopathology (Rorke et al.

1996; Burger et al. 1998). IHC of SMARCB1 or SMARCA4 is needed to confirm the diagnosis (Judkins et al. 2004; Schneppenheim et al. 2010). Furthermore, DNA methylation profiling is required to determine the molecular subtype.

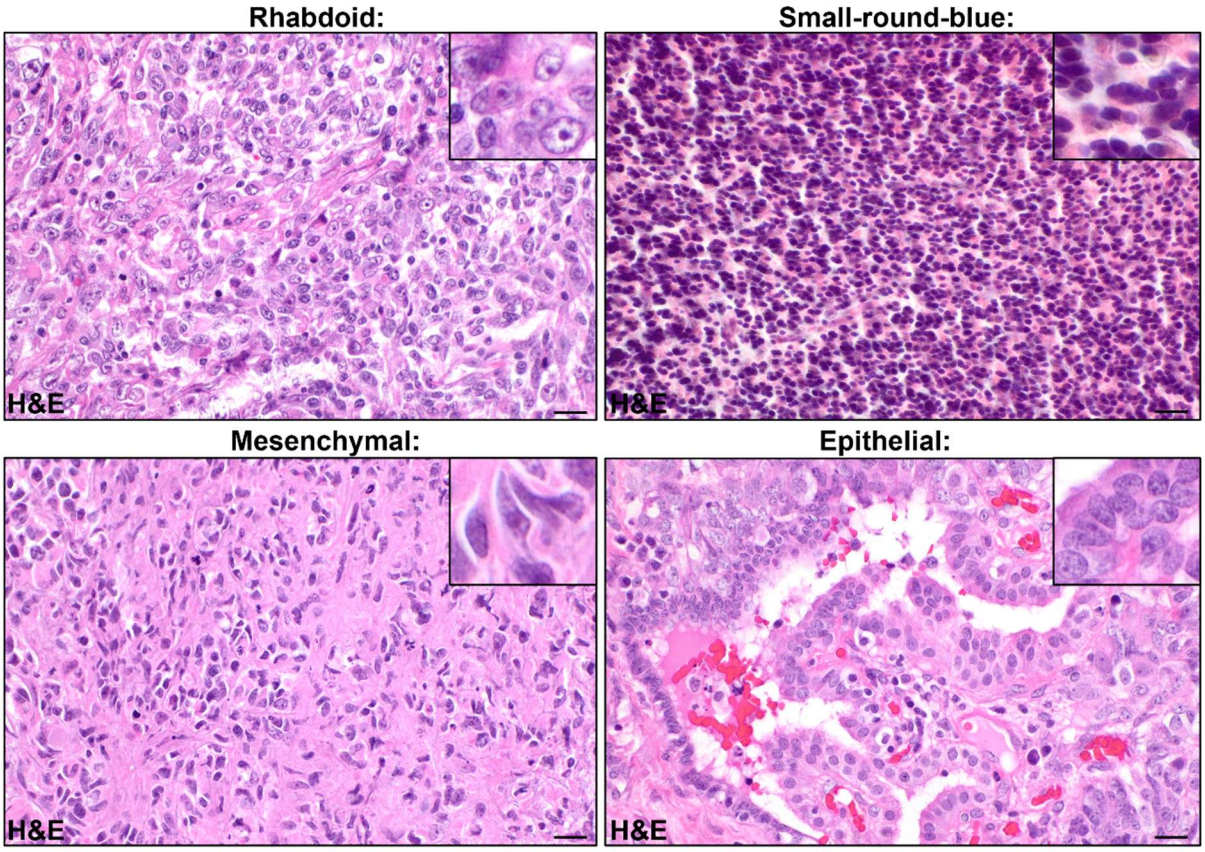

Figure 3: AT/RT morphological patterns. Hematoxylin and Eosin (H&E) stainings of rhabdoid, small-round-blue, mesenchymal, and epithelial areas of AT/RT biopsies. Scale bars indicate 20 µm.

1.7 Cellular origins of AT/RT

The cells of origin of a tumor are defined as the cells that acquire the first genetic deficit. It is very important to identify the cellular origins of the different tumor entities and subtypes, because it potentially allows an earlier diagnosis and a better prediction of the tumor development and behavior. In addition, this knowledge helps to develop targeted therapies for the distinct entities (Visvader 2011).

The cellular origins of AT/RT mainly remain unknown. Due to the different localizations, ages, molecular profiles, and mutations, distinct cellular origins are assumed for the DNA methylation subtypes. For AT/RT-SHH and AT/RT-MYC, hypotheses regarding the cellular origins exist because there are mouse models developing tumors with similar features and single-cell RNA sequencing (scRNAseq) data that validated these features (see section 1.8). But for AT/RT-

TYR and AT/RT-SMARC4, mouse models are lacking, and the cellular origins are completely unknown.

AT/RT-SHH are supposed to arise from neural progenitors (Jessa et al. 2019; Graf et al. 2022), more precisely from the midbrain-hindbrain boundary or the ganglionic eminence, depending on the localization of the tumor (Lobón-Iglesias et al. 2023).

Contrary, AT/RT-MYC are assumed to arise from pluripotent germ cells (PGCs), which are specialized precursors of the gametes occurring in the epiblast stadium (Shahbazi 2020; Graf et al. 2022). Other studies in mice showed that a *Smarcb1* loss in the early neural crest led to the development of RT with characteristics of eMRT (extracranial tumors) or AT/RT-MYC (intracranial tumors; Vitte et al. 2017). Custers et al. confirmed this finding by phylogenetic analyses of eMRT (Custers et al. 2021).

These hypotheses derive from different mouse models, which will be described in the following section.

1.8 AT/RT mouse models

Mouse models are essential to investigate the development of tumors to get insights into the cellular origins and developmental timepoints. This knowledge is mandatory for the development of targeted therapies, which then need to be tested in appropriate mouse models. Because, adequate mouse models for AT/RT are lacking, the cellular origins of these tumors remaining largely unknown.

To identify the cellular origins, numerous genetically modified mouse models were generated. As homozygous *Smarcb1* knockout in embryonic stem cells led to embryonic death of mice, and heterozygous loss only resulted in MRT-like tumors (Roberts et al. 2002; Klochendler-Yeivin et al. 2006), the *Cre/loxP* system was used for the generation of further models. The *Cre/loxP* system allows a targeted gene knockout in specific cells and at specific timepoints. Basically, the gene of interest is flanked by *loxP* sites (*fl* = *floxed* = *flanked by loxP*), enabling recognition by the *Cre* recombinase, which then cuts off the flanked gene at the *loxP* sites. The resected DNA ligates at its *loxP* sites and will be degraded, which results in a knockout of the respective gene. By combining the *Cre* recombinase with specific promoters that are only expressed in specific cells at specific timepoints, a targeted knockout can be induced (Ray et al. 2000). The expression can also be controlled by using $CreER^{T2}$ recombinases, which can be induced by tamoxifen (Tam; Feil et al. 2009). In this case, the promoter only determines the target cells, but the start of expression is controlled by the application of tamoxifen. This is how different *Smarcb1*-deficient mouse models were generated. $Math1\text{-}cre::Smarcb1^{fl/fl}$ mice have not developed any tumors, but they suffered from severe malformations of the cerebellum.

Math1 starts to be expressed at E9.5 in the rhombic lip and hindbrain precursors (Moreno et al. 2014). *Rosa-26-creER^{T2}::Smarcb1$^{fl/fl}$* and *Sox2-creER^{T2}::Smarcb1$^{fl/fl}$* mice developed intracranial and extracranial RT. These showed similarities to human AT/RT-SHH and AT/RT-MYC, depending on the timepoint of tamoxifen application (between E6.5 and E10.5) and the localization of the tumors (Han et al. 2016; Graf et al. 2022). *Rosa-26-creER^{T2}::Smarcb1$^{fl/fl}$* mice, induced at E6.5, had a tumor penetrance of 40% with a median age of disease onset of 17 weeks. *Rosa26* is broadly expressed in the entire murine brain. *Sox2-creER^{T2}::Smarcb1$^{fl/fl}$* mice, induced at E6.5, had a lower tumor penetrance with only 22%, and also the median age was higher, with 27 weeks, compared to the *Rosa-26-creER^{T2}::Smarcb1$^{fl/fl}$* mice. *Sox2* expression starts in the neural plate and neuroepithelium, and therefore, it targets neural progenitors. *P0-cre::Smarcb1$^{fl/fl}$* mice target the neural crest starting at E9.5 and developed tumors similar to human AT/RT-MYC or eMRT (Vitte et al. 2017). Furthermore, there is a model with an additional *p53* knockout: *hGFAP-cre::Smarcb1$^{fl/fl}$::p53$^{fl/fl}$*. These mice developed AT/RT-like tumors originating from the cerebellum, with an age of onset distributed across a 12-month period (earliest after 4 weeks), but with 100% tumor penetrance. *hGFAP* expression starts at E13.5 in astrocyte precursors like radial glia (Ng et al. 2015). In summary, it was previously possible to generate AT/RT-like tumors, similar to AT/RT-SHH and AT/RT-MYC, but the mice were relatively old in comparison to human patients, and tumors did not arise consistently. A pediatric model is still lacking, as well as a model for AT/RT-TYR in general.

The same approach was used to generate a high number of different *Smarca4*-deficient mice, and some examples are described in this section. Heterozygous and homozygous knockouts of *Smarca4* resulted in embryonal death or early death after birth, and no tumors (Bultman et al. 2000). This was also observed in *Rosa26-creER^{T2}::Smarca4$^{fl/fl}$* mice (Singh et al. 2016). Other mouse models suffered from developmental disorders and early death, like *Math1-cre::Smarca4$^{fl/fl}$* mice presenting with a hypoplastic cerebellum (Moreno et al. 2014) and *hGFAP-cre::Smarca4$^{fl/fl}$* mice with underdeveloped cerebral and cerebellar structures (Holdhof et al. 2020b). *Math1-creER^{T2}::Smarca4$^{fl/fl}$* mice, with induction at postnatal day 3 (P3), demonstrated increased proliferation of granular cell precursors (GCPs; Holdhof et al. 2021a), and *Sox2-creER^{T2}::Smarca4$^{fl/fl}$* mice (induction between E6.5 and E14.5) suffered from impaired brain and eye development (Holdhof et al. 2021b). Overall, a *Smarca4* loss induced severe developmental disorders in mice, which emphasizes an important role in embryonal development. A *Smarca4*-deficient mouse model that develops RT-like tumors is completely lacking.

1.9 Tumor progression, recurrence, and therapy resistance

The development of therapy resistance is the main cause for treatment failure. Different theories regarding the underlying mechanisms, how the tumors progress or recur under therapy, exist.

Overall, it is assumed that tumor recurrences arise from dormant tumor cells. These cells are characterized by drug resistance and immune escape. Dormancy is a quiescent state with tumor cells being viable but not proliferative, which can be activated by different stimuli (Phan and Croucher 2020; Damen et al. 2021; Wang et al. 2024; Tufail et al. 2025). There are different types of dormancy: Cellular, immunological, and angiogenic dormancy. As described above, cellular dormancy refers to a quiescent state of tumor cells, which are in a reversible cell cycle arrest. Angiogenic dormancy describes a tumor state where tumor growth is restricted due to insufficient blood supply, for instance, when no new blood vessels are formed. Lastly, the immunological dormancy refers to tumor cells being strictly controlled by the immune system, which can lead to the inhibition of proliferation (Tufail et al. 2025).

Mechanisms for the induction of dormancy can be genetic or epigenetic alterations, as well as influences from the TME, for instance, the ECM. Stimuli for reversing dormancy are directly associated with the development of tumor recurrences by reactivating the proliferation of the tumor cells. The TME is supposed to be one of the main contributors. It can provide stimuli for sustaining dormancy or reactivating proliferation. Within the TME, interleukins and growth factors, such as TGF-β, were found to act as such reactivating stimuli. Additionally, alterations in the ECM remodeling can induce proliferation. Respective alterations mainly include increased stiffness and cross-linking (Barkan et al. 2010; Comba et al. 2022; Tufail et al. 2025).

In the context of dormancy, cancer stem cells (CSCs) have reached high interest. These are cancer cells with a stem cell-like character, which are known to be able to initiate and control tumor growth. In addition, they can enter a quiescent dormancy state and evade therapies that mainly target proliferating cells. After reactivation, they can induce the initiation and proliferation of tumor cells, leading to the development of recurrences. Overall, CSCs are characterized by latent metabolism and therapy resistance, which can induce tumor proliferation. They are capable of performing self-proliferation and also of transforming into a dormant state (Esmatabadi et al. 2016; Tufail et al. 2025).

Nevertheless, not only dormancy and CSC are supposed to be the drivers of tumor recurrence. Another hypothesis is that recurrence is induced by neosis. Neosis is a type of cell division found in cancer, which is different compared to mitosis and meiosis (Esmatabadi et al. 2016). It is active in the senescent phase of some cells, which is a quiescent, non-proliferative state at the end of the mitotic life span (Rajaraman et al. 2006). Neosis is characterized by nuclear

budding for chromosome distribution and asymmetric cytokinesis. The cells resulting from neosis are small, aneuploid, and mitotically active. Overall, neosis can prolong the mitotic life span of tumor cells, which could result in tumor progression or recurrence after reactivation of senescent cells (Rajaraman et al. 2006; Esmatabadi et al. 2016).

The third hypothesis regarding the induction of tumor recurrence is phoenix rising. This is a mechanism where apoptotic cells, such as those induced by therapy, send signals that stimulate growth and division of neighboring cells. This could induce and promote the formation of new tumor cells that develop to tumor recurrences (Li et al. 2010; Huang et al. 2011; Esmatabadi et al. 2016).

In conclusion, various hypotheses regarding tumor progression and recurrence exist, but the exact mechanisms are not completely clear, and they might differ between different tumor entities. Overall, tumor recurrences arising from therapy-resistant dormant cells are a widely distributed theory for many CNS tumor entities, like glioblastoma and medulloblastoma (MB; Rusu et al. 2019; Holmberg et al. 2024).

1.10 Aim of this work

Overall, this work focuses on the characterization of the development of AT/RT. The project is divided into two parts:

The first part deals with the identification and characterization of mechanisms regarding tumor progression and recurrence in AT/RT. For this purpose, we collected paired AT/RT primary tumors and recurrences of all DNA methylation subtypes. We investigated differences on histological, DNA methylation, and gene expression level. Therefore, we performed clustering analyses, identified CNVs and differentially expressed genes and pathways. For this, we generated bulk- and snRNAseq data, which were further used to identify and characterize therapy-resistant cells. Our findings were validated *in vitro* and by a correlation with clinical parameters.

The second aim was to identify the cellular origins of AT/RT-SMARCA4 and AT/RT-TYR. For these two subtypes, the cellular origins remain completely unknown, whereas for AT/RT-SHH and AT/RT-MYC at least hypotheses, resulting from mouse models and scRNAseq analyses, exist. As there are no mouse models for either, the aim was to generate models that could give insights into the development of AT/RT-SMARCA4 and AT/RT-TYR. No *Smarca4*-deficient mice have developed any tumors so far, and therefore, we aimed to test promotor-driven *Cre* lines that worked for the generation of *Smarcb1*-deficient RT-like tumors. For AT/RT-TYR, we wanted to identify cell type signatures using histopathology and gene expression profiles, which we then aimed to specifically target with an appropriate promoter-driven *Cre* line.

Taken together, this work aimed to further identify the developmental processes of AT/RT by investigating their cellular origins and mechanisms of therapy resistance and recurrence. This is important to identify novel targets for therapeutic approaches.

2. Publication 1

Recurrent atypical teratoid/rhabdoid tumors (AT/RT) reveal discrete features of progression on histology, epigenetics, copy number profiling, and transcriptomics

Pascal D. Johann*, Lea Altendorf*, Emma-Maria Efremova, Till Holsten, Mona Steinbügl, Karolina Nemes, Alicia Eckhardt, Catena Kresbach, Michael Bockmayr, Arend Koch, Christine Haberler, Manila Antonelli, John DeSisto, Martin U. Schuhmann, Peter Hauser, Reiner Siebert, Susanne Bens, Marcel Kool, Adam L. Green, Martin Hasselblatt, Michael C. Frühwald*, Ulrich Schüller*

Acta Neuropathologica 2023

*These authors contributed equally to this work

Acta Neuropathologica
https://doi.org/10.1007/s00401-023-02608-7

ORIGINAL PAPER

Recurrent atypical teratoid/rhabdoid tumors (AT/RT) reveal discrete features of progression on histology, epigenetics, copy number profiling, and transcriptomics

Pascal D. Johann[1,2,3] · Lea Altendorf[4,5] · Emma-Maria Efremova[4,5] · Till Holsten[4,5,6] · Mona Steinbügl[1] · Karolina Nemes[1] · Alicia Eckhardt[4,5,7] · Catena Kresbach[4,5,6,8] · Michael Bockmayr[4,5,8] · Arend Koch[9] · Christine Haberler[10,11] · Manila Antonelli[12] · John DeSisto[13] · Martin U. Schuhmann[15] · Peter Hauser[16] · Reiner Siebert[17] · Susanne Bens[17] · Marcel Kool[2,3,18] · Adam L. Green[13,14] · Martin Hasselblatt[19] · Michael C. Frühwald[1] · Ulrich Schüller[4,5,6]

Received: 21 April 2023 / Revised: 22 June 2023 / Accepted: 26 June 2023
© The Author(s) 2023

Abstract
Atypical teratoid/rhabdoid tumors (AT/RT) are the most common malignant brain tumors manifesting in infancy. They split into four molecular types. The major three (AT/RT-SHH, AT/RT-TYR, and AT/RT-MYC) all carry mutations in *SMARCB1*, the fourth quantitatively smaller type is characterized by *SMARCA4* mutations (AT/RT-SMARCA4). Molecular characteristics of disease recurrence or metastatic spread, which go along with a particularly dismal outcome, are currently unclear. Here, we investigated tumor tissue from 26 patients affected by AT/RT to identify signatures of recurrences in comparison with matched primary tumor samples. Microscopically, AT/RT recurrences demonstrated a loss of architecture and significantly enhanced mitotic activity as compared to their related primary tumors. Based on DNA methylation profiling, primary tumor and related recurrence were grossly similar, but three out of 26 tumors belonged to a different molecular type or subtype after second surgery compared to related primary lesions. Copy number variations (CNVs) differed in six cases, showing novel gains on chromosome 1q or losses of chromosome 10 in recurrences as the most frequent alterations. To consolidate these observations, our cohort was combined with a data set of unmatched primary and recurrent AT/RT, which demonstrated chromosome 1q gain and 10 loss in 18% ($n=7$) and 11% ($n=4$) of the recurrences ($n=38$) as compared to 7% ($n=3$) and 0% ($n=0$) in the primary tumors ($n=44$), respectively. Similar to the observations made by DNA methylation profiling, RNA sequencing of our cohort revealed AT/RT primary tumors and matched recurrences clustering closely together. However, a number of genes showed significantly altered expression in AT/RT-SHH recurrences. Many of them are known tumor driving growth factors, involved in embryonal development and tumorigenesis, or are cell-cycle-associated. Overall, our work identifies subtle molecular changes that occur in the course of the disease and that may help define novel therapeutic targets for AT/RT recurrences.

Keywords AT/RT · Rhabdoid tumor · Pediatric cancer · Recurrent tumor · DNA methylation · RNA sequencing

Introduction

Malignant rhabdoid tumors (MRTs) mainly affect infants and young children. They are known for their highly aggressive behaviour and dismal prognosis with 5-year overall survival (OS) ranging from 0% to 78% depending on risk groups [11, 30]. Most commonly, they are located in the central nervous system (CNS, 66%), where they are termed atypical teratoid/rhabdoid tumors (AT/RT).

AT/RT may be divided into four molecular types, which differ in their clinical behaviour, genetics, epigenetic signature, and gene expression profile. The three main types are AT/RT-SHH, AT/RT-TYR, AT/RT-MYC and AT/RT-SMARCA4 is only rarely represented [16, 17, 29]. AT/RT-SHH tumors can further be divided into three subtypes that differ by localization, clinical outcome and methylation profile: AT/RT-SHH-1A, AT/RT-SHH-1B, and AT/

Pascal D. Johann, Lea Altendorf, Michael C. Frühwald, and Ulrich Schüller have contributed equally to this work.

Extended author information available on the last page of the article

Published online: 14 July 2023

RT-SHH-2 [9]. In 95% of all AT/RT, the underlying genetic cause is a mutation of the *SMARCB1* gene [3]. SMARCB1 is part of the SWItch/sucrose non-fermentable (SWI/SNF) complex, which is involved in gene regulation and tumor development [31]. *SMARCB1* mutations are already present in the germline in up to 30% of patients, who then suffer from a rhabdoid tumor predisposition syndrome 1 (RTPS1; OMIM #609322) [10, 25]. In rare cases, the *SMARCA4* gene is affected instead [14, 24] (AT/RT-SMARCA4). If the mutation is already presented in the germline, patients suffer from a rhabdoid tumor predisposition syndrome 2 (RTPS2; OMIM #613325) [10, 25]. Patients with tumors of this molecular type carry germline mutations even more often than patients with *SMARCB1* mutated AT/RT, present at younger age, and suffer from an inferior prognosis with shorter survival times. The best prognosis is observed for AT/RT-TYR, especially when patients are older than 12 months [11, 30].

The treatment of AT/RT is challenging, and progression is inevitabley observed, if the tumor is non-responsive to therapy. Even if patients reach remission following gross total resection, tumors recur in up to 50% of patients. In fact, only very few of patients suffering from recurrences are still alive 5 years following diagnosis of a recurrence [8, 26]. Molecular alterations, which are responsible for or contribute to tumor progression or recurrence, are currently largely unknown. It will be helpful to identify these molecular alterations and thus possible therapeutic targets for patients with recurrent tumors. Biopsies of AT/RT recurrences are only rarely available. This has impeded the research on specific histological and molecular features and the development of targeted therapies in the past.

In this study, samples of a relatively large and unique cohort of 26 patients, all suffering from recurrent AT/RT, were analyzed. We summarize the clinical course of the patients and provide in-depth molecular data comparing primary and recurrent tumor samples using histological analysis, DNA methylation profiling, and RNA sequencing.

Materials and methods

Data sets

Clinical information was derived from the databases of the EU-RHAB registry. EU-RHAB has received continuous ethical approval (Ethics Committee University of Münster, Germany 2009-532-f-S, most recently amended 17AUG2021). Genomic, histological, DNA methylation, and RNA sequencing data were collected from the different laboratories Hamburg, Heidelberg, Denver, Kiel, and Ulm. Resampling was performed during autopsy for cases 13, 19, 20, and 21, and via biopsy or resection in all other cases (Table 1). Reference data sets consist of unpublished or published data summarized in Supplementary Tables 1 and 2.

Histology and immunohistochemistry

Tumor samples were fixed in 4% formaldehyde for 24 h. Subsequently, they were dehydrated, embedded in paraffin, and sectioned at 4 µm. Hematoxylin and Eosin (H&E) staining was performed using standard protocols. Immunohistochemical stainings were done using a Ventana System (Roche) according to manufacturers' specifications. The antibodies rabbit anti-Ki67 (Abcam #ab16667, 1:200) and mouse anti-BAF47 (BD Biosciences #612110, 1:50) were used for Ki67 and SMARCB1 stainings. For 19 patients, the mitotic figures of ten high power fields (HPF) were counted for each primary tumor and related recurrence with subsequent comparison of the averages. Ki67-positive nuclei of 16 cases were counted and the frequency was compared between primary and recurrent AT/RT. Significance was determined using a *t* test for paired data. SMARCB1-deficiency was identified by immunohistochemical staining using anti-SNF5/SMARCB1 antibody (Abcam #ab88589, 1:50). For SMARCA4-deficient cases, anti-BRG1 antibody (Abcam #ab110641, 1:25) was used.

DNA methylation profiling

The DNA of the tumor samples from FFPE tissue was isolated using "Maxwell® FFPE DNA Kit" (Promega) according to manufacturer's specifications. For KRYO-conserved samples, the DNA was isolated using the "High Pure PCR Template Preparation Kit" (Roche). Bisulfite conversion was performed with the "EZ DNA Methylation Kit" (Zymo Research) using 100–500 ng DNA. FFPE DNA was cleaned and converted using the "DNA Clean & Concentrator-5 Kit" (Zymo Research) and the "Infinium HD FFPE DNA Restore Kit" (Illumina). This cleaning and conversion step was not necessary for KRYO DNA. In a final step, the methylation status of 450,000 or 850,000 CpG sites was analyzed on an "iScan device" (Illumina) after hybridizing the DNA to a "HumanMethylation450" or a "MethylationEPIC" BeadChip array (Illumina), respectively.

Identification of molecular types based on DNA methylation data

The tumor entity and molecular types AT/RT-SHH, AT/RT-MYC, and AT/RT-TYR were identified using the brain tumor classifier (v12.5, www.molecularneuropathology.org), which is a platform for DNA methylation-based classification of CNS tumors. Results were validated by *t*-stochastic neighbour embedding (*t*-SNE) analysis. So far, the classifier cannot identify AT/RT-SMARCA4 or AT/RT-SHH

Table 1 Molecular and clinical data of all analyzed patients with samples for primary AT/RT and recurrences ($n=26$)

Case No	Sex	Age of onset [years]	Localization	Molecular type and subtype	Resection status	Pathogenic *SMARCB1* germline variant	Time to first re-sampling [months]	Therapy protocol	Follow-up [months]	Status
1	m	5.0	Supratentorial	SHH-1A	Subtotal resection	Wild type	30.5	Rhabdoid 07	70.5	Dead
2	m	1.8	Supratentorial	SHH-1B	Subtotal resection	Wild type	41.0	EU-RHAB	57.4	Alive
3	m	1.6	Supratentorial	TYR	Subtotal resection	wild Type	25.5	Rhabdoid 07	59.2	Dead
4	m	0.1	Infratentorial	TYR	Subtotal resection	Wild type	5.0	EU-RHAB	12.0	Dead
5	f	2.0	Supratentorial	SHH-1B	n.a.	n.a.	3.3	HIT SKK 87	10.6	Dead
6	m	2.0	Supratentorial	MYC	Subtotal resection	n.a.	1.5	EU-RHAB	6.1	Dead
7	f	0.4	Infratentorial	SHH-2	Subtotal resection	c.170delTG	4.5	Rhabdoid 07	23.3	Dead
8	m	0.1	Infratentorial	TYR	Subtotal resection	Wild type	4.0	EU-RHAB	10.0	Dead
9	f	1.0	Infratentorial	TYR	Gross total resection	Wild type	5.3	Rhabdoid 07	85.3	Alive
10	m	2.0	Infratentorial/spinal	MYC/SHH-2	Subtotal resection	c.118C > T	n.a.	EU-RHAB	90.0	Alive
11	m	5.0	Supratentorial	SHH-1A	n.a.	Wild type	16.5	n.a.	99.2	Alive
12	f	0.9	Infratentorial	SHH-2/SHH-1A	Subtotal resection	c.157C > T p.R53X	48.0	EU-RHAB	48.0	Dead
13	m	10.0	n.a.	MYC	n.a.	c.157C > T p.Arg53*	n.a.	n.a.	n.a.	Dead
14	m	2.1	Infratentorial	TYR	Subtotal resection	Wild type	5.5	EU-RHAB	24.0	Dead
15	m	2.2	Supratentorial	SHH-1B	Gross total resection	n.a.	6.0	EU-RHAB	45.0	Dead
16	m	5.0	Supratentorial	SHH-1A	Subtotal resection	Wild type	32.5	EU-RHAB	9.0	Dead
17	f	1.0	Supratentorial	TYR	n.a.	n.a.	10.0	n.a.	n.a.	n.a.
18	m	2.5	Supratentorial	MYC	Gross total resection	Yes	11.0	Individual	17.6	Dead
19	m	2.7	Supratentorial	SHH-1B	Subtotal resection	n.a.	18.0	DFCI protocol	18.0	Dead
20	m	3.2	Supratentorial	SHH-1A	Subtotal resection	n.a.	15.0	DFCI protocol	15.0	Dead
21	f	1.3	Supratentorial	SHH-2/SHH-1B	Biopsy	c.118C > T	10.0	Individual	10.0	Dead
22	m	0.7	Infratentorial	MYC	Gross total resection	n.a.	6.0	Individual	6.0	Dead
23	m	0.6	Supratentorial	SHH-1A	n.a.	Wild type	6.7	EU-RHAB	16.0	Dead
24	m	1.4	Infratentorial	SMARCA4	n.a.	Wild type[a]	n.a.	n.a.	28.0	Dead
25	f	2.0	Supratentorial	SHH-1A	Subtotal resection	yes	37.0	EU-RHAB	37.9	Alive
26	m	1.2	Infratentorial	TYR	n.a.	yes	5.0	n.a.	5.0	Alive

Table including characteristics of all cases with paired primary tumors and recurrences. The cases 1, 6, and 7 had two recurrences and the case 7 also two primary tumors. Molecular type of each tumor was determined using brain tumor classifier (v12.5) (www.molecularneuropathology.org) and AT/RT-SHH subtypes were determined according to *t*-SNE plot (Fig. 3b). AT/RT-SMARCA4 was identified by *SMARCA4* mutation. Types or subtypes of cases 10, 12, and 21, and localization of case 10 are listed as primary tumor/recurrence

m male, *f* female, *n.a.* not available, *DOX* doxorubicin, *ICE* ifosfamide, carboplatinum, etoposide, *VCA* vincristine, cyclophosphamide, actinomycin, *VCD* vincristine, cyclophosphamide, doxorubicin, *TMZ* temozolomide, *DTIC* dacarbazine

[a]Pathogenic *SMARCA4* germline variant (c.2335 G > A)

Re-sampling was performed during autopsy for cases 13, 19, 20, 21 and via biopsy or resection in all other cases. Therapy according to EU-RHAB included either 9 alternate courses (3 × DOX, ICE, VCA) or 6 alternate courses (2 × DOX, ICE, VCA), followed by high-dose chemotherapy with Carboplatin/Thiotepa, with both arms involving intraventricular methotrexate (MTX) until start of radiotherapy (RTX). RTX was administered if the patient was older than 18 months of age. Rhabdoid 2007 included 9 cycles of chemotherapy (5 × VCD and 4 × ICE) and intraventricular chemotherapy (MTX or MTX/cytarabine/hydrocortisone) until start of RTX. RTX was only applied to children of more than 18 months of age. The HIT SKK 87 trial involved procarbazine, ifosfamide, etoposide, MTX, cytarabine and cisplatinum as induction therapy given in two cycles, followed by maintenance therapy with procarbazine, MTX and vincristine until start of RTX. The Dana Farber Cancer Institute (DFCI) protocol consisted of a modified IRS-III regimen involving VCR, ACT D, cyclophosphamide, cisplatin, DOX, and TMZ in lieu of DTIC as well as intrathecal chemotherapy with MTX, cytarabine and hydrocortisone and focal (M0) or CSI (M +) RTX

subtypes. AT/RT-SHH-1A, AT/RT-SHH-1B and AT/RT-SHH-2 were allocated to our cases based on a *t*-SNE analysis. AT/RT-SMARCA4 cases were identified by *SMARCA4* mutation. Therefore, classifier scores only refer to AT/RT-SHH, AT/RT-MYC, and AT/RT-TYR. To demonstrate how the 26 cases of our cohort fit into the landscape of established AT/RT subtypes, we also included a large cohort of reference cases from all known molecular types ($n = 138$). Reference data sets consist of unpublished or published data summarized in Supplementary Tables 1 and 2.

RNA sequencing

RNA isolation from FFPE and KRYO tissue samples was performed using "Maxwell® RSC RNA FFPE Kit" (Promega). An "RNA 6000 Nano Chip" was inserted on an "Agilent 2100 Bioanalyzer" (Agilent Technologies) to analyze RNA integrity. Next, depletion of ribosomal RNA was performed using the "RiboCop rRNA Depletion Kit" (Lexogen). Subsequently, the "CORALL Total RNA-Seq Library Prep Kit" (Lexogen) was used for the generation of a RNA sequencing library. Concentration measurement was performed for all samples with the "Qubit 2.0 Fluorometer" (Thermo Fisher Scientific) and the distribution of the final libraries' fragment lengths was determined using the "DNA High Sensitivity Chip", again on an "Agilent 2100 Bioanalyzer" (Agilent Technologies). The concentration of all samples was adjusted to 2 nM to pool them at equimolar concentrations. Sequencing of the library pool was done on a "NextSeq500" (Illumina) with 1×75 bp, with 24.5 to 35.1 million reads per sample.

Bioinformatics and statistics of DNA methylation data

DNA methylation analysis was performed using raw IDAT files resulting from DNA methylation profiling. The files were processed and visualized using "R Studio" (version 4.1.3). IDAT files were loaded using the *minfi* package (version 1.40.0). Data from 450 k and EPIC arrays were combined and preprocessed using the *Noob* function for normalization. All probes containing SNPs within two nucleotides around a CpG site were removed as well as probes targeting the sex chromosomes. Probes which did not explicitly target the human genome were removed from analysis. Batch effects introduced due to different array and conservation types were removed using *ComBat*-function from *sva* R package (version 3.42.0). To make sure that primary tumors and related recurrences belonged to the same patient, a genotype matching was performed. By identification of common SNPs, we could ensure if primary tumor and recurrence belonged to one patient. Finally, the 1000 CpG sites with the largest standard deviation across all patient samples were chosen for further analysis of DNA methylation data. A heatmap was created using the R package *ComplexHeatmap* (version 2.10.0). The clustering distance metric for columns and rows was defined as "Pearson". In addition, the clustering method for columns and rows was set as "average". A *t*-SNE analysis was implemented using the R package *Rtsne* (version 0.16)). The values for the *t*-SNE analysis were calculated by defining the "eigenvalue k" as "$k = 50$", and 100 random numbers were created using "set.seed(100)". The arguments for *Rtsne* function were set as "max_iter = 2000" and "perplexity = 20". Changes of molecular type or subtype were visualized in an alluvial plot using *ggalluvial* package. Primary-recurrence variation was defined as the Jensen–Shannon divergence (JSD) between recurrences and related primary tumors based on the 1000 CpG sites with the largest standard deviation using the *philentropy* R package. Significant differences in global DNA methylation patterns for all CpG sites were determined using a Wilcoxon test for independent samples. For methylation-derived copy number variations (CNV), the individual copy number profiles were calculated based on raw methylated/unmethylated signals using the *conumee* R package (version 1.28.0). Ratios were normalized against reference samples and cutoff using the local (arm segment) threshold 0.25 and -0.25, respectively.

Bioinformatics and statistics of RNA sequencing data

Raw RNA sequencing count data were used as input for the analysis in "R Studio" (version 4.1.3). As a first step, matching HUGO symbols for the ENSEMBL IDs were added using the *biomaRt* package (version 2.52.0). Repetitively counted genes were identified and removed as well as genes from sex chromosomes. Batch effects due to different conservation types and the integration of reference cases were corrected using *ComBat_Seq* function from *sva* package (version 3.44.0). In the next step, the *DESeq2* package (version 1.36.0) was used to perform *DESeq2* analysis of raw count data. The resulting data were normalized using variance stabilized transformation (VST). Finally, the 1000 most variable genes, identified by standard deviation, were chosen for cluster analysis. A heatmap and a *t*-SNE plot were created as described for the DNA methylation data. Primary-recurrence variation was defined as the Jensen–Shannon divergence (JSD) between recurrences and related primary tumors based on the 1000 most variable genes using the *philentropy* R package. For the selection of the differentially expressed genes, all genes, identified by *DESeq2* analysis, with a significant p value ($p_{\text{adjusted}} < 0.05$) after Benjamini–Hochberg (BH) adjustment and a $\log_2$ fold change ($\log_2 \text{FC}) > 1$ were chosen. This was done for each molecular type, separately. Differentially expressed genes between primary and recurrent AT/RT were visualized in volcano plots

created with the *EnhancedVolcano* package (version 1.14.0). Log_2 of *DESeq2*-normalized counts of three upregulated and three downregulated genes in recurrences was compared to matched primary tumors. Statistical analysis was performed using *DESeq2*. Pathway analyses were performed using the *gsePathway* function of the *ReactomePA* package (version 1.40.0) with a gene list ranked by log_2 FC as input and Reactome pathways. The results were visualized using *cnetplot* function of the *enrichplot* package (version 1.16.2).

Immune cell infiltration

The infiltration of immune cells in the present tumor samples was quantified based on raw DNA methylation data and RNA sequencing count data. The estimation of the infiltration with tumor-infiltrating lymphocytes (TILs), $CD4^+$ T cells, and $CD8^+$ T cells was performed by calculation of the DIMEimmune scores according to Safaei et al. [23] using DNA methylation data. The infiltration with additional cell populations was computed from RNA sequencing data using a deconvolution method optimized for brain tumors [4, 5]. This method quantified the infiltration with T cells, $CD8^+$ T cells, cytotoxic lymphocytes, B lineage cells, NK cells, monocytic lineage cells, myeloid dendritic cells, neutrophils, endothelial cells, and fibroblasts. Significant differences were determined using a *t*-test for paired data.

Data Availability

The DNA methylation and RNA sequencing data of paired primary and recurrent AT/RT of this study are deposited at NCBI Gene Expression Omnibus (GEO; https://www.ncbi.nlm.nih.gov/geo). They are accessible through GEO Series accession numbers GSE228091 (DNA methylation) and GSE228101 (RNA sequencing).

Results

Assembly of a cohort of 26 patients with primary AT/RT and tissue from matched recurrences

A cohort of 26 patients with primary AT/RT and matched recurrences are the basis of the current study (Table 1, Fig. 1). DNA methylation profiling classified them as AT/RT-SHH, AT/RT-TYR, and AT/RT-MYC using brain tumor classifier and the subtypes AT/RT-SHH-1A, AT/RT-SHH-1B, and AT/RT-SHH-2 were assigned using *t*-SNE analysis. AT/RT-SMARCA4 was identified by *SMARCA4* mutation. The patients #1, 6, and 7 had two recurrences, and case 7 included two primary tumor samples. Each primary tumor and related recurrence had the same mutations in *SMARCB1* or *SMARCA4* (Table 1) and genotype matching confirmed

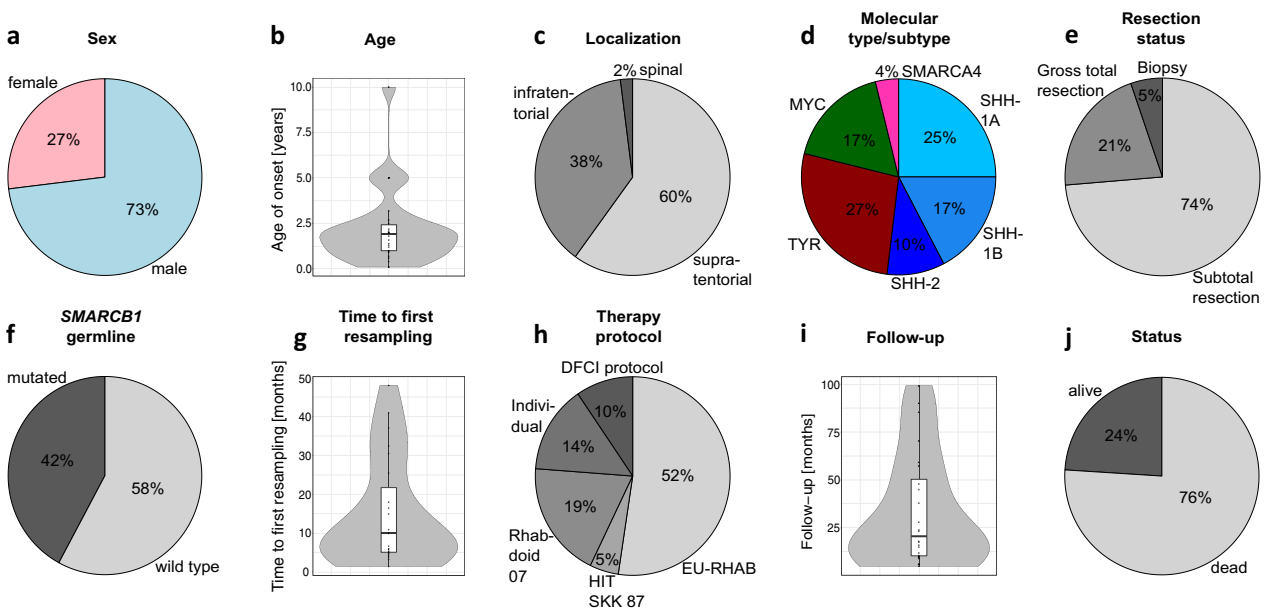

Fig. 1 Overview of molecular and clinical data referring to primary tumors of all analyzed patients with samples for primary AT/RT and recurrences ($n=26$). **a** Proportion of the gender ($n=26/26$). **b** Age distribution in years at diagnosis ($n=26/26$). **c** Proportion of the localization of primary and recurrent AT/RT ($n=50/52$). **d** Proportion of the molecular types and subtypes in primary tumors and recurrences ($n=52/52$). **e** Proportion of the resection status after surgery of the primary AT/RT ($n=19/26$). **f** Proportion of pathogenic *SMARCB1* germline variants ($n=19/26$). **g** Distribution of time of the first resampling in months ($n=23/26$). **h** Proportion of therapy protocols ($n=21/26$). **i** Distribution of the follow-up in months ($n=24/26$). **j** Proportion of alive and dead patients ($n=25/26$)

that they belonged to one patient based on the identification of common SNPs. Most of the AT/RT pairs (73%, $n = 19/26$) were from male patients (Fig. 1a), and average age of disease onset was 2.2 years (Fig. 1b). Patients, who were older than or equal to 5 years ($n = 4/26$) belonged exclusively to the AT/RT-SHH or AT/RT-MYC types, whereas patients with AT/RT-TYR tumors were very young with six out of seven cases being younger than 2 years at disease onset (Table 1). The majority of primary tumors and recurrences (60%, $n = 30/50$) was located supratentorially, 38% ($n = 19/50$) were infratentorial, and the recurrence of patient #10 was spinal (2%, $n = 1/50$, Fig. 1c). Five out of seven AT/RT-TYR and two out of three AT/RT-SHH-2 cases were localized infratentorially (Table 1). A proportion of 25% (n = 13/52) of all tumors belonged to the AT/RT-SHH-1A subtype, 17% ($n = 9/52$) to AT/RT-SHH-1B, 10% ($n = 5/52$) to SHH-2, 27% ($n = 14/52$) to AT/RT-TYR, 17% (n = 9/52) to AT/RT-MYC, and 4% ($n = 2/52$) to AT/RT-SMARCA4 (Fig. 1d). All of these observations and distributions are in line with the current literature [9, 11, 15, 16].

Furthermore, in most of the patients a subtotal resection of their primary AT/RT was achieved (74%, $n = 14/19$), whereas approximately a quarter received gross total resections (21%, $n = 4/19$). For one patient only a biopsy was performed (5%, $n = 1/19$, Fig. 1e). The single patient with the AT/RT-SMARCA4 tumor and almost half of all analyzed patients (42%, $n = 8/19$) revealed a pathogenic germline variant (Fig. 1f). The average time to first resampling ($n = 23$) was 15.1 months (Fig. 1g). Approximately half of the patients received a therapeutic approach according to EU-RHAB recommendations (52%, $n = 11/21$), whereas the other patients received therapies according to the Dana Farber Cancer Institute (DFCI) protocol (10%, $n = 2/21$), Rhabdoid 2007 (19%, n = 4/21), and HIT SKK 87 trial (5%, $n = 1/21$). An individual therapy was applied in the cases of three patients (14%, $n = 3/21$, Fig. 1h). The average follow-up of the patients was 33.5 months (Fig. 1i) with 76% (n = 19/25) of the patients having passed away at the time of data acquisition (Fig. 1j).

Histology of recurrent AT/RT reveals increased mitotic activity and loss of architecture

The primary tumors and their recurrences (Table 1) were analyzed histologically using microscopy of H&E and Ki67 staining. As opposed to primary specimens (Fig. 2a, e), H&E-stained recurrences revealed a loss of architecture with features of primary AT/RT, such as mesenchymal, epithelial, or rhabdoid architectures [34] being less prominent (Fig. 2c, g). The number of mitotic figures was significantly increased in recurrences ($p = 0.04$, Fig. 2a, c, e, g, i). Ki67 staining resulted in a significantly intensified labeling in recurrences, with an average of approximately 48% Ki67-positive nuclei, compared to 34% in primary tumors ($p = 0.017$, Fig. 2b, d, f, h, j). This suggests that recurrent tumors undergo changes that may be related to additional molecular alterations and even more aggressive tumor growth.

Epigenetic profiles and molecular type and subtype affiliations remain stable in most AT/RT recurrences

The normalized DNA methylation values for the 1000 most variable CpG sites was visualized for each primary and second neoplasm of the 26 patients. To show how these cases fit into the landscape of established AT/RT

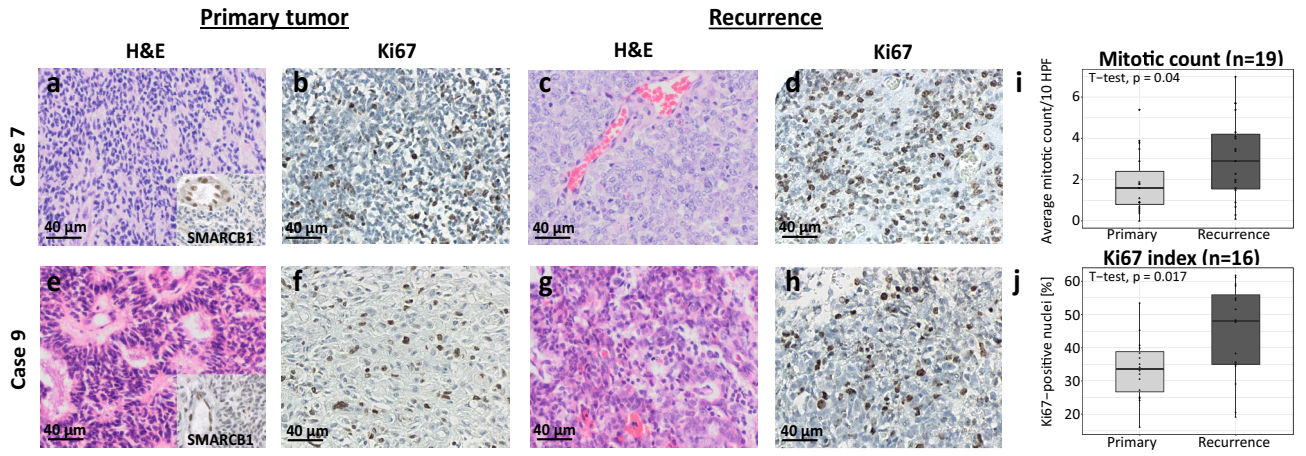

Fig. 2 Histological features of recurrent AT/RT compared to primary tumors. Recurrent tumors demonstrate loss of architecture, increased number of mitotic figures using H&E staining (**a**, **c**, **e**, **g**), and intensified Ki67 labeling (**b**, **d**, **f**, **h**). All samples showed negative SMARCB1 staining (**a**, **e**: square box below right), confirming the diagnosis of AT/RT. **i** Mitotic activity increased in recurrent tumors. **j** Ki67 index was heightened in recurrent AT/RT compared to primary tumors. *HPF* high-power-field

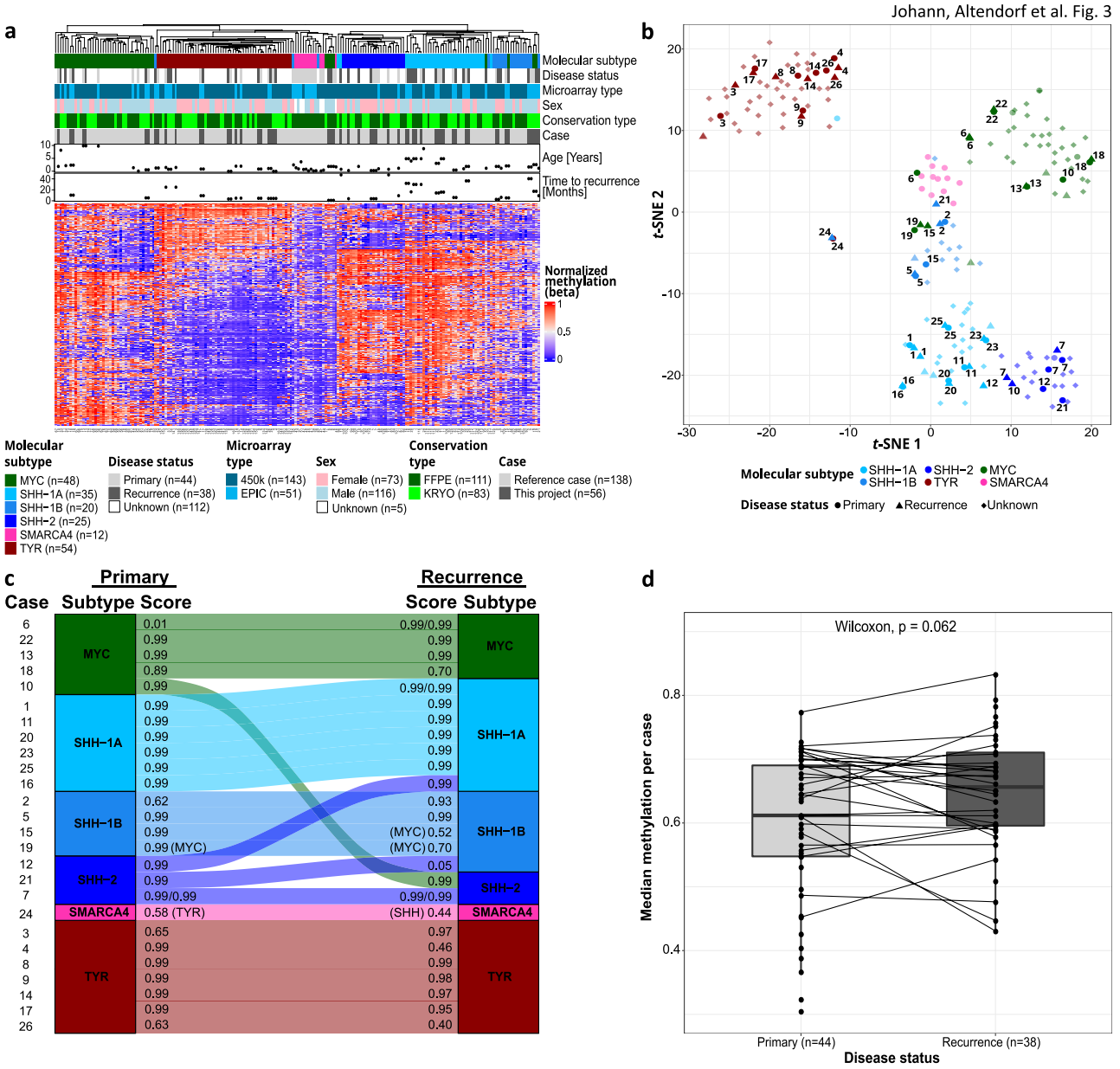

Fig. 3 DNA methylation patterns of primary and recurrent AT/RT. **a** Unsupervised hierarchical clustering of matched AT/RT primary tumors and recurrences and reference cases ($n=138$) based on the 1000 most variable CpG sites. Case numbers indicate patients as listed in Table 1 and Supplementary Table 1. Mostly, primary tumors and recurrences clustered in the same molecular type or subtype independent of time to recurrence. **b** *t*-SNE plot of methylation signature using the 1000 most variable CpG sites. Position of samples mostly suggests similarity between primary and recurrent tumor data. Furthermore, samples predominantly clustered in accordance to the brain tumor classifier disease subgroup results (v12.5, www.molecularneuropathology.org). Transparent dots are the reference cases and not annotated. **c** Alluvial plot of molecular type and subtype alterations in second neoplasms compared to primary tumors according to heatmap and *t*-SNE (**a**, **b**). The cases 10, 12, and 21 changed their molecular type or subtype. Classifier scores were calculated using brain tumor classifier (v12.5, www.molecularneuropathology.org) for AT/RT-SHH, AT/RT-MYC and AT/RT-TYR. According to classifier results, case 19 and the recurrence of case 15 belonged to AT/RT-MYC, but unsupervised hierarchical clustering and *t*-SNE (**a**, **b**), assigned them to AT/RT-SHH-1B. In the following analyses they are annotated as AT/RT-SHH-1B. AT/RT-SHH subtypes AT/RT-SHH-1A, AT/RT-SHH-1B, and AT/RT-SHH-2 were assigned based on *t*-SNE analysis. Case 24 results in low scores for other molecular types, since AT/RT-SMARCA4 is unknown by the brain tumor classifier. Cases 1, 6, and 7 included two recurrences and case 7 also two primary tumors. **d** Median methylation per case based on all measured CpG sites was calculated. Globally, primary and recurrent tumor levels did not differ significantly (Wilcoxon-test; $p=0.062$)

subtypes, we also included a large cohort of reference cases from all known molecular types ($n = 138$, Fig. 3a, b). Unsupervised hierarchical clustering and *t*-SNE analysis of these data demonstrated six clusters matching the molecular types AT/RT-SHH, AT/RT-TYR, AT/RT-MYC, and AT/RT-SMARCA4 and subtypes AT/RT-SHH-1A, AT/RT-SHH-1B, AT/RT-SHH-2. Primary tumors and recurrences were distributed homogeneously over these types and subtypes and did not form their own clusters, indicating that epigenetic changes were subtle and that the profile of a recurrent tumor remained similar to its primary match in most cases. All but three cases showed close neighborhood of primary and recurrent tumors in the unsupervised hierarchical clustering (Fig. 3a) and *t*-SNE analysis (Fig. 3b), which also shows that most AT/RT did not change their molecular type or subtype based on DNA methylation profiling. However, the primary tumor of case 10 belonged to ATRT–MYC and the lesion after second surgery to ATRT–SHH-2, which was also confirmed by brain tumor classifier (v12.5, www.molecularneuropathology.org, [7]). The second neoplasms of cases 12 and 21 belonged to a different subtype within the ATRT–SHH type (Fig. 3c). All three patients suffered from RTPS1.

On DNA methylation level, no significant correlation between primary-recurrence variation and time to recurrence was observed (Supplementary Fig. 1). The primary-recurrence variation was defined as the Jensen–Shannon divergence (JSD) between recurrences and related primary tumors based on the 1000 CpG sites with the largest standard deviation.

We further did not detect significant changes in the global median DNA methylation of primary tumors and related recurrences after integration of our cohort into a data set with unmatched primary ($n = 17$) and recurrent ($n = 9$) AT/RT, regardless of the molecular type (Supplementary Fig. 2). This observation remained stable when evaluating all AT/RT samples together ($p = 0.062$, Fig. 3d).

In conclusion, the majority of the AT/RT recurrences was grossly similar compared to their related primary tumors on DNA methylation level. Three out of 26 AT/RT had a different molecular type or subtype after second surgery, whereas 23 recurrences retained their type/subtype and clustered with their matched primary tumors.

CNV analysis reveals enhanced chromosome 1q gain and loss of chromosome 10 in AT/RT recurrences

CNV analysis was performed to identify further differences between AT/RT primaries and recurrences. CNVs of the recurrences were in general similar to matched primary tumors. Nevertheless, there was a number of cases with different CNVs. The recurrences of cases 1, 7, 10, 20, 21, and 25 showed altered CNVs (Fig. 4a), which included two of the cases that changed their molecular type or rather subtype (cases 10 and 21; Fig. 3b, c). This highlights molecular differences between primary and recurrent tumors for these cases. One of the most common alterations in our cohort was chromosome 1q gain (Fig. 4b), which was confirmed in 7% of primary tumors (n = 3/44) and in 18% of recurrences (n = 7/38; Fig. 4c) after integration of our cohort into the above-mentioned data set of unmatched primary and recurrent AT/RT. Thus, a novel chromosome 1q gain was observed in 11% of the recurrences (Fig. 4b, c), and a loss of chromosome 10 was observed in four out of 38 cases (11%) of all recurrences, but not in primary tumors (Fig. 4b, d). Nearly all copy number variations of our cohort were identified in the AT/RT-SHH types, whereas the other molecular groups seemed to have stable CNVs (Fig. 4a). In general, a loss of chromosome 22q was observed in most cases of all molecular types, which is associated with the *SMARCB1* loss. Other cases had a focal deletion on chromosome 22q, also affecting *SMARCB1*.

Altogether, differences were observed in the CN profile of chromosomes 1q and 10 for AT/RT-SHH recurrences (Supplementary Fig. 3). Genes located in chromosomes 1q and 10 should be further investigated as potential prognostic biomarkers for AT/RT-SHH recurrences.

Fig. 4 Overview of all cases with different methylation-derived copy number variation (CNV) of primary ($n = 44$) and recurrent ($n = 38$) AT/RT. Individual copy number profiles were calculated based on raw methylated/unmethylated signals using *conumee* package in "R Studio". Profile segments were defined by the span of the chromosome arms. To define, which ratio of methylated-to-unmethylated signal is considered as copy number gain or loss, ratios were normalized against reference samples and cutoff using the local (arm segment) threshold 0.25 and − 0.25, respectively. **a** Overview of cases of our cohort with different CNV of matched primary and recurrent AT/RT. **b** Cumulative CNV of primary tumors ($n = 44$) and recurrences ($n = 38$). **c** Fraction of primary and recurrent tumor samples that showed chromosome 1q gain. Chromosome 1q gain was more often observed in recurrences (18%, $n = 7$) compared to primary tumors (7%, $n = 3$). Exemplary CNV plot showed chromosome 1q gain in the primary tumor of case 15. **d** Fraction of primary and recurrent tumor samples that showed chromosome 10 loss. Chromosome 10 loss was only observed in recurrences (11%, $n = 4$), but not in primary tumors (0%, $n = 0$). Exemplary CNV plot showed chromosome 10 loss in the first recurrence of case 7

Primary tumors and matched recurrences maintain stable immune cell infiltrates but demonstrate decreased infiltration with myeloid dendritic cells in AT/RT-SHH

As is well-known, the environment of a tumor supports its growth and metastatic spread [13, 20]. We analyzed the

a

Case No.	Primary tumors		Recurrences	
	Molecular subtype	CNV	Molecular subtype	CNV
1	SHH-1A	46,XY,+(1)q21.2-q44,-(16)q12.1-q24.3,-(22)q11.1-q13.33	SHH-1A	46,XY,+(1)q21.2-q44,-(3)q13.32-q27.3,-(14)q24.3-q32.33,-(16)q12.1-q24.3,-(22)q11.1-q13.33
			SHH-1A	46,XY,+(1)q21.2-q44,-(5)q13.3-q14.1,-(16)q12.1-q24.3,-(22)q11.1-q13.33
7	SHH-2	46,XX,-(22)q11.23	SHH-2	46,XX,-(10)p11.21-p15.3,q11.21-q26.3,-(22)q11.21-q13.33
	SHH-2	46,XX,-(22)q11.21-q13.33	SHH-2	46,XX,-(22)q11.23
10	MYC	46,XY,-(1)p36.13-p36.33,-(6)q.25.2-q25.3,+(8)p11.21-p.23.3,q11.21-24.3,-(15)q11.2-q22.2,-(22)q11.1-13.33	SHH-2	46,XY,-(10)p11.21-p15.3,q11.21-q26.3,-(22)q11.21-q13.33
20	SHH-1A	46,XY,-(22)q11.23	SHH-1A	46,XY,-(6)q12-q27,-(22)q11.22-q13.33
21	SHH-2	46,XX,-(6)p22.3-p23,-(22)q11.23	SHH-1B	46,XX,-(22)q11.23
25	SHH-1A	46,XX,-(22)q11.23	SHH-1A	46,XX,+(1)q21.1-q44,-(3)q22.1-q25.3,-(5)p15.31,-(10)p14-p15.2,-(22)q11.23

b

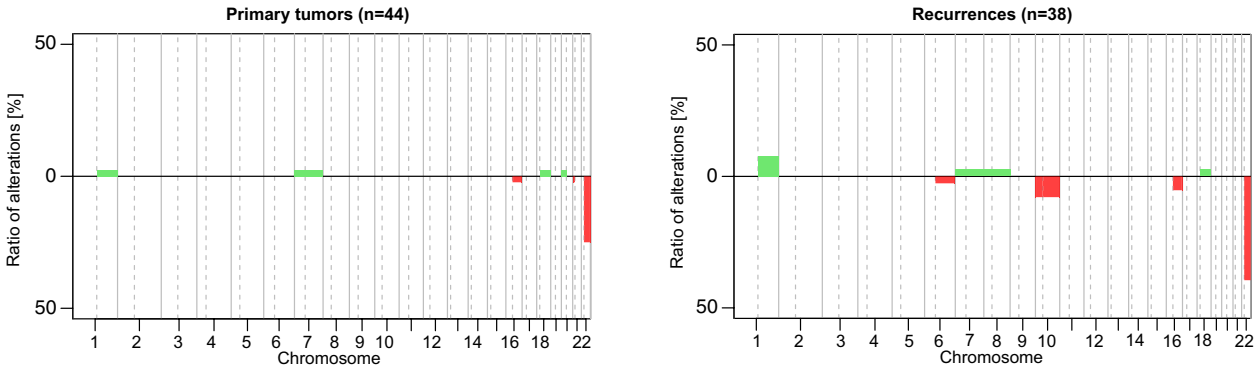

c

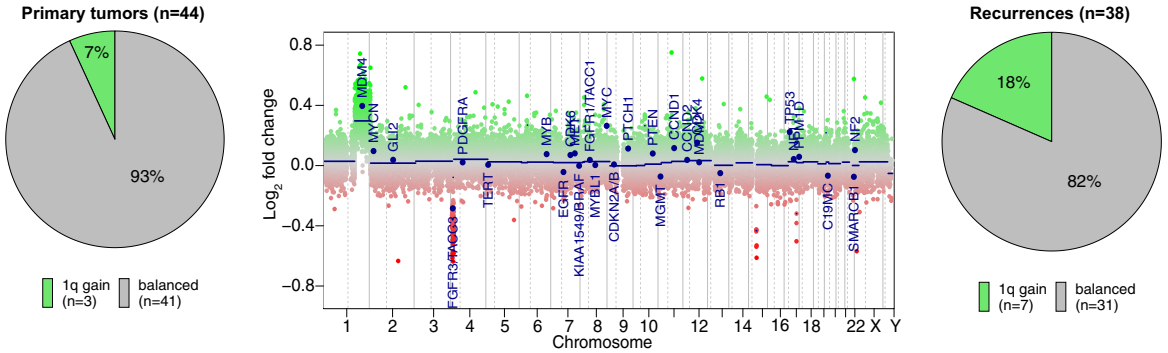

d

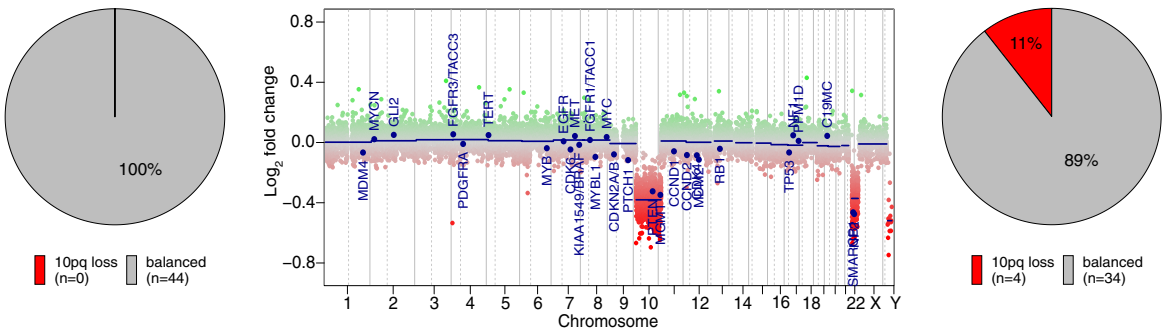

immune cell infiltration of primary and recurrent AT/RT by calculating the DIMEimmune scores from DNA methylation data [23] and scores from RNA sequencing data using a deconvolution method optimized for brain tumors [4, 5]. These scores were first compared in all AT/RT (Supplementary Fig. 4). This revealed stable immune cell infiltration. When analyzing each of the molecular types separately, infiltration with myeloid dendritic cells was significantly downregulated in AT/RT-SHH tumors ($p=0.048$, Supplementary Fig. 5j). For AT/RT-TYR, the sample size ($n=2$) was too small to achieve meaningful results (Supplementary Fig. 6), whereas the immune cell infiltration for AT/RT-MYC did not differ significantly in primaries and recurrences (Supplementary Fig. 7).

RNA sequencing analysis reveals differentially expressed genes in primary and recurrent AT/RT

Normalized expression of the 1000 most variable genes was visualized for each case in a heatmap (Fig. 5a) and a *t*-SNE plot (Fig. 5b) together with reference data ($n=33$). As for DNA methylation, both analyses resulted in clusters matching more or less the molecular types and subtypes with equal distributions of primary tumors and recurrences. The switch of the molecular type or rather subtype for cases 10 and 21, identified by DNA methylation analysis earlier, was observed in RNA expression-based clustering again. In addition, the recurrence of case 3 was not located in the AT/RT-TYR cluster anymore but switched to AT/RT-SHH. The recurrence of case 16 was located in the AT/RT-SHH-1B cluster and not in the AT/RT-SHH-1A cluster in contrast to DNA methylation data (Fig. 3a, b). Variation of primary tumors and recurrences was positively correlated with the time to recurrence ($R=0.74$, $p=0.0094$, Fig. 5c). Recurrences which did not cluster together with their related primary tumors in the heatmap and *t*-SNE plot, had a high primary-recurrence variation and these tumors had a long time to recurrence compared to tumors with smaller variations.

Analysis of differentially expressed genes between primary and recurrent AT/RT was performed for each molecular type, separately, using paired data of 13 patients. This resulted in distinct genes and gene sets. Most of the 13 analyzed patients belonged to the AT/RT-SHH type ($n=7$, Fig. 5d). After correction for multiple testing, upregulated genes in recurrences were *RGL2*, *NPIPA5*, *TMEM259*, *KAT2A*, and *CA4*. In primary tumors, *EGFR*, *MACC1,* and *EMP2* were upregulated, next to 13 other genes. Three up- or downregulated genes were chosen for further comparison of the $\log_2$ of *DESeq2*-normalized count data between primary and recurrent AT/RT (Fig. 5e–j), confirming that there were significant differences. In summary, only 21 genes were differentially expressed when comparing primary and recurrent AT/RT-SHH tumors, making a pathway analysis less meaningful. A large number of differentially expressed genes was identified in AT/RT-MYC tumors (Supplementary Fig. 8a), which were further investigated using pathway analyses. This revealed cell cycle-associated genes, HDACs deacetylate/HATs acetylate histones, and genes involved in general metabolism. Immune system-associated pathways and genes were downregulated in recurrences compared to primary tumors (Supplementary Fig. 8b). Analyses of AT/RT-TYR cases resulted in an array of differentially expressed genes, but results differed from AT/RT-MYC (Supplementary Fig. 8c). On one hand, genes involved in signaling by receptor tyrosine kinases and transmission across chemical synapses as well as genes associated with the neuronal system showed increased expression in recurrences. On the other hand, genes involved in developmental processes, such as the development of the neuronal system, including ROBO receptor signaling, were downregulated in recurrences. Disease- and stress-related genes and genes involved in the immune system were downregulated (Supplementary Fig. 8d).

Fig. 5 RNA sequencing analysis of primary and recurrent AT/RT. Case numbers indicate patients as listed in Table 1 and Supplementary Tables 1 and 2. Raw RNA sequencing data were processed using *DESeq2* and normalized using variance stabilized transformation (VST) in R Studio. Batch effects introduced by conservation type and microarray type were corrected using the ComBat_Seq method. **a** Unsupervised hierarchical clustering of matched AT/RT primary tumors and recurrences and reference cases ($n=33$) based on the 1000 most variable genes. Mostly, primary tumors and recurrences clustered in the same molecular type or subtype. The assignment of the molecular types and subtypes was taken from DNA methylation results. **b** *t*-SNE plot using the 1000 most variable genes. Position of samples mostly suggests similarity between primary and recurrent tumor data. Furthermore, samples predominantly clustered in accordance to the brain tumor classifier disease subgroup results. The transparent dots are the reference cases and are not annotated. **c** Positive correlation ($R=0.74$, $p=0.0094$) of primary-recurrence variation and time to recurrence [months]. Primary-recurrence variation was defined as the Jensen–Shannon divergence (JSD) between recurrences and related primary tumors based on the 1000 most variable genes. **d** Volcano plot of differentially expressed genes between primary and recurrent AT/RT. Significant genes with a $\log_2$ fold change >1 are colored in red for upregulated genes in primary tumors and in green for upregulated genes in recurrences. Highlighted genes were selected for further analysis. **e**–**j** *DESeq2*-normalized counts of paired primary and recurrent AT/RT for *EGFR* (**e**), *MACC1* (**f**), *EMP2* (**g**), *RGL2* (**h**), *KAT2A* (**i**), and *CA4* (**j**). Statistical analysis was performed using *DESeq2*

Discussion

Our analyses demonstrate both, differences and commonalities between AT/RT primary tumors and recurrences on a morphological and molecular level. Histology revealed an enhanced mitotic activity in recurrences, which could be associated with enhanced tumor growth.

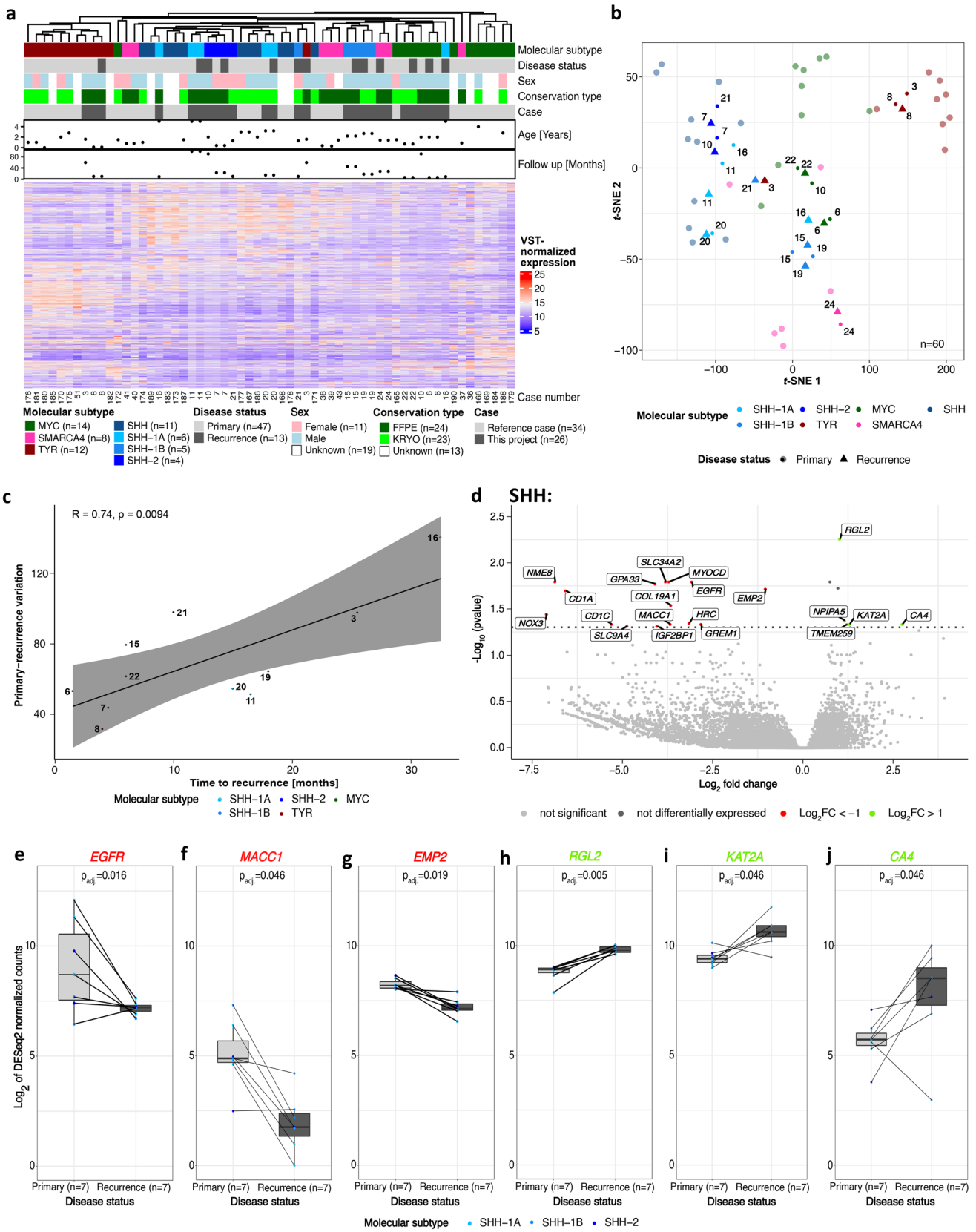
a
Molecular subtype
Disease status
Sex
Conservation type
Case
Age [Years]
Follow up [Months]
VST-normalized expression
Case number
Molecular subtype
MYC (n=14)
SMARCA4 (n=8)
TYR (n=12)
SHH (n=11)
SHH–1A (n=6)
SHH–1B (n=5)
SHH–2 (n=4)
Disease status
Primary (n=47)
Recurrence (n=13)
Sex
Female (n=11)
Male
Unknown (n=19)
Conservation type
FFPE (n=24)
KRYO (n=23)
Unknown (n=13)
Case
Reference case (n=34)
This project (n=26)
b
t-SNE 1
t-SNE 2
n=60
Molecular subtype
SHH–1A
SHH–1B
SHH–2
TYR
MYC
SMARCA4
SHH
Disease status
Primary
Recurrence
c
R = 0.74, p = 0.0094
Primary−recurrence variation
Time to recurrence [months]
Molecular subtype
SHH–1A
SHH–1B
SHH–2
TYR
MYC
d
SHH:
-Log10 (pvalue)
Log2 fold change
RGL2
SLC34A2
NME8
MYOCD
GPA33
EGFR
COL19A1
EMP2
CD1A
CD1C
MACC1
HRC
NPIPA5
KAT2A
CA4
NOX3
SLC9A4
IGF2BP1
GREM1
TMEM259
not significant
not differentially expressed
Log2FC < −1
Log2FC > 1
e
EGFR
padj.=0.016
f
MACC1
padj.=0.046
g
EMP2
padj.=0.019
h
RGL2
padj.=0.005
i
KAT2A
padj.=0.046
j
CA4
padj.=0.046
Log2 of DESeq2 normalized counts
Primary (n=7)
Recurrence (n=7)
Disease status
Molecular subtype
SHH–1A
SHH–1B
SHH–2

By analyzing DNA methylation data of 26 primary tumors and matched recurrences, stable global DNA methylation was observed for most cases. In addition, recurrences mostly belonged to the same methylation class as the related primary tumors. For three out of the 26 recurrences, the methylation class was different, suggesting that they show molecular alterations compared to primary tumors.

A limited number of studies investigate the stability of molecular type allocation in recurrent tumors: for medulloblastomas, it has recently been observed that in a cohort of 57 patients, 56 retained their molecular type upon recurrence [21]. Similarly, Zhao et al. detected a relatively stable methylation phenotype in ependymoma recurrences compared to the respective primaries [32]. Thus, the observed frequency might be in the range of what is to be expected.

As an alternative explanation for these mismatches, it is also possible that these lesions were metachronous tumors in the context of a tumor predisposition. Multiple AT/RT of different molecular types have previously been observed in patients with rhabdoid tumor predisposition syndrome, suffering from synchronous/metachronous or secondary tumors [25, 28]. Indeed, patients #10, 12, and 21 suffered from a rhabdoid tumor predisposition syndrome 1 (RTPS1) due to pathogenic *SMARCB1* germline variants that may have caused multiple independent tumor lesions, but the five other cases with RTPS1 did not demonstrate multiple independent tumors. Though, it was already assumed that patient #10 did not suffer from two independent primary tumors, indicating a clonal origin of the tumors [19]. The recurrence of patient #12 was distant from the primary tumor on a molecular level and, together with the underlying pathogenic germline variant, it may be a metachronous tumor. Recurrences with the same molecular type or rather subtype as their matched primary tumors clustered together, which led to the initial assumption that they seem to have similar DNA methylation patterns. Therefore, CNVs based on DNA methylation data were analyzed as well.

CNVs may influence tumor predisposition meaning that different CNVs could lead to different tumor progression [18]. Therefore, the CNVs of AT/RT primaries and recurrences were compared together with a number of unmatched primary and recurrent AT/RT. Remarkable differences were an increased chromosome 1q gain (11%, $n=4$) and an enhanced chromosome 10 loss (11%, $n=4$) in recurrences as compared to primaries. So far, chromosome 1q gain has been associated with an inferior prognosis in different studies of ependymomas [1, 12] and nephroblastomas [2]. Its role in AT/RT deserves further investigation. This is particularly important as chromosome 1q gain is known to induce overexpression of the *MDM4* gene, which contains a p53 tumor suppressor binding domain and inhibits its activity. It may thus represent a potential prognostic marker in AT/RT recurrences.

In addition to general CNV pattern changes between primaries and recurrences, CNV analysis further revealed differences between AT/RT molecular types. CNV alterations, including chromosome 1q gain and chromosome 10 loss, were almost only detected in the AT/RT-SHH type. AT/RT-TYR, AT/RT-MYC, and AT/RT-SMARCA4 showed similar CNVs in primary tumors and recurrences. Despite a generally high homogeneity in the CNV inventory of primaries and recurrences, these differences in AT/RT-SHH merit further investigation.

RNA sequencing analysis revealed differentially expressed genes of AT/RT primary tumors and recurrences. Most of the cases belonged to AT/RT-SHH but, nevertheless, only few genes were significantly differentially expressed compared to AT/RT-MYC and AT/RT-TYR. This could be due to the heterogeneity within the AT/RT-SHH type, which has been shown to be further divided into three subtypes. These AT/RT-SHH subtypes could not be investigated independently due to the small sample size. Nevertheless, the results of the AT/RT-SHH type were most meaningful, whereas the patient number for AT/RT-MYC ($n=3$) and AT/RT-TYR ($n=2$) cases were very small. There remains an urgent need to analyze more samples of these molecular types to consolidate our findings.

Five genes were upregulated in AT/RT-SHH recurrences: *RGL2*, *NPIPA5*, *TMEM259*, *KAT2A*, and *CA4*. While the biological function of these genes seems to be diverse, some of these (such as *RGL2*) have been ascribed pro-metastatic functions in other tumor entities [6, 27, 33]. Further studies are necessary to corroborate their biological role in AT/RT-SHH recurrences. The same holds true for 16 genes that were overexpressed in AT/RT-SHH primaries.

For AT/RT-MYC and AT/RT-TYR, there was a higher number of differentially expressed genes. Therefore, a pathway analysis was performed to identify pathways and gene sets, to which the differentially expressed genes were assigned. In general, the sample sizes were small for both with $n=3$ for AT/RT-MYC and $n=2$ for AT/RT-TYR. While a statistically sound analysis for AT/RT-TYR was precluded by small sample size, AT/RT-MYC results showed an overexpression of cell cycle-associated genes in recurrences (Supplementary Fig. 8b), which matched our observations of increased mitotic activity in recurrences (Fig. 2). Furthermore, HDACs deacetylate and HATs acetylate histones were enriched gene sets in AT/RT-MYC recurrences. So far, imbalances in the expression of HATs and HDACs have been associated with tumor development and they are known therapeutic targets [22]. Signalling by receptor tyrosine kinases and transmission across chemical synapses were upregulated pathways in AT/RT-TYR recurrences. To name a particularly salient example of an overexpressed gene, *GABRG2*, which encodes a Gamma-Aminobutyric

Acid (GABA) receptor, was overexpressed with a $\log_2$ fold change of about 20, which was much higher compared to all other genes, making it an interesting target for further study.

In conclusion, primary and recurrent AT/RT differed in their histology. An increased mitotic activity and a loss of architecture were observed in recurrences. However, global DNA methylation pattern were very similar for primary and recurrent AT/RT. Most recurrences clustered close to their matching primary tumors and only three out of 26 cases belonged to a different molecular type or subtype after second surgery. Nevertheless, CNV analysis revealed an increased chromosome 1q gain and chromosome 10 loss, mainly in AT/RT-SHH recurrences. Furthermore, 21 differentially expressed cancer-associated genes were identified in AT/RT-SHH recurrences. These genes could be interesting candidates for specific therapeutic targets for this type and should be further investigated in vitro and in vivo. Enriched pathways and gene sets were also identified in AT/RT-MYC and AT/RT-TYR recurrences but need to be further consolidated by more samples.

Supplementary Information The online version contains supplementary material available at https://doi.org/10.1007/s00401-023-02608-7.

Acknowledgements This study was supported by the Deutsche Forschungsgemeinschaft (FR 1516/4-1). MF received funds by the Deutsche Krebshilfe (DKH 70113981). EU-RHAB is supported by the Deutsche Kinderkrebsstiftung (A2018/27). US was further supported by the Fördergemeinschaft Kinderkrebszentrum Hamburg. LA received a fellowship from the Burkhard Meyer Stiftung. PDJ received funding by the German Cancer Aid (Max Eder program) and the Else Kröner Fresenius Stiftung. RS received grant support for infrastructure by the KinderKrebsInitiative Buchholz/Holm-Seppensen and by Deutsche Krebshilfe 70114040.

Funding Open Access funding enabled and organized by Projekt DEAL.

Open Access This article is licensed under a Creative Commons Attribution 4.0 International License, which permits use, sharing, adaptation, distribution and reproduction in any medium or format, as long as you give appropriate credit to the original author(s) and the source, provide a link to the Creative Commons licence, and indicate if changes were made. The images or other third party material in this article are included in the article's Creative Commons licence, unless indicated otherwise in a credit line to the material. If material is not included in the article's Creative Commons licence and your intended use is not permitted by statutory regulation or exceeds the permitted use, you will need to obtain permission directly from the copyright holder. To view a copy of this licence, visit http://creativecommons.org/licenses/by/4.0/.

References

1. Araki A, Chocholous M, Gojo J, Dorfer C, Czech T, Heinzl H et al (2016) Chromosome 1q gain and tenascin-C expression are candidate markers to define different risk groups in pediatric posterior fossa ependymoma. Acta Neuropathol Commun 4:88. https://doi.org/10.1186/s40478-016-0349-9
2. van Belzen IAEM, van Tuil M, Badloe S, Strengman E, Janse A, Verwiel ETP et al (2022) Molecular Characterization Reveals Subclasses of 1q Gain in Intermediate Risk Wilms Tumors. Cancers (Basel). https://doi.org/10.3390/cancers14194872
3. Biegel JA, Zhou JY, Rorke LB, Stenstrom C, Wainwright LM, Fogelgren B (1999) Germ-line and acquired mutations of INI1 in atypical teratoid and rhabdoid tumors. Cancer Res 59:74–79
4. Bockmayr M, Klauschen F, Maire LC, RutkowskiWestphalLamszus SMK et al (2019) Immunologic profiling of mutational and transcriptional subgroups in pediatric and adult high-grade gliomas. Cancer Immunol Res 7:1401–1411. https://doi.org/10.1158/2326-6066.CIR-18-0939
5. Bockmayr M, Mohme M, Klauschen F, Winkler B, Budczies J, Rutkowski S et al (2018) Subgroup-specific immune and stromal microenvironment in medulloblastoma. Oncoimmunology. https://doi.org/10.1080/2162402X.2018.1462430
6. Bum-Erdene K, Ghozayel MK, Xu D, Meroueh SO (2022) Covalent fragment screening identifies Rgl2 RalGEF cysteine for targeted covalent inhibition of Ral GTPase activation. ChemMedChem. https://doi.org/10.1002/cmdc.202100750
7. Capper D, Jones DTW, Sill M, Hovestadt V, Schrimpf D, Sturm D et al (2018) DNA methylation-based classification of central nervous system tumours. Nature 555:469–474. https://doi.org/10.1038/nature26000
8. Carey SS, Huang J, Myers JR, Mostafavi R, Orr B, Michalik LH et al (2022) Outcomes for children with recurrent atypical teratoid rhabdoid tumor: a single institution study with updated molecular and germline analysis. Neuro Oncol 24:i8. https://doi.org/10.1093/neuonc/noac079.021
9. Federico A, Thomas C, Miskiewicz K, Woltering N, Zin F, Nemes K et al (2022) ATRT–SHH comprises three molecular subgroups with characteristic clinical and histopathological features and prognostic significance. Acta Neuropathol 143:697–711. https://doi.org/10.1007/s00401-022-02424-5
10. Foulkes WD, Kamihara J, Evans DGR, Brugières L, Bourdeaut F, Molenaar JJ et al (2017) Cancer surveillance in Gorlin syndrome and rhabdoid tumor predisposition syndrome. Clin Cancer Res 23:e62–e67
11. Frühwald MC, Hasselblatt M, Nemes K, Bens S, Steinbügl M, Johann PD et al (2020) Age and DNA methylation subgroup as potential independent risk factors for treatment stratification in children with atypical teratoid/rhabdoid tumors. Neuro Oncol 22:1006–1017. https://doi.org/10.1093/neuonc/noz244
12. Gojo J, Lötsch D, Spiegl-Kreinecker S, Pajtler KW, Neumayer K, Korbel P et al (2017) Telomerase activation in posterior fossa group A ependymomas is associated with dismal prognosis and chromosome 1q gain. Neuro Oncol 19:1183–1194. https://doi.org/10.1093/neuonc/nox027
13. Hanahan D, Weinberg R (2011) Hallmarks of cancer: the next generation. Cell 144:646–674. https://doi.org/10.1016/j.cell.2011.02.013.2
14. Hasselblatt M, Nagel I, Oyen F, Bartelheim K, Russell RB, Schüller U et al (2014) SMARCA4-mutated atypical teratoid/rhabdoid tumors are associated with inherited germline alterations and poor prognosis. Acta Neuropathol 128:453–456. https://doi.org/10.1007/s00401-014-1323-x
15. Ho B, Johann PD, Grabovska Y, De Dieu Andrianteranagna MJ, Yao F, Frühwald M et al (2020) Molecular subgrouping of atypical teratoid/rhabdoid tumors—a reinvestigation and current consensus. Neuro Oncol 22:613–624
16. Holdhof D, Johann PD, Spohn M, Bockmayr M, Safaei S, Joshi P et al (2020) Atypical teratoid/rhabdoid tumors (ATRTs) with SMARCA4 mutation are molecularly distinct from SMARCB1-deficient cases. Acta Neuropathol 141:291–301. https://doi.org/10.1007/s00401-020-02250-7

17. Johann PD, Erkek S, Zapatka M, Kerl K, Buchhalter I, Hovestadt V et al (2016) Atypical teratoid/rhabdoid tumors are comprised of three epigenetic subgroups with distinct enhancer landscapes. Cancer Cell 29:379–393. https://doi.org/10.1016/j.ccell.2016.02.001
18. Krepischi ACV, Pearson PL, Rosenberg C (2012) Germline copy number variations and cancer predisposition. Future Oncol 8:441–450. https://doi.org/10.2217/fon.12.34
19. Modena P, Sardi I, Brenca M, Giunti L, Buccoliero AM, Pollo B et al (2013) Case report: long-term survival of an infant syndromic patient affected by atypical teratoid-rhabdoid tumor. BMC Cancer. https://doi.org/10.1186/1471-2407-13-100
20. Quail DF, Joyce JA (2017) The microenvironmental landscape of brain tumors. Cancer Cell 31:326–341. https://doi.org/10.1016/j.ccell.2017.02.009
21. Richardson S, Hill RM, Kui C, Lindsey JC, Grabovksa Y, Keeling C et al (2022) Emergence and maintenance of actionable genetic drivers at medulloblastoma relapse. Neuro Oncol 24:153–165. https://doi.org/10.1093/neuonc/noab178
22. Ropero S, Esteller M (2007) The role of histone deacetylases (HDACs) in human cancer. Mol Oncol 1:19–25. https://doi.org/10.1016/j.molonc.2007.01.001
23. Safaei S, Mohme M, Niesen J, Schüller U, Bockmayr M (2021) DIMEimmune: Robust estimation of infiltrating lymphocytes in CNS tumors from DNA methylation profiles. Oncoimmunology 10:1–14. https://doi.org/10.1080/2162402X.2021.1932365
24. Schneppenheim R, Frühwald MC, Gesk S, Hasselblatt M, Jeibmann A, Kordes U et al (2010) Germline nonsense mutation and somatic inactivation of SMARCA4/BRG1 in a family with rhabdoid tumor predisposition syndrome. Am J Hum Genet 86:279–284. https://doi.org/10.1016/j.ajhg.2010.01.013
25. Sredni ST, Tomita T (2015) Rhabdoid tumor predisposition syndrome. Pediatr Dev Pathol 18:49–58. https://doi.org/10.2350/14-07-1531-MISC.1
26. Steinbügl M, Nemes K, Gruhle M, Johann PD, Joao Gil-da-Costa M, Ebinger M et al (2022) Outcome and therapeutic interventions in relapsed and refractory ATRT—the EU-RHAB Perspective. Neuro Oncol 24(Suppl 1):4–4. https://doi.org/10.1093/neuonc/noac079.008
27. Sun MS, Yuan LT, Kuei CH, Lin HY, Chen YL, Chiu HW et al (2021) Rgl2 drives the metastatic progression of colorectal cancer via preventing the protein degradation of β-catenin and kras. Cancers (Basel). https://doi.org/10.3390/cancers13081763
28. Thomas C, Knerlich-Lukoschus F, Reinhard H, Johann PD, Sturm D, Sahm F et al (2019) Two molecularly distinct atypical teratoid/rhabdoid tumors (or tumor components) occurring in an infant with rhabdoid tumor predisposition syndrome 1. Acta Neuropathol 137:847–850. https://doi.org/10.1007/s00401-019-02001-3
29. Torchia J, Golbourn B, Feng S, Ho KC, Sin-Chan P, Vasiljevic A et al (2016) Integrated (epi)-Genomic analyses identify subgroup-specific therapeutic targets in CNS rhabdoid tumors. Cancer Cell 30:891–908. https://doi.org/10.1016/j.ccell.2016.11.003
30. Upadhyaya SA, Robinson GW, Onar-Thomas A, Orr BA, Johann P, Wu G et al (2021) Relevance of molecular groups in children with newly diagnosed atypical teratoid rhabdoid tumor: results from prospective St. Jude multi-institutional trials. Clin Cancer Res 27:2879–2889. https://doi.org/10.1158/1078-0432.CCR-20-4731
31. Wilson BG, Roberts CWM (2011) SWI/SNF nucleosome remodellers and cancer. Nat Rev Cancer 11:481–492. https://doi.org/10.1038/nrc3068
32. Zhao S, Li J, Zhang H, Qi L, Du Y, Kogiso M et al (2022) Epigenetic alterations of repeated relapses in patient-matched childhood ependymomas. Nat Commun. https://doi.org/10.1038/s41467-022-34514-z
33. Zinatizadeh MR, Zarandi PK, Keshavarz-Fathi M, Yousefi MH, Rezaei N (2022) The role of ral signaling and post translational modifications (PTMs) of Ras in cancer. Genome Instab Dis 3:22–32. https://doi.org/10.1007/s42764-022-00059-0
34. Zin F, Cotter JA, Haberler C, Dottermusch M, Neumann J, Schüller U et al (2021) Histopathological patterns in atypical teratoid/rhabdoid tumors are related to molecular subgroup. Brain Pathol. https://doi.org/10.1111/bpa.12967

Publisher's Note Springer Nature remains neutral with regard to jurisdictional claims in published maps and institutional affiliations.

Authors and Affiliations

Pascal D. Johann[1,2,3] · Lea Altendorf[4,5] · Emma-Maria Efremova[4,5] · Till Holsten[4,5,6] · Mona Steinbügl[1] · Karolina Nemes[1] · Alicia Eckhardt[4,5,7] · Catena Kresbach[4,5,6,8] · Michael Bockmayr[4,5,8] · Arend Koch[9] · Christine Haberler[10,11] · Manila Antonelli[12] · John DeSisto[13] · Martin U. Schuhmann[15] · Peter Hauser[16] · Reiner Siebert[17] · Susanne Bens[17] · Marcel Kool[2,3,18] · Adam L. Green[13,14] · Martin Hasselblatt[19] · Michael C. Frühwald[1] · Ulrich Schüller[4,5,6]

✉ Ulrich Schüller
u.schueller@uke.de

1 Paediatric and Adolescent Medicine, Swabian Children's Cancer Center Augsburg, EU-RHAB Trial Center, Germany and Bavarian Cancer Research Center (BZKF), Augsburg, Germany

2 Hopp Children's Cancer Center (KiTZ), Heidelberg, Germany

3 Division of Pediatric Neurooncology, German Cancer Research Center (DKFZ) and German Cancer Research Consortium (DKTK), Heidelberg, Germany

4 Department of Pediatric Hematology and Oncology, University Medical Center Hamburg-Eppendorf, Hamburg, Germany

5 Research Institute Children's Cancer Center Hamburg, Martinistraße 52, N63, 20251 Hamburg, Germany

6 Institute of Neuropathology, University Medical Center Hamburg-Eppendorf, Hamburg, Germany

7 Department of Radiotherapy and Radio-Oncology, University Medical Center Hamburg-Eppendorf, Hamburg, Germany

8 Mildred Scheel Cancer Career Center HaTriCS4, University Medical Center Hamburg-Eppendorf, Hamburg, Germany

9 Institute of Neuropathology, Charité, Universitätsmedizin Berlin, Berlin, Germany

[10] Institute of Neurology, Medical University of Vienna, Vienna, Austria

[11] Comprehensive Cancer Center, Medical University of Vienna, Vienna, Austria

[12] Department of Radiological, Oncological and Anatomic Pathology Sciences, Università Sapienza, Rome, Italy

[13] Morgan Adams Foundation Pediatric Brain Tumor Research Program, Children's Hospital Colorado, Aurora, CO, USA

[14] Department of Pediatrics, University of Colorado Denver, Aurora, CO, USA

[15] Division of Pediatric Neurosurgery, Department of Neurosurgery, Eberhard Karl's University Hospital of Tübingen, Tübingen, Germany

[16] Second Department of Pediatrics, Semmelweis University, Budapest, Hungary

[17] Institute of Human Genetics, Ulm University & Ulm University Medical Center, Ulm, Germany

[18] Princess Máxima Center for Pediatric Oncology, Utrecht, The Netherlands

[19] Institute of Neuropathology, University Hospital Münster, Münster, Germany

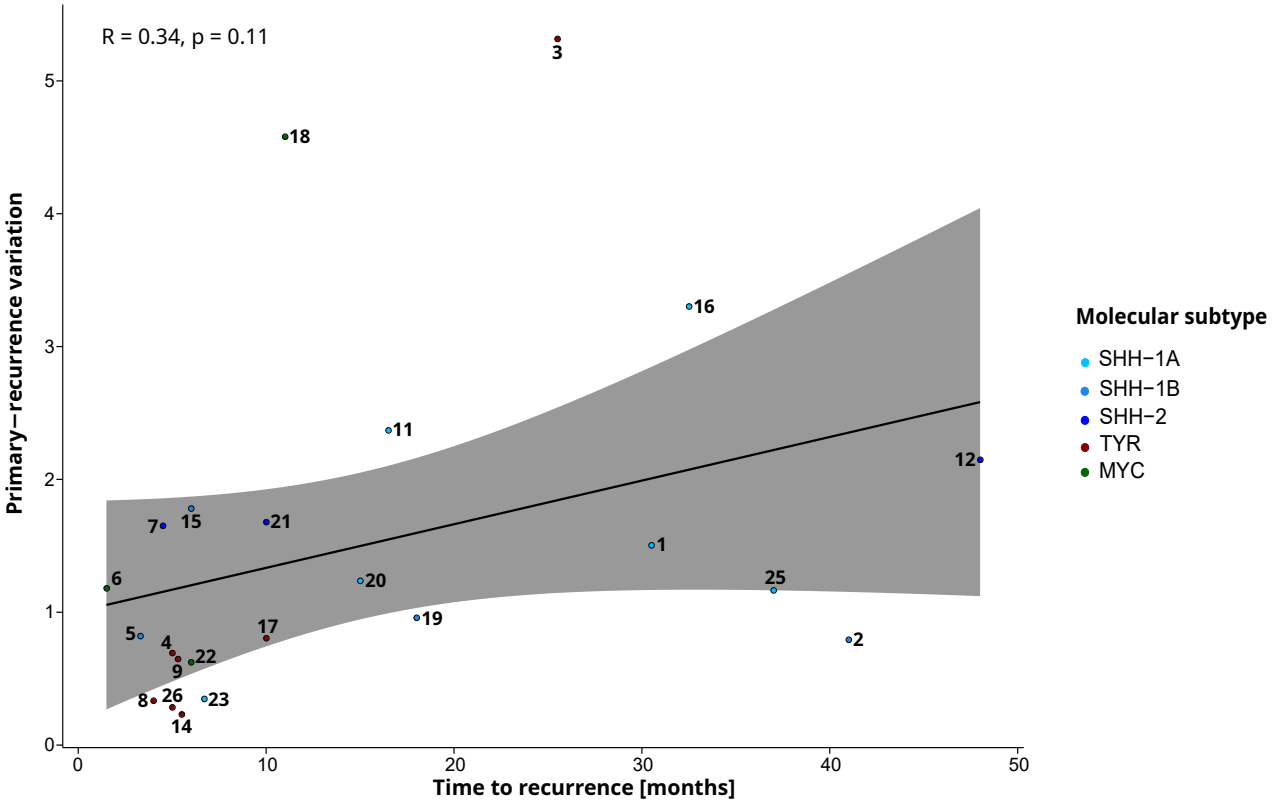

Supplementary Fig. 1: Correlation of primary-recurrence variation and time to recurrence based on DNA methylation data. Primary-recurrence variation was defined as the Jensen-Shannon divergence between primary tumors and related recurrences based on the 1,000 CpG sites with the largest standard deviation. No correlation was observed on DNA methylation level.

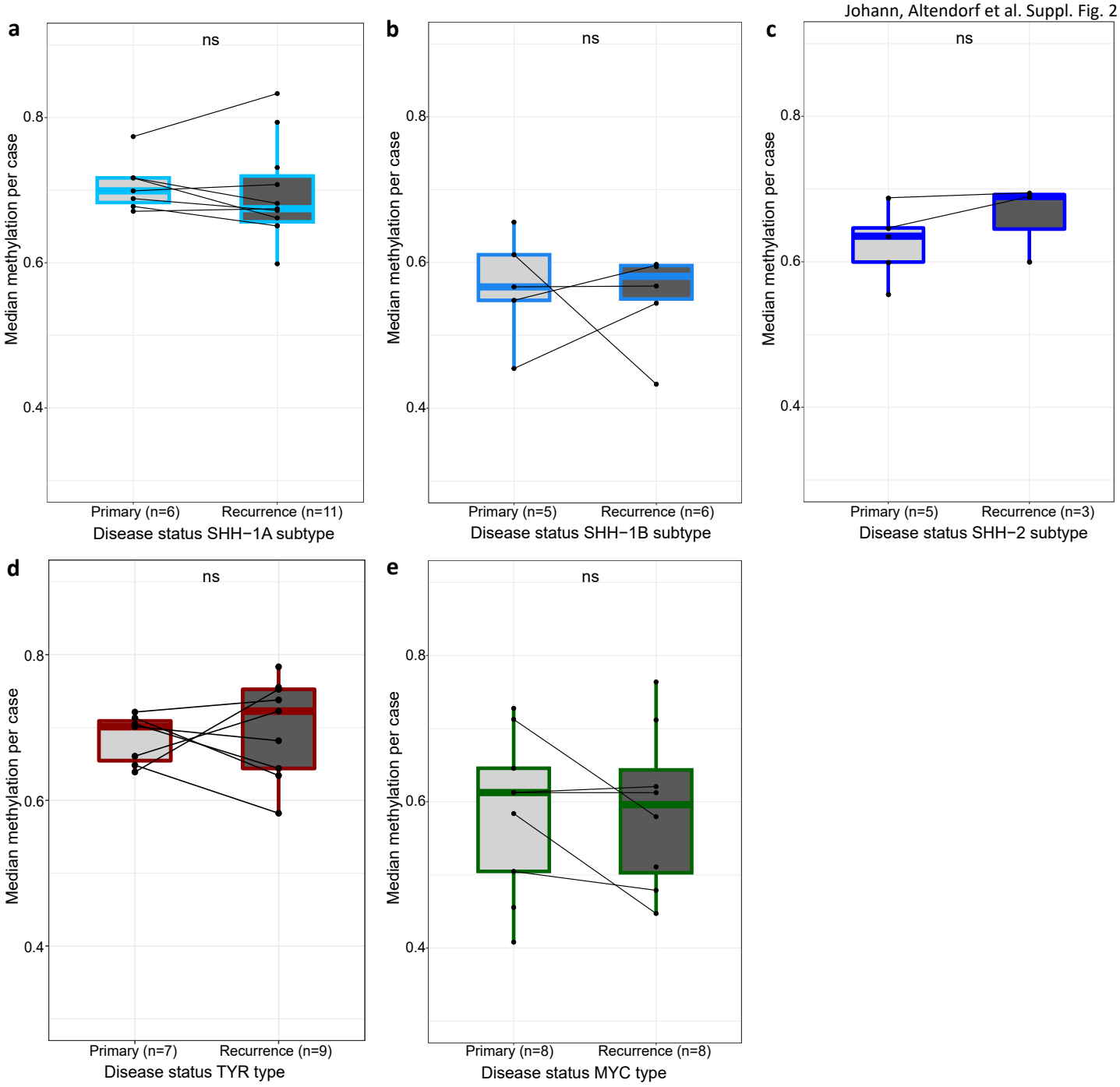

Supplementary Fig. 2: Global DNA methylation patterns of primary and recurrent AT/RT for each molecular type and subtype. Median methylation per case for each molecular type and subtype based on all CpG sites was calculated. **a - e** No significant differences of median methylation per case between disease states can be detected for AT/RT-SHH-1A (**a**), AT/RT-SHH-1B (**b**), AT/RT-SHH-2 (**c**), AT/RT-TYR (**d**), and AT/RT-MYC (**e**). Significance of methylation levels between primary and recurrent tumors was determined using a Wilcoxon test.

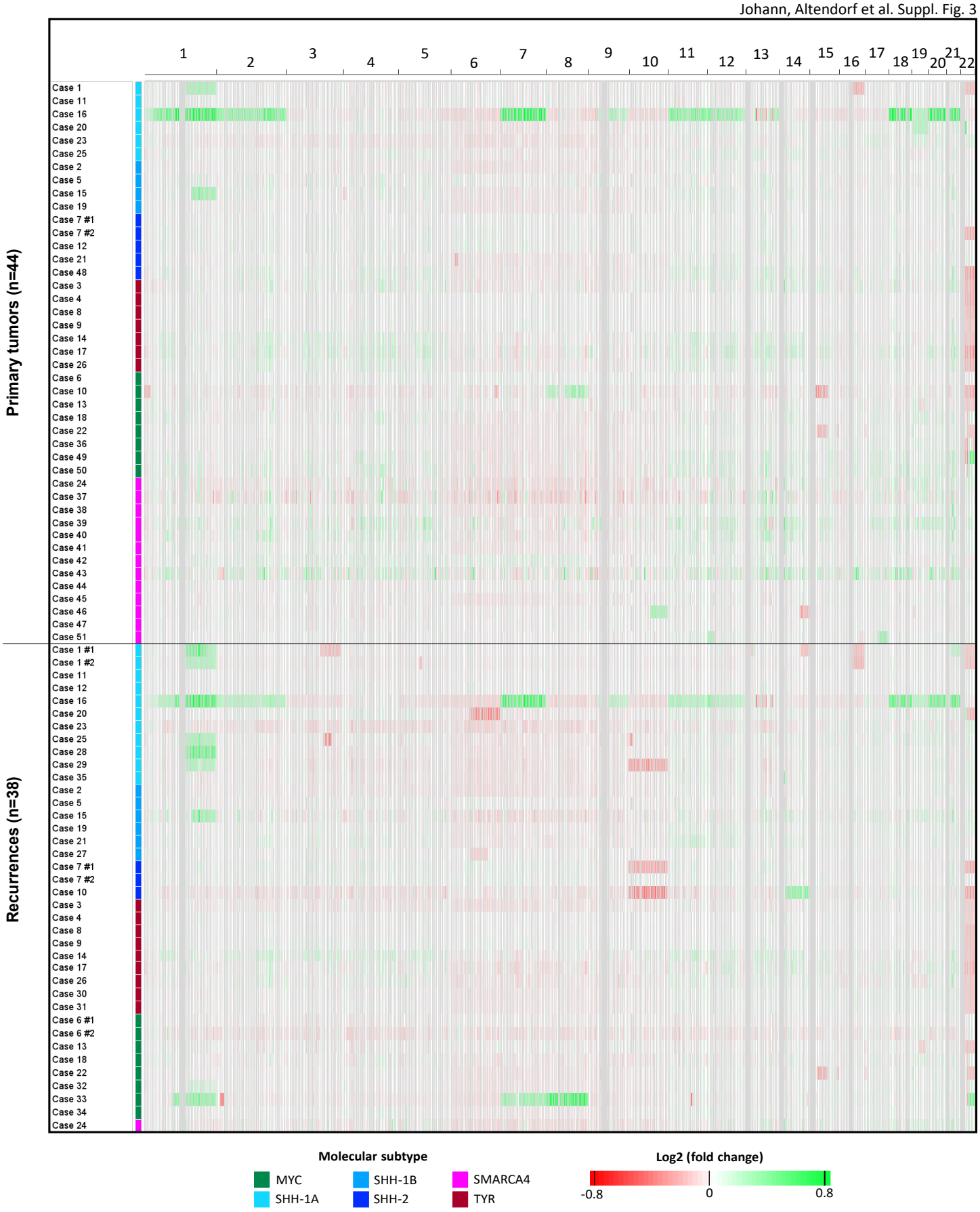

Supplementary Fig. 3: Methylation-derived copy number variation (CNV) of all primary (n=44) and recurrent (n=38) AT/RT. Individual copy number (CN) profiles were created using Integrative Genomics Viewer "IGV" based on raw methylated/ unmethylated signals. Green indicates a CN gain and red a CN loss. CNV profiles were sorted by disease status.

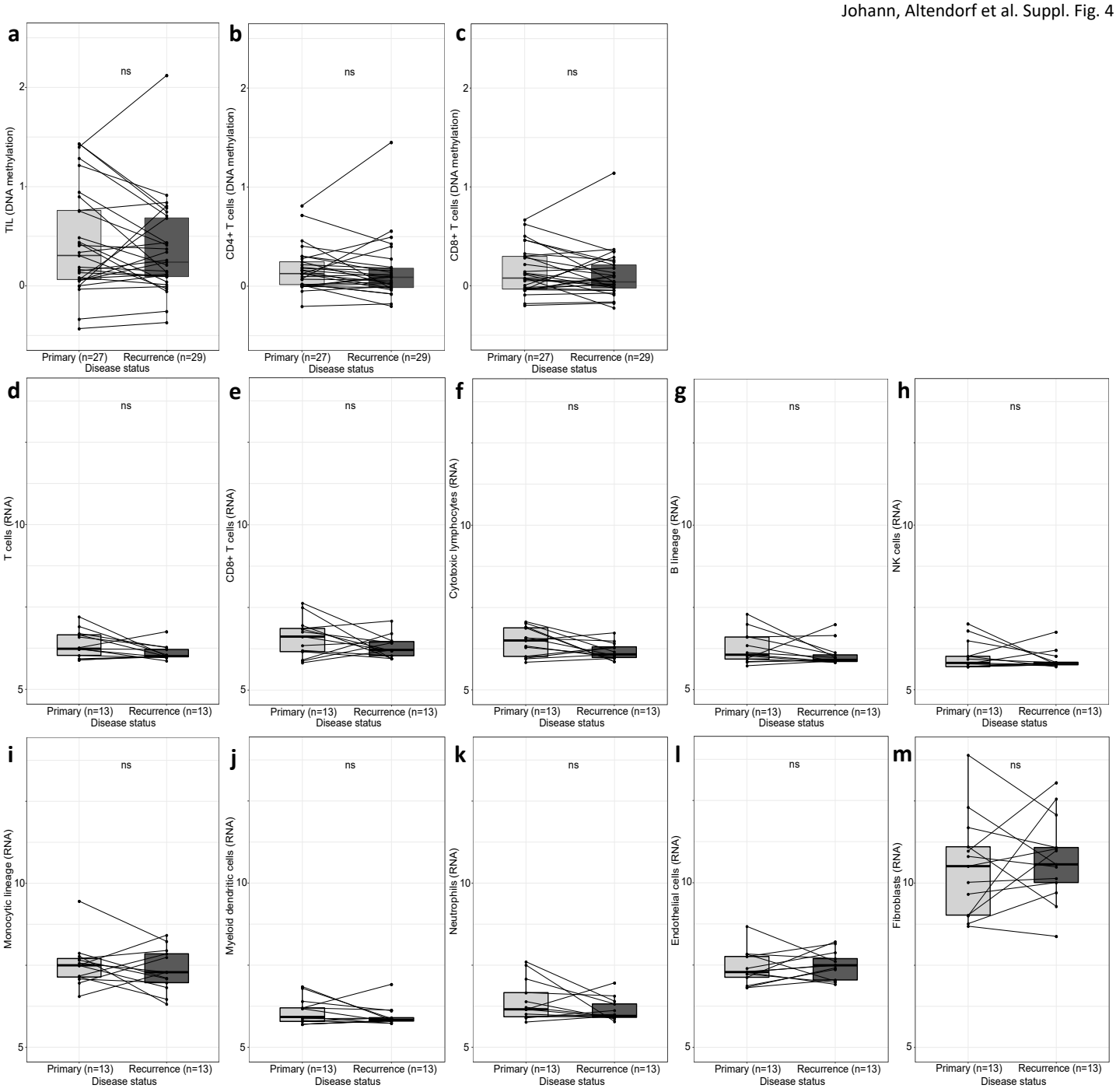

Supplementary Fig. 4: Estimation of immune cell infiltrates in primary tumors compared to recurrences of AT/RT. a - c DIMEimmune scores for infiltration with tumor-infiltrating lymphocytes (TILs) (**a**), $CD4^+$ T cells (**b**), and $CD8^+$ T cells (**c**) were normalized and calculated according to Safaei et al. (2021) using DNA methylation data. Each primary tumor was paired with related recurrence. Statistical analysis was performed using a t-test for paired data. **d - m** Scores for ten additional cell populations, T cells (**d**), $CD8^+$ T cells (**e**), cytotoxic lymphocytes (**f**), B lineage cells (**g**), NK cells (**h**), monocytic lineage cells (**i**), myeloid dendritic cells (**j**), neutrophils (**k**), endothelial cells (**l**), and fibroblasts (**m**), were calculated using RNA sequencing data according to Bockmayr et al. (2018, 2019). Each primary tumor was paired with related recurrence. Statistical analysis was performed using a t-test for paired data.

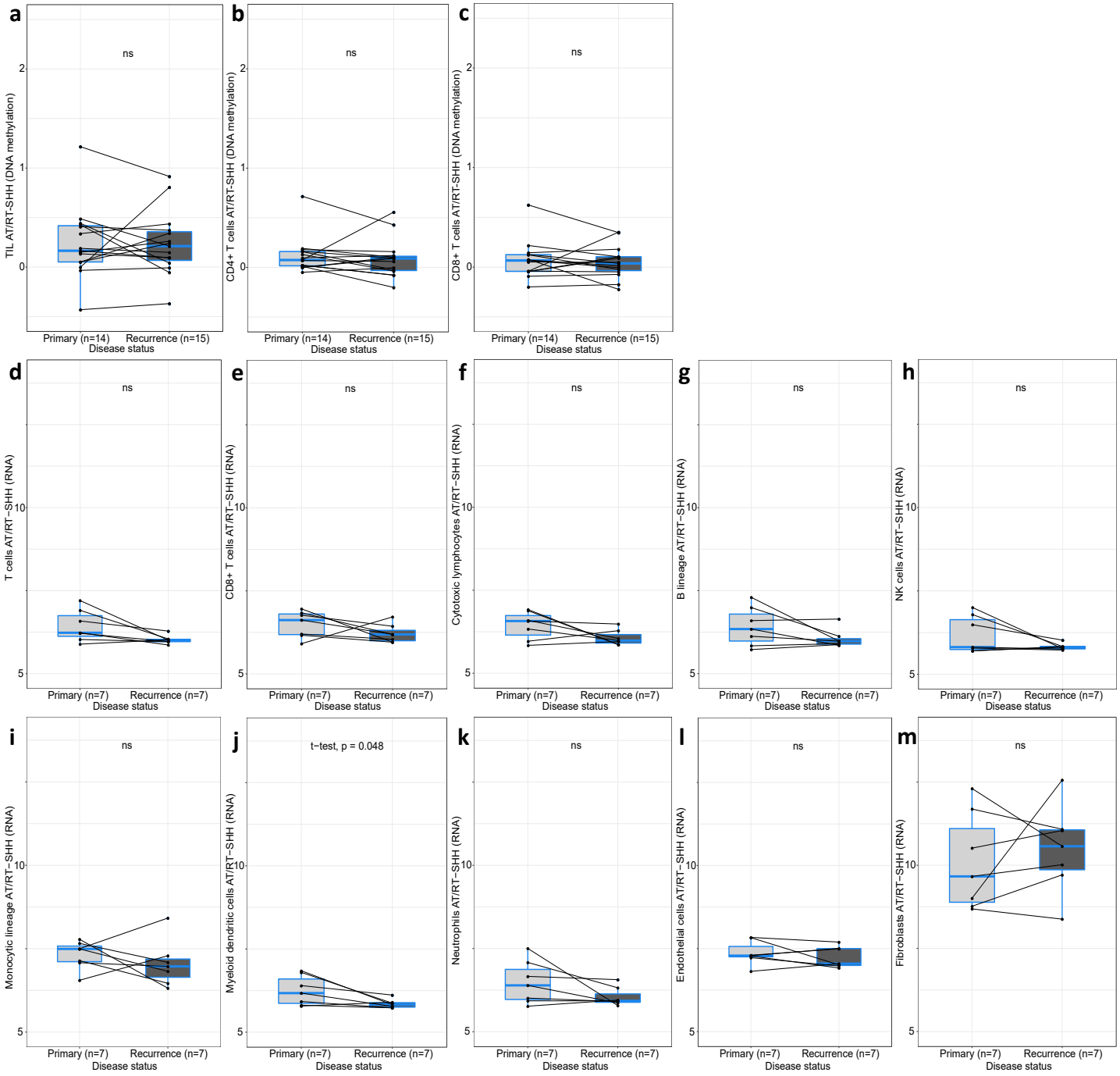

Supplementary Fig. 5: Estimation of immune cell infiltrates in primary tumors compared to recurrences of AT/RT-SHH. a - c DIMEimmune scores for infiltration with tumor-infiltrating lymphocytes (TILs) (**a**), $CD4^+$ T cells (**b**), and $CD8^+$ T cells (**c**) were normalized and calculated according to Safaei et al. (2021) using DNA methylation data. Each primary tumor was paired with related recurrence of the SHH subtype. Statistical analysis was performed using a t-test for paired data. **d - m** Scores for ten additional cell populations, T cells (**d**), $CD8^+$ T cells (**e**), cytotoxic lymphocytes (**f**), B lineage cells (**g**), NK cells (**h**), monocytic lineage cells (**i**), myeloid dendritic cells (**j**), neutrophils (**k**), endothelial cells (**l**), and fibroblasts (**m**), were calculated using RNA sequencing data according to Bockmayr et al. (2018, 2019). Each primary tumor was paired with related recurrence of the SHH subtype. Statistical analysis was performed using a t-test for paired data.

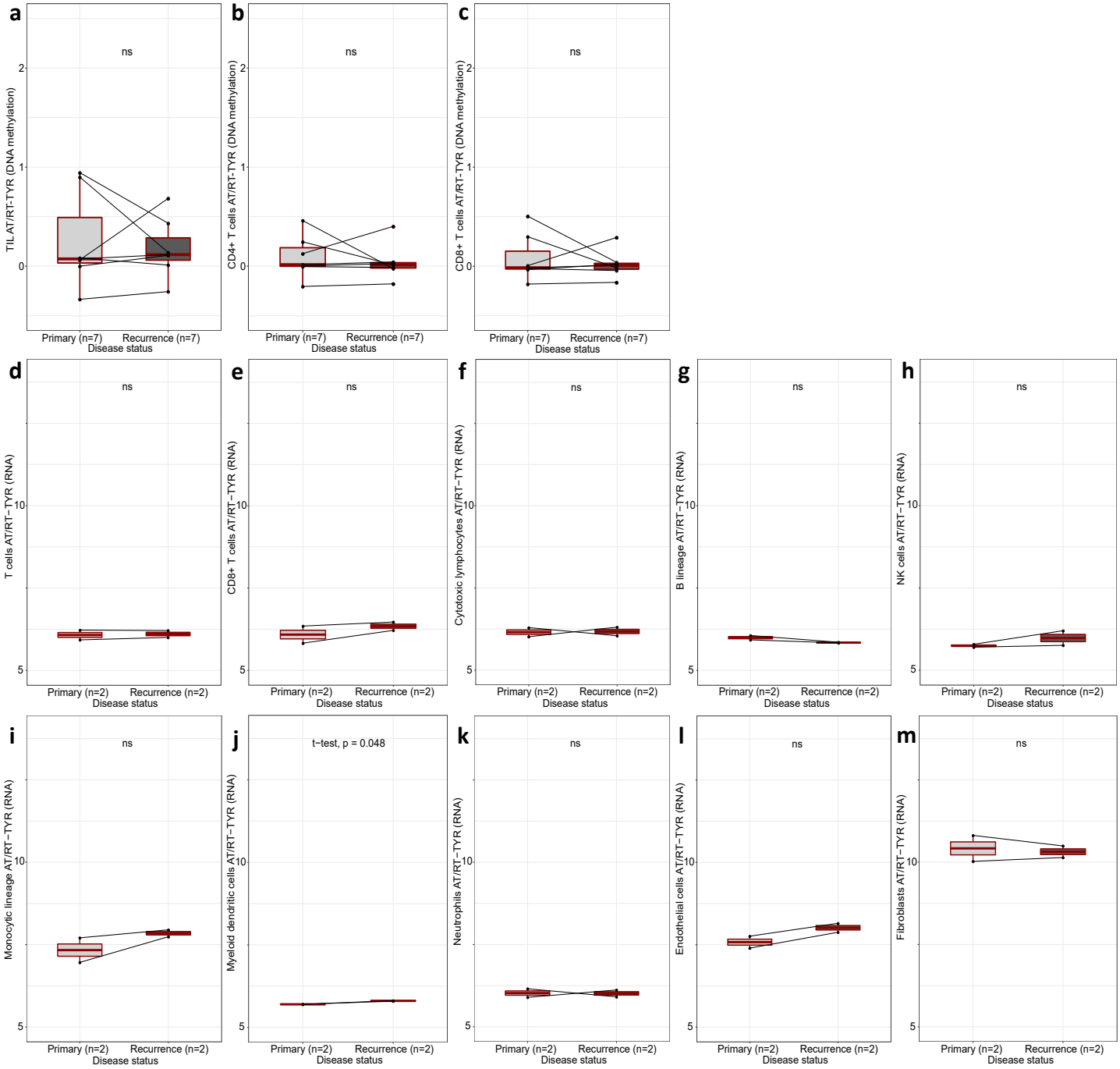

Supplementary Fig. 6: Estimation of immune cell infiltrates in primary tumors compared to recurrences of AT/RT-TYR. a - c DIMEimmune scores for infiltration with tumor-infiltrating lymphocytes (TILs) (**a**), $CD4^+$ T cells (**b**), and $CD8^+$ T cells (**c**) were normalized and calculated according to Safaei et al. (2021) using DNA methylation data. Each primary tumor was paired with related recurrence of the TYR subtype. Statistical analysis was performed using a t-test for paired data. **d - m** Scores for ten additional cell populations, T cells (**d**), $CD8^+$ T cells (**e**), cytotoxic lymphocytes (**f**), B lineage cells (**g**), NK cells (**h**), monocytic lineage cells (**i**), myeloid dendritic cells (**j**), neutrophils (**k**), endothelial cells (**l**), and fibroblasts (**m**), were calculated using RNA sequencing data according to Bockmayr et al. (2018, 2019). Each primary tumor was paired with related recurrence of the TYR subtype. Statistical analysis was performed using a t-test for paired data.

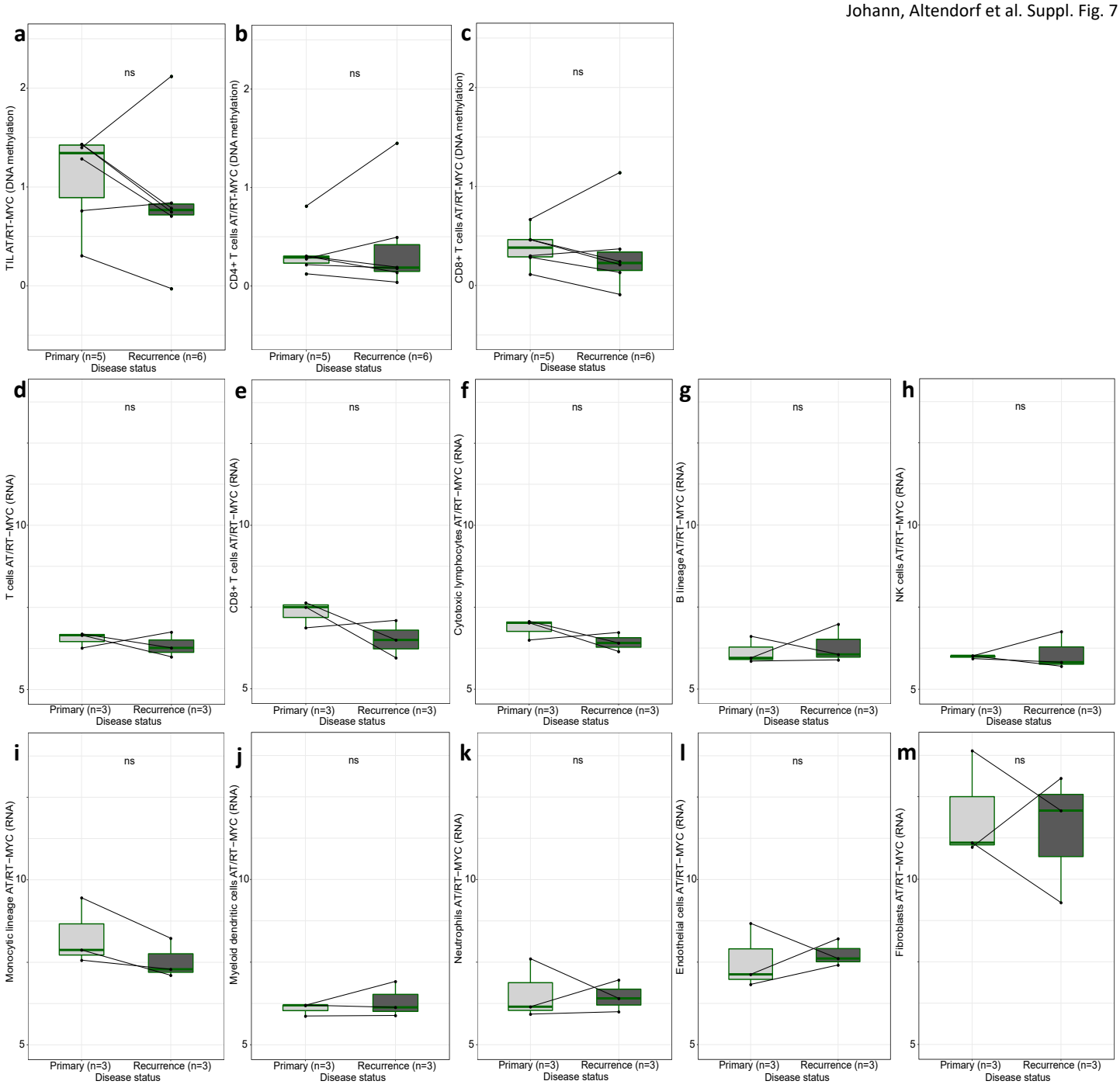

Supplementary Fig. 7: Estimation of immune cell infiltrates in primary tumors compared to recurrences of AT/RT-MYC. a - c DIMEimmune scores for infiltration with tumor-infiltrating lymphocytes (TILs) (**a**), $CD4^+$ T cells (**b**), and $CD8^+$ T cells (**c**) were normalized and calculated according to Safaei et al. (2021) using DNA methylation data. Each primary tumor was paired with related recurrence of the MYC subtype. Statistical analysis was performed using a t-test for paired data. **d - m** Scores for ten additional cell populations, T cells (**d**), $CD8^+$ T cells (**e**), cytotoxic lymphocytes (**f**), B lineage cells (**g**), NK cells (**h**), monocytic lineage cells (**i**), myeloid dendritic cells (**j**), neutrophils (**k**), endothelial cells (**l**), and fibroblasts (**m**), were calculated using RNA sequencing data according to Bockmayr et al. (2018, 2019). Each primary tumor was paired with related recurrence of the MYC subtype. Statistical analysis was performed using a t-test for paired data.

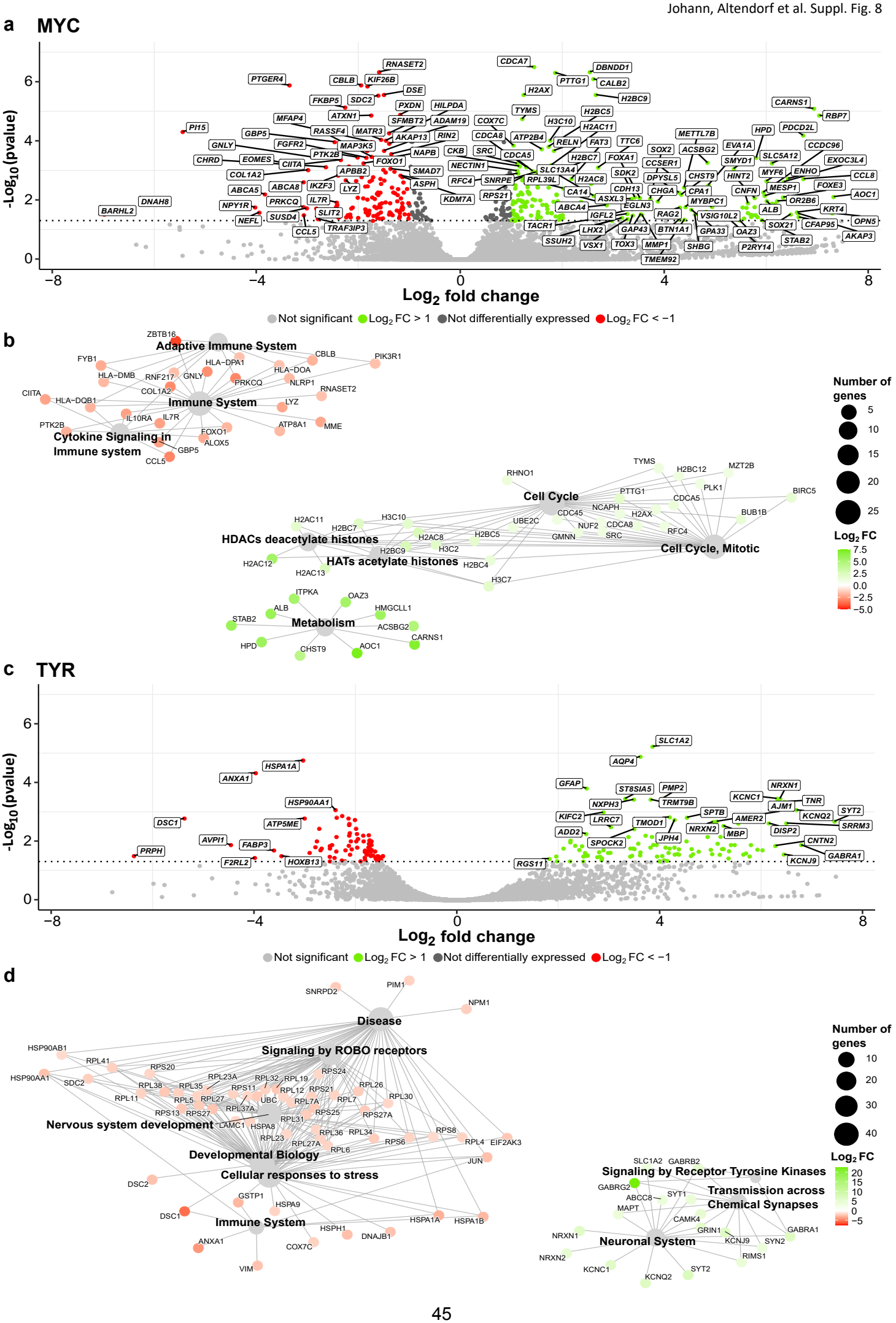
a
MYC
-Log10(pvalue)
Log2 fold change
Not significant
Log2 FC > 1
Not differentially expressed
Log2 FC < −1
b
Adaptive Immune System
Immune System
Cytokine Signaling in Immune system
Cell Cycle
Cell Cycle, Mitotic
HDACs deacetylate histones
HATs acetylate histones
Metabolism
Number of genes
Log2 FC
c
TYR
-Log10(pvalue)
Log2 fold change
Not significant
Log2 FC > 1
Not differentially expressed
Log2 FC < −1
d
Disease
Signaling by ROBO receptors
Nervous system development
Developmental Biology
Cellular responses to stress
Immune System
Signaling by Receptor Tyrosine Kinases
Transmission across Chemical Synapses
Neuronal System
Number of genes
Log2 FC

Supplementary Fig. 8: Differentially expressed genes and pathways in AT/RT-MYC and AT/RT-TYR primary tumors and recurrences. a + c Volcano plots of differentially expressed genes between primary and recurrent AT/RT-MYC (**a**) and AT/RT-TYR (**c**). Significant genes with a $\log_2$ fold change > 1 are colored in red for upregulated genes in primary tumors and in green for upregulated genes in recurrences. **b + d** Enriched pathways and genes in AT/RT-MYC (**b**) and AT/RT-TYR (**d**) recurrences. Colors indicate the $\log_2$ FC of the gene expression. Green dots mark a positive $\log_2$ FC and red dots a negative. The size of the pathway dots indicates the number of involved genes in the pathways.

3. Publication 2

Generation of new transgenic SMARCA4-deficient mouse models results in neuromuscular weakness and paralysis of limbs

Sina Neyazi*, Lea Altendorf*, Dora Schwetje, Carolin Göbel, Melanie Schoof, Dörthe Holdhof, Ulrich Schüller

Brain Pathology 2022

*These authors contributed equally to this work

Check for updates

Received: 14 September 2022 | Accepted: 19 December 2022

DOI: 10.1111/bpa.13146

RESEARCH LETTER

Brain Pathology

Generation of new transgenic SMARCA4-deficient mouse models results in neuromuscular weakness and paralysis of limbs

Sina Neyazi[1,2,3] | **Lea Altendorf**[1,2] | **Dora Schwetje**[1,2,4] | **Carolin Göbel**[1,2] | **Melanie Schoof**[1,2] | **Dörthe Holdhof**[1,2] | **Ulrich Schüller**[1,2,5]

[1]Department of Pediatric Hematology and Oncology, University Medical Center Hamburg-Eppendorf, Hamburg, Germany

[2]Research Institute Children's Cancer Center Hamburg, Hamburg, Germany

[3]Department of Pediatric Oncology, Dana-Farber Cancer Institute Boston, Massachusetts, USA

[4]Research Group Anatomy, School of Medicine and Health Studies, Carl von Ossietzky University Oldenburg, Oldenburg, Germany

[5]Institute of Neuropathology, University Medical Center Hamburg-Eppendorf, Hamburg, Germany

Correspondence
Ulrich Schüller, Research Institute Children's Cancer Center Hamburg, Martinistraße 52, D-20251 Hamburg, Germany.
Email: u.schueller@uke.de

Funding information
Fördergemeinschaft Kinderkrebs-Zentrum Hamburg; Wilhelm Sander-Stiftung

KEYWORDS: mouse model, rhabdoid tumors, SMARCA4

The SWItch/sucrose non-fermentable (SWI/SNF) complex is an ATP-dependent chromatin-remodeling complex, which is crucially involved in the regulation of gene expression. Many physiological processes during the development of the nervous system essentially rely on transcriptional regulation through the SWI/SNF complex, such as the differentiation of Schwann cells, which are required for the myelination of peripheral nerves [1]. Besides its regulatory role in normal cellular development, the SWI/SNF complex is known to be deregulated in various human cancers, either by mutations in genes encoding the subunits of the complex or by overexpression of these genes. In fact, alterations in at least one of the genes that make up the complex are observed in a large number of malignancies [1, 2]. Mutations in *SMARCA4*, which is one of the two ATPase subunits of the SWI/SNF complex, are not only frequently found in various carcinoma types of adult patients, but have also been described as driver mutations in the development of a subset of pediatric rhabdoid tumors (RT) [3]. RT are rare, highly aggressive embryonal tumors mostly affecting young children, with a poor prognosis, and an overall survival of 17 months. They comprise RT of the central nervous system (CNS), which are known as atypical teratoid/rhabdoid tumors (AT/RT), RT of the kidney (RTK), and malignant RT of the soft tissue (MRT). All RT show a biallelic inactivation of the SWI/SNF subunits SMARCB1 or SMARCA4 [2, 3]. Mutations in *SMARCB1* leading to the development of RT have been characterized by various mouse models, whereas, to date, SMARCA4 deficiency has never caused RT development in vivo. So far, there is no cell line for SMARCA4-deficient RT. Therefore, in vitro and in vivo models for SMARCA4-deficient RT are urgently needed to better understand the oncogenesis and to develop potential treatment options.

Recently, neural crest cells were suggested as one potential cellular origin of SMARCB1-deficient RT [2]. Such cells express the glycoprotein myelin protein zero (MPZ, P0), which is also known to be the major structural protein in peripheral myelin. In a previous study, *P0-Cre* mice were used to conditionally delete *Smarcb1*, which resulted in the development of RT [4]. In addition, genomic and single-cell transcriptomic analyses of human RT-derived organoids revealed a shared cellular lineage of *SMARCB1*-mutated RT cells and neural crest-derived Schwann cells [2]. To examine, whether P0 also marks cells of origin of SMARCA4-deficient RT, we crossed

Sina Neyazi and Lea Altendorf contributed equally

This is an open access article under the terms of the Creative Commons Attribution-NonCommercial-NoDerivs License, which permits use and distribution in any medium, provided the original work is properly cited, the use is non-commercial and no modifications or adaptations are made.
© 2022 The Authors. *Brain Pathology* published by John Wiley & Sons Ltd on behalf of International Society of Neuropathology.

17503639, 0, Downloaded from https://onlinelibrary.wiley.com/doi/10.1111/bpa.13146 by Staats- Und Universitätsbiblio, Wiley Online Library on [29/12/2022]. See the Terms and Conditions (https://onlinelibrary.wiley.com/terms-and-conditions) on Wiley Online Library for rules of use; OA articles are governed by the applicable Creative Commons License

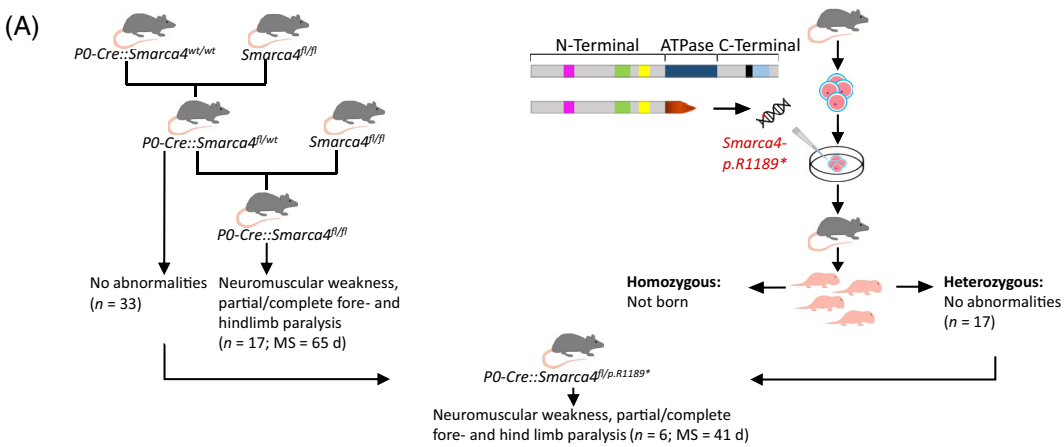

(B)

Score	Name	Gait	Grid
0	No symptoms	Normal	Normal
1	Neuromuscular weakness	Mildly abnormal gait	No difficulty to hold on grid
2	Partial hind limb paralysis	Abnormal gait with intermitted dragging of both hind limbs	Mild difficulty to hold on grid, slipping of the grid
3	Complete hind limb paralysis	Abnormal gait with permitted dragging of both hind limbs	Inability to hold on grid
4	Partial fore- and hind limb paralysis	Abnormal gait with permitted dragging of both hind limbs	Difficulty to hold on grid with fore limbs

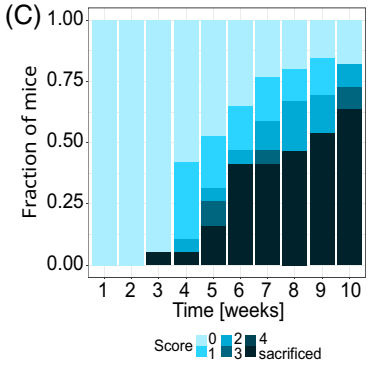

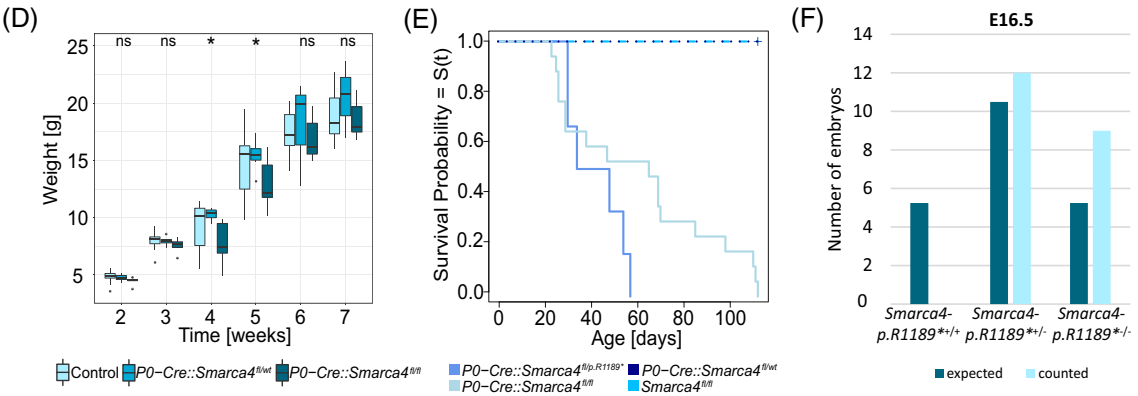

FIGURE 1 Development and characterization of SMARCA4-deficient mouse models. (A) *P0-Cre* mice were crossed with *Smarca4*$^{fl/fl}$ mice. A second mouse model was created by insertion of the *Smarca4* point mutation c.3565C>T (p.R1189*), which is a nonsense mutation leading to a truncated protein with impaired function, by pronuclear injection into 1-cell stage embryos in vitro using CRISPR/Cas9. The third mouse model *P0-Cre::Smarca4*$^{fl/p.R1189*}$ was created by crossing *P0-Cre::Smarca4*$^{fl/wt}$ with *Smarca4-p.R1189**$^{+/-}$ mice. MS, median survival; d, days. (B) Score for the analysis of symptoms of *P0-Cre::Smarca4*$^{fl/fl}$ mice adapted from Weider et al. (C) Symptoms of *P0-Cre::Smarca4*$^{fl/fl}$ mice ($n = 19$, according to B) during an observation period of 10 weeks. (D) Body weight of *P0-Cre::Smarca4*$^{fl/fl}$, *P0-Cre::Smarca4*$^{fl/wt}$, and control mice ($n_{total} = 33$) over 7 weeks. (E) Kaplan Meier plot of *P0-Cre::Smarca4*$^{fl/fl}$ mice (MS = 65 d), *P0-Cre::Smarca4*$^{fl/wt}$ mice, *P0-Cre::Smarca4*$^{fl/p.R1189*}$ mice (MS = 41 d), and *Smarca4*$^{fl/fl}$ control mice. (F) Expected numbers of each point mutation genotype were calculated according to Mendel and compared to the counted mice of each genotype at E16.5.

P0-Cre mice [5] with *Smarca4*$^{fl/fl}$ mice [6] to generate *P0-Cre::Smarca4*$^{fl/wt}$ ($n = 33$) and *P0-Cre::Smarca4*$^{fl/fl}$ mice ($n = 17$). As a control, *P0-Cre::Smarcb1*$^{fl/fl}$ mice ($n = 23$) were produced by crossing *P0-Cre* mice [5] with *Smarcb1*$^{fl/fl}$ mice [7]. All mice were bred on a C57BL/6J background and mice of both sexes were used for the study.

No abnormalities were observed in heterozygous mice (*P0-Cre::Smarca4*$^{fl/wt}$), but all homozygous mice developed neuromuscular weakness and partial or complete fore- and hind limb paralysis within 10 weeks (Figure 1A). To further analyze and classify this phenotype, a score for the symptoms of *P0-Cre::Smarca4*$^{fl/fl}$ mice was adapted from Weider et al. [8] (Figure 1B). Symptoms started at 3 weeks of age and increased continuously as visualized in Figure 1C. Body weight control revealed that homozygous mice were significantly lighter compared to heterozygous

17503639, 0, Downloaded from https://onlinelibrary.wiley.com/doi/10.1111/bpa.13146 by Staats- Und Universitätsbiblio, Wiley Online Library on [29/12/2022]. See the Terms and Conditions (https://onlinelibrary.wiley.com/terms-and-conditions) on Wiley Online Library for rules of use; OA articles are governed by the applicable Creative Commons License

and control mice after 4 ($p = 0.018$) and 5 weeks ($p = 0.028$, Figure 1D). Mice were sacrificed based on the severity of paralysis and weight loss. The median overall survival was 65 days (Figure 1E). However, none of these mice developed tumors, as shown by thorough macroscopic inspection of all mice and histological analyses of the brains and kidneys in a subset of mice. Additionally, control mice with the genotype *P0-Cre::Smarcb1*$^{fl/fl}$ ($n = 23$) developed the same neuromuscular phenotype after the age of 10 weeks without any clinical or macroscopic signs of tumor development.

Since SMARCA4 loss in other cell types than neural crest cells previously failed to model RT development as well, our goal was to develop a mouse model that mimics the human situation more specifically. Therefore, we next generated *Smarca4-p.R1189** knock-in mice carrying a constitutive point mutation. The same mutation had previously been described in the germline of a family with RT predisposition syndrome leading to the development of RT during infancy of two siblings [9]. Knock-in mice were generated by pronuclear injection in 1-cell stage embryos after induction of a c.3565C>T (p.R1189*) point mutation via CRISPR/Cas9.

In human patients, this mutation leads to a nonsense-mediated decay of the transcript [9] (Figure 1A). Mice carrying a heterozygous *Smarca4-p.R1189** point mutation ($n = 17$) did not show any abnormalities over the observation period of 1 year. However, none of the 75 mice that were born after further crossing of heterozygous mice and none of the embryos genotyped at embryonal day 10.5 (E10.5) and E16.5 had a homozygous genotype, suggesting an early embryonal death of mice homozygous for *Smarca4-p.R1189** (Figure 1F).

Finally, *P0-Cre::Smarca4*$^{fl/wt}$ mice were crossed with *Smarca4-p.R1189**$^{+/-}$ mice for the generation of *P0-Cre::Smarca4*$^{fl/p.R1189*}$ mice. In this way, a constitutive mutation–similar to a human germline mutation - and a conditional mutation in neural crest cells were combined to recapitulate the potential situation in pediatric patients with RT predisposition syndrome and to potentially avoid embryonic death of the mice. All *P0-Cre::Smarca4*$^{fl/p.R1189*}$ mice ($n = 6$) showed a uniform phenotype similar to *P0-Cre::Smarca4*$^{fl/fl}$ mice, with neuromuscular weakness and paralysis of the fore- and hind limbs (Figure 1A) and a median overall survival of 41 days (Figure 1E). These results indicate that a homozygous *Smarca4-p.R1189** mutation is impairing SMARCA4 function in mice, but they also indicate that a recombination of *Smarca4* through the above described *P0-Cre* strain is still insufficient for tumor development, even if the other allele carries a constitutive loss-of-function mutation.

In conclusion, homozygous *Smarca4* mutations introduced in the *P0-Cre* mouse line used in this study cause neuromuscular weakness and paralysis of the fore- and hind limbs. A similar phenotype was previously observed in Schwann cell-specific transgenic *DHH-Cre::Smarca4*$^{fl/fl}$ [8] and *DHH-Cre::Smarcb1*$^{fl/fl}$ mice [4]. In both *DHH-Cre* mouse lines, the observed phenotype could be attributed to an impaired myelination of peripheral nerves. Further analyses of our *P0-Cre::Smarca4*$^{fl/fl}$ mouse model confirmed genomic recombination of *Smarca4*$^{fl/fl}$ alleles (Figure S1A) and loss of SMARCA4 (Figure S1D,E) together with *Cre*-expression (Figure S1A) in the peripheral nerves of *P0-Cre::Smarca4*$^{fl/fl}$ mice. Here, we could prove that myelination of peripheral nerves is also impaired in our *P0-Cre::Smarca4*$^{fl/fl}$ mouse model. Histopathological assessment using toluidine blue staining (TBO) revealed thinner and impaired myelin sheaths surrounding axons of sciatic nerves of *P0-Cre::Smarca4*$^{fl/fl}$ mice (Figure S1H,I) compared to *Smarca4*$^{fl/fl}$ control mice (Figure S1F,G). Histological assessment of thigh muscles of *P0-Cre::Smarca4*$^{fl/fl}$ mice (Figure S1L,M) also revealed abnormalities in contrast to *Smarca4*$^{fl/fl}$ control mice (Figure 1J,K) showing a neurogenic image of muscle tissue with angular atrophic myocytes (Supplementary Figure 1M) in muscles that were innervated by impaired sciatic nerves. No histological abnormalities were detected in the spinal cord of *P0-Cre::Smarca4*$^{fl/fl}$ mice (Figure 1P,Q) compared to *Smarca4*$^{fl/fl}$ control mice (Figure S1N,O).

The similarity of phenotypes caused by a *Smarca4*-knockout in *DHH-Cre*, which starts to be expressed at E12.5 [4], and our *P0-Cre*, which is presumably expressed from E13.5 onwards [10] indicates that both *Cre*-lines target a cellular compartment, which requires a functional SWI/SNF complex for proper myelination of peripheral nerves. However, these results highlight that the choice of the *Cre*-driver is critical for targeting the exact cellular population of origin for a tumor type of interest. For example, previous tumor generation in a *P0-Cre::Smarcb1*$^{fl/fl}$ mouse strain, in which *P0-Cre* has been shown to be expressed at E9.5 [4], could not be reproduced in another *P0-Cre* mouse strain, for which the expression first starts at E13.5 [10]. Overall, our results indicate that the initiation of RT from neural crest-derived cells might require an inactivation of *Smarca4* earlier than E13.5 or that RT originate from a different cell type. While such early time points have previously been identified for the development of *Smarcb1*-mutated RT [4], the exact temporal window for the initiation of SMARCA4-deficient RT and the cells of origin remain to be determined. In fact, the developmental time point of origin may even be earlier than for SMARCB1-mutated RT, since the median age of diagnosis is significantly lower in patients with SMARCA4-deficient AT/RT [3].

ACKNOWLEDGMENTS

We thank Vanessa Thaden and Jacqueline Tischendorf for excellent technical support. We thank Michael Reuter and Helen Morrison for the generous gift of *P0-Cre* mice. We acknowledge the great support of the Small Animal Core facility at the Leibniz-Institute of Virology. We also want to thank Irm Hermanns-Borgmeyer and Uwe

17503639, 0, Downloaded from https://onlinelibrary.wiley.com/doi/10.1111/bpa.13146 by Staats- Und Universitätsbiblio, Wiley Online Library on [29/12/2022]. See the Terms and Conditions (https://onlinelibrary.wiley.com/terms-and-conditions) on Wiley Online Library for rules of use; OA articles are governed by the applicable Creative Commons License

Borgmeyer from the Transgenic Animal Unit at the Center for Molecular Neurobiology (ZMNH) for assistance with generating *Smarca4-p.R1189** mice.

FUNDING INFORMATION

This work was supported by the Wilhelm-Sander Stiftung, the Fördergemeinschaft Kinderkrebszentrum Hamburg and the University Cancer Center Hamburg.

CONFLICT OF INTEREST

The authors declare no conflicts of interest.

DATA AVAILABILITY STATEMENT

Data sharing is not applicable to this article as no new data were created or analyzed in this study.

ORCID

Ulrich Schüller https://orcid.org/0000-0002-8731-1121

REFERENCES

1. Fröb F, Wegner M. The role of chromatin remodeling complexes in Schwann cell development. Glia. 2020;68(8):1596–603.
2. Custers L, Khabirova E, Coorens THH, Oliver TRW, Calandrini C, Young MD, et al. Somatic mutations and single-cell transcriptomes reveal the root of malignant rhabdoid tumours. Nat Commun. 2021;12(1):1407.
3. Holdhof D, Johann PD, Spohn M, Bockmayr M, Safaei S, Joshi P, et al. Atypical teratoid/rhabdoid tumors (ATRTs) with *SMARCA4* mutation are molecularly distinct from *SMARCB1*-deficient cases. Acta Neuropathol. 2020;141(2):291–301.
4. Vitte J, Gao F, Coppola G, Judkins AR, Giovannini M. Timing of Smarcb1 and Nf2 inactivation determines schwannoma versus rhabdoid tumor development. Nat Commun. 2017;8(1):1–12.
5. Feltri ML, D'Antonio M, Previtali S, Fasolini M, Messing A, Wrabetz L. P0-Cre transgenic mice for inactivation of adhesion molecules in Schwann cells. Ann N Y Acad Sci. 1999;883:116–23.
6. Sumi-Ichinose C, Ichinose H, Metzger D, Chambon P. SNF2-BRG1 is essential for the viability of F9 murine embryonal carcinoma cells. Mol Cell Biol. 1997;17(10):5976–86.
7. Roberts CWM, Leroux MM, Fleming MD, Orkin SH. Highly penetrant, rapid tumorigenesis through conditional inversion of the tumor suppressor gene *Snf5*. Cancer Cell. 2002;2(5):415–25.
8. Weider M, Küspert M, Bischof M, Vogl MR, Hornig J, Loy K, et al. Chromatin-remodeling factor Brg1 is required for Schwann cell differentiation and myelination. Dev Cell. 2012;23(1):193–201.
9. Schneppenheim R, Frühwald MC, Gesk S, Hasselblatt M, Jeibmann A, Kordes U, et al. Germline nonsense mutation and somatic inactivation of *SMARCA4*/*BRG1* in a family with Rhabdoid tumor predisposition syndrome. Am J Hum Genet. 2010;86(2):279–84.
10. Feltri ML, Graus Porta D, Previtali SC, Nodari A, Migliavacca B, Cassetti A, et al. Conditional disruption of beta 1 integrin in Schwann cells impedes interaction with axons. J Cell Biol. 2002;156(1):199–209.

SUPPORTING INFORMATION

Additional supporting information can be found online in the Supporting Information section at the end of this article.

How to cite this article: Neyazi S, Altendorf L, Schwetje D, Göbel C, Schoof M, Holdhof D, et al. Generation of new transgenic SMARCA4-deficient mouse models results in neuromuscular weakness and paralysis of limbs. Brain Pathology. 2022. e13146. https://doi.org/10.1111/bpa.13146

17503639, 0, Downloaded from https://onlinelibrary.wiley.com/doi/10.1111/bpa.13146 by Staats- Und Universitätsbibliо, Wiley Online Library on [29/12/2022]. See the Terms and Conditions (https://onlinelibrary.wiley.com/terms-and-conditions) on Wiley Online Library for rules of use; OA articles are governed by the applicable Creative Commons License

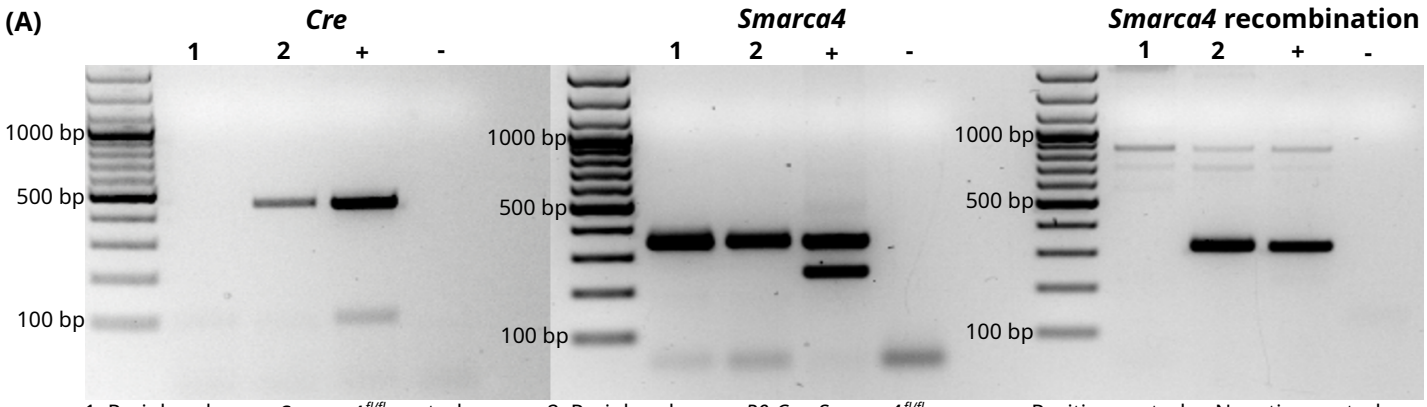

1: Peripheral nerve *Smarca4*$^{fl/fl}$ control mouse; 2: Peripheral nerve *P0-Cre::Smarca4*$^{fl/fl}$ mouse; +: Positive control; -: Negative control

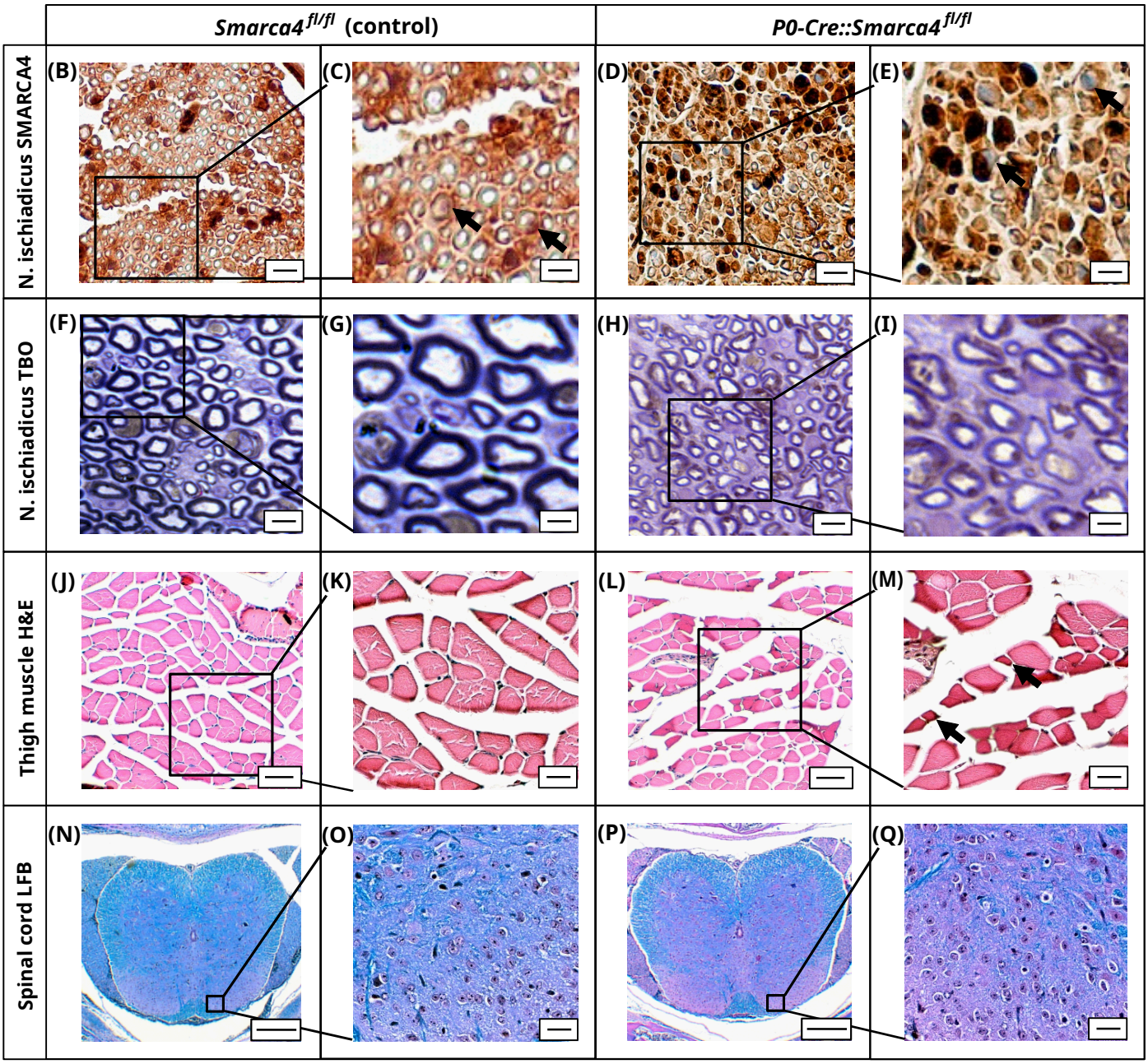

Supplementary Figure 1: Investigation of the neuromuscular phenotype of *P0-Cre::Smarca4*$^{fl/fl}$ mice. A: Genotyping of peripheral nerves of *P0-Cre::Smarca4*$^{fl/fl}$ mice (2) and *Smarca4*$^{fl/fl}$ control mice (1) shows *Cre* expression (448 bp; control: 100 bp), the presence of the homozygous *Smarca4*^{fl} allele (wt: 241 bp; fl: 387 bp), and the presence of the recombined *Smarca4*^{fl} allele (313 bp). +: Positive control; -: Negative control. **B-Q:** Immunohistochemical stainings of peripheral nerves (N. ischiadicus; A-I), thigh muscles (J-M), and spinal cord (N-Q) of *P0-Cre::Smarca4*$^{fl/fl}$ mice and *Smarca4*$^{fl/fl}$ control mice. **B-E:** SMARCA4 staining shows SMARCA4 loss in *P0-Cre::Smarca4*$^{fl/fl}$ mice (D+E). Arrows mark example nuclei with SMARCA4 loss (E). SMARCA4 is expressed in *Smarca4*$^{fl/fl}$ control mice (B+C). Arrows mark example nuclei with SMARCA4 expression (C). Scale bars of B+D correspond to 10 µm and of C+E to 5 µm. **F-I:** Semi-thin sections, stained using toluidine blue (TBO), reveal thinner myelin sheaths in *P0-Cre::Smarca4*$^{fl/fl}$ mice (H+I) compared to *Smarca4*$^{fl/fl}$ control mice (F+G). Scale bars of F+H correspond to 5 µm and of G+I to 2.5 µm. **J-M:** H&E staining of axial sections of thigh muscles shows angular atrophy in *P0-Cre::Smarca4*$^{fl/fl}$ mice (L+M) in contrast to *Smarca4*$^{fl/fl}$ control mice (J+K). Arrows mark example angular atrophic myocytes (M). Scale bars of J+L correspond to 50 µm and of K+M to 20 µm. **N-Q:** Luxol staining (LFB) of axial sections of the spinal cord does not show a difference between *P0-Cre::Smarca4*$^{fl/fl}$ mice (P+Q) and *Smarca4*$^{fl/fl}$ control mice (N+O). Scale bars of N+P correspond to 200 µm and of O+Q to 20 µm.

4. Unpublished manuscript 1

Therapy-resistance in AT/RT is driven by epithelial-mesenchymal transition, extracellular matrix changes, and enrichment of *CD1A*$^{+}$ *CD207*$^{+}$ dendritic cells

Lea Altendorf, Anton Althammer, Rajanya Roy, Karoline Hack, Flavia W. de Faria, Arend Koch, Vanessa Thaden, Melanie Schoof, Martin U. Schuhmann, Peter Hauser, Pascal D. Johann, Martin Hasselblatt, Michael C. Frühwald, Kornelius Kerl, Ulrich Schüller

Under review: Neuro-Oncology 2025

To be submitted to Neuro-Oncology

Title

Therapy-resistance in AT/RT is driven by epithelial-mesenchymal transition, extracellular matrix changes, and enrichment of *CD1A*$^{+}$ *CD207*$^{+}$ dendritic cells

Authors

Lea Altendorf[1,2], Anton Althammer[1,2,3], Rajanya Roy[4], Karoline Hack[1,2], Flavia W. de Faria[4], Arend Koch[5], Vanessa Thaden[1,2], Melanie Schoof[1,2], Martin U. Schuhmann[6], Peter Hauser[7], Pascal D. Johann[8,9,10], Martin Hasselblatt[11], Michael C. Frühwald[8], Kornelius Kerl[4], and Ulrich Schüller[1,2,12]

[1]Department of Pediatric Hematology and Oncology, University Medical Center Hamburg-Eppendorf, Germany
[2]Research Institute Children's Cancer, University Medical Center Hamburg-Eppendorf, Germany
[3]Mildred Scheel Cancer Career Center HaTriCS4, University Medical Center Hamburg-Eppendorf, Hamburg, Germany.
[4]Department of Pediatric Hematology and Oncology, University Medical Center Münster, Germany
[5]Institute of Neuropathology, Charité – Universitätsmedizin Berlin, Germany
[6]Division of Pediatric Neurosurgery, Department of Neurosurgery, Eberhard Karl's University Hospital of Tübingen, Germany
[7]Second Department of Pediatrics, Semmelweis University, Budapest, Hungary
[8]Paediatric and Adolescent Medicine, Swabian Children's Cancer Center Augsburg, EU-RHAB trial center, Germany
[9]Hopp Children's Cancer Center (KiTZ), German Cancer Research Center (DKFZ) and German Cancer Research Consortium (DKTK), Heidelberg, Germany
[10]Division of Pediatric Neurooncology, German Cancer Research Center (DKFZ) and German Cancer Research Consortium (DKTK), Heidelberg, Germany
[11]Institute of Neuropathology, University Hospital Münster, Germany
[12]Institute of Neuropathology, University Medical Center Hamburg-Eppendorf, Germany

Running Title:

snRNA sequencing of primary and recurrent AT/RT

Corresponding author:

Ulrich Schüller, MD
Research Institute Children's Cancer Center Hamburg
Martinistraße 52, N63, D-20251 Hamburg, Germany
Phone: +49-40-426051240
Fax: +49-40-741040350
E-mail: u.schueller@uke.de

Total word count: 4985

Words in abstract: 247

Words in references: 1155

Words in figure legends: 1215

Abstract

Background:
Atypical teratoid/rhabdoid tumors (AT/RT) are the most common malignant brain tumors during infancy and associated with a dismal prognosis. The majority of patients suffer from progressions or recurrences, but underlying mechanisms remain largely unknown.

Methods:
To identify mechanisms of progression and recurrence, we performed single-nucleus RNA sequencing of eight primary-recurrence pairs. Tumor cells and cells of the tumor microenvironment (TME) were analysed separately. Therapy-resistant tumor cells were identified through the comparison of global gene expression profiles between primary and recurrent tumor cell populations using *CIBERSORT*. Histopathology, *in vitro* experiments, bulk RNA sequencing, and survival analyses were performed for validation.

Results:
Paired primary and recurrent AT/RT tumor samples showed significant differences in their gene expression profiles. The TME of AT/RT recurrences was characterized by enrichment of *CD1A*$^{+}$ *CD207*$^{+}$ dendritic cells (DCs), which were *per se* associated with inferior survival in relapsed patients. Differentially expressed genes of AT/RT-MYC primary tumor cells that potentially persist after therapy, were involved in the organization of the extracellular matrix (ECM), developmental processes, and diverse immune signalling pathways. In addition, recurrences demonstrated a significantly higher proportion of cells undergoing partial epithelial-mesenchymal transition (pEMT) compared to primary tumors, a feature that we

confirmed following treating AT/RT-MYC tumor cells *in vitro*. Finally, patients with primary tumors strongly expressing respective genes displayed a significantly worse survival.

Conclusions:

We identified pEMT, ECM remodeling, and enrichment of *CD1A*$^+$ *CD207*$^+$ DCs as potential mechanisms of therapy resistance in AT/RT which could be employed to improve therapy in the future.

Keywords

AT/RT, therapy resistance, single-nucleus RNA sequencing, pEMT, *CD1A*$^+$ *CD207*$^+$ dendritic cells

Key points:

- *CD1A*$^+$ *CD207*$^+$ DCs are enriched in AT/RT recurrences
- Progression of AT/RT-MYCs is associated with ECM remodeling, cytokine signaling, and pEMT
- Gene expression signatures of therapy-resistance in primary AT/RT-MYC indicate worse survival of patients

Importance of the Study:

The majority of the AT/RT patients suffer from tumor progression or recurrence after about 5.4 months on average, and only 35% of the patients are alive five years following a recurrence or progression. Targeted therapies are currently lacking, and it is assumed that resistant cells persist following standard treatment. Developing novel treatments that effectively target these resistant cells is urgently needed and requires comprehensive molecular characterization. In this context, we identified enhanced extracellular matrix (ECM) remodeling, increased cytokine signaling, and partial epithelial-mesenchymal transition (pEMT) as distinctive features of AT/RT-MYC therapy resistance. Additionally, the tumor microenvironment (TME) plays a critical role in driving tumor progression and recurrence. Our findings highlight the presence of *CD1A*$^+$ *CD207*$^+$ dendritic cells (DCs) within the AT/RT TME as potential therapeutic targets worthy of further investigation.

Introduction

Atypical teratoid/rhabdoid tumors (AT/RT) are malignant tumors of the central nervous system (CNS) mainly affecting infants and young children. They are characterized by an aggressive, infiltrative growth and a very poor prognosis, with a median overall survival (OS) ranging from 9 to 17 months, depending on risk groups[1].

AT/RT are assigned to four different DNA methylation subtypes. These differ regarding their clinical characteristics, genetics, and gene expression profiles[2,3]. 95% of all AT/RT patients belong to the three subtypes AT/RT-SHH, AT/RT-MYC, and AT/RT-TYR that are characterized by *SMARCB1* mutations[3,4]. In very rare cases, a *SMARCA4* mutation is the underlying genetic cause[5,6]. These cases belong to a distinct subtype, AT/RT-SMARCA4[2]. Both SMARCB1 and SMARCA4 are part of the SWItch/sucrose non-fermentable (SWI/SNF) complex, which is involved in the packaging of the DNA to histones and therefore, the accessibility of the DNA and the regulation of gene expression. They are also known to act as tumor suppressors[7]. Often, the mutations are already present in the germline, which is associated with the rhabdoid tumor predisposition syndrome 1 (RTPS1; OMIM #609322) for patients with *SMARCB1* mutations and rhabdoid tumor predisposition syndrome 2 (RTPS2; OMIM #613325) for *SMARCA4*-mutated patients. AT/RT patients received surgery followed by chemotherapy. Radiotherapy is not generally recommended for patients younger than three years but applied on a single case basis, and targeted therapies are still lacking. In line with the fact that the prognosis is very poor, AT/RT often progress or recur, matching the observation of pronounced therapy resistance in AT/RT patients[8]. Previously, differences between paired primary and recurrent AT/RT, regarding their histology, proliferative activity, copy-number and gene expression profiles were identified[9]. Nevertheless, the identification of therapy-resistant tumor cells is outstanding. Thorough characterization of therapy-resistant and recurrent AT/RT tumor cells is urgently needed to identify novel therapeutic targets overcoming resistance.

Here, we describe the transcriptomic differences between eight paired AT/RT primary and recurrent tumors including TME on a single-nucleus level. Furthermore, primary tumor cells with similarity to paired recurrences were identified and characterized in this study. We assume that such cells are therapy-resistant and develop to recurrences. Characterization of these cells and respective mechanisms might therefore result in the identification of novel treatment targets. In this framework, we identified enrichment of *CD1A*$^{+}$ *CD207*$^{+}$ DCs and increased ECM remodelling and pEMT in the context of therapy resistance.

Material and methods

Data sets

Patient data were derived from the databases of the EU-RHAB registry. EU-RHAB has received continuous ethical approval (Ethics Committee University of Münster, Germany 2009-532-f-S, most recently amended 17AUG2021). Case numbers 1 to 26 were assigned to the patients according to Johann, Altendorf et al. (2023)[9]. Cases 27 and 28 were added to this study. Clinical and molecular information are summarized in Figure 1A and Supplementary Table 1.

Isolation of cells from FFPE tissue and single-nucleus RNA sequencing (snRNAseq)

Single-nucleus RNA sequencing (snRNAseq) of formalin-fixed paraffin-embedded (FFPE) tissue was performed with the Chromium Single Cell Flex Gene Expression Assay (10x Genomics). Cells were isolated according to the demonstrated protocol “Isolation of Cells from FFPE Tissue Sections for Chromium Fixed RNA Profiling”, Document Number CG000632 Rev B (10x Genomics) using a gentleMACS Octo Dissociator (#130-134-029, Miltenyi Biotec). FFPE scrolls were dissociated using the Enzyme Mix containing Liberase TH (# 5401151001, Millipore Sigma). Probe hybridization and multiplex library preparation were performed using the 10x Genomics Sample Preparation Kit PN-1000414, 16 rxns, according to the protocol “Chromium Fixed RNA Profiling Reagent Kits for Multiplexed Samples”, Document Number CG000527 Rev E (10x Genomics). The resulting pooled libraries, with one 10x Genomics barcode per tumor sample, were sequenced as dual-index libraries in the sequencing core facility of the University Medical Center Münster, on NextSeq 2000 (Illumina) and NovaSeq 6000 (Illumina) sequencing systems, and a recovery of 80,000 cells for each library was targeted.

snRNAseq data processing, integration, and clustering

The *10x Genomics Cell Ranger v8.0.1* software was used for demultiplexing, barcode processing and assignment, single-nucleus counting, alignment to the human reference genome GRCh38-2024-A, and finally for Feature Barcode Matrix generation. Filtered Feature Barcode Matrices for each sample were processed in *R Studio* (version 4.4.1). Normalization, scaling, principal component analysis (PCA), shared nearest-neighbor graph construction (snn-graph), clustering and uniform manifold approximation and projection (UMAP) were performed via the *Seurat* (version 5.1.0) pipeline[10]. Data were merged and normalized using the *SCTransform()* function, correcting for the percentage of mitochondrial counts. Only nuclei with more than 200 and less than 2500 detected genes and less than 5% mitochondrial reads

were included in further analysis. Processed data were visualized in UMAPs using 10 neighboring points in local approximation of manifold structure and a resolution of 0.5 for *Seurat* cluster assignment. To identify resistant primary tumor cells over all samples, a stronger integration using the *FindIntegrationAnchors()* and *IntegrateData()* functions, both included in the *Seurat* package, was performed.

TME cells were extracted from the raw data based on gene expression profiles. Normalization and processing were done as described above. Integration was performed utilizing *RunHarmony()* from the R package *harmony* (version 1.2.3)[11] with the sample ID as a covariate after *RunPCA()* following the developers' recommendations.

Annotation of the tumor microenvironment (TME)

The TME was annotated in a two-step procedure of automated and manual cross-validation as recommended[12]. Automated annotation was performed utilizing the *Azimuth* (version 0.5.0) algorithm[13] following the developers' recommendations. Therefore, *RunAzimuth()* was called with the herein published TME as query dataset and a custom reference built via *AzimuthReference()* from a high-quality TME dataset of 13 glioblastomas previously published as reference dataset[14]. Manual annotation was performed based on canonical markers. For myelomonocytic cells (monocytes, macrophages, and DCs), an additional published meta-analysis was used to verify annotation[15].

Differential Abundance Testing for the TME

Differential abundance testing was performed by assigning cells to partially overlapping neighborhoods on a nearest neighbor graph and subsequent fitting a generalized linear model (GLM) to account for the developmental nature of especially myelomonocytic cells. Therefore, we utilized the R package *miloR* (version 2.3.1)[16]. A nearest neighbor graph was imported from *Seurat's FindNeighbors()* function via *miloR's buildFromAdjacency()* function, as described in the developers' vignettes. Grouping into overlapping neighborhood groups, visualization, and statistical testing followed the developers' recommendations. For the latter, a GLM comparing primary versus recurrent tumors was fitted, incorporating tumor DNA methylation subtype, patient ID, recurrence status, and experimental batches as covariates. Correction for multiple testing was performed by calculating the spatial false discovery rate (sFDR < 0.1) accounting for overlap between neighborhoods following the developers' recommendations. Neighborhoods were mapped back to the original populations to identify the differentially abundant populations.

Cell-cell communication and trajectory inference

To identify potential interactions between cells with consecutive activation of downstream gene targets, we utilized the package *nichenetr* (version 2.2.0)[17] following the developers' recommendations. Myelomonocytic cells were set as receivers, whereas tumor cells and all TME cells were set as sender cells. An expression of 5% of one population's cells was used as the minimum threshold to include ligand-target pairs in the analysis. The top ten activated genes were selected to perform ligand-target predictions. To account for cell-cell communications, for which ligand-receptor interactions are described but whose downstream targets remain to be deciphered, the package *CellChat* (version 2.1.2)[18] was applied according to the developers' recommendations. For the TME of primary and recurrent cases separately, myelomonocytic cells were set as sources to use. Trajectory inference was performed using the package *Slingshot* (version 2.14.0)[19] on the subset of myelomonocytic cells of the TME. Neighborhood groups calculated via *miloR* were used to identify trajectory groups.

CIBERSORT analysis

As the basis for the *CIBERSORT* analysis, integrated data sets of all AT/RT-MYC primary tumor cells and all AT/RT-MYC recurrence tumor cells, with a resolution of 0.5 for *Seurat* cluster assignment, were used. Pseudobulk values for each *Seurat* cluster were calculated using the *AggregateExpression()* function, and similarities between the single clusters were estimated using *CIBERSORT()* function (perm = 500) of the *IOBR* package (version 0.99.0)[20]. *CIBERSORT* was also used for the deconvolution of previously published bulk RNA sequencing (bulk RNAseq) data[9]. The herein published single cell data served as a reference with tumor cells grouped by their respective DNA methylation subtype and TME cells by their neighborhood group calculated via *miloR*. Pseudobulk values for each of these groups were calculated. Comparisons between primary and recurrent samples were performed via a one-sided student's *t*-test, with $p < 0.05$ being considered to indicate statistical significance.

Differentially expressed genes and pathways

Differentially expressed genes between the different tumor clusters were identified using the *FindAllMarkers()* function of the *Seurat* package (version 5.1.0). Significant differentially expressed genes with an adjusted p-value < 0.05 (Benjamini-Hochberg (BH) adjustment) and a $\log_2$ fold change > 1 and < -1 were used for pathway analysis. The *Reactome Pathway* database was used for gene set enrichment analysis using the *gsePathway()* function included in the *ReactomePA* package (version 1.50.0)[21]. Results were visualized in a *cnetplot* with the *enrichplot* package (version 1.26.6)[22].

Differentially expressed genes between different TME cell clusters or between primary and recurrent samples within one TME cell cluster were analysed as specified below using a generalized linear model (GLM). Pseudobulk data were created based on the DNA methylation subtype, patient ID, recurrence status, and identified cell type via *Seurat's AggregateExpression()* function, and differential gene expressions (DEG) of raw count data were analysed via the package *DESeq* (version 1.46.0)[23], embedded in *Seurat's FindMarkers()* function following the developers' recommendations. Genes with an adjusted p-value < 0.05 after multiple testing correction via BH adjustment were considered to be significant.

Annotation of Cancer Cell States

To assign the tumor cells to commonly used pan-cancer cell states, gene sets and cell states of Barkley et al. (2022)[24] were used as a reference. The mean gene expression of the integrated data sets for each of these gene sets was calculated, and the cell state with the highest mean expression was identified for each cell. The cell state fractions were visualized in bar plots using the *ggplot2* package (version 3.5.1)[25]. Statistics were calculated using two-sided paired *t*-tests.

Histology and immunohistochemistry (IHC)

All human AT/RT tumor samples were fixed in 4% formaldehyde. Cell lines were pelletized, washed with 1× PBS, and fixed in 4% formaldehyde. After that, the cells were washed three times with 1× PBS with subsequent embedding in 3% agarose. Fixed tumor samples and agarose-embedded cells were dehydrated, embedded in paraffin, and sectioned at 2 µm. Hematoxylin and Eosin (H&E) staining was performed using standard protocols. IHC was done using a Ventana System (Roche) according to the manufacturers' specifications. The antibodies mouse anti-EMA/anti-Mucin-1 (DAKO #M0613, 1:200) and mouse anti-CD1A (Novocastra #NCL-L-CD1a-235, 1:50) were used for epithelial membrane antigen (EMA) and CD1A stainings. EMA stainings were quantified in *ImageJ* (version 1.54f, Java 1.8.0_322) by calculating the EMA-positive area of scans of the whole slides, normalized to the total tumor area, according to the macro (Suppl. Table 2). For input images, color deconvolution for H DAB vectors was performed and Colour_2 was selected. Statistics were calculated using one-sided and two-sided paired *t*-tests.

Cell culture

The two patient-derived AT/RT-MYC cell lines BT-16 and CHLA-266 were used. Cells were cultured according to manufacturer specifications. To generate therapy-resistant cells, each

cell line was treated with 1 µM doxorubicin. After 24 h, media were changed and 5 µM etoposide were added. Again, after 24 h, media were renewed and 1 µM vincristine was added. Most of the cells died after treatment, but after about two weeks, resistant cells grew again. Cells were harvested for IHC and RNA sequencing. For the latter, cell pellets were resuspended in Trizol and RNA was isolated according to standard protocols.

Bulk RNA sequencing

RNA concentration was measured using a Qubit 4 Fluorometer (Thermo Fisher Scientific). The quantity for each sample was adjusted to 10 ng in order to pool them at equimolar concentrations. The library was prepared using the SMART-Seq Stranded kit (Takara Bio) according to the manufacturer's specifications. Sequencing of the library pool was done on a NovaSeq X Plus (Illumina), using 2 × 101 bp. Subsequently, demultiplexing was performed with *Illumina bcl2fastq* (version 2.20) and the adapters were trimmed with *Skewer* (version 0.2.2)[26]. The reads were aligned to the human genome hg38 using *STAR*[27]. The transcripts were counted as feature counts, and they were used as input for the raw count table, which was processed in *R Studio* (version 4.4.1). Matching HUGO symbols for the ENSEMBL IDs were added using the *biomaRt* package (version 2.62.0)[28]. Repetitively counted genes and genes from sex chromosomes were removed. The *DESeq2* package (version 1.46.0)[23] was used to identify all differentially expressed genes with a p-value < 0.05 after BH adjustment, which were visualized in Volcano Plots using the *EnhancedVolcano* package (version 1.24.0)[29].

Survival analysis

Survival analyses were performed based on bulk RNAseq data of a cohort of AT/RT-MYC patients (Suppl. Table 3). Only patients with known overall survival (OS), progression-free survival (PFS), and clinical status (dead or alive) were included. These data were gathered with the help of EU-RHAB. At first, the cohort was separated into one group expressing a high number of upregulated genes identified in primary tumor clusters 2, 4, and 5 (Suppl. Table 4), with a $\log_2$ gene expression > 2, and one group expressing a low number of these genes using the best cutoff. For further analyses, only patients with a minimum follow-up of 17 months were selected and separated into long and short survivors at the median. For the TME analysis, bulk RNAseq data of AT/RT patients of all DNA methylation subtypes were stratified into two groups based on the abundance of *CD1A*$^+$ *CD207*$^+$ cells in the respective recurrent tumor samples analysed via IHC, bulk RNAseq, or snRNAseq as described above. Kaplan-Meier curves[30] were generated using the *ggsurvfit* package (version 1.1.0)[31]. Comparisons of survival curves were performed via two-sided Log-Rank tests, with p < 0.05 being considered to indicate

statistical significance using the package *survival* (version 3.6.4)[32]. Time to event was calculated as the time from the first diagnosis of AT/RT until the time of death. Censoring was noticed at the last time of contact if the patient was still alive. To identify differentially expressed genes and pathways of long vs. short survivors, the *DESeq2* package (version 1.46.0)[23] was used, and all genes with a p-value < 0.05 after BH adjustment and a $\log_2$ fold change > 1 were chosen. Again, the *Reactome Pathway* database was used for gene set enrichment analysis using the *gsePathway()* function included in the *ReactomePA* package (version 1.50.0)[21]. Results were visualized in a *dotplot* with the *enrichplot* package (version 1.26.6)[22].

Results

snRNAseq analysis of eight paired primary and recurrent AT/RT showed distinct gene expression profiles

The cohort of 26 patients with primary AT/RT and matched recurrences of Johann, Altendorf et al. (2023)[9] was extended by two additional pairs. For eight of these primary-recurrence pairs, snRNAseq was performed (Figure 1A, Suppl. Table 1). The SCT-normalized dataset comprising all samples was visualized using a Uniform Manifold Approximation and Projection (UMAP) for dimension reduction (n = 15,399 cells), resulting in distinct clusters for the tumor cells (n = 8 clusters) and the TME (n = 4 clusters). The TME was characterized by clusters of cells from all samples (Fig. 1B-C). Most of the cells of the TME were macrophages, followed by fibroblasts, endothelial cells, monocytes, T-cells, and B-cells. The tumor cells of AT/RT-MYC (n = 4 cases) and AT/RT-SHH (n = 1 case) formed distinct clusters. AT/RT-TYR tumor cells of all patients (n = 3 cases) were mixed in one cluster, indicating more similar gene expression profiles of AT/RT-TYR compared to the other DNA methylation subtypes (Fig. 1D). Paired primary and recurrent tumor samples showed a distinct separation of their gene expression profiles within one cluster (Fig. 1E), leading to the assumption that there are gradual transcriptomic differences on a single-nucleus level between paired primary and recurrent AT/RT tumor cells.

Differential abundance testing reveals a novel CD1A$^+$ CD207$^+$ tumor-associated DC predominant in the TME of recurrent AT/RT

To analyse the TME of AT/RT in more detail, TME cells (n = 3286) were distinguished from tumor cells (n = 11,677) via gene expression profiles. Re-integration via *harmony* (Fig. 2A) identified well-separated clusters, which were assigned to their respective cell types (Fig. 2B, Suppl. Fig. 1A-C). To decipher compositional changes in cell populations, we performed differential abundance testing. We applied a generalized linear model (GLM) on subpopulations, so-called neighborhood groups, defined via partially overlapping nearest-neighbor graphs with subsequent spatial false discovery rate (sFDR) for multiple testing correction utilizing *miloR* (Fig. 2C). This approach identified significant abundance differences between primary and recurrent samples in neighborhood group 9 (Fig. 2D) with predominant abundance of the respective cells, which were identified as dendritic cells (DCs), in recurrent AT/RT. Differential gene expression analysis of the identified DCs revealed a *CD1A*$^+$ *CD207*$^+$ *FCER1A*$^+$ *TACSTD2*$^+$ and *CSF1R*^{high} (Suppl. Fig. 1D) expression profile. Neighborhoods were mapped back, and the identified *CD1A*$^+$ *CD207*$^+$ expression profile was visualized, comparing primary to recurrent samples (Fig. 2E). CD1A immunohistochemical staining of ten samples (Fig. 1A), exemplarily shown in Figure 2F, resulted in three pairs with predominance of CD1A-

positive cells in the recurrence and only one pair with predominance in the primary tumor. The remaining pairs were negative for CD1A. These findings validated our bioinformatic calculations. Previously published bulk RNAseq data[9] were deconvoluted using *CIBERSORT* to identify this cell type using the herein published single cell dataset as a reference. This approach showed a significant (p = 0.049, one-sided *t*-test) enrichment of the observed tumor-associated DCs in recurrent AT/RT (Fig. 2G). Cell-cell communication inference via *nichenetr* identified a robustly enriched *TGF-β1*- and *TGF-β2*-induced signaling in recurrent AT/RT (Suppl. Fig. 2A-D) which might induce the observed *CD1A*$^{+}$ *CD207*$^{+}$ DCs. Trajectory inference using *Slingshot* suggested periphery-derived monocytes as ontogenetic precursors (Suppl. Fig. 2E), and noticeable negativity for *TMEM119*, *CD163*, and *LGALS3* was observed (Suppl. Fig. 2F-H). Our study showed an increased, yet non-significant, *FOXP3*-ratio among TILs (Suppl. Fig. 2I) supporting the hypothesis of an additional effect on immune effector cells. Following this hypothesis, engagement of the T-cell immunoreceptor TIGIT via tumor-associated DCs was found via *CellChat* (Suppl. Fig. 2 J). To assess the influence of these previously unrecognized tumor-associated DCs on clinical outcome data, patients were stratified into two groups using bulk RNAseq data based on the abundance of *CD1A*$^{+}$ *CD207*$^{+}$ cells in the respective recurrent tumor samples. Patients with *CD1A*$^{+}$ *CD207*$^{+}$ DCs had a significantly shorter overall survival compared to patients without such cells (p = 0.009, two-sided Log-Rank test; Fig. 2H).

A subset of AT/RT-MYC primary tumor cells showing high similarity to recurrences was characterized by altered ECM organization, developmental processes, and immune system pathways

The AT/RT-MYC primary and recurrent tumor cells of the cases 6, 18, 27, and 28 formed separated clusters, indicating distinct gene expression profiles (Fig. 3A). For AT/RT-TYR, case 3 was excluded here due to a small number of tumor cells. The primary and recurrent tumor cells of cases 17 and 26 showed more similar gene expression profiles compared to AT/RT-SHH and AT/RT-MYC (Fig. 3B). Primary and recurrent AT/RT-SHH tumor cells showed a clear separation in the UMAP (Fig. 3C). Due to the relatively low number of samples and cells belonging to AT/RT-TYR and AT/RT-SHH, further analyses focused on AT/RT-MYC tumor cells. A stronger integration of the snRNAseq data of the AT/RT-MYC tumor cells was performed in order to identify molecular mechanisms of tumor progression and recurrence occurring in all patients. This was done for all primary and recurrent tumor cells separately. After that, seven *Seurat* clusters were identified for the primary tumor cells (Fig. 3D-E) and six *Seurat* clusters for the recurrences (Fig. 3F-G). Using *CIBERSORT*, primary tumor clusters 2, 4, and 5 revealed the highest similarity to the recurrences (Fig. 3H). Quantifying the cells belonging to these clusters for each sample confirmed the presence of these cells in all

samples (Fig. 3I). The top 15 upregulated *Reactome* pathways and associated genes in such cells are visualized in Figure 3H (Suppl. Table 4). As one of the top pathways, the organization of the ECM was altered. Furthermore, immune system-associated pathways were upregulated, like increased cytokine signaling as well as alterations in the adaptive and innate immune system. In addition, a number of upregulated genes were involved in metabolic processes, signal transduction, hemostasis, and developmental processes.

AT/RT-MYC recurrences displayed an increased proportion of cells undergoing pEMT as compared to primary tumors

To further characterize molecular differences between primary and recurrent AT/RT-MYC tumor cells, each cell was assigned to a cancer cell state according to Barkley et al. (2022)[24]. Comparison of the proportion of the cancer cell states of AT/RT-MYC primary tumors and recurrences resulted in an increased number of cells undergoing partial epithelial-mesenchymal transition (pEMT) in the recurrences ($p = 0.0026$, two-sided paired *t*-test, Fig. 4A-B, Suppl. Fig. 3A-D). Our findings in the snRNAseq data were confirmed using bulk RNAseq data of paired AT/RT-MYC primary tumors and recurrences ($p = 0.045$, two-sided paired *t*-test, Suppl. Fig. 3E-F)[9]. Increased pEMT in AT/RT-MYC recurrences was further investigated by using antibodies against the epithelial membrane antigen (EMA) for IHC of paired AT/RT-MYC primary tumors and recurrences (Fig. 4C). Quantification of the EMA-positive area for three pairs resulted in a decreased EMA expression in AT/RT-MYC recurrences in three out of five pairs with two out of five pairs showing similar EMA expression ($p = 0.035$, one-sided paired *t*-test, Fig. 4D). We then treated two AT/RT-MYC cell lines using doxorubicin, etoposide, and vincristine on three consecutive days with subsequent regrowth for investigating changes in the proportion of pEMT. H&E and EMA stainings were done for each cell line before and after treatment, resulting in a decreased EMA expression after treatment for BT-16 ($p = 4.5\times10^{-6}$, two-sided paired *t*-test) and CHLA-266 ($p = 4.8\times10^{-6}$, two-sided paired *t*-test, Fig. 4E). Investigation of the H&E stainings revealed a lower cell density and larger distances between the cells after treatment. Bulk RNAseq confirmed our observations by resulting in an upregulated gene expression of pEMT marker genes (Fig. 4F). In addition, the top 15 upregulated genes of AT/RT-MYC primary tumor clusters 2, 4, and 5, containing the potentially therapy-resistant cells, were almost all increased in both cell lines after treatment (Fig. 4G).

AT/RT-MYC patients overexpressing genes identified in potentially therapy-resistant cells showed worse survival

Next, we investigated the clinical impact of our findings. To this end, we collected a cohort of bulk RNAseq data of 25 AT/RT-MYC primary tumors (Suppl. Table 3). We separated the cohort into one group expressing a high number of genes identified in the potentially therapy-resistant primary tumor cells (primary tumor clusters 2, 4, and 5) and another group expressing a low number of these genes. The age and sex distributions were equal in these two groups. and no differences between the resection and metastases status as well as the applied therapy protocols were observed (Suppl. Table 3). Patients highly expressing this gene signature, showed inferior overall survival (OS, $p = 0.039$, two-sided Log-Rank test, Fig. 5A-B, Suppl. Fig. 4A-D). This led to the conclusion that high expression of genes overexpressed in potentially therapy-resistant AT/RT-MYC primary tumor cells is associated with worse OS. Furthermore, we compared the gene expression profiles of long vs. short survivors by using the same cohort of bulk RNAseq data. Upregulated pathways in potentially therapy-resistant AT/RT-MYC primary tumor cells (primary tumor clusters 2, 4, and 5; Fig. 5C) were compared to upregulated pathways in short survivors (Fig. 5D). The top 15 pathways were visualized, resulting in five out of 15 overlapping pathways (highlighted in red). These were cytokine signaling, including signaling by interleukins, developmental biology, and hemostasis, including platelet activation, signaling, and aggregation. In addition, the pathways collagen chain trimerization and collagen biosynthesis and modifying enzymes are characterized by similar gene sets and functions as the *Reactome* pathway ECM organization. In summary, increased cytokine signaling, developmental processes, hemostasis, and ECM organization were not only associated with primary AT/RT-MYC tumor cells being highly similar to recurrences and potentially therapy-resistant, but also correlated with poor survival in AT/RT-MYC patients.

Discussion

Previously, we have identified molecular differences of paired primary and recurrent AT/RT on DNA methylation, gene expression, and histological level[9], but for the identification of exact molecular mechanisms and novel therapeutic targets, more detailed analyses were required. We characterized eight pairs on a single-nucleus level. Our analyses confirmed the existence of molecular differences between primary and recurrent AT/RT, not only in the tumor cells, but also in the TME. Additionally, therapy-resistant cells and promising therapeutic targets were identified, shedding light on mechanisms of tumor progression and recurrence.

To decipher compositional changes in TME cell populations, we performed differential abundance testing, as the preferred method for TME analyses[12]. Usually applied count models as poisson or negative binomial regression models presume discrete data and fail to capture successively maturing myelomonocytic cells sufficiently. To mitigate this, we applied a generalized linear model (GLM) on subpopulations identified by partially overlapping nearest-neighbor graphs using *miloR*. The cells enriched in AT/RT recurrences were identified as DCs differentiated similarly to Langerhans cells (LHCs)[33] - a previously undescribed feature in TME landscapes of CNS tumors. Cell-cell communication inference revealed that *TGF-β1*- and *TGF-β2*-induced signaling might activate these *CD1A*$^+$ *CD207*$^+$ DCs in AT/RT recurrences, a finding consistent with previous studies on LHCs, which was also demonstrated by *in vitro* purification of such cells from different progenitors via *TGF-β*[34]. *TGF-β* is known for inducing *CD4*$^+$ *CD25*$^+$ *FOXP3*$^+$ regulatory T-cells (Tregs)[35] and a high ratio of *FOXP3*$^+$ tumor-infiltrating lymphocytes (TILs), whose abundance in CNS tumors correlates with poor prognosis[36]. Patients with *CD1A*$^+$ *CD207*$^+$ DC enrichment in AT/RT recurrences had a shorter OS, supporting their potential role in Treg induction and tumor tolerance via TIGIT engagement. Taken together, this novel *CD1A*$^+$ *CD207*$^+$ tumor-associated DC represents a clinical risk factor that is dependent on *TGF-β*, as already described for different carcinomas, e.g. squamous cell carcinoma[37]. The exclusive expression of *CD207* on this novel tumor-associated DC in the context of the CNS makes it a promising novel target for future immunotherapies. Additionally, our data indicate TIGIT inhibition as a promising therapeutic approach in recurrent AT/RT[38].

To further identify resistance mechanisms, AT/RT-MYC primary tumor cells with high similarity to recurrences were identified over all AT/RT-MYC samples. We hypothesize that these cells persist following therapy and develop to recurrences. In general, it is assumed that tumor recurrences arise from dormant tumor cells, characterized by drug resistance and immune escape[39]. Due to the high similarity to AT/RT-MYC recurrences, we assumed that primary tumor clusters 2, 4, and 5 contain such therapy-resistant cells. They were characterized by an altered ECM organization, among other features. The ECM is generally known to support tumor progression in different tumor entities, by acting as a biomechanical barrier and by

protecting the tumor from anticancer agents[40]. In addition, different therapies induce ECM remodeling, leading to the occurrence of therapy-resistant cells. These findings make the ECM a promising target for novel therapies[40]. Previously, the ECM component Type I collagen (COL1A1), which was also overexpressed in therapy-resistant AT/RT-MYC primary tumor cells, was identified as a negative prognostic marker[41]. COL1A1 is also associated with EMT as a marker for mesenchymal-like cells[41], supporting the idea that non-epithelial cells drive progression[42]. Furthermore, we observed increased cytokine signaling, which is also associated with tumor progression in different entities. On the one hand, cytokines can induce EMT and the development to dormant tumor cells. Both EMT and dormant tumor cells play an important role in therapy resistance and tumor progression. On the other hand, cytokine signaling is involved in the ECM remodeling through cancer-associated fibroblast activation[43]. Furthermore, imbalanced hemostasis was associated with tumor progression, especially due to increased platelet aggregation[44], whereas altered developmental processes correlate with EMT by regulating the fate of embryonic and malignant cells. Additionally, it is associated with tumor progression and recurrence in diverse entities[45].

To better understand transcriptional heterogeneity as a driver of tumor progression, recurrence, and failure of existing therapies[46], we assigned each AT/RT-MYC tumor cell to a pan-cancer cell state[24], which revealed increased pEMT in AT/RT-MYC recurrences. As described above, EMT is associated with tumor progression and recurrence in many ways. Therefore, we investigated epithelial and mesenchymal genes using IHC. Treated AT/RT-MYC cell lines were not only showing a decreased number of epithelial cells, they were also characterized by an altered morphology with lose cell-cell contacts[47]. Bulk RNAseq confirmed our observations. Not only pEMT marker genes were upregulated in the cells after treatment, in addition, the top upregulated genes in therapy-resistant tumor cells (identified by snRNAseq analyses), were overexpressed.

Finally, we observed a correlation between overexpression of the genes identified in potentially therapy-resistant cells and the OS of AT/RT-MYC patients. This confirmed our hypothesis that the occurrence of therapy-resistant cells is associated with tumor progression and recurrence, and therefore, with an inferior prognosis. We further investigated the top five upregulated genes in therapy-resistant cells, *ETS1*, *LAPTM5*, *LPL*, *CRIP1*, and *C1QB*. High *ETS1* and *LAPTM5* expression was correlated to inferior survival of AT/RT-MYC patients. *ETS1* has previously been characterized as a negative prognostic marker in carcinomas, e.g. squamous cell carcinomas, and may play a crucial role in invasiveness, EMT, ECM, and therapy resistance, which matches our observations in AT/RT-MYC. Inhibition of *ETS1* resulted in enhanced sensitivity to anti-tumor drugs in squamous cell carcinoma cells[48]. *ETS1* expression is regulated by *TGF-β*[48] which we previously identified in the context of *CD1A*$^{+}$ *CD207*$^{+}$ DC activation, and therefore, *TGF-β* seems to play a role in both tumor cells and TME alterations

regarding tumor progression and recurrence. The lysosomal transmembrane protein 5 (*LAPTM5*) was previously found to be increased in the context of tumor progression in different entities[49] and could be another target for AT/RT-MYC therapy. *LAPTM5* was recently found to be associated with shorter OS in glioblastomas, there facilitating chemotherapy-resistance in glioblastomas[50], potentially via activation of NFKB. In conclusion, *ETS1* and *LAPTM5*, as well as TGF-β signaling, might be promising targets to inhibit AT/RT-MYC tumor progression.

Overall, we identified promising molecular characteristics of therapy resistance in AT/RT, including enrichment of *CD1A*$^{+}$ *CD207*$^{+}$ DCs in the TME, increased ECM remodeling and pEMT, which should be considered as targets for novel therapeutic approaches.

Required statements

Ethics

EU-RHAB has received continuous ethical approval (Ethics Committee University of Münster, Germany 2009-532-f-S, most recently amended 17AUG2021).

Funding

This study was supported by the Deutsche Forschungsgemeinschaft (FR 1516/4-1). MF received funds from the Deutsche Krebshilfe (DKH 70113981). EU-RHAB is supported by the Deutsche Kinderkrebsstiftung (A2018/27). US was further supported by the Fördergemeinschaft Kinderkrebszentrum Hamburg. LA received a fellowship from the Burkhard Meyer Stiftung. PDJ received funding by the German Cancer Aid (Max Eder program) and the Else Kröner Fresenius Stiftung. KK received funding from the Deutsche Forschungsgemeinschaft (KE 2004/4-1; KE 2004/11-1).

Conflict of Interest

None.

Authorship

LA and US designed the study. Material collection was performed by US, AK, MUS, and KK. snRNAseq data were generated by RR, FWDF, and KK. Clinical information was contributed by MCF, MH, and PDJ. Data analysis was performed by LA and AA (TME). Cell culture experiments were performed by LA and VT. The manuscript was written by LA and AA. The figures were designed by LA and AA. All authors contributed to the revision of the manuscript.

Data availability

All generated data of this study are deposited at NCBI Gene Expression Omnibus (GEO; https://www.ncbi.nlm.nih.gov/geo). The snRNAseq data of paired primary and recurrent AT/RT are accessible through GEO Series accession number GSE298139. Bulk RNAseq data of AT/RT MYC primary tumors were obtained from Johann, Altendorf et al. (2023)[9], Johann et al. (2016)[3], or were generated for this study. These data are accessible through GEO Series accession number GSE298140. Bulk RNAseq data of the untreated and treated AT/RT-MYC cell lines are accessible via GSE298141.

Acknowledgements

The AT/RT-MYC cell lines BT-16 and CHLA-266 were kind gifts from Dr. rer. nat. Daniel Merk from Tübingen. The IHC of all human samples and cell lines was kindly performed by the histology lab of the Institute of Neuropathology of the University Medical Center Hamburg-Eppendorf. We also thank Vanessa Thaden and Jacqueline Tischendorf for excellent technical support.

References

1. Frühwald MC, Hasselblatt M, Nemes K, et al. Age and DNA methylation subgroup as potential independent risk factors for treatment stratification in children with atypical teratoid/rhabdoid tumors. *Neuro Oncol*. 2020;22(7):1006-1017. doi:10.1093/neuonc/noz244

2. Holdhof D, Johann PD, Spohn M, et al. Atypical teratoid/rhabdoid tumors (ATRTs) with SMARCA4 mutation are molecularly distinct from SMARCB1-deficient cases. *Acta Neuropathol*. 2020;141(2):291-301. doi:10.1007/s00401-020-02250-7

3. Johann PD, Erkek S, Zapatka M, et al. Atypical Teratoid/Rhabdoid Tumors Are Comprised of Three Epigenetic Subgroups with Distinct Enhancer Landscapes. *Cancer Cell*. 2016;29(3):379-393. doi:10.1016/j.ccell.2016.02.001

4. Biegel JA, Zhou JY, Rorke LB, Stenstrom C, Wainwright LM, Fogelgren B. Germ-line and acquired mutations of INI1 in atypical teratoid and rhabdoid tumors. *Cancer Res*. 1999;59(1):74-79.

5. Schneppenheim R, Frühwald MC, Gesk S, et al. Germline Nonsense Mutation and Somatic Inactivation of SMARCA4/BRG1 in a Family with Rhabdoid Tumor Predisposition Syndrome. *Am J Hum Genet*. 2010;86(2):279-284. doi:10.1016/j.ajhg.2010.01.013

6. Hasselblatt M, Nagel I, Oyen F, et al. SMARCA4-mutated atypical teratoid/rhabdoid tumors are associated with inherited germline alterations and poor prognosis. *Acta Neuropathol*. 2014;128(3):453-456. doi:10.1007/s00401-014-1323-x

7. Wilson BG, Roberts CWM. SWI/SNF nucleosome remodellers and cancer. *Nat Rev Cancer*. 2011;11(7):481-492. doi:10.1038/nrc3068

8. Gastberger K, Fincke VE, Mucha M, Siebert R, Hasselblatt M, Frühwald MC. Current Molecular and Clinical Landscape of ATRT – The Link to Future Therapies. *Cancer Manag Res*. 2023;15:1369-1393. doi:10.2147/CMAR.S379451

9. Johann PD, Altendorf L, Efremova EM, et al. Recurrent atypical teratoid/rhabdoid tumors (AT/RT) reveal discrete features of progression on histology, epigenetics, copy number profiling, and transcriptomics. *Acta Neuropathol*. 2023;146(3):527-541. doi:10.1007/s00401-023-02608-7

10. Hao Y, Stuart T, Kowalski MH, et al. Dictionary learning for integrative, multimodal and scalable single-cell analysis. *Nat Biotechnol*. 2024;42(2):293-304. doi:10.1038/s41587-023-01767-y

11. Korsunsky I, Millard N, Fan J, et al. Fast, sensitive and accurate integration of single-cell data with Harmony. *Nat Methods*. 2019;16(12):1289-1296. doi:10.1038/s41592-019-0619-0

12. Heumos L, Schaar AC, Lance C, et al. Best practices for single-cell analysis across modalities. *Nat Rev Genet*. 2023;24(8):550-572. doi:10.1038/s41576-023-00586-w

13. Hao Y, Hao S, Andersen-Nissen E, et al. Integrated analysis of multimodal single-cell data. *Cell*. 2021;184(13):3573-3587.e29. doi:10.1016/j.cell.2021.04.048

14. Pombo Antunes AR, Scheyltjens I, Lodi F, et al. Single-cell profiling of myeloid cells in glioblastoma across species and disease stage reveals macrophage competition and specialization. *Nat Neurosci*. 2021;24(4):595-610. doi:10.1038/s41593-020-00789-y

15. Mulder K, Patel AA, Kong WT, et al. Cross-tissue single-cell landscape of human monocytes and macrophages in health and disease. *Immunity*. 2021;54(8):1883-1900.e5. doi:10.1016/j.immuni.2021.07.007

16. Dann E, Henderson NC, Teichmann SA, Morgan MD, Marioni JC. Differential abundance testing on single-cell data using k-nearest neighbor graphs. *Nat Biotechnol*. 2022;40(2):245-253. doi:10.1038/s41587-021-01033-z

17. Browaeys R, Saelens W, Saeys Y. NicheNet: modeling intercellular communication by linking ligands to target genes. *Nat Methods*. 2020;17(2):159-162. doi:10.1038/s41592-019-0667-5

18. Jin S, Guerrero-Juarez CF, Zhang L, et al. Inference and analysis of cell-cell communication using CellChat. *Nat Commun*. 2021;12(1). doi:10.1038/s41467-021-21246-9

19. Street K, Risso D, Fletcher RB, et al. Slingshot: Cell lineage and pseudotime inference for single-cell transcriptomics. *BMC Genomics*. 2018;19(1). doi:10.1186/s12864-018-4772-0

20. Newman AM, Liu CL, Green MR, et al. Robust enumeration of cell subsets from tissue expression profiles. *Nat Methods*. 2015;12(5):453-457. doi:10.1038/nmeth.3337

21. Yu G, He QY. ReactomePA: An R/Bioconductor package for reactome pathway analysis and visualization. *Mol Biosyst*. 2016;12(2):477-479. doi:10.1039/c5mb00663e

22. Yu G, Gao CH. enrichplot: Visualization of Functional Enrichment Result. Published online 2025. doi:10.18129/B9.bioc.enrichplot

23. Love MI, Huber W, Anders S. Moderated estimation of fold change and dispersion for RNA-seq data with DESeq2. *Genome Biol*. 2014;15(12). doi:10.1186/s13059-014-0550-8

24. Barkley D, Moncada R, Pour M, et al. Cancer cell states recur across tumor types and form specific interactions with the tumor microenvironment. *Nat Genet*. 2022;54(8):1192-1201. doi:10.1038/s41588-022-01141-9

25. Wickham H. ggplot2: Elegant Graphics for Data Analysis. Published online 2016. doi:10.1007/978-3-319-24277-4_9

26. Jiang H, Lei R, Ding SW, Zhu S. Skewer: a fast and accurate adapter trimmer for next-generation sequencing paired-end reads. *BMC Bioinformatics*. 2014;15:182. http://www.biomedcentral.com/1471-2105/15/182

27. Dobin A, Davis CA, Schlesinger F, et al. STAR: Ultrafast universal RNA-seq aligner. *Bioinformatics*. 2013;29(1):15-21. doi:10.1093/bioinformatics/bts635

28. Durinck S, Spellman PT, Birney E, Huber W. Mapping identifiers for the integration of genomic datasets with the R/ Bioconductor package biomaRt. *Nat Protoc*. 2009;4(8):1184-1191. doi:10.1038/nprot.2009.97

29. Blighe K, Rana S, Lewis M. EnhancedVolcano: Publication-ready volcano plots with enhanced colouring and labeling. Published online 2025. doi:10.18129/B9.bioc.EnhancedVolcano

30. Kaplan EL, Meier P. Nonparametric Estimation from Incomplete Observations. *J Am Stat Assoc*. 1958;53(282):457-481.

31. Sjoberg D, Baillie M, Fruechtenicht C, Haesendonckx S, Treis T. ggsurvfit: Flexible Time-to-Event Figures. R package version 1.1. Published online 2025.

32. Therneau TM, Lumley T, Atkinson E, Crowson C. A package for survival analysis in R. Published online 2024. doi:10.32614/CRAN.package.survival

33. Liu X, Zhu R, Luo Y, et al. Distinct human Langerhans cell subsets orchestrate reciprocal functions and require different developmental regulation. *Immunity*. 2021;54(10):2305-2320.e11. doi:10.1016/j.immuni.2021.08.012

34. Yasmin N, Konradi S, Eisenwort G, et al. β-Catenin Promotes the Differentiation of Epidermal Langerhans Dendritic Cells. *J Investig Dermatol*. 2013;133(5):1250-1259. doi:10.1038/jid.2012.481

35. Zhou L, Lopes J e, Chong MMW, et al. TGF-β-induced Foxp3 inhibits Th17 cell differentiation by antagonizing RORγt function. *Nature*. 2008;453(7192):236-240.

36. Gooden MJM, De Bock GH, Leffers N, Daemen T, Nijman HW. The prognostic influence of tumour-infiltrating lymphocytes in cancer: A systematic review with meta-analysis. *Br J Cancer*. 2011;105(1):93-103. doi:10.1038/bjc.2011.189

37. Minesaki A, Kai K, Kuratomi Y, Aishima S. Infiltration of CD1a-positive dendritic cells in advanced laryngeal cancer correlates with unfavorable outcomes post-laryngectomy. *BMC Cancer*. 2021;21(1):973. doi:10.1186/s12885-021-08715-6

38. Guan X, Hu R, Choi Y, et al. Correction to: Anti-TIGIT antibody improves PD-L1 blockade through myeloid and Treg cells (Nature, (2024), 627, 8004, (646-655), 10.1038/s41586-024-07121-9). *Nature*. 2024;627(8005):E11. doi:10.1038/s41586-024-07280-9

39. Damen MPF, van Rheenen J, Scheele CLGJ. Targeting dormant tumor cells to prevent cancer recurrence. *FEBS J*. 2021;288(21):6286-6303. doi:10.1111/febs.15626

40. Winkler J, Abisoye-Ogunniyan A, Metcalf KJ, Werb Z. Concepts of extracellular matrix remodelling in tumour progression and metastasis. *Nat Commun*. 2020;11(1). doi:10.1038/s41467-020-18794-x

41. Comba A, Faisal SM, Dunn PJ, et al. Spatiotemporal analysis of glioma heterogeneity reveals COL1A1 as an actionable target to disrupt tumor progression. *Nat Commun*. 2022;13(1). doi:10.1038/s41467-022-31340-1

42. Ramaswamy S, Ross KN, Lander ES, Golub TR. A molecular signature of metastasis in primary solid tumors. *Nat Genet*. 2003;33(1):49-54. doi:10.1038/ng1060

43. Yi M, Li T, Niu M, et al. Targeting cytokine and chemokine signaling pathways for cancer therapy. *Signal Transduct Target Ther*. 2024;9(1). doi:10.1038/s41392-024-01868-3

44. Falanga A, Marchetti M. Hemostatic biomarkers in cancer progression. *Thromb Res*. 2018;164:S54-S61. doi:10.1016/j.thromres.2018.01.017

45. Van Lent J, Baggiolini A. Harmony in chaos: understanding cancer through the lenses of developmental biology. *Mol Oncol*. 2024;18(4):793-796. doi:10.1002/1878-0261.13594

46. Alizadeh AA, Aranda V, Bardelli A, et al. Toward understanding and exploiting tumor heterogeneity. *Nat Med*. 2015;21(8):846-853. doi:10.1038/nm.3915

47. Sacco JL, Gomez EW. Epithelial–Mesenchymal Plasticity and Epigenetic Heterogeneity in Cancer. *Cancers (Basel)*. 2024;16(19). doi:10.3390/cancers16193289

48. Sakamoto K, Endo K, Sakamoto K, et al. EHF suppresses cancer progression by inhibiting ETS1-mediated ZEB expression. *Oncogenesis*. 2021;10(3). doi:10.1038/s41389-021-00313-2

49. Sun PP, Liao SX, Sang P, Liu MM, Yang J Bin. Lysosomal transmembrane protein 5: Impact on immune cell function and implications for immune-related deficiencies. *Heliyon*. 2024;10(17). doi:10.1016/j.heliyon.2024.e36705

50. Berberich A, Bartels F, Tang Z, et al. LAPTM5-CD40 Crosstalk in Glioblastoma Invasion and Temozolomide Resistance. *Front Oncol*. 2020;10:747. doi:10.3389/fonc.2020.00747

Figure Legends

Fig. 1: Overview of all samples and UMAPs of the snRNAseq data of all primary and recurrent AT/RT, including tumor cells and TME. A: Overview of all samples and present data used in this study as extension to Johann, Altendorf et al. (2023)[9]. **B:** UMAP using 10 neighboring points of *SCT*-normalized counts of all cells (n = 15,399), annotated by samples. **C:** UMAP of all cells (n = 15,399), with annotated TME and DNA methylation subtypes assigned. **D:** UMAP of all cells (n = 15,399), annotated by DNA methylation subtypes. **E:** UMAP of all cells (n = 15,399), annotated by status (primary or recurrence).

Fig. 2: Annotation and investigation of cellular abundances of the TME on a single-nucleus level. A: UMAP using 10 neighboring points of *harmony*-integrated data of the TME only (n = 3286), annotated by samples. **B:** UMAP of the TME only (n = 3286), annotated by status (primary or recurrence). Cell types were annotated using a two-step procedure of automated (*Azimuth*) and manual cross-validation. **C:** Assignment of AT/RT TME cells to partially overlapping neighborhoods on the UMAP of A and B using *miloR*. **D:** GLM comparing primary versus recurrent AT/RT TME cells with tumor DNA methylation subtype, patient ID, recurrence status, and experimental batches as covariates. Correction for multiple testing was performed by calculating the spatial false discovery rate (sFDR < 0.1). Each dot represents one neighborhood. **E:** UMAP of the TME only (n = 3286), annotated by *CD1A*$^+$ *CD207*$^+$ expression in primary (left, n = 18/1208 positive cells) and recurrent TME cells (right, n = 107/2078 positive cells). **F:** IHC staining of the CD1A protein, exemplary for AT/RT-TYR case 17 (primary tumor and paired recurrence). Scale bars indicate 40 µm. **G:** Heatmap of *CIBERSORT* results for the deconvolution of previously published bulk RNAseq data of paired primary and recurrent AT/RT[9]. A one-sided *t*-test revealed enrichment of *CD1A*$^+$ *CD207*$^+$ DCs in recurrent AT/RT (p = 0.049). **H:** OS of a cohort of AT/RT patients separated into two groups based on the abundance of *CD1A*$^+$ *CD207*$^+$ cells in the respective recurrent tumor samples analysed via IHC, bulk RNAseq, or snRNAseq. Patients with *CD1A*$^+$ *CD207*$^+$ DCs had a significantly shorter OS compared to patients without (p = 0.009, two-sided Log-Rank test).

Fig. 3: Analysis of tumor cells only and identification of AT/RT-MYC primary tumor cells with high similarity to recurrences. A: UMAP using 10 neighboring points of *SCT*-normalized counts of AT/RT-MYC tumor cells only (n = 5047), annotated by samples. **B:** UMAP of AT/RT-TYR tumor cells only (n = 3031), annotated by samples. **C:** UMAP of AT/RT-SHH tumor cells only (n = 3599), annotated by samples. **D:** Integrated UMAP using 10 neighboring points of all AT/RT-MYC primary tumor cells (n = 3188), annotated by *Seurat* clusters. **E:** Bar plot showing the distribution of all MYC primary tumor cells over the primary tumor clusters,

annotated by sample. **F:** Integrated UMAP of all AT/RT-MYC recurrence tumor cells (n = 1859), annotated by *Seurat* clusters. **G:** Bar plot showing the distribution of all MYC recurrence tumor cells over the recurrence tumor clusters, annotated by sample. **H:** Heatmap of *CIBERSORT* results for investigating similarities between AT/RT-MYC primary tumor clusters and recurrence tumor clusters, showing highest *CIBERSORT* scores for primary tumor clusters 2, 4, and 5. **I:** Bar plot showing the distribution of the potentially therapy-resistant AT/RT-MYC primary tumor clusters 2, 4, and 5 over the primary tumor samples. **J:** Upregulated genes and *Reactome* pathways in potentially therapy-resistant AT/RT-MYC primary tumor cells (primary tumor clusters 2, 4, and 5) compared to all other primary tumor cells.

Fig. 4: Cancer cell states of AT/RT-MYC tumor cells according to Barkley et al. (2022)[24] **and *in vitro* validation using patient-derived AT/RT-MYC cell lines. A:** Distribution of cancer cell states of integrated AT/RT-MYC recurrence tumor cells compared to AT/RT-MYC primary tumor cells, resulting in an increased proportion of cells undergoing pEMT (p = 0.0026, two-sided paired *t*-test). **B:** Distribution of cancer cell states of AT/RT-MYC primary tumor clusters 2, 4, and 5 (potentially therapy-resistant cells) compared to AT/RT-MYC primary tumor clusters 0, 1, 3, and 6 showed no significant difference between the proportion of cells undergoing pEMT (p = 0.35, two-sided paired *t*-test). **C:** IHC staining of the EMA protein, exemplary for AT/RT-MYC case 18 (primary tumor and paired recurrence). Scale bars indicate 20 µm. **D:** Quantification of EMA IHC for five AT/RT-MYC primary-recurrence pairs resulted in decreased EMA-positive area in recurrences for three pairs, two pairs showed similar EMA expression (p = 0.035, one-sided paired *t*-test). **E:** *In vitro* validation of the distribution of epithelial cells using two AT/RT-MYC cell lines: BT-16 and CHLA-266. H&E and IHC EMA staining was performed before and after treatment with a combination of doxorubicin, etoposide, and vincristine. Quantification of the EMA staining resulted in decreased EMA-positive area after the treatment BT-16 ($p = 4.5\times10^{-6}$, two-sided paired *t*-test) and CHLA-266 ($p = 4.8\times10^{-6}$, two-sided paired *t*-test). Scale bars indicate 20 µm. **F:** Volcano Plot of bulk RNAseq data showing differentially expressed genes of BT-16 and CHLA-266 untreated (red) vs. BT-16 and CHLA-266 treated with doxorubicin, etoposide, and vincristine (green) with pEMT marker genes annotated[24]. Most of the pEMT marker genes were upregulated after treatment. **G:** Volcano Plot of bulk RNAseq data showing differentially expressed genes of BT-16 and CHLA-266 untreated (red) vs. BT-16 and CHLA-266 treated with doxorubicin, etoposide, and vincristine (green) with marker genes of potentially therapy-resistant AT/RT-MYC primary tumor cells (primary tumor cluster 2, 4, and 5) annotated. Most of the marker genes of potentially therapy-resistant cells were upregulated after treatment.

Fig. 5: Survival analyses of AT/RT-MYC patients in correlation with the expression of genes identified in potentially therapy-resistant primary tumor cells. A: PFS of a cohort of AT/RT-MYC patients separated into two groups using the best cut-off. There was no difference in the PFS of patients with an overexpression of a high number of genes identified in potentially therapy-resistant AT/RT-MYC primary tumor cells (primary tumor clusters 2, 4, and 5; n = 9) compared to the patients with a low number of these genes (n = 13, p = 0.075, two-sided Log-Rank test). **B:** OS of a cohort of AT/RT-MYC patients separated into two groups using the best cut-off. Patients with an overexpression of a high number of genes identified in potentially therapy-resistant AT/RT-MYC primary tumor cells (primary tumor clusters 2, 4, and 5; n = 11) had a significantly worse OS compared to the patients with a low number of these genes (n = 14, p = 0.039, two-sided Log-Rank test). **C:** Dot plot of the top 15 *Reactome* pathways upregulated in potentially therapy-resistant AT/RT-MYC primary tumor cells (primary tumor clusters 2, 4, and 5). The size of the dots indicated the gene set size, and the dots were colored according to their adjusted p-value. The pathways marked in red were overlapping pathways with D. The pathways marked in orange had similar functions to pathways in D. **D:** Dot plot of the top 15 *Reactome* pathways upregulated in AT/RT-MYC patients with short survival and/or disease progression (according to C and D). The size of the dots indicated the gene set size, and the dots were colored according to their adjusted p-value. The pathways marked in red were overlapping pathways with C. The pathways marked in orange had similar functions to pathways in C.

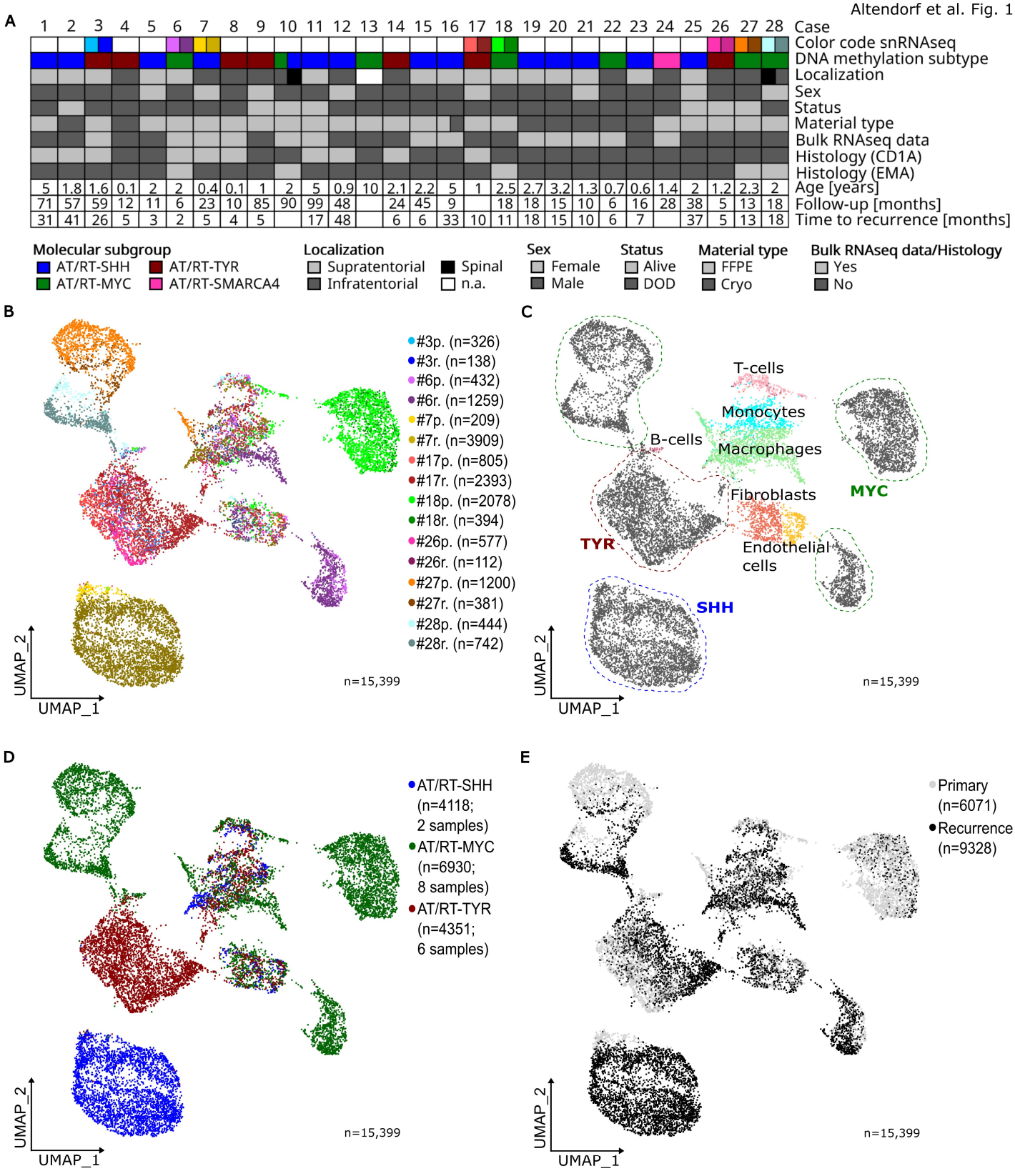
A
Case
Color code snRNAseq
DNA methylation subtype
Localization
Sex
Status
Material type
Bulk RNAseq data
Histology (CD1A)
Histology (EMA)
Age [years]
Follow-up [months]
Time to recurrence [months]
Molecular subgroup
AT/RT-SHH
AT/RT-TYR
AT/RT-MYC
AT/RT-SMARCA4
Localization
Supratentorial
Infratentorial
Spinal
n.a.
Sex
Female
Male
Status
Alive
DOD
Material type
FFPE
Cryo
Bulk RNAseq data/Histology
Yes
No
B
#3p. (n=326)
#3r. (n=138)
#6p. (n=432)
#6r. (n=1259)
#7p. (n=209)
#7r. (n=3909)
#17p. (n=805)
#17r. (n=2393)
#18p. (n=2078)
#18r. (n=394)
#26p. (n=577)
#26r. (n=112)
#27p. (n=1200)
#27r. (n=381)
#28p. (n=444)
#28r. (n=742)
n=15,399
UMAP_2
UMAP_1
C
T-cells
Monocytes
B-cells
Macrophages
MYC
Fibroblasts
TYR
Endothelial cells
SHH
n=15,399
UMAP_2
UMAP_1
D
AT/RT-SHH (n=4118; 2 samples)
AT/RT-MYC (n=6930; 8 samples)
AT/RT-TYR (n=4351; 6 samples)
n=15,399
UMAP_2
UMAP_1
E
Primary (n=6071)
Recurrence (n=9328)
n=15,399
UMAP_2
UMAP_1

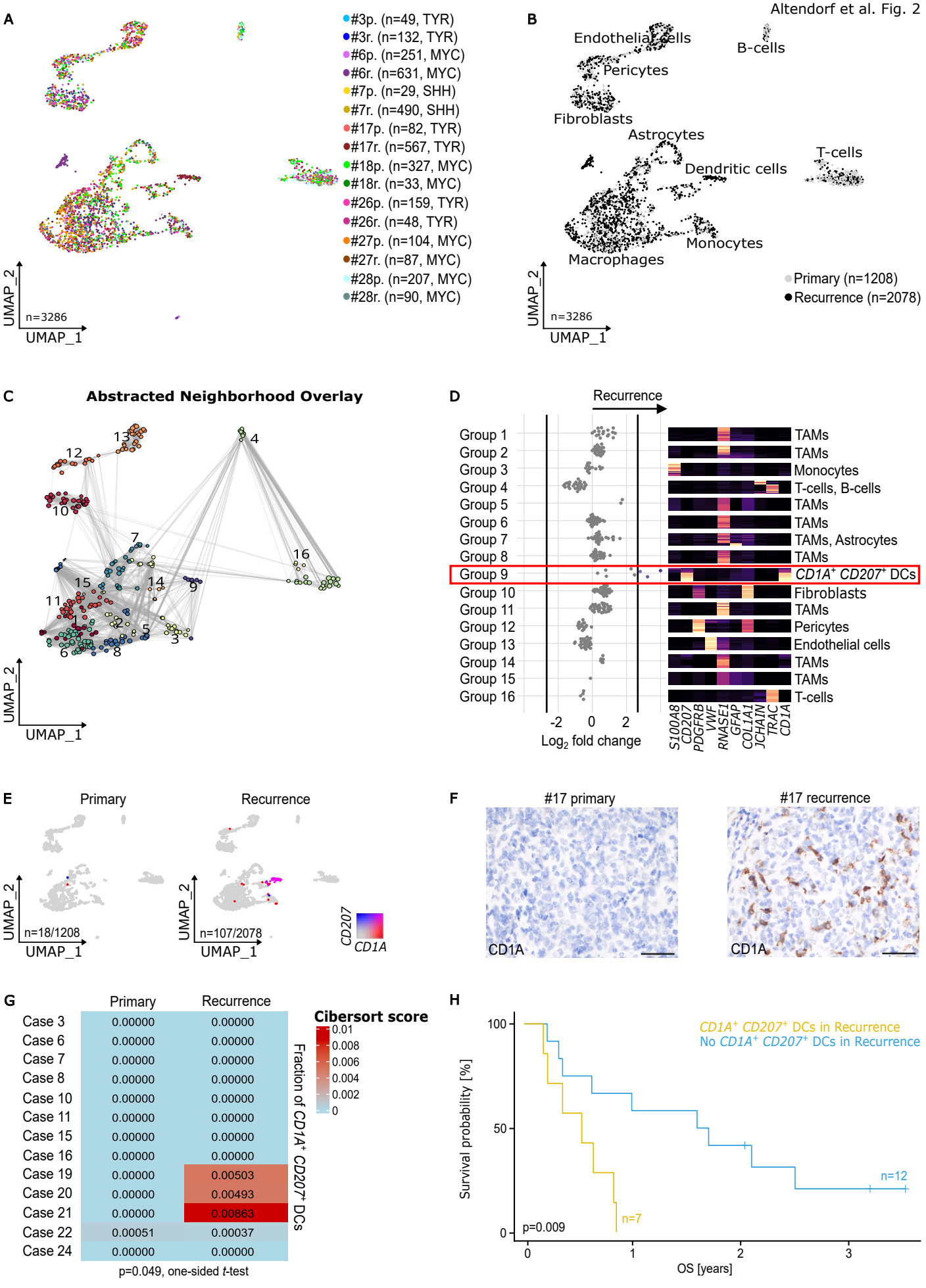
A
#3p. (n=49, TYR)
#3r. (n=132, TYR)
#6p. (n=251, MYC)
#6r. (n=631, MYC)
#7p. (n=29, SHH)
#7r. (n=490, SHH)
#17p. (n=82, TYR)
#17r. (n=567, TYR)
#18p. (n=327, MYC)
#18r. (n=33, MYC)
#26p. (n=159, TYR)
#26r. (n=48, TYR)
#27p. (n=104, MYC)
#27r. (n=87, MYC)
#28p. (n=207, MYC)
#28r. (n=90, MYC)
UMAP_2
UMAP_1
n=3286
B
Endothelial cells
B-cells
Pericytes
Fibroblasts
Astrocytes
T-cells
Dendritic cells
Monocytes
Macrophages
Primary (n=1208)
Recurrence (n=2078)
UMAP_2
UMAP_1
n=3286
C
Abstracted Neighborhood Overlay
UMAP_2
UMAP_1
D
Recurrence
Group 1
Group 2
Group 3
Group 4
Group 5
Group 6
Group 7
Group 8
Group 9
Group 10
Group 11
Group 12
Group 13
Group 14
Group 15
Group 16
TAMs
TAMs
Monocytes
T-cells, B-cells
TAMs
TAMs
TAMs, Astrocytes
TAMs
CD1A+ CD207+ DCs
Fibroblasts
TAMs
Pericytes
Endothelial cells
TAMs
TAMs
T-cells
-2
0
2
Log2 fold change
S100A8
CD207
PDGFRB
VWF
RNASE1
GFAP
COL1A1
JCHAIN
TRAC
CD1A
E
Primary
Recurrence
UMAP_2
UMAP_1
n=18/1208
n=107/2078
CD207
CD1A
F
#17 primary
#17 recurrence
CD1A
CD1A
G
Primary
Recurrence
Case 3 0.00000 0.00000
Case 6 0.00000 0.00000
Case 7 0.00000 0.00000
Case 8 0.00000 0.00000
Case 10 0.00000 0.00000
Case 11 0.00000 0.00000
Case 15 0.00000 0.00000
Case 16 0.00000 0.00000
Case 19 0.00000 0.00503
Case 20 0.00000 0.00493
Case 21 0.00000 0.00863
Case 22 0.00051 0.00037
Case 24 0.00000 0.00000
Cibersort score
0.01
0.008
0.006
0.004
0.002
0
Fraction of CD1A+ CD207+ DCs
p=0.049, one-sided t-test
H
CD1A+ CD207+ DCs in Recurrence
No CD1A+ CD207+ DCs in Recurrence
Survival probability [%]
100
50
0
n=12
n=7
p=0.009
0
1
2
3
OS [years]

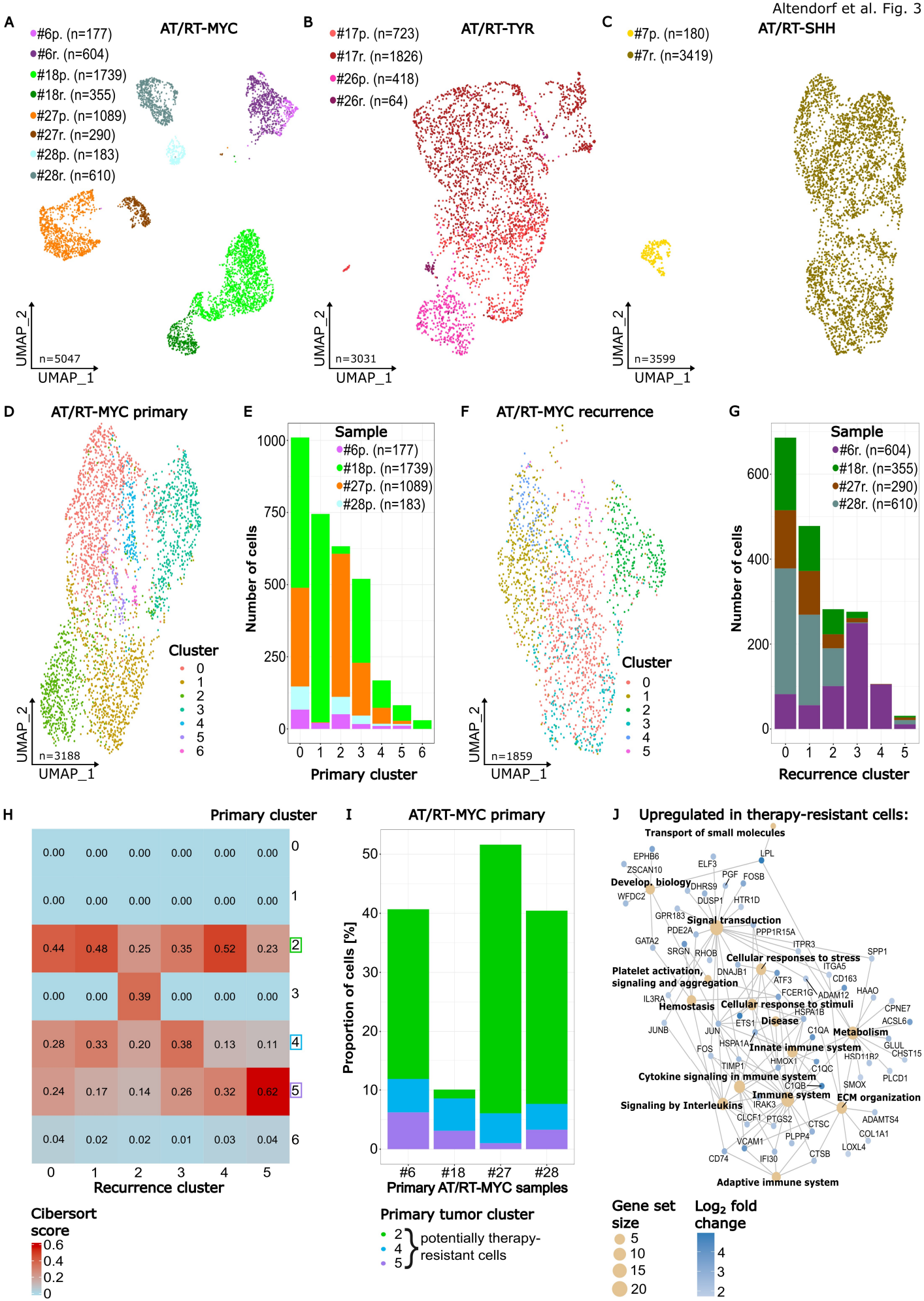
A
AT/RT-MYC
#6p. (n=177)
#6r. (n=604)
#18p. (n=1739)
#18r. (n=355)
#27p. (n=1089)
#27r. (n=290)
#28p. (n=183)
#28r. (n=610)
UMAP_2
UMAP_1
n=5047
B
AT/RT-TYR
#17p. (n=723)
#17r. (n=1826)
#26p. (n=418)
#26r. (n=64)
n=3031
C
AT/RT-SHH
#7p. (n=180)
#7r. (n=3419)
n=3599
D
AT/RT-MYC primary
Cluster
0
1
2
3
4
5
6
n=3188
E
Sample
#6p. (n=177)
#18p. (n=1739)
#27p. (n=1089)
#28p. (n=183)
Number of cells
Primary cluster
F
AT/RT-MYC recurrence
n=1859
G
Sample
#6r. (n=604)
#18r. (n=355)
#27r. (n=290)
#28r. (n=610)
Recurrence cluster
H
Primary cluster
Recurrence cluster
Cibersort score
I
AT/RT-MYC primary
Proportion of cells [%]
Primary AT/RT-MYC samples
Primary tumor cluster
potentially therapy-resistant cells
J
Upregulated in therapy-resistant cells:
Transport of small molecules
Develop. biology
Signal transduction
Cellular responses to stress
Platelet activation, signaling and aggregation
Hemostasis
Cellular response to stimuli
Disease
Metabolism
Innate immune system
Cytokine signaling in immune system
Immune system
Signaling by Interleukins
ECM organization
Adaptive immune system
Gene set size
Log2 fold change

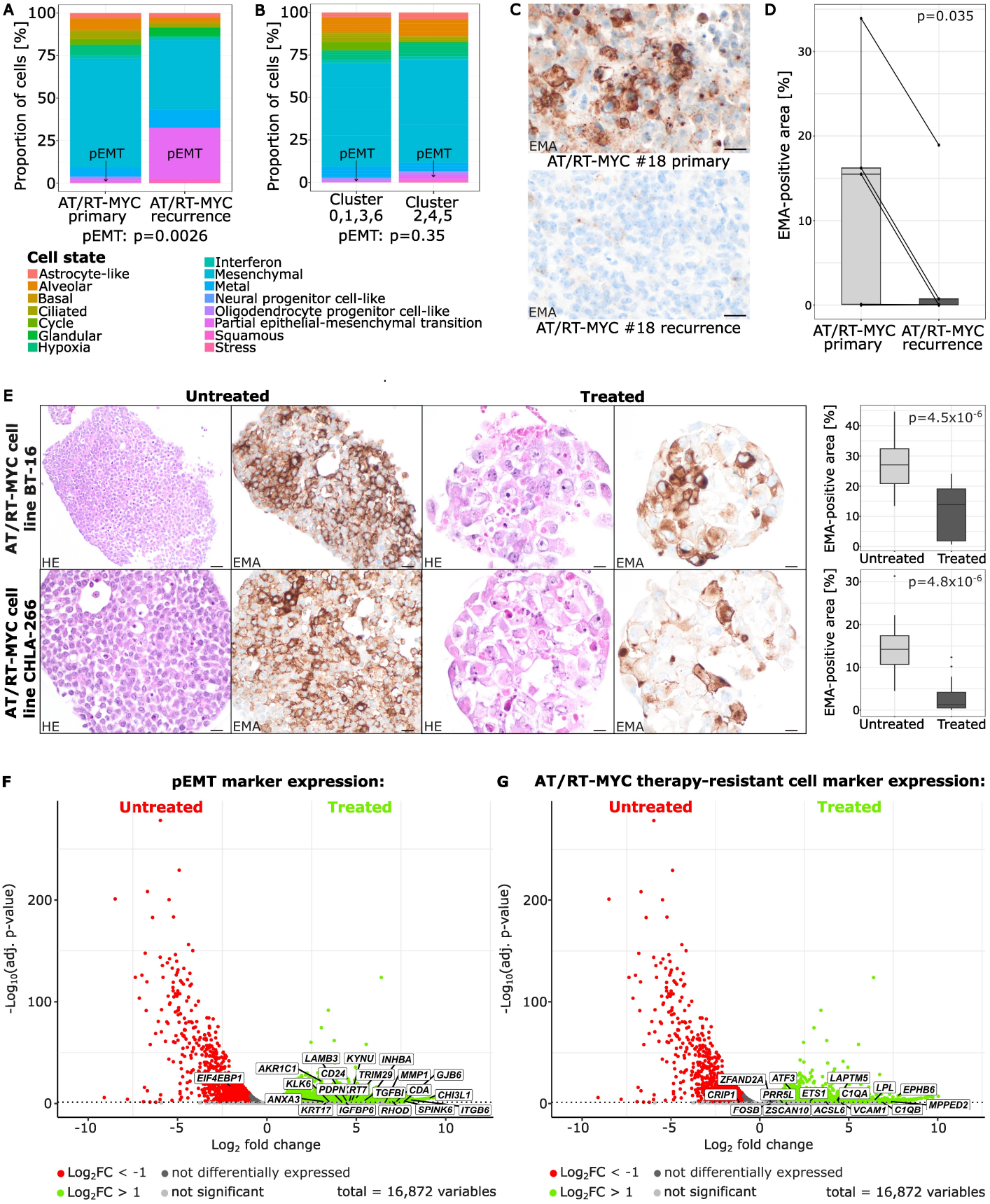
A
Proportion of cells [%]
pEMT
AT/RT-MYC primary
AT/RT-MYC recurrence
pEMT: p=0.0026
B
Cluster 0,1,3,6
Cluster 2,4,5
pEMT: p=0.35
Cell state
Astrocyte-like
Alveolar
Basal
Ciliated
Cycle
Glandular
Hypoxia
Interferon
Mesenchymal
Metal
Neural progenitor cell-like
Oligodendrocyte progenitor cell-like
Partial epithelial-mesenchymal transition
Squamous
Stress
C
EMA
AT/RT-MYC #18 primary
AT/RT-MYC #18 recurrence
D
p=0.035
EMA-positive area [%]
E
Untreated
Treated
AT/RT-MYC cell line BT-16
AT/RT-MYC cell line CHLA-266
HE
EMA
p=4.5x10-6
p=4.8x10-6
F
pEMT marker expression:
G
AT/RT-MYC therapy-resistant cell marker expression:
-Log10(adj. p-value)
Log2 fold change
Log2FC < -1
Log2FC > 1
not differentially expressed
not significant
total = 16,872 variables

Correlation of survival and expression of genes identified in potentially therapy-resistant AT/RT-MYC tumor cells:

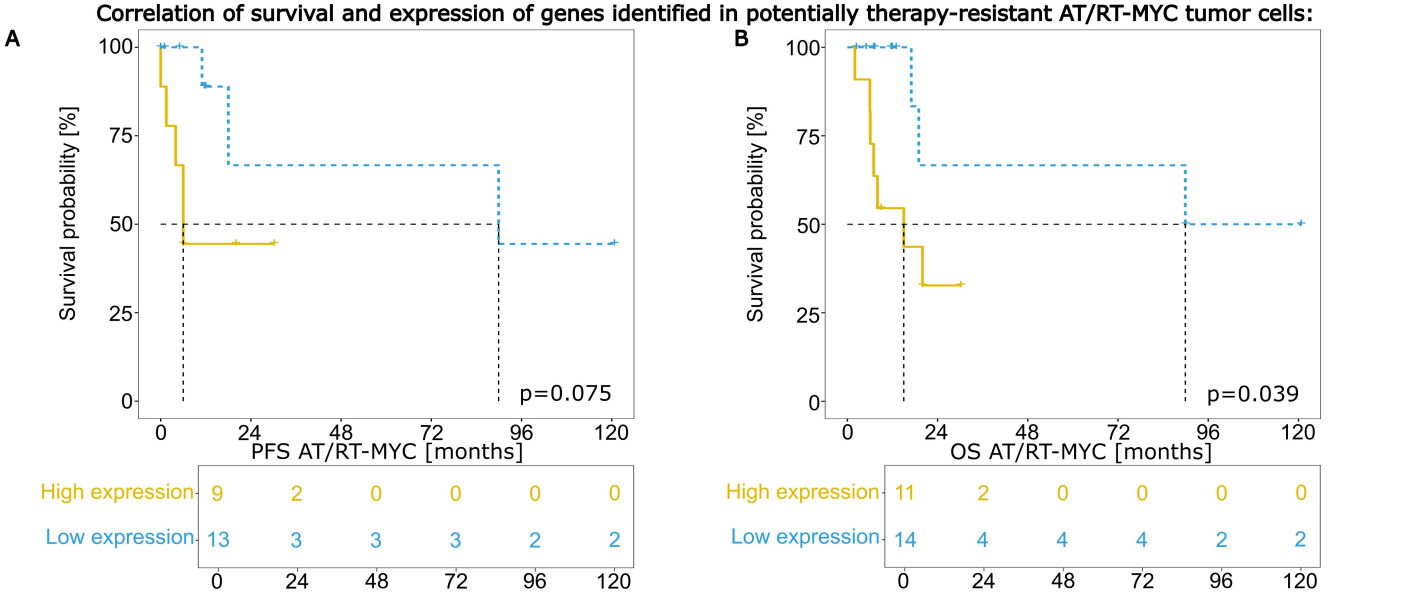

C Upregulated in resistant AT/RT-MYC primary tumor cells:

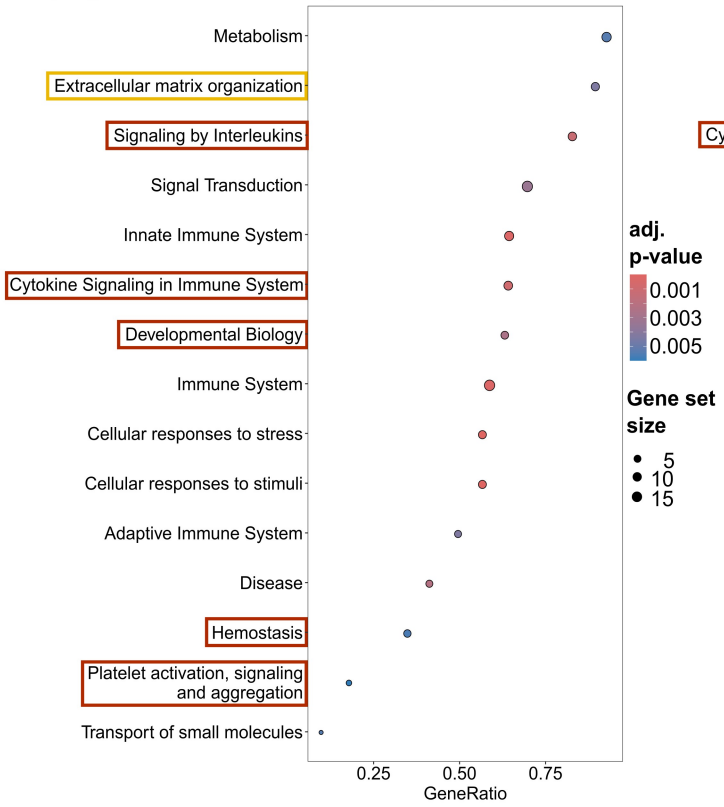

D Upregulated in patients with short survival/progression:

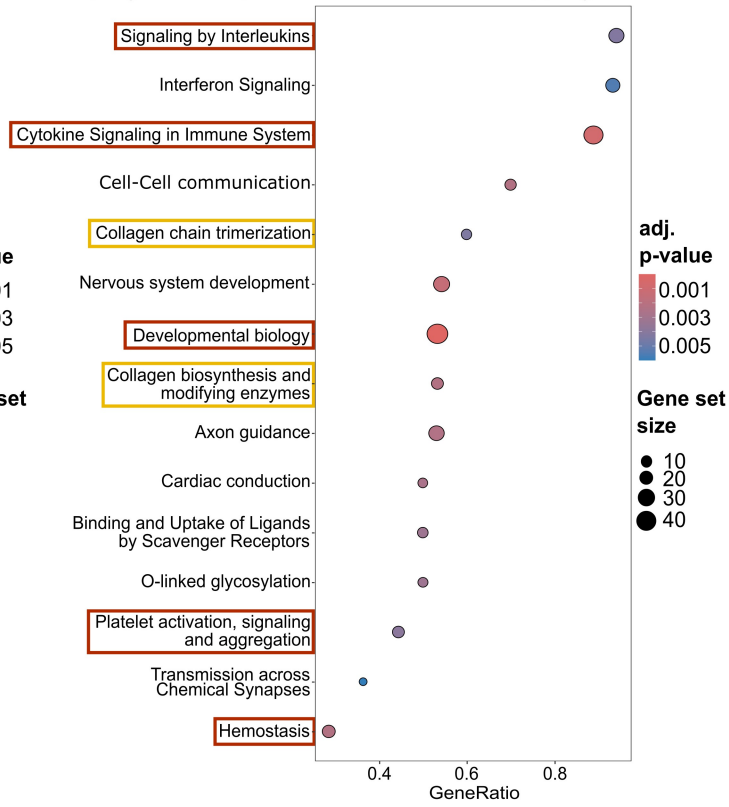

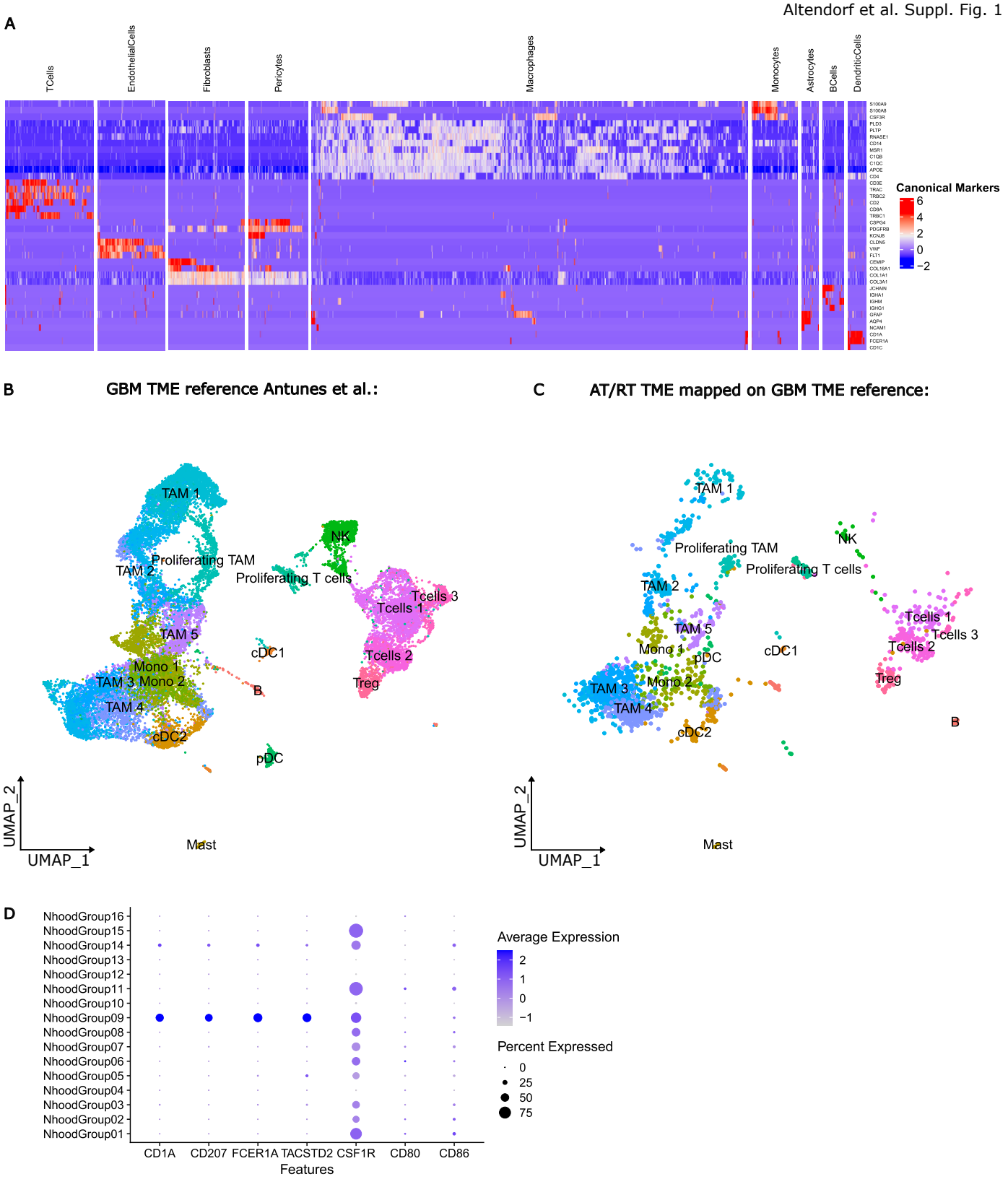

Suppl. Fig. 1: Manual and automated annotation of the AT/RT TME and neighborhood group characterization. A: Heatmap showing canonical markers of each cell type for manual annotation of the TME. **B:** UMAP of the GBM TME reference data set of Antunes et al. used for annotation via *Azimuth*. **C:** UMAP of the AT/RT TME mapped on the Antunes et al. GBM TME reference UMAP using *Azimuth*. **D:** Dot plot showing differential gene expression analysis of neighborhood group 9 vs. all other neighborhood groups resulted in a *CD1A*$^{+}$ *CD207*$^{+}$ *FCER1A*$^{+}$ *TACSTD2*$^{+}$ and *CSF1R*^{high} expression profile.

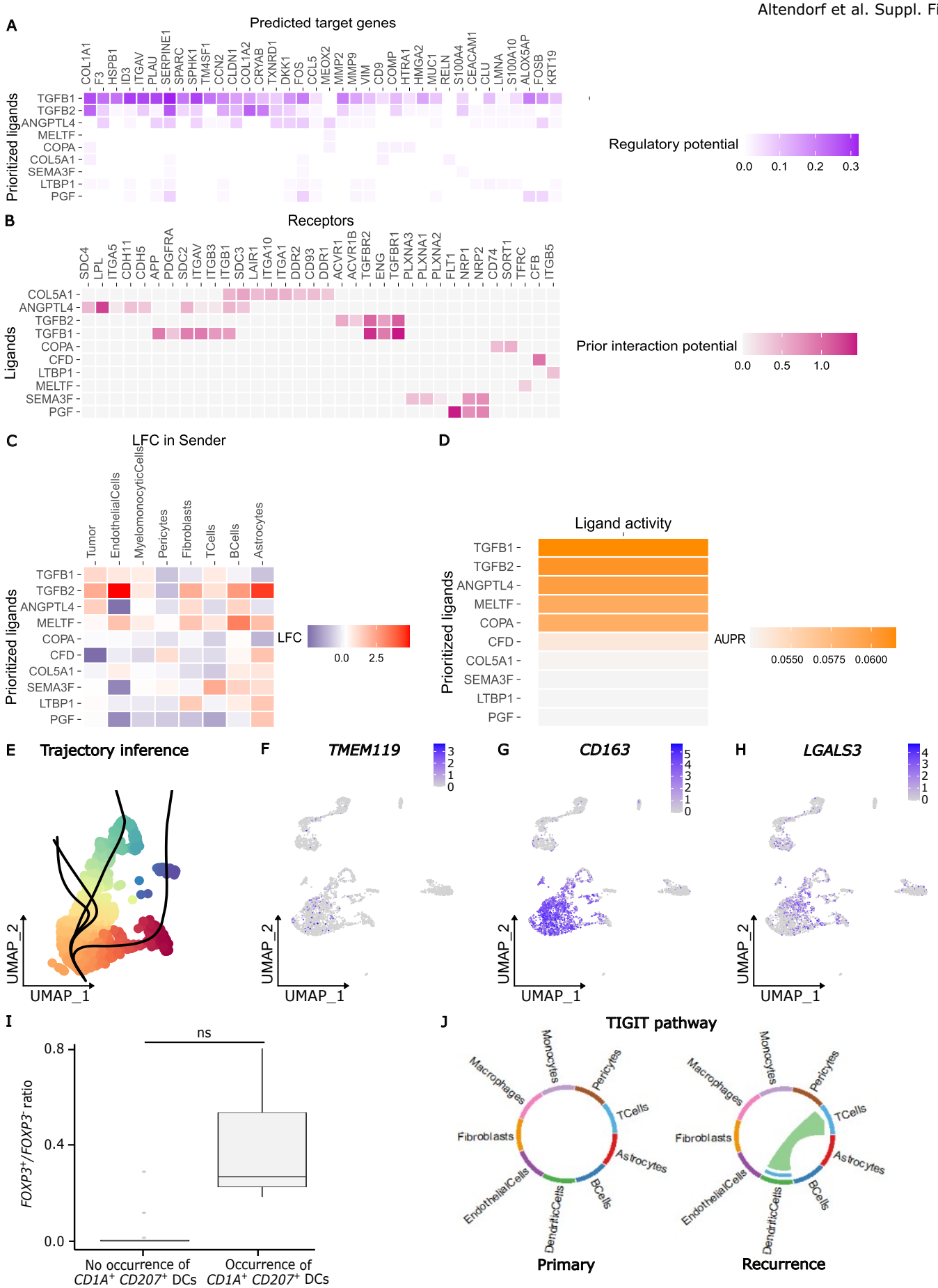

Suppl. Fig. 2: Cell-cell communication analyses of the AT/RT TME. A: Heatmap of *nichenetr* cell-cell communication results showing ligand-target gene interactions, indicating a robustly enriched *TGF-β1*- and *TGF-β2*-induced signaling in recurrent AT/RT. **B:** Heatmap of *nichenetr* cell-cell communication results showing ligand-receptor interactions. **C:** Heatmap of *nichenetr* cell-cell communication results showing ligand-cell type interactions. **D:** Heatmap of *nichenetr* cell-cell communication results showing ligand activity. **E:** Trajectory inference using *Slingshot* mapped on the UMAP of *harmony*-integrated TME cells suggested periphery-derived monocytes as ontogenetic precursors. **F:** *FeaturePlot* showing *TMEM119* expression in the TME cells, resulting in negativity for *CD1A*$^+$ *CD207*$^+$ DCs. **G:** *FeaturePlot* showing *CD163* expression in the TME cells, resulting in negativity for *CD1A*$^+$ *CD207*$^+$ DCs. **H:** *FeaturePlot* showing *LGALS3* expression in the TME cells, resulting in negativity for *CD1A*$^+$ *CD207*$^+$ DCs. **I:** Ratios of *FOXP3*$^+$ to *FOXP3*$^-$ T-cells were calculated as the ratio of cells in the T-cell cluster exhibiting an expression of *FOXP3* > 0.5 to all other cells of this cluster. A one-sided *t*-test did not result in a significant difference between primary and recurrent AT/RT. **J:** *CellChat* results for the TIGIT pathway show an interaction of tumor-associated DCs and T-cells in AT/RT recurrences.

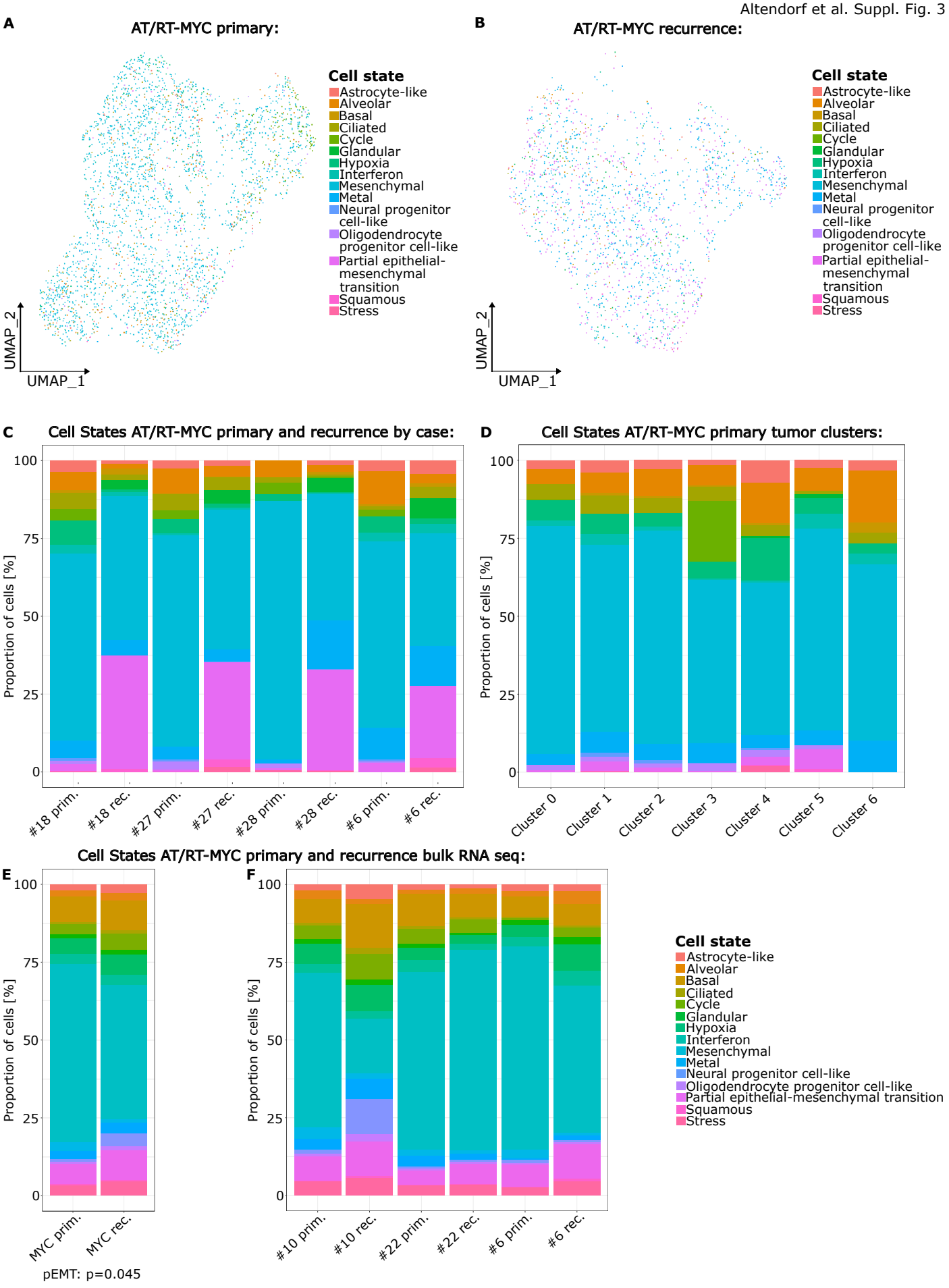

Suppl. Fig. 3: Cancer cell states of AT/RT-MYC scRNA and bulk RNA sequencing data according to Barkley et al. (2022) [31]. A: Integrated UMAP using 10 neighboring points of all AT/RT-MYC primary tumor cells (n = 3188), annotated by Cancer Cell States. **B:** Integrated UMAP of all AT/RT-MYC recurrence tumor cells (n = 1859), annotated by Cancer Cell States. **C:** Distribution of cancer cell states of integrated AT/RT-MYC recurrence tumor cells compared to AT/RT-MYC primary tumor cells for each case. **D:** Distribution of cancer cell states for each AT/RT-MYC primary tumor cluster. **E:** Distribution of cancer cell states using bulk RNA sequencing data of AT/RT-MYC recurrence tumors compared to AT/RT-MYC primary tumors, resulting in an increased proportion of cells undergoing pEMT ($p = 0.045$, two-sided paired *t*-test). **F:** Distribution of cancer cell states using bulk RNA sequencing data of AT/RT-MYC recurrence tumors compared to AT/RT-MYC primary tumors for each case.

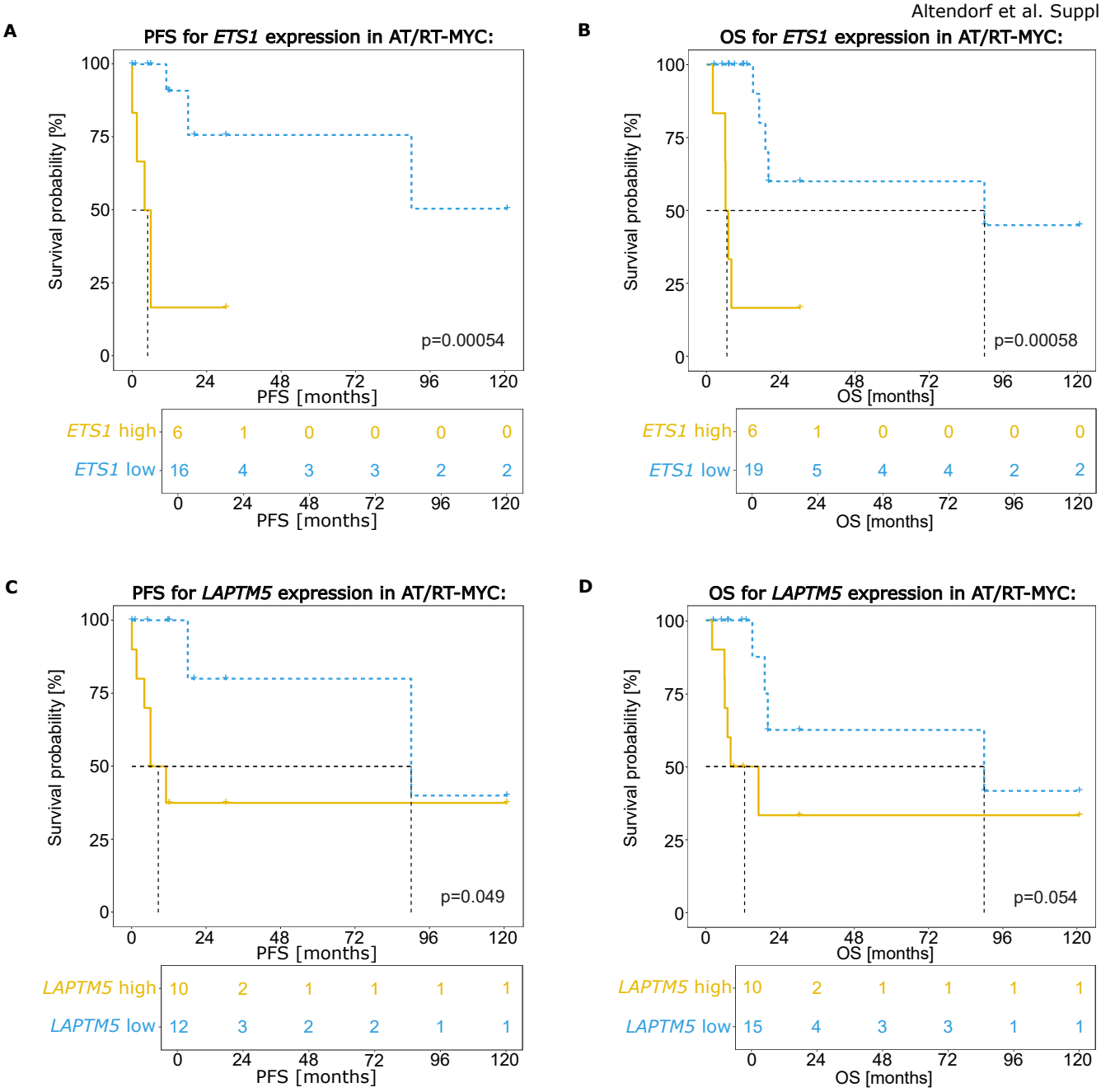

Suppl. Fig. 4: Survival analyses of AT/RT-MYC patients in correlation with the expression of the top upregulated genes identified in potentially therapy-resistant primary tumor cells. A: PFS of a cohort of AT/RT-MYC patients separated into two groups using the best cutoff for *ETS1* expression. The group with high *ETS1* expression (n = 6) had a significantly worse PFS compared to the group with low *ETS1* expression (n = 16, p = 0.00054, two-sided Log-Rank test). **B:** OS of a cohort of AT/RT-MYC patients separated into two groups using the best cutoff for *ETS1* expression. The group with high *ETS1* expression (n = 6) had a significantly worse OS compared to the group with low *ETS1* expression (n = 19, p = 0.00058, two-sided Log-Rank test). **C:** PFS of a cohort of AT/RT-MYC patients separated into two groups using the best cutoff for *LAPTM5* expression. The group with high *LAPTM5* expression (n = 10) had a significantly worse OS compared to the group with low *LAPTM5* expression (n = 12, p = 0.049, two-sided Log-Rank test). **D:** OS of a cohort of AT/RT-MYC patients separated into two groups using the best cutoff for *LAPTM5* expression. The group with high *LAPTM5* expression (n = 10) had no significantly different OS compared to the group with low *LAPTM5* expression (n = 15, p = 0.054, two-sided Log-Rank test).

5. Unpublished manuscript 2

Molecular and histological analyses of AT/RT-TYR suggest the choroid plexus of the fourth ventricle as cellular origin

Lea Altendorf, Levke-Sophie Peter, Karoline Hack, Matthias Dottermusch, Svenja Tonn, Rajanya Roy, Michael J Holtzman, Christian Thomas, Kornelius Kerl, Melanie Schoof, Martin Hasselblatt, Ulrich Schüller

Unpublished manuscript 2025

Title:

Molecular and histological analyses of AT/RT-TYR suggest the choroid plexus of the fourth ventricle as cellular origin

Authors:

Lea Altendorf[1,2], Levke-Sophie Peter[1,2], Karoline Hack[1,2], Matthias Dottermusch[3], Svenja Tonn[1,2], Rajanya Roy[4], Michael J Holtzman[5], Christian Thomas[6], Kornelius Kerl[4], Melanie Schoof[1,2], Martin Hasselblatt[6], and Ulrich Schüller[1,2,3]

[1]Department of Pediatric Hematology and Oncology, University Medical Center Hamburg-Eppendorf, Germany
[2]Research Institute Children's Cancer, University Medical Center Hamburg-Eppendorf, Germany
[3]Institute of Neuropathology, University Medical Center Hamburg-Eppendorf, Germany
[4]Department of Pediatric Hematology and Oncology, University Medical Center Münster, Germany
[5]Pulmonary and Critical Care Medicine, Department of Medicine, Washington University, St. Louis, MO, USA
[6]Institute of Neuropathology, University Hospital Münster, Germany

Running Title:

Cellular origin of AT/RT-TYR

Corresponding author:

Ulrich Schüller, MD
Research Institute Children's Cancer Center Hamburg
Martinistraße 52, N63, D-20251 Hamburg, Germany
Phone: +49-40-426051240
Fax: +49-40-741040350
E-mail: u.schueller@uke.de

Abstract:

Background:

Atypical teratoid/rhabdoid tumors (AT/RT) are aggressive pediatric tumors of the central nervous system (CNS). They are characterized by *SMARCB1* or *SMARCA4* mutations and split into the four DNA methylation subtypes AT/RT-TYR, AT/RT-SHH, AT/RT-MYC, and AT/RT-SMARCA4. Each of these subtypes has distinct clinical characteristics, with AT/RT-TYR most frequently occurring in the fourth ventricle. However, details on tumor initiation as well as the cellular origins remain largely unknown. Notably, mouse models for AT/RT-TYR providing insights into tumor development and prerequisites to explore treatment strategies, are completely lacking.

Methods:

To identify the cellular origin of AT/RT-TYR, tumor cells were investigated using histology, bulk and single-nucleus RNA sequencing data. *CIBERSORT* analysis was performed to calculate similarities between AT/RT-TYR tumor cells and non-neoplastic cell types of the CNS. Genetically engineered mouse models with a conditional, Cre/loxP-induced Smarcb1 loss were generated.

Results:

Here, we show that AT/RT-TYR were significantly more frequently intermingled with fourth ventricle choroid plexus (CP) tissue compared to other infratentorial brain tumors. The tumor cells heavily expressed CP markers. Analyses of bulk- and single-nucleus RNA sequencing data across various brain tumor entities and cell populations of the developing normal brain revealed a clear resemblance of the AT/RT-TYR to the CP of the fourth ventricle. Finally, *Foxj1-cre::Smarcb1*$^{fl/fl}$ mice showed loss of Smarcb1 in early CP progenitors, which gave rise to large, atypical, monociliary CP cells with gene expression most similar to human AT/RT-TYR.

Conclusions:

Analyses of human AT/RT-TYR as well as murine CP cells lacking Smarcb1 point towards the CP of the fourth ventricle as a potential cellular origin of AT/RT-TYR.

Keywords:

AT/RT-TYR, choroid plexus, cellular origin, mouse model

Key points:

- Histopathological and transcriptomic features of the choroid plexus were enriched in AT/RT-TYR
- *CIBERSORT* analyses revealed the highest similarity of AT/RT-TYR to the choroid plexus
- *Foxj1-cre::Smarcb1*$^{fl/fl}$ mice showed large, atypical CP cells with similarity to human AT/RT-TYR at gene expression level

Introduction:

Atypical teratoid/rhabdoid tumors (AT/RT) belong to the most common tumors of the central nervous system (CNS) during infancy. Their prognosis is very poor, with a median overall survival of 9-17 months[1–3], which is in line with the fact that tumors often progress or recur after a short time[4]. Targeted therapies are lacking because appropriate targets remain unknown. In addition, the cellular origin and detailed developmental processes of these tumors are currently undescribed, but this knowledge might help to identify novel therapeutic targets. Previously, four distinct DNA methylation subtypes were identified, which also differ regarding their gene expression profiles and clinical characteristics[4,5]. AT/RT-TYR, AT/RT-SHH, and AT/RT-MYC are characterized by *SMARCB1* mutations[6–8], whereas a small proportion of tumors show *SMARCA4* mutations and therefore belong to the AT/RT-SMARCA4 subtype[9,10]. Overall, no further recurrent alterations were identified in AT/RT. SMARCB1 and SMARCA4 are part of the SWItch/sucrose non-fermentable (SWI/SNF) complex, which is an ATP-dependent chromatin-remodeling complex[11]. This complex is involved in the histone structure of the DNA and the regulation of gene expression. In previous studies on genetically engineered AT/RT mouse models, neural progenitors and neural crest progenitors were assumed to be the cellular origin of AT/RT-SHH and AT/RT-MYC, respectively[12,13]. For AT/RT-TYR and AT/RT-SMARCA4, mouse models that could give insights into their cellular origins and serve as models for preclinical therapy approaches are lacking. AT/RT-TYR is the second most frequent AT/RT DNA methylation subtype, which is mainly diagnosed in very young patients with a median age of 12 months. The tumors are mainly located infratentorial (78%) and about a quarter of the patients suffer from rhabdoid tumor predisposition syndrome 1 (RTPS1; OMIM #609322), presenting germline mutations[9,14,15]. The identification of the cellular origin and developmental time point is urgently needed and the generation of an AT/RT-TYR mouse model might give insights into the mechanisms of tumor development. Additionally, a mouse model is required to develop novel targeted therapies and test them in mice.

Examination of AT/RT-TYR MRI scans revealed that infratentorial tumors mainly occur in the fourth ventricle[16]. As the choroid plexus (CP) is located inside the ventricle, we hypothesize that CP precursors of the fourth ventricle are the cellular origin of these embryonal tumors.

Here, we investigated AT/RT-TYR for the occurrence of CP signatures on the histological and gene expression levels in comparison with the other AT/RT DNA methylation subtypes and CNS tumor entities. In addition, we induced an early *Smarcb1* knockout in the CP of the fourth ventricle in mice in order to analyze morphological and molecular changes of the CP in comparison to human AT/RT-TYR.

Material and Methods:

Samples and data sets

Scans of 53 Hematoxylin and Eosin (H&E) stainings of infratentorial AT/RT and of 100 medulloblastoma (MB) were collected for the investigation of intermingled CP tissue occurrence. In addition, 17 cases were collected for FOXJ1 and OTX2 stainings, as well as 67 cases for KIR7.1 stainings. Bulk RNA sequencing (RNAseq) data of 36 AT/RT[17] were included. Transcriptomic data of a variety of human CNS tumors[18] were used as a reference. In addition, bulk RNAseq data of choroid plexus carcinoma (CPC)[19] and myxopapillary ependymoma (MPE)[20] were taken from a previously published cohort. For *CIBERSORT* analyses, single-cell RNA sequencing (scRNAseq) data sets of the developing human cerebellum[21] and the developing murine forebrain and pons[22] were used. Single-nucleus RNA sequencing (snRNAseq) data of eight human primary AT/RT were generated for this study. An overview of all samples is summarized in Supplementary Table 1.

Genetically engineered mouse models

Mice were kept on a 12 h dark/light cycle, and water and food were available *ad libitum*. Animals of both sexes were used for the experiments. All experimental procedures were approved by the Government of Hamburg, Germany (N099/2019 and N015/2025). Mice were maintained on a C57BL/6J background. By crossing *Foxj1-cre* mice[23] with *Smarcb1*$^{fl/fl}$ mice[24], we generated *Foxj1-cre::Smarcb1*$^{fl/fl}$ mice. For the generation of *Foxj1-cre::lsl-Lin28a::Smarcb1*$^{fl/fl}$ mice, we crossed *Foxj1-cre::Smarcb1*$^{fl/fl}$ mice with *lsl-Lin28a*$^{+}$ mice[25,26]. Fatemapping experiments were performed using *Foxj1-cre::lsl-R26tdRFP*$^{fl/wt}$ mice, resulting from crossing *Foxj1-cre* with *lsl-R26tdRFP*$^{fl/fl}$ mice[27]. Genotyping was performed by PCR analysis using genomic DNA derived from ear punches or tail biopsies. 5'-TCCGGGCTGCCACGACCAA-3' (*cre* forward) and 5'-GGCGCGGCAACACCATTTT-3' (*cre* reverse) primers were used to detect the *cre* transgene (448 bp), 5'-CACCATGCCCCCACCTCCCCTACA-3' (*Smarcb1* forward), 5'-CAGGAAAATGGATGCAACTAAGAT-3' (*Smarcb1* reverse), and 5'-GGTGGGGGTGGGGTGGGATTAGAT-3' (control) primers for *Smarcb1* (*wt*: 203 bp, *fl*: 300 bp, control: 600 bp), 5'-ATCTTATCATGTCTGGATCCCC-3' (*mLin28a* forward) and 5'-CGCAGTTGTAGCACCTGTCTC-3' (*mLin28a* reverse) primers for *Lin28a* (500 bp), and 5'-AAAGTCGCTCTGAGTTGTTAT-3' (*tdRFP fl/wt*), 5'-GCGAAGAGTTTGTCCTCAACC-3' (*tdRFP fl*), and 5'-GGAGCGGGAGAAATGGATATG-3' (*tdRFP wt*) primers for *tdRFP* (*wt*: 600 bp, *fl*: 250 bp). Mice were monitored daily and were sacrificed by cervical dislocation at

postnatal day 30 (P30) for examination of the brains. *Foxj1-cre::lsl-R26tdRFP*$^{fl/wt}$ mice were also investigated at embryonal day 10.5 (E10.5) using Caesarean section.

H&E staining, immunohistochemistry, and quantification

All murine brains and embryos as well as human AT/RT tumor samples were fixed in 4% formaldehyde, with subsequent dehydration and embedding in paraffin. For H&E staining and immunohistochemistry (IHC), 2 µm sagittal sections were prepared. H&E staining was performed using standard protocols. IHC was performed using a Ventana System (Roche) according to the manufacturers' specifications and the following primary antibodies: Mouse anti-BAF47 (BD Biosciences #612110, 1:50), rabbit anti-FOXJ1 (#HPA0057614 Sigma-Aldrich, 1:500), mouse anti-OTX2 (#1H12C4B5 Thermo Fisher Scientific, 1:2000), rabbit anti-ARL13B (#17711-1-AP Proteintech, 1:200), rabbit anti-LIN28A (#3978 Cell Signaling Tech, 1:50) for LIN28A stainings, and anti-KIR7.1[28] (1:2000). CP nuclei were investigated in *ImageJ* (version 1.54f, Java 1.8.0_322). The mean nuclei area was determined by measuring and averaging 20 nuclei per sample manually. The cells containing eccentric chromatin were also counted manually. To determine the nuclei in a row, the angle between each cell was measured by drawing a segmented line between each individual nucleus and running the macro (Suppl. Table 2). Nuclei in a row/column were defined by the following criteria: 1) a column must include at least three cells with 2) the angle between each cell ranging from −155 to −179° or 155 to 180°, and 3) the cells cannot be >20 pixels apart[29]. Statistics were calculated using two-sided *t*-tests.

RNA isolation and bulk RNA sequencing

The murine CP of the fourth ventricle was dissected at P30 using sterile forceps and a stereo microscope. The tissue was resuspended in Trizol, and RNA was isolated according to standard protocols. RNA concentration was determined using a Qubit 4 Fluorometer (Thermo Fisher Scientific) and 10 ng of each sample were inserted for library construction. The SMART-Seq stranded kit (Takara Bio) was used for library preparation according to the manufacturer's specifications. Sequencing of the library was performed on a NovaSeq X Plus (Illumina), using 2 × 101 bp, and demultiplexing was done with *Illumina bcl2fastq* (version 2.20). The adapters were trimmed with *Skewer* (version 0.2.2)[30]. The reads were aligned to the human genome hg38 using *STAR*[31], with subsequent feature count generation as input for the raw count table. The following analyses were performed in *R Studio* (version 4.4.1). Matching HUGO symbols for the ENSEMBL IDs were added using the *biomaRt* package (version 2.62.0)[32]. The counts were filtered by removing repetitively counted genes and genes from sex chromosomes.

Finally, the 10,000 most variable genes, identified by standard deviation, were chosen for visualization in a *t*-SNE plot using the *Rtsne* package (version 0.17)[33].

Differential gene expression analyses

Gene expression array data of Sturm et al. (2016)[18] and bulk RNAseq data of Johann, Altendorf et al. (2023)[17] and Thomas et al. (2021)[19] were integrated. Each data set was processed separately by applying *VST*-normalization, included in the *DESeq2* package (version 1.46.0)[34], and z-score normalization. The resulting count tables were merged, and batch effects resulting from different species and array types were corrected using *limma* (version 3.62.2)[35]. *DESeq2* differential gene expression analysis of integrated count data was performed. All genes with a p-value < 0.05 after Benjamini-Hochberg (BH) adjustment were considered as differentially expressed. *DESeq2*-normalized counts for selected genes were visualized in box plots created with *ggplot2* (version 3.5.1)[36]. Differentially expressed genes between the AT/RT DNA methylation subtypes were visualized in a volcano plot using the function *EnhancedVolcano()* of the *EnhancedVolcano* package (version 1.24.0)[37].

Cross-species analysis

A cross-species analysis was performed in *R Studio* (version 4.4.1) to compare the murine to the human transcriptome. Data sets of Sturm et al. (2016)[18], Johann, Altendorf et al. (2023)[17], and Thomas et al. (2021)[19] were used as human references of CNS tumors. For the validation of this analysis, bulk RNAseq data of *Math1-cre::Smo$^{fl/wt}$* mice, which develop MB-SHH, were integrated[38]. Each data set was processed separately with subsequent integration as described in the section *Differential gene expression analyses*. The 1,000 most variable genes among all samples were calculated, and results were visualized in a heatmap using the *ComplexHeatmap* package (version 2.22.0)[39]. The clustering distance metric for columns and rows was defined as *"pearson".* Additionally, the clustering method for columns and rows was set as *"average"*.

CIBERSORT analyses

CIBERSORT analysis was performed for deconvolution of AT/RT bulk- and snRNAseq data. For snRNAseq data, the tumor microenvironment (TME) was excluded, and pseudobulk values of all tumor cells for each DNA methylation subtype were calculated using the *AggregateExpression()* function, included in the *Seurat* package (version 5.1.0)[40]. As a reference data set, annotated scRNAseq data of Aldinger et al. (2021)[21] were used, which are

comprised of the cell types of the human developmental cerebellum (9 post-conceptional weeks (PCW) - 21 PCW), also containing CP. scRNAseq data of Jessa et al. (2019)[22], containing data of developing mouse brains from E12 – P6, were used as a second reference. Pseudobulk values for each cell type were calculated as described above. As technical controls, bulk RNAseq data of CPC[19] and MPE[20], both with known cellular origin, were integrated. Similarities between each tumor entity, or rather DNA methylation subtype, and the cell types of the reference data set were estimated using the *CIBERSORT()* function (perm = 500) of the *IOBR* package (version 0.99.0)[41] in *R Studio* (version 4.4.1).

Isolation of cells from FFPE tissue and single-nucleus RNA sequencing (snRNAseq)

The Chromium Single Cell Flex Gene Expression Assay from 10x Genomics was used to generate snRNAseq data from formalin-fixed paraffin-embedded (FFPE) tissue by isolating the cells according to the demonstrated protocol “Isolation of Cells from FFPE Tissue Sections for Chromium Fixed RNA Profiling”, Document Number CG000632 Rev B, from 10x Genomics, using a gentleMACS Octo Dissociator (#130-134-029, Miltenyi Biotec). The Enzyme Mix containing Liberase TH (# 5401151001, Millipore Sigma) was used for the dissociation of the FFPE scrolls. Probe hybridization and subsequent multiplex library preparation were performed using the 10x Genomics Sample Preparation Kit PN-1000414, 16 rxns, according to the protocol “Chromium Fixed RNA Profiling Reagent Kits for Multiplexed Samples”, Document Number CG000527 Rev E, from 10x Genomics. Sequencing of the resulting dual-index libraries was performed in the sequencing core facility of the University Medical Center Münster on NextSeq 2000 (Illumina) and NovaSeq 6000 (Illumina) sequencing systems, and a recovery of 80,000 cells for each library was targeted.

SnRNAseq data processing and clustering

Demultiplexing, barcode processing and assignment, single-nucleus counting, and alignment to the human reference genome GRCh38-2024-A were performed using the *10x Genomics Cell Ranger v8.0.1* software. Resulting Feature Barcode Matrices for each sample were processed in *R Studio* (version 4.4.1) using the *Seurat* package (version 5.1.0)[40]. This includes normalization, scaling, principal component analysis (PCA), shared nearest-neighbor graph construction (snn-graph), clustering, and uniform manifold approximation and projection (UMAP). The processed data were merged and normalized using the *SCTransform()* function, correcting for the percentage of mitochondrial counts. In addition, only nuclei with more than 200 and less than 2500 detected genes and less than 5% mitochondrial reads were included in further analysis. Final UMAPs were generated using 10 neighboring points in local approximation of manifold structure and a resolution of 0.5 for *Seurat* cluster assignment. The

FeaturePlot() function was applied for visualization of the expression of selected genes. The tumor microenvironment (TME) was annotated in a two-step procedure of automated and manual cross-validation as recommended. Automated annotation was performed using *SingleR* (version 2.8.0)[42] with the *ENCODE* reference, received by using the *BlueprintEncodeData()* function[43]. Manual annotation was performed based on canonical markers. Chromosome 22 status was investigated using the *inferCNV* package (version 1.22.0)[44] with the chromosome information from hg38. The TME cells were used as reference cells and all tumor cells as input. CNVs were calculated using *infercnv::run* (settings: analysis_mode = “samples”, cutoff = 0.1, cluster_by_groups = TRUE, denoise = TRUE, HMM = TRUE).

Results

Thorough examination of AT/RT biopsies revealed histological features of the CP predominant in infratentorial AT/RT-TYR

The goal was to identify the cellular origin of AT/RT-TYR. As AT/RT-TYR were mainly localized in the fourth ventricle[16], which also contains the CP, we hypothesize that CP precursors are the cellular origin of these infratentorial tumors. This study was based on 104 unique AT/RT samples (Suppl. Table 1) and the investigated AT/RT-TYR were mostly located infratentorial (91%; n = 31/34). We examined H&E stainings of 31 infratentorial AT/RT-TYR, 13 infratentorial AT/RT-SHH, and nine infratentorial AT/RT-MYC for the occurrence of intermingled CP tissue, which was enriched in AT/RT-TYR (35%; n = 11/31). For the other subtypes, no or rather only a few cases with intermingled CP were observed (AT/RT-SHH: n = 0; AT/RT-MYC: n = 1; Fig. 1A-C). For AT/RT-TYR, it appeared like the tumors arose from the CP (Fig. 1D-I; Suppl. Fig. 1A-F), which strengthens the hypothesis of the CP being the cellular origin. To compare this finding to other cerebellar tumors, we investigated 100 MB, with 25 each of MB-SHH, MB-WNT, MB-G3, and MB-G4 for the occurrence of CP. 16% of the examined MB-WNT (n = 4/25) and MB-G4 (n = 4/25), as well as 4% of the MB-G3 (n = 1/25) showed CP, but none of these tumors was intermingled with the CP tissue (Suppl. Table 1; Suppl. Fig. 2A-C). In addition, papillary structures, similar to CP, were observed in 77% of the investigated AT/RT-TYR (n = 24/31; Suppl. Table 1; Suppl. Fig. 1G-L). This similarity of the AT/RT tumor cells to CP was further investigated using IHC of CP markers. Three characteristic marker genes FOXJ1, involved in ciliogenesis[45], OTX2, a key regulator of embryonic stem cell differentiation[46], and KIR7.1, a marker for CP epithelial cells[47], were selected. We observed FOXJ1 expression in all AT/RT-TYR cases (n = 9/9), as well as in one AT/RT-SHH case (n = 1/5; Fig. 1J-N). OTX2 expression was exclusively observed in AT/RT-TYR (n = 4/9; Fig. 1O-S). In addition, 17 of 26 AT/RT-TYR were positive for KIR7.1, whereas only two out of 27 AT/RT-SHH showed KIR7.1 positivity (Fig. 1T-X). No AT/RT-MYC case was positive for any of these markers. Overall, we observed predominant expression of the CP markers FOXJ1, OTX2, and KIR7.1 in AT/RT-TYR using IHC.

Transcriptomic analysis of a variety of CNS tumors revealed increased expression of CP marker genes in AT/RT-TYR

We investigated the expression of CP marker genes over several CNS tumor entities using bulk RNAseq data. Differential gene expression analysis was performed with *DESeq2*, and the *DESeq2*-normalized expression of the three aforementioned CP marker genes, *FOXJ1*, *OTX2*, and *KIR7.1* was compared between the different CNS tumor entities, or rather DNA methylation

subtypes. CPC are known to originate from the CP, and therefore showed a high expression of these marker genes as expected (Fig. 2A-C). *FOXJ1* expression was upregulated in AT/RT-TYR compared to AT/RT-SHH (p = 0.026) and most of the other entities. *FOXJ1*, a marker for ciliogenesis, was also upregulated in the ependymoma (EPN) subtypes EPN-RELA and EPN-YAP, which arise from ciliated ependymal cells[48,49] (Fig. 2A). *OTX2* was upregulated in AT/RT-TYR compared to both AT/RT-SHH (p = 0.0011) and AT/RT-MYC (p = 0.0003). High expression was also observed in the MB subtypes MB-WNT, MB-G3, and MB-G4, previously described in the literature[50]. Significantly lower *OTX2* expression was detected in all other CNS tumor entities (Fig. 2B). In addition, *KIR7.1* was significantly upregulated in AT/RT-TYR compared to AT/RT-SHH (p = 0.0036), AT/RT-MYC (p = 0.0004), and the other CNS tumor entities (Fig. 2C). To compare the expression of a larger number of CP marker genes, differentially expressed genes between AT/RT-TYR vs. AT/RT-SHH and AT/RT-MYC were identified, resulting in an overexpression of the most characteristic hindbrain CP marker genes *FOXJ1*, *OTX2*, *KIR7.1*, *CYB5R2*, *PPM1B*, *LMX1A*, *TTR*, *TRPM3*, *MITF*, and *ENPP2*[51] in AT/RT-TYR (Fig. 2D). These observations confirmed the similarity of AT/RT-TYR to CP on the gene expression level. Furthermore, the similarity of the different AT/RT DNA methylation subtypes to cell types of the developing human cerebellum was investigated using *CIBERSORT* analysis. As a technical control, bulk RNAseq data of CPC and MPE were integrated, resulting in the highest *CIBERSORT* scores for their cellular origins, CP and ependymal cells. For AT/RT-SHH and AT/RT-MYC, no clear match was detected, but for AT/RT-TYR, the highest score was calculated for the CP, which confirmed the similarity to the CP on the gene expression level (Fig. 2E, Suppl. Fig. 3A).

CP cells were identified in snRNAseq data of AT/RT-TYR, showing high transcriptomic similarity to the tumor cells

SnRNAseq data of five AT/RT-TYR cases, two AT/RT-MYC cases, and one AT/RT-SHH case were generated and integrated using *SCT*-normalization. These were visualized in a UMAP for dimension reduction (n = 14,759 cells), resulting in distinct clusters for the tumor cells (n = 9 clusters) and the TME (n = 7 clusters; Fig. 3A-B). The TME was characterized by clusters of cells from all samples, and respective cell types were identified based on canonical marker expression (Fig. 3A-B). Gene expression of markers for healthy CP tissue, *TTR* and *FOLR1*, was investigated using *FeaturePlots*, resulting in one cluster showing high expression of respective genes, comprised of cells of four different AT/RT-TYR samples (n = 42; Fig. 3B-D). Other CP marker genes that are also known to be expressed in tumor cells of CPC, among others, showed similar gene expression over the AT/RT-TYR tumor cells and probably healthy CP cells (Suppl. Fig. 3C-F). To confirm that these are healthy CP cells and not AT/RT-TYR

tumor cells, the chromosome 22 status was investigated using *inferCNV*. *SMARCB1* is located on chromosome 22, and AT/RT-TYR are characterized by monosomy of chromosome 22 and AT/RT-MYC by broad deletions of chromosome 22, which could both be visualized using *inferCNV*. This analysis demonstrated a chromosome 22 loss in all AT/RT-TYR and AT/RT-MYC tumor cells. The cells showing strong expression of *TTR* and *FOLR1* demonstrated a retained chromosome 22 status, confirming that these are indeed healthy CP cells (Fig. 3E). The healthy CP cells showed proximity to the AT/RT-TYR tumor cells in the UMAP, indicating similar gene expression profiles. In addition, *CIBERSORT* analysis was repeated by using pseudobulk data of the AT/RT tumor cells for each DNA methylation subtype after excluding the TME. *CIBERSORT* analysis did not result in a clear match for AT/RT-SHH and AT/RT-MYC, but the similarity score for AT/RT-TYR to CP was increased compared to Figure 2E (Suppl. Fig. 3B).

Foxj1-cre::Smarcb1$^{fl/fl}$ mice demonstrated an abnormal CP of the fourth ventricle with a similar gene expression profile to human AT/RT-TYR

As no previously generated mouse model for AT/RT targets the fourth ventricle CP (Suppl. Table 3, Suppl. Fig. 4A-E), we aimed to generate a model that induces an early Smarcb1 loss in these cells. At first, we generated *Foxj1-cre::lsl-R26tdRFP$^{fl/wt}$* mice to investigate the Foxj1 expression at different time points. The first histological examination was possible at E10.5, which demonstrated an RFP signal in plexus precursor cells of the rhombomeres r1R (Fig. 4A). At P30, the majority of the CP cells of the fourth ventricle were positive for RFP (Fig. 4B), as well as the ependymal cells lining the ventricle (Fig. 4B, Suppl. Fig. 5D). This was exclusive for the CP and ependymal cells. Afterwards, we generated *Foxj1-cre::Smarcb1$^{fl/fl}$* mice (Fig. 4C), which were born with an expected Mendelian ratio (Fig. 4D). These mice did not develop any neurological symptoms over six months (n = 10). Three mice were sacrificed after 30 days for histopathological examinations of the CP of the fourth ventricle (Fig. 4E). Sagittal sections of the brains were used for H&E stainings and IHC stainings of SMARCB1, OTX2, and ARL13B (Fig. 4F-M). The CP of control mice demonstrated a characteristic cobblestone-like arrangement of the cells (Fig. 4F), as well as SMARCB1 and OTX2 expression in all cells (Fig. 4G-H). Multiciliated CP and ependymal cells were visualized by ARL13B stainings (Fig. 4I). In contrast, mutant mice demonstrated a loss of architecture (Fig. 4J) and a SMARCB1 loss in the majority of the CP cells (Fig. 4K). OTX2 expression was similar compared to the control mice (Fig. 4L). ARL13B stainings revealed that CP cells were monociliary as opposed to control mice, whereas ependymal cells remained multiciliary (Fig. 4M, Suppl. Fig. 5D-H). Human AT/RT-TYR were included for comparison of the IHC. These demonstrated papillary tumor regions (Fig. 4N, Suppl. Fig. 1G, H, J, K), characterized by SMARCB1 loss and OTX2

expression (Fig. 4O-P, Suppl. Fig. 1I, L), similar to the murine CP. In addition, AT/RT-TYR tumor cells were monociliary (Fig. 4Q), as were CP cells of the mutant mice. The loss of the cobblestone-like CP architecture was further investigated in *Foxj1-cre::Smarcb1$^{fl/fl}$* mice. Not only did the arrangement of the cells differ compared to the control mice, but also the CP nuclei demonstrated an altered phenotype (Fig. 4R-S). On the one hand, the nuclei were larger compared to the control CP ($p = 0.036$; Fig. 4T). On the other hand, the nuclei were characterized by unequally distributed chromatin, demonstrating a higher number of nuclei containing eccentric chromatin ($p = 0.025$; Fig. 4U). The arrangement of the nuclei was also evaluated by quantifying the nuclei in a row as a feature of the cobblestone-like pattern of the CP. The proportion of nuclei in a row was decreased in the mutant CP ($p = 0.046$, Fig. 4V). This above-described phenotype was exclusive to the nuclei of the fourth ventricle CP. In the third ventricle CP, Smarcb1 loss only occurred in a few cells (Suppl. Fig. 5A-C), and the nuclei of the ependyma did not show any morphological alterations (Suppl. Fig. 5D-I). Next, a cross-species analysis was performed to compare the CP of *Foxj1-cre::Smarcb1$^{fl/fl}$* mice to different human CNS tumor entities. Control and mutant CP demonstrated distinct gene expression profiles as visualized in a Volcano Plot showing differentially expressed genes. Among others, genes of the Wnt signaling pathway were upregulated in mutant CP (Suppl. Fig. 5J). Afterwards, the data were integrated with transcriptomic data of human CNS tumors and of murine MB-SHH from *Math1-cre::Smo$^{fl/wt}$* mice. The 1,000 most variable genes between all samples were visualized in a heatmap. Murine MB-SHH clustered together with human MB-SHH, which served as technical control for these analyses. The CP of *Foxj1-cre::Smarcb1$^{fl/fl}$* mice clustered together with human AT/RT-TYR, which confirmed the similarity of the mutant CP to human AT/RT-TYR on the gene expression level (Fig. 4W, Suppl. Fig. 5K). As these mice did not develop any tumors, a second genetic alteration was introduced. As no further recurrent mutations than *SMARCB1* or *SMARCA4* are known in human AT/RT, we additionally overexpressed *Lin28a* in our mouse model, because previously, 23% of all investigated human AT/RT showed immunopositivity for LIN28A[26]. Therefore, we generated *Foxj1-cre::lsl-Lin28a::Smarcb1$^{fl/fl}$* mice (Suppl. Fig. 6A-C), which did not develop any neurological symptoms over six months either ($n = 3$). Histological examination at P30 revealed a similar phenotype compared to *Foxj1-cre::Smarcb1$^{fl/fl}$* mice (Suppl. Fig. 6D-K).

Discussion

This study demonstrated that precursors of the fourth ventricle CP should be considered as the cellular origin of infratentorial AT/RT-TYR. Not only proximity of these tumors to the CP was observed, in addition, we identified CP signatures at the histopathological and gene expression levels. Murine fourth ventricle CP with early induced Smarcb1 loss demonstrated morphological and transcriptomic similarities to human AT/RT-TYR.

At first, we want to highlight that the predominant occurrence of intermingled CP tissue in AT/RT-TYR was not only coming from the localization of these tumors in proximity to the fourth ventricle CP. We clearly saw that CP tissue was not only present at AT/RT-TYR biopsies, it appeared like there was a transition from the healthy CP (SMARCB1 retained) to the tumor (SMARCB1 lost). This was not the case for other cerebellar tumors like MB, where a clear separation between CP and tumor was observed at examined biopsies. This strengthens our hypothesis that infratentorial AT/RT-TYR originate and arise from the CP of the fourth ventricle.

Another underpinning was the upregulation of CP marker genes compared to the other DNA methylation subtypes and other CNS tumor entities. Using snRNAseq data, we identified a cluster of healthy CP cells that only consists of cells from AT/RT-TYR samples, which is in line with the predominance of CP at biopsies in AT/RT-TYR. These cells clustered right next to the AT/RT-TYR tumor cells with no clear separation in a UMAP, which demonstrated high similarity on the gene expression level. *CIBERSORT* analyses supported our suggestion by resulting in the highest similarity of AT/RT-TYR for CP. These analyses have not resulted in a clear match for AT/RT-SHH and AT/RT-MYC. This is probably due to the fact that the cell of origin is not included in the data set of the developing cerebellum. AT/RT-MYC and AT/RT-SHH are mostly located supratentorial. AT/RT-MYC can also occur in the spinal cord, and therefore, no cerebellar precursors are expected as cellular origins. For AT/RT-MYC, an extra-CNS origin is assumed, with the neural crest being involved in the development of these tumors[12,52–54]. AT/RT-SHH are assumed to arise from neural progenitors, more precisely from the midbrain-hindbrain boundary or the ganglionic eminence, depending on the localization of these tumors[12,55]. By using a murine data set[22] as a reference, no clear match was observed either. In addition, the scores of AT/RT-TYR and CPC for the CP were lower. This is probably due to the species differences resulting from using a murine reference data set. Furthermore, this data set only includes data from the forebrain and pons, and therefore, cerebellar cell types are lacking. The CP in this data set is derived from the third and lateral ventricles, which exhibits transcriptomic differences compared to the fourth ventricle CP.

So far, no genetically engineered mouse model for AT/RT-TYR exists, which could give insights into the cellular origins of these tumors. Probably, the cell of origin was not targeted by previous mouse models. *Math1-cre::Smarcb1$^{fl/fl}$*, *Nestin-cre::Smarcb1$^{fl/fl}$*, *Rosa-cre^{ERT2}::Smarcb1$^{fl/fl}$*, and *Sox2-cre^{ERT2}::Smarcb1$^{fl/fl}$* mice have not targeted the fourth ventricle

CP at all. *Olig1-cre::Smarcb1$^{fl/fl}$* mice induced a Smarcb1 loss in a few cells, but according to the Allen Developing Mouse Brain Atlas (https://developingmouse.brain-map.org), Olig1 shows patchy expression starting at E13.5 in the fourth ventricle CP, which is later compared to Foxj1. We assume that a Smarcb1 loss is much too late at this time point for development of AT/RT-TYR. Next to AT/RT-SMARCA4, AT/RT-TYR patients are the youngest, and therefore, it is assumed that tumors develop early during embryonal development. For this reason, an early embryonal loss of Smarcb1 is required in mice, which is the case for *Foxj1-cre*. Nevertheless, *Foxj1-cre::Smarcb1$^{fl/fl}$* mice did not develop any tumors, which leads to the conclusion that a second genetic alteration is required for tumor development. This is not the case for human AT/RT-TYR, because there are no further recurrent alterations other than *SMARCB1* mutations[56]. Several studies of other CNS tumor entities have shown that a second genetic alteration is necessary in mice, which is lacking in the human tumors. For example, an astrocytoma mouse model required an *Nf1* mutation in addition to *Tp53*[57]. This is even known for an AT/RT mouse model, which was characterized by a Tp53 loss in addition to Smarcb1. These *GFAP-cre::Smarcb1$^{fl/fl}$::p53$^{fl/fl}$* mice developed cerebellar tumors after five months, but the fourth ventricle CP was not targeted by *GFAP-cre*[58]. In addition, *Smarcb1$^{+/-}$::p53$^{+/-}$* mice developed malignant rhabdoid tumors (MRT)[59]. Here, we induced an additional Lin28a overexpression, which was also not sufficient to generate murine tumors. Although we see LIN28A overexpression in human AT/RT, it was not described that LIN28A has driver functions in these tumors, and therefore, another tumorigenesis-associated genetic alteration should be induced in future experiments.

Foxj1-cre::Smarcb1$^{fl/fl}$ mice demonstrated a Smarcb1 loss in the majority of the fourth ventricle CP cells, but in the supratentorial third ventricle CP, only a few cells demonstrated a Smarcb1 loss. This matches previous observations that demonstrated a patchy *Foxj1-cre* expression in the third ventricle CP, whereas the fourth and lateral ventricles showed widespread expression[60]. Hence, we did not observe morphological differences between the control and mutant CP of the third ventricle.

As one observed morphological difference between control and mutant CP of the fourth ventricle, mutant CP cells were monociliary. Monocilia are also known as primary cilia[61], and these were previously found in the context of AT/RT. Several studies showed that primary cilia were enriched in AT/RT-TYR[8,62], which we confirmed by ARL13B IHC. Additionally, the occurrence of monocilia was associated with enhanced aggressiveness of AT/RT[62]. This finding shows that monocilia are an important feature of AT/RT-TYR, which we recapitulated in our mouse model, which again confirms the similarity to AT/RT-TYR. Mao et al. showed that *Foxj1* expression highly influences the CP cilia[63], and by using *Foxj1-cre* mice, the CP cilia were specifically targeted, which explains the morphological changes.

But not only the CP cilia were altered, additionally, the fourth ventricle CP nuclei of *Foxj1-cre::Smarcb1$^{fl/fl}$* mice demonstrated morphological differences. One observation was that the chromatin was not equally distributed and appeared as eccentric chromatin. This phenotype is known for euchromatin that is characterized by open, unfolded chromatin, which allows active transcription[64]. This could be due to the Smarcb1 loss which might disrupt the normal function of the SWI/SNF complex, which is responsible for the chromatin accessibility. We hypothesize that not only the Smarcb1 loss led to the euchromatic structure, in addition, activated Wnt signaling might have an influence on this phenotype. Johann et al. previously reported the Wnt signaling pathway as one of the top upregulated pathways in AT/RT-TYR[8]. Furthermore, we observed that genes of the Wnt signaling pathway were upregulated in *Foxj1-cre::Smarcb1$^{fl/fl}$* mice compared to the control. This leads to the conclusion that Wnt signaling plays a role in AT/RT-TYR as well as in our mouse model. The Wnt signaling pathway was previously associated with changes in the chromatin structure, which was shown by Assays for Transposase-Accessible Chromatin sequencing (ATACseq) and RNAseq experiments[65]. It has been shown that active Wnt signaling led to the opening of the chromatin, which resulted in an euchromatic phenotype[66,67].

In conclusion, we identified and characterized CP signatures in AT/RT-TYR at histopathological and gene expression levels. These CP signatures were significantly enriched in AT/RT-TYR compared to the other DNA methylation subtypes and other CNS tumor entities. For an AT/RT-TYR mouse model, we generated *Foxj1-cre::Smarcb1$^{fl/fl}$* mice, which did not develop tumors, but demonstrated large, atypical CP nuclei. The CP cells were monociliary as human AT/RT-TYR and they showed similar gene expression profiles compared to human AT/RT-TYR. Overall, we assume that a second genetic alteration in fourth ventricle CP precursors is required in addition to a *Smarcb1* loss.

Required statements

Ethics

All animal experiments were approved by the Government of Hamburg, Germany (N099/2019 and N015/2025).

Funding

This study was supported by the Deutsche Forschungsgemeinschaft (FR 1516/4-1). US was further supported by the Fördergemeinschaft Kinderkrebszentrum Hamburg. LA received a fellowship from the Burkhard Meyer Stiftung. KK received funding from the Deutsche Forschungsgemeinschaft (KE 2004/4-1; KE 2004/11-1).

Conflict of Interest

None.

Authorship

LA and US designed the study. Material collection for H&E and IHC examinations was performed by MD, MH, and US. KIR7.1 IHC was done by MH. SnRNAseq data were generated by RR and KK. Data analysis was performed by LA. MJH contributed the *Foxj1-cre* mice. Animal experiments were also performed by LA. LSP, KH, MD, and MS supported the animal experiments. ST performed the investigation of the medulloblastoma samples. The manuscript was written by LA. The figures were designed by LA. All authors contributed to the revision of the manuscript.

References

1. Bachu VS, Shah P, Jimenez AE, et al. Clinical predictors of survival for patients with atypical teratoid/rhabdoid tumors. *Child's Nerv Syst*. 2022;38(7):1297-1306. doi:10.1007/s00381-022-05511-w

2. Dufour C, Beaugrand A, Le Deley MC, et al. Clinicopathologic prognostic factors in childhood atypical teratoid and rhabdoid tumor of the central nervous system: A multicenter study. *Cancer*. 2012;118(15):3812-3821. doi:10.1002/cncr.26684

3. Ostrom QT, Chen Y, De Blank PM, et al. The descriptive epidemiology of atypical teratoid/rhabdoid tumors in the United States, 2001-2010. *Neuro Oncol*. 2014;16(10):1392-1399. doi:10.1093/neuonc/nou090

4. Frühwald MC, Hasselblatt M, Nemes K, et al. Age and DNA methylation subgroup as potential independent risk factors for treatment stratification in children with atypical teratoid/rhabdoid tumors. *Neuro Oncol*. 2020;22(7):1006-1017. doi:10.1093/neuonc/noz244

5. Upadhyaya SA, Robinson GW, Onar-Thomas A, et al. Relevance of molecular groups in children with newly diagnosed atypical teratoid rhabdoid tumor: Results from prospective St. Jude multi-institutional trials. *Clin Cancer Res*. 2021;27(10):2879-2889. doi:10.1158/1078-0432.CCR-20-4731

6. Ho B, Johann PD, Grabovska Y, et al. Molecular subgrouping of atypical teratoid/rhabdoid tumors - A reinvestigation and current consensus. *Neuro Oncol*. 2020;22(5):613-624. doi:10.1093/neuonc/noz235

7. Torchia J, Golbourn B, Feng S, et al. Integrated (epi)-Genomic Analyses Identify Subgroup-Specific Therapeutic Targets in CNS Rhabdoid Tumors. *Cancer Cell*. 2016;30(6):891-908. doi:10.1016/j.ccell.2016.11.003

8. Johann PD, Erkek S, Zapatka M, et al. Atypical Teratoid/Rhabdoid Tumors Are Comprised of Three Epigenetic Subgroups with Distinct Enhancer Landscapes. *Cancer Cell*. 2016;29(3):379-393. doi:10.1016/j.ccell.2016.02.001

9. Holdhof D, Johann PD, Spohn M, et al. Atypical teratoid/rhabdoid tumors (ATRTs) with SMARCA4 mutation are molecularly distinct from SMARCB1-deficient cases. *Acta Neuropathol*. 2020;141(2):291-301. doi:10.1007/s00401-020-02250-7

10. Schneppenheim R, Frühwald MC, Gesk S, et al. Germline Nonsense Mutation and Somatic Inactivation of SMARCA4/BRG1 in a Family with Rhabdoid Tumor Predisposition Syndrome. *Am J Hum Genet*. 2010;86(2):279-284. doi:10.1016/j.ajhg.2010.01.013

11. Wilson BG, Roberts CWM. SWI/SNF nucleosome remodellers and cancer. *Nat Rev Cancer*. 2011;11(7):481-492. doi:10.1038/nrc3068

12. Graf M, Interlandi M, Moreno N, et al. Single-cell transcriptomics identifies potential cells of origin of MYC rhabdoid tumors. *Nat Commun*. 2022;13(1). doi:10.1038/s41467-022-29152-4

13. Han ZY, Richer W, Fréneaux P, et al. The occurrence of intracranial rhabdoid tumours in mice depends on temporal control of Smarcb1 inactivation. *Nat Commun*. 2016;7. doi:10.1038/ncomms10421

14. Biegel JA, Zhou JY, Rorke LB, Stenstrom C, Wainwright LM, Fogelgren B. Germ-line and acquired mutations of INI1 in atypical teratoid and rhabdoid tumors. *Cancer Res*. 1999;59(1):74-79.

15. Sredni ST, Tomita T. Rhabdoid tumor predisposition syndrome. *Pediatr Dev Pathol*. 2015;18(1):49-58. doi:10.2350/14-07-1531-MISC.1

16. Nowak J, Nemes K, Hohm A, et al. Magnetic resonance imaging surrogates of molecular subgroups in atypical teratoid/rhabdoid tumor. *Neuro Oncol*. 2018;20(12):1672-1679. doi:10.1093/neuonc/noy111

17. Johann PD, Altendorf L, Efremova EM, et al. Recurrent atypical teratoid/rhabdoid tumors (AT/RT) reveal discrete features of progression on histology, epigenetics, copy number profiling, and transcriptomics. *Acta Neuropathol*. 2023;146(3):527-541. doi:10.1007/s00401-023-02608-7

18. Sturm D, Orr BA, Toprak UH, et al. New Brain Tumor Entities Emerge from Molecular Classification of CNS-PNETs. *Cell*. 2016;164(5):1060-1072. doi:10.1016/j.cell.2016.01.015

19. Thomas C, Soschinski P, Zwaig M, et al. The genetic landscape of choroid plexus tumors in children and adults. *Neuro Oncol*. 2021;23(4):650-660. doi:10.1093/neuonc/noaa267

20. Bockmayr M, Harnisch K, Pohl LC, et al. Comprehensive profiling of myxopapillary p y yp with relapsing disease. *Neuro Oncol*. 2022;24(10):1689-1699. doi:10.1093/neuonc/noac088

21. Aldinger KA, Thomson Z, Phelps IG, et al. Spatial and cell type transcriptional landscape of human cerebellar development. *Nat Neurosci*. 2021;24(8):1163-1175. doi:10.1038/s41593-021-00872-y

22. Jessa S, Blanchet-Cohen A, Krug B, et al. Stalled developmental programs at the root of pediatric brain tumors. *Nat Genet*. 2019;51(12):1702-1713. doi:10.1038/s41588-019-0531-7

23. Zhang Y, Huang G, Shornick LP, et al. A transgenic FOXJ1-Cre system for gene inactivation in ciliated epithelial cells. *Am J Respir Cell Mol Biol*. 2007;36(5):515-519. doi:10.1165/rcmb.2006-0475RC

24. Roberts CWM, Leroux MM, Fleming MD, Orkin SH. Highly penetrant, rapid tumorigenesis through conditional inversion of the tumor suppressor gene Snf5. *Cancer Cell*. 2002;2(5):415-425. doi:10.1016/S1535-6108(02)00185-X

25. Peng S, Chen LL, Lei XX, et al. Genome-Wide Studies Reveal That Lin28 Enhances the Translation of Genes Important for Growth and Survival of Human Embryonic Stem Cells. *Stem Cells*. 2011;29(3):496-504. doi:10.1002/stem.591

26. Rao S, Rajeswarie RT, Chickabasaviah Yasha T, Nandeesh BN, Arivazhagan A, Santosh V. LIN28A, a sensitive immunohistochemical marker for Embryonal Tumor with Multilayered Rosettes (ETMR), is also positive in a subset of Atypical Teratoid/Rhabdoid Tumor (AT/RT). *Child's Nervous System*. 2017;33(11):1953-1959. doi:10.1007/s00381-017-3551-6

27. Luche H, Weber O, Nageswara Rao T, Blum C, Fehling HJ. Faithful activation of an extra-bright red fluorescent protein in "knock-in" Cre-reporter mice ideally suited for lineage tracing studies. *Eur J Immunol*. 2007;37(1):43-53. doi:10.1002/eji.200636745

28. Nakamura N, Suzuki Y, Sakuta H, Ookata K, Kawahara K, Hirose S. Inwardly rectifying K+ channel Kir7.1 is highly expressed in thyroid follicular cells, intestinal epithelial cells and choroid plexus epithelial cells : implication for a functional coupling with Na+,K+-ATPase. *Biochem J*. 1999;342:329-336.

29. Killion CH, Mitchell EH, Duke CG, Serra R. Mechanical loading regulates organization of the actin cytoskeleton and column formation in postnatal growth plate. *Mol Biol Cell*. 2017;28(14):1862-1870. doi:10.1091/mbc.E17-02-0084

30. Jiang H, Lei R, Ding SW, Zhu S. Skewer: a fast and accurate adapter trimmer for next-generation sequencing paired-end reads. *BMC Bioinformatics*. 2014;15:182. http://www.biomedcentral.com/1471-2105/15/182

31. Dobin A, Davis CA, Schlesinger F, et al. STAR: Ultrafast universal RNA-seq aligner. *Bioinformatics*. 2013;29(1):15-21. doi:10.1093/bioinformatics/bts635

32. Durinck S, Spellman PT, Birney E, Huber W. Mapping identifiers for the integration of genomic datasets with the R/ Bioconductor package biomaRt. *Nat Protoc*. 2009;4(8):1184-1191. doi:10.1038/nprot.2009.97

33. Krijthe JH. Rtsne: T-Distributed Stochastic Neighbor Embedding using Barnes-Hut Implementation. Published online 2015. doi:https://github.com/jkrijthe/Rtsne

34. Love MI, Huber W, Anders S. Moderated estimation of fold change and dispersion for RNA-seq data with DESeq2. *Genome Biol*. 2014;15(12):1-21. doi:10.1186/s13059-014-0550-8

35. Ritchie ME, Phipson B, Wu D, et al. Limma powers differential expression analyses for RNA-sequencing and microarray studies. *Nucleic Acids Res*. 2015;43(7):e47. doi:10.1093/nar/gkv007

36. Wickham H. ggplot2: Elegant Graphics for Data Analysis. Published online 2016. doi:10.1007/978-3-319-24277-4_9

37. Blighe K, Rana S, Lewis M. EnhancedVolcano: Publication-ready volcano plots with enhanced colouring and labeling. Published online 2025. doi:10.18129/B9.bioc.EnhancedVolcano

38. Schüller U, Heine VM, Mao J, et al. Acquisition of Granule Neuron Precursor Identity Is a Critical Determinant of Progenitor Cell Competence to Form Shh-Induced Medulloblastoma. *Cancer Cell*. 2008;14(2):123-134. doi:10.1016/j.ccr.2008.07.005

39. Gu Z. Complex heatmap visualization. *iMeta*. 2022;1(3). doi:10.1002/imt2.43

40. Hao Y, Hao S, Andersen-Nissen E, et al. Integrated analysis of multimodal single-cell data. *Cell*. 2021;184(13):3573-3587.e29. doi:10.1016/j.cell.2021.04.048

41. Newman AM, Liu CL, Green MR, et al. Robust enumeration of cell subsets from tissue expression profiles. *Nat Methods*. 2015;12(5):453-457. doi:10.1038/nmeth.3337

42. Aran D, Looney AP, Liu L, et al. Reference-based analysis of lung single-cell sequencing reveals a transitional profibrotic macrophage. *Nat Immunol*. 2019;20(2):163-172. doi:10.1038/s41590-018-0276-y

43. Martens JHA, Stunnenberg HG. BLUEPRINT: Mapping human blood cell epigenomes. *Haematologica*. 2013;98(10):1487-1489. doi:10.3324/haematol.2013.094243

44. Tickle T, Tirosh I, Georgescu C, Brown M, Haas B. inferCNV of the Trinity CTAT Project. Published online 2019. doi:https://github.com/broadinstitute/inferCNV

45. Zhang Y, Huang G, Shornick LP, et al. A Transgenic FOXJ1-Cre System for Gene Inactivation in Ciliated Epithelial Cells. *Am J Respir Cell Mol Biol*. 2007;36(5):515-519. doi:10.1165/rcmb.2006-0475RC

46. Prochiantz A, Di Nardo AA. Homeoprotein signaling in the developing and adult nervous system. *Neuron*. 2015;85(5):911-925. doi:10.1016/j.neuron.2015.01.019

47. Hasselblatt M, Böhm C, Tatenhorst L, et al. Identification of Novel Diagnostic Markers for Choroid Plexus Tumors. *Am J Surg Pathol*. 2006;30(1):66-74. doi:10.1097/01.pas.0000176430.88702.e0

48. Servidei T, Lucchetti D, Navarra P, Sgambato A, Riccardi R, Ruggiero A. Cell-of-Origin and Genetic, Epigenetic, and Microenvironmental Factors Contribute to the Intra-Tumoral Heterogeneity of Pediatric Intracranial Ependymoma. *Cancers (Basel)*. 2021;13(23):6100. doi:10.3390/cancers13236100

49. Poppleton H, Gilbertson RJ. Stem cells of ependymoma. *Br J Cancer*. 2007;96(1):6-10. doi:10.1038/sj.bjc.6603519

50. Adamson DC, Shi Q, Wortham M, et al. OTX2 Is Critical for the Maintenance and Progression of Shh-Independent Medulloblastomas. *Cancer Res*. 2010;70(1):181-191. doi:10.1158/0008-5472.CAN-09-2331

51. Dani N, Herbst RH, McCabe C, et al. A cellular and spatial map of the choroid plexus across brain ventricles and ages. *Cell*. 2021;184(11):3056-3074.e21. doi:10.1016/j.cell.2021.04.003

52. Huhtala L, Karabiyik G, Rautajoki KJ. Development and epigenetic regulation of Atypical teratoid/rhabdoid tumors in the context of cell-of-origin and halted cell differentiation. *Neurooncol Adv*. 2024;6(1):vdae162. doi:10.1093/noajnl/vdae162

53. Custers L, Khabirova E, Coorens THH, et al. Somatic mutations and single-cell transcriptomes reveal the root of malignant rhabdoid tumours. *Nat Commun*. 2021;12(1):1-11. doi:10.1038/s41467-021-21675-6

54. Vitte J, Gao F, Coppola G, Judkins AR, Giovannini M. Timing of Smarcb1 and Nf2 inactivation determines schwannoma versus rhabdoid tumor development. *Nat Commun*. 2017;8(1):1-12. doi:10.1038/s41467-017-00346-5

55. Lobón-Iglesias MJ, Andrianteranagna M, Han ZY, et al. Imaging and multi-omics datasets converge to define different neural progenitor origins for ATRT-SHH subgroups. *Nat Commun*. 2023;14(1). doi:10.1038/s41467-023-42371-7

56. Hasselblatt M, Isken S, Linge A, et al. High-resolution genomic analysis suggests the absence of recurrent genomic alterations other than SMARCB1 aberrations in atypical teratoid/rhabdoid tumors. *Genes Chromosomes Cancer*. 2013;52(2):185-190. doi:10.1002/gcc.22018

57. Zhu Y, Guignard F, Zhao D, et al. Early inactivation of p53 tumor suppressor gene cooperating with NF1 loss induces malignant astrocytoma. *Cancer Cell*. 2005;8(2):119-130. doi:10.1016/j.ccr.2005.07.004

58. Ng JMY, Martinez D, Marsh ED, et al. Generation of a mouse model of atypical teratoid/rhabdoid tumor of the central nervous system through combined deletion of Snf5 and p53. *Cancer Res*. 2015;75(21):4629-4639. doi:10.1158/0008-5472.CAN-15-0874

59. DelBove J, Kuwahara Y, Mora-Blanco EL, et al. Inactivation of SNF5 cooperates with p53 loss to accelerate tumor formation in Snf5(+/-);p53(+/-) mice. *Mol Carcinog*. 2009;48(12):1139-1148. doi:10.1002/mc.20568

60. Lobas MA, Helsper L, Vernon CG, et al. Molecular heterogeneity in the choroid plexus epithelium: the 22-member γ-protocadherin family is differentially expressed, apically localized, and implicated in CSF regulation. *J Neurochem*. 2012;120(6):913-927. doi:10.1111/j.1471-4159.2011.07587.x

61. Barsch F, Niedermair T, Mamilos A, et al. Physiological and Pathophysiological Aspects of Primary Cilia-A Literature Review with View on Functional and Structural Relationships in Cartilage. *Int J Mol Sci*. 2020;21(14). doi:10.3390/ijms21144959

62. Blümel L, Qin N, Berlandi J, et al. Primary cilia contribute to the aggressiveness of atypical teratoid/rhabdoid tumors. *Cell Death Dis*. 2022;13(9):806. doi:10.1038/s41419-022-05243-4

63. Mao S, Song R, Jin S, et al. Multicilia dynamically transduce Sonic Hedgehog signaling to regulate choroid plexus functions. *Cell Rep*. 2025;44(3). doi:10.1016/j.celrep.2025.115383

64. Morrison O, Thakur J. Molecular Complexes at Euchromatin, Heterochromatin and Centromeric Chromatin. *Int J Mol Sci*. 2021;22(13):6922. doi:10.3390/ijms22136922

65. Pagella P, Söderholm S, Nordin A, et al. The time-resolved genomic impact of Wnt/β-catenin signaling. *Cell Syst*. 2023;14(7):563-581.e7. doi:10.1016/j.cels.2023.06.004

66. Matoba N, Le BD, Valone JM, et al. Wnt activity reveals context-specific genetic effects on gene regulation in neural progenitors. *bioRxiv* . Published online February 7, 2023. doi:10.1101/2023.02.07.527357

67. Nordin A, Chakraborty C, Jonasson M, et al. Wnt signaling alters CTCF binding patterns and global chromatin structure. *bioRxiv*. Published online January 22, 2024. doi:10.1101/2024.01.22.576696

Figure Legends

Figure 1: Histological examination of AT/RT for the occurrence of CP signatures. A: Investigation of 31 H&E stainings of infratentorial AT/RT-TYR revealed intermingled CP tissue for 35% of the cases (n = 11). **B:** Investigation of 13 H&E stainings of infratentorial AT/RT-SHH revealed an absence of CP tissue for all cases. **C:** Investigation of nine H&E stainings of infratentorial AT/RT-MYC revealed intermingled CP tissue for 11% of the cases (n = 1). **D-I:** Exemplary H&E and SMARCB1 stainings of AT/RT-TYR biopsies intermingled with CP. Scale bars in D and G indicate 50 µm. Scale bars in E, F, H, and I indicate 10 µm. **J-M:** FOXJ1 IHC of an exemplary human CP (J), AT/RT-TYR (K), AT/RT-SHH (L), and AT/RT-MYC (M). Scale bars indicate 10 µm. **N:** Quantification of FOXJ1 IHC revealed 9/9 positive AT/RT-TYR cases, 1/5 AT/RT-SHH cases, and 0/6 AT/RT-MYC cases. **O-R:** OTX2 IHC of an exemplary human CP (O), AT/RT-TYR (P), AT/RT-SHH (Q), and AT/RT-MYC (R). Scale bars indicate 10 µm. **S:** Quantification of OTX2 IHC revealed 4/9 positive AT/RT-TYR cases, 0/5 AT/RT-SHH cases, and 0/6 AT/RT-MYC cases. **T-W:** KIR7.1 IHC of an exemplary human CP (T), AT/RT-TYR (U), AT/RT-SHH (V), and AT/RT-MYC (W). Scale bars indicate 10 µm. **X:** Quantification of KIR7.1 IHC revealed 17/26 positive AT/RT-TYR cases, 2/27 AT/RT-SHH cases, and 0/14 AT/RT-MYC cases.

Figure 2: CP gene signatures in bulk RNAseq data of AT/RT DNA methylation subtypes and different CNS tumors. A: Box plot showing the *DESeq2* normalized counts for *FOXJ1*. No significant difference between AT/RT-TYR and AT/RT-MYC (p = 0.13), but between AT/RT-TYR and AT/RT-SHH (p = 0.026) was observed. **B:** Box plot showing the *DESeq2* normalized counts for *OTX2*. Significant differences between AT/RT-TYR and AT/RT-MYC (p = 0.0003) and between AT/RT-TYR and AT/RT-SHH (p = 0.0011) were observed. **C:** Box plot showing the *DESeq2* normalized counts for *KIR7.1*. Significant differences between AT/RT-TYR and AT/RT-MYC (p = 0.0004) and between AT/RT-TYR and AT/RT-SHH (p = 0.0036) were observed. **D:** Volcano plot showing differentially expressed genes between AT/RT-TYR (n = 9) vs. AT/RT-MYC (n = 9) and AT/RT-SHH (n = 18). Hindbrain CP markers[51] were annotated, showing an overexpression in AT/RT-TYR. **E:** *CIBERSORT* analysis for bulk RNAseq data of AT/RT-TYR (n = 9), AT/RT-SHH (n = 18), AT/RT-MYC (n = 9), CPC (n = 5), and MPE (n = 37). Cerebellar cell types of Aldinger et al. (2021)[21] were used as an scRNAseq reference. The highest scores of AT/RT-TYR and CPC were calculated for CP, of MPE for ependymal cells, and for AT/RT-SHH and AT/RT-MYC no clear match was observed. GCP: Granule cell precursors; eCN: Excitatory cerebellar interneurons; UBC: Unipolar brush cells; OPC: Oligodendrocyte progenitor cells; prog.: Progenitors; Inh.: Inhibitory; Mol.: Molecular.

Figure 3: Identification of CP cells in snRNAseq data of AT/RT-TYR. A: UMAP using 10 neighboring points of *SCT*-normalized counts of all cells (n = 14,759), annotated by cell types. TME cells were annotated manually via canonical markers and automatically via *SingleR* using *ENCODE*. **B:** UMAP of all cells (n = 14,759), annotated by samples. **C:** FeaturePlot of all cells (n = 14,759), showing CP marker gene *TTR* expression. *TTR* was highly expressed in a cluster identified as CP (n = 42 cells). **D:** FeaturePlot of all cells (n = 14,759), showing CP marker gene *FOLR1* expression. *FOLR1* was highly expressed in a cluster identified as CP (n = 42 cells). **E:** UMAP of all cells (n = 14,759), annotated by chromosome 22 status, identified using *inferCNV*. Chromosome 22 was retained in the CP cluster. **F:** *CIBERSORT* analysis for snRNAseq data of AT/RT-SHH (n = 1), AT/RT-MYC (n = 2), and AT/RT-TYR (n = 5). Only tumor cells were used to generate pseudobulk data. Cerebellar cell types of Aldinger et al. (2021)[21] were used as an scRNAseq reference. The highest score of AT/RT-TYR was calculated for CP, and for AT/RT-SHH and AT/RT-MYC no clear match was observed. GCP: Granule cell precursors; eCN: Excitatory cerebellar interneurons; UBC: Unipolar brush cells; OPC: Oligodendrocyte progenitor cells; prog.: Progenitors; Inh.: Inhibitory; Mol.: Molecular.

Figure 4: Histological and molecular examination of murine *Foxj1-cre::Smarcb1$^{fl/fl}$* CP at P30. A: RFP IHC of the rhombomeres (CP progenitors), midbrain, and hindbrain of *Foxj1-cre::lsl-R26tdRFP$^{fl/wt}$* mice at E10.5. Scale bar indicates 20 µm. **B:** RFP IHC of the CP and hindbrain of *Foxj1-cre::lsl-R26tdRFP$^{fl/wt}$* mice at P30. Scale bar indicates 50 µm. **C:** Breeding scheme of crossing *Foxj1-cre* and *Smarcb1$^{fl/fl}$* mice for the generation of *Foxj1-cre::Smarcb1$^{fl/fl}$* mice. **D:** Bar plot showing no significant difference between the proportion of born mice for each genotype. 25% were expected for each genotype according to the Mendelian ratio. **E:** H&E of a sagittal brain section of a *Foxj1-cre::Smarcb1$^{fl/fl}$* mouse at P30. Scale bar indicates 2 µm. **F-I:** Exemplary H&E (F), SMARCB1 (G), OTX2 (H), and ARL13B (I) stainings of a fourth ventricle CP of a control mouse at P30. Scale bars indicate 20 µm. **J-M:** Exemplary H&E (J), SMARCB1 (K), OTX2 (L), and ARL13B (M) stainings of a fourth ventricle CP of a *Foxj1-cre::Smarcb1$^{fl/fl}$* mouse at P30. Scale bars indicate 20 µm. **N-Q:** Exemplary H&E (N), SMARCB1 (O), OTX2 (P), and ARL13B (Q) stainings of a human AT/RT-TYR. Scale bars indicate 20 µm. **R:** Zoom in of H&E staining of a control mouse CP (F). Scale bar indicates 20 µm. **S:** Zoom in of H&E staining of a *Foxj1-cre::Smarcb1$^{fl/fl}$* mouse CP (G). Scale bar indicates 20 µm. **T:** Box plot showing the average nuclei area for control (n = 3) and *Foxj1-cre::Smarcb1$^{fl/fl}$* mice (n = 3), resulting in a larger area for mutant mice (p = 0.036). **U:** Box plot showing the proportion of nuclei containing eccentric chromatin for control (n = 3) and *Foxj1-cre::Smarcb1$^{fl/fl}$* mice (n = 3), resulting in a higher proportion for mutant mice (p = 0.025). **V:** Box plot showing the proportion of nuclei in a row for control (n = 3) and *Foxj1-cre::Smarcb1$^{fl/fl}$* mice (n = 3), resulting in a decreased proportion for mutant mice (p = 0.046). **W:** Heatmap

showing the 1,000 most variable genes resulting from bulk RNAseq data of the CP from *Foxj1-cre::Smarcb1*$^{fl/fl}$ mice (murine mutant CP, n = 3), murine MB-SHH from *Math1-cre::Smo*$^{fl/wt}$ mice[38] (murine MB-SHH, n = 3), and a variety of human CNS tumors derived from Sturm et al. (2016)[18], Johann, Altendorf et al. (2023)[17], and Thomas et al. (2021)[19].

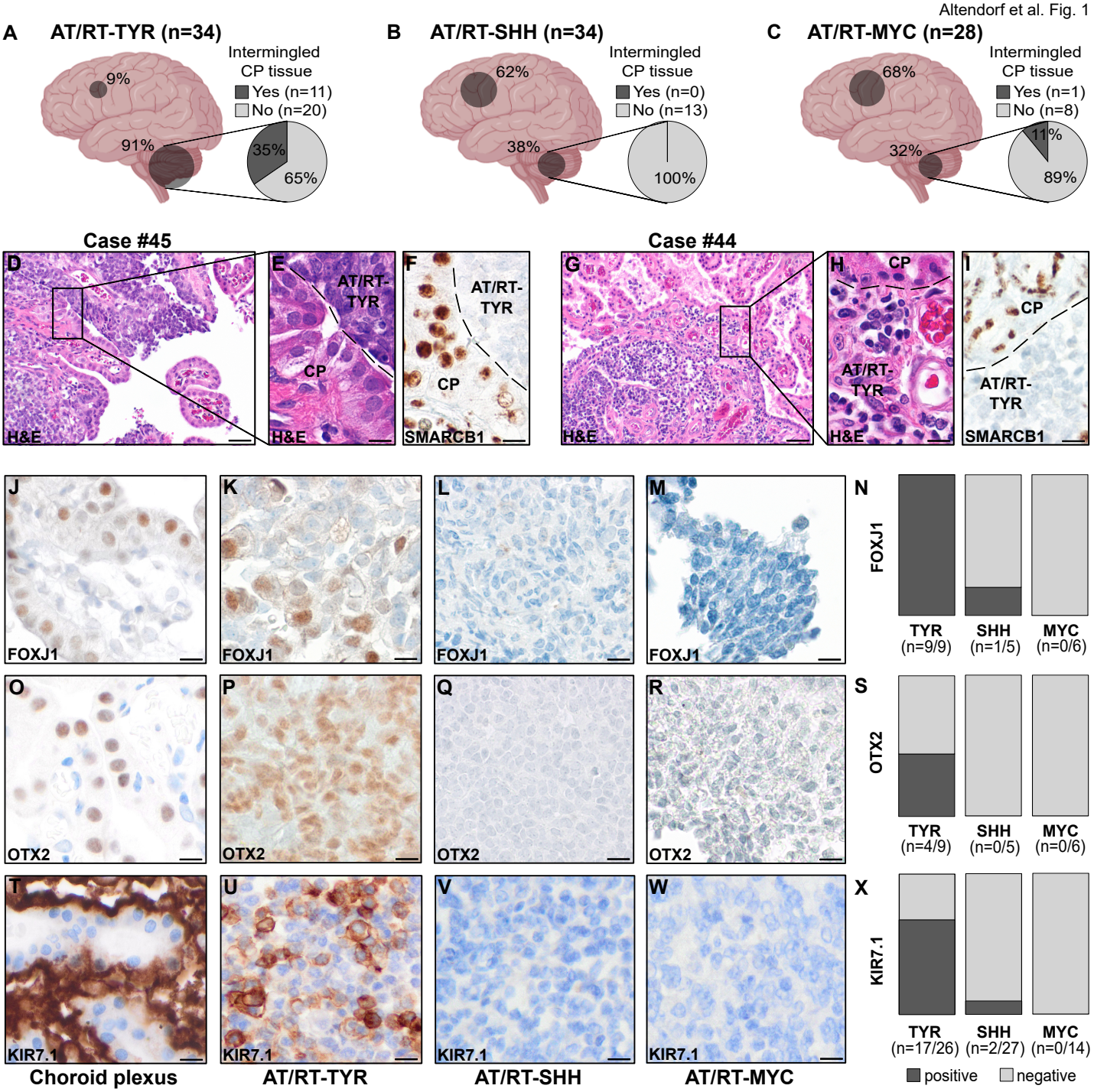
A
AT/RT-TYR (n=34)
9%
91%
Intermingled CP tissue
Yes (n=11)
No (n=20)
35%
65%
B
AT/RT-SHH (n=34)
62%
38%
Intermingled CP tissue
Yes (n=0)
No (n=13)
100%
C
AT/RT-MYC (n=28)
68%
32%
Intermingled CP tissue
Yes (n=1)
No (n=8)
11%
89%
Case #45
Case #44
D
H&E
E
AT/RT-TYR
CP
H&E
F
AT/RT-TYR
CP
SMARCB1
G
H&E
H
CP
AT/RT-TYR
H&E
I
CP
AT/RT-TYR
SMARCB1
J
FOXJ1
K
FOXJ1
L
FOXJ1
M
FOXJ1
N
FOXJ1
TYR (n=9/9)
SHH (n=1/5)
MYC (n=0/6)
O
OTX2
P
OTX2
Q
OTX2
R
OTX2
S
OTX2
TYR (n=4/9)
SHH (n=0/5)
MYC (n=0/6)
T
KIR7.1
U
KIR7.1
V
KIR7.1
W
KIR7.1
X
KIR7.1
TYR (n=17/26)
SHH (n=2/27)
MYC (n=0/14)
positive
negative
Choroid plexus
AT/RT-TYR
AT/RT-SHH
AT/RT-MYC

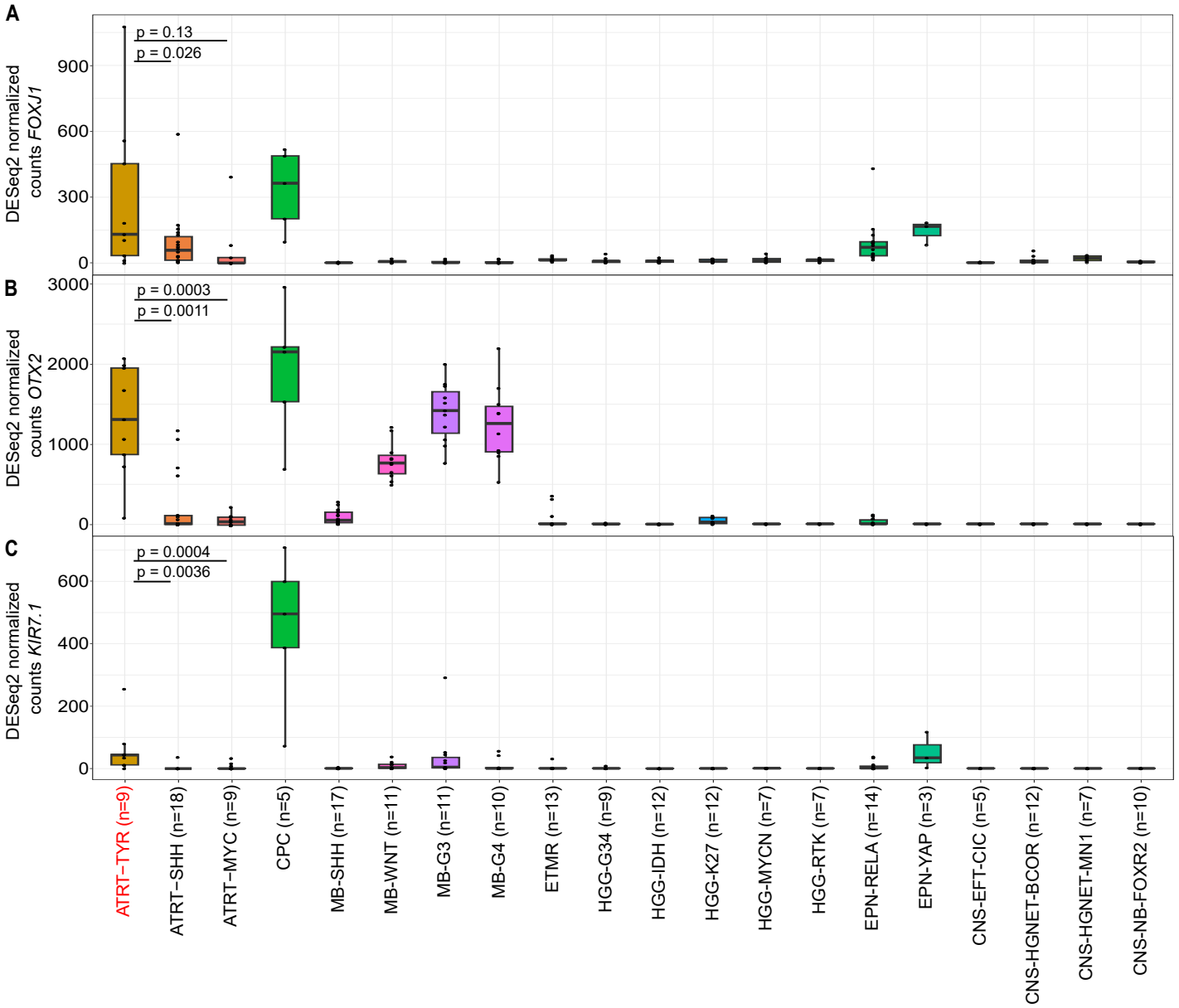
A
p = 0.13
p = 0.026
DESeq2 normalized counts FOXJ1
B
p = 0.0003
p = 0.0011
DESeq2 normalized counts OTX2
C
p = 0.0004
p = 0.0036
DESeq2 normalized counts KIR7.1
ATRT−TYR (n=9)
ATRT−SHH (n=18)
ATRT−MYC (n=9)
CPC (n=5)
MB-SHH (n=17)
MB-WNT (n=11)
MB-G3 (n=11)
MB-G4 (n=10)
ETMR (n=13)
HGG-G34 (n=9)
HGG-IDH (n=12)
HGG-K27 (n=12)
HGG-MYCN (n=7)
HGG-RTK (n=7)
EPN-RELA (n=14)
EPN-YAP (n=3)
CNS-EFT-CIC (n=5)
CNS-HGNET-BCOR (n=12)
CNS-HGNET-MN1 (n=7)
CNS-NB-FOXR2 (n=10)

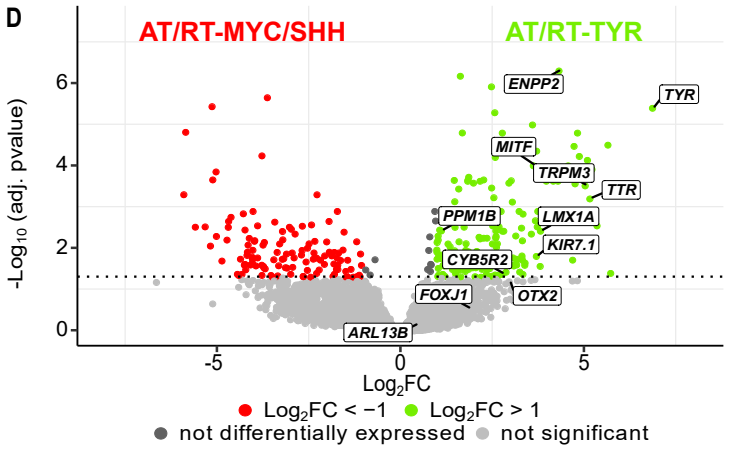
D
AT/RT-MYC/SHH
AT/RT-TYR
ENPP2
TYR
MITF
TRPM3
TTR
PPM1B
LMX1A
KIR7.1
CYB5R2
FOXJ1
OTX2
ARL13B
-Log10 (adj. pvalue)
Log2FC
Log2FC < −1
Log2FC > 1
not differentially expressed
not significant

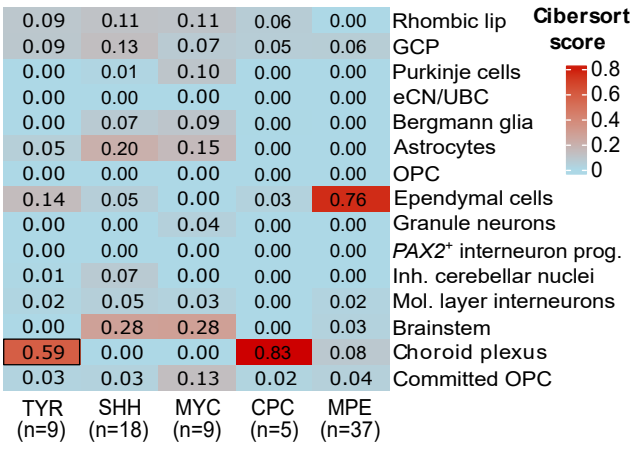
E
Cibersort score
0.8
0.6
0.4
0.2
0
Rhombic lip 0.09 0.11 0.11 0.06 0.00
GCP 0.09 0.13 0.07 0.05 0.06
Purkinje cells 0.00 0.01 0.10 0.00 0.00
eCN/UBC 0.00 0.00 0.00 0.00 0.00
Bergmann glia 0.00 0.07 0.09 0.00 0.00
Astrocytes 0.05 0.20 0.15 0.00 0.00
OPC 0.00 0.00 0.00 0.00 0.00
Ependymal cells 0.14 0.05 0.00 0.03 0.76
Granule neurons 0.00 0.00 0.04 0.00 0.00
PAX2+ interneuron prog. 0.00 0.00 0.00 0.00 0.00
Inh. cerebellar nuclei 0.01 0.07 0.00 0.00 0.00
Mol. layer interneurons 0.02 0.05 0.03 0.00 0.02
Brainstem 0.00 0.28 0.28 0.00 0.03
Choroid plexus 0.59 0.00 0.00 0.83 0.08
Committed OPC 0.03 0.03 0.13 0.02 0.04
TYR (n=9)
SHH (n=18)
MYC (n=9)
CPC (n=5)
MPE (n=37)

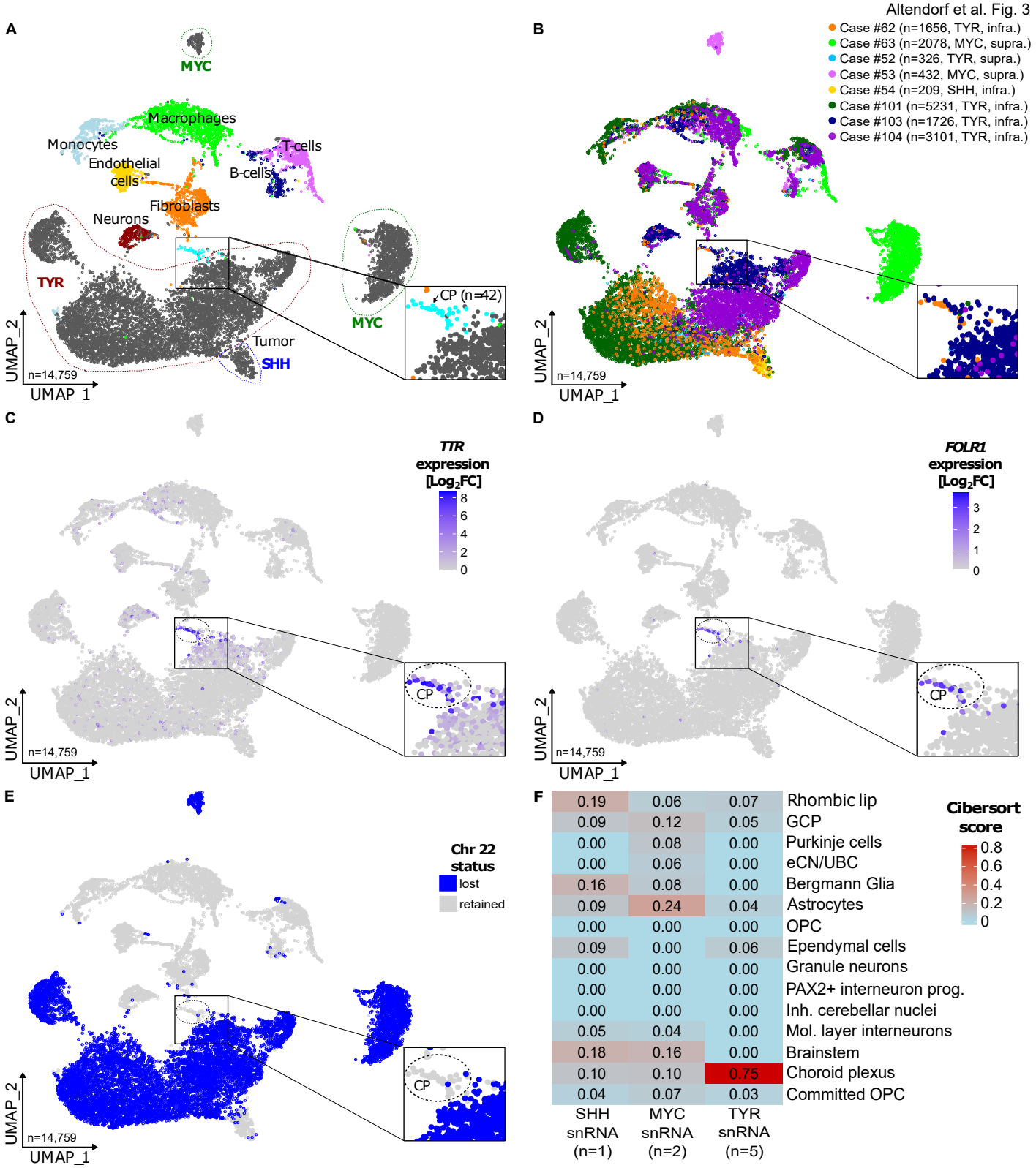
A
MYC
Macrophages
Monocytes
T-cells
Endothelial cells
B-cells
Fibroblasts
Neurons
TYR
CP (n=42)
MYC
Tumor
SHH
UMAP_2
n=14,759
UMAP_1
B
Case #62 (n=1656, TYR, infra.)
Case #63 (n=2078, MYC, supra.)
Case #52 (n=326, TYR, supra.)
Case #53 (n=432, MYC, supra.)
Case #54 (n=209, SHH, infra.)
Case #101 (n=5231, TYR, infra.)
Case #103 (n=1726, TYR, infra.)
Case #104 (n=3101, TYR, infra.)
C
TTR expression [Log2FC]
8
6
4
2
0
CP
D
FOLR1 expression [Log2FC]
3
2
1
0
E
Chr 22 status
lost
retained
F
Rhombic lip 0.19 0.06 0.07
GCP 0.09 0.12 0.05
Purkinje cells 0.00 0.08 0.00
eCN/UBC 0.00 0.06 0.00
Bergmann Glia 0.16 0.08 0.00
Astrocytes 0.09 0.24 0.04
OPC 0.00 0.00 0.00
Ependymal cells 0.09 0.00 0.06
Granule neurons 0.00 0.00 0.00
PAX2+ interneuron prog. 0.00 0.00 0.00
Inh. cerebellar nuclei 0.00 0.00 0.00
Mol. layer interneurons 0.05 0.04 0.00
Brainstem 0.18 0.16 0.00
Choroid plexus 0.10 0.10 0.75
Committed OPC 0.04 0.07 0.03
SHH snRNA (n=1)
MYC snRNA (n=2)
TYR snRNA (n=5)
Cibersort score
0.8
0.6
0.4
0.2
0

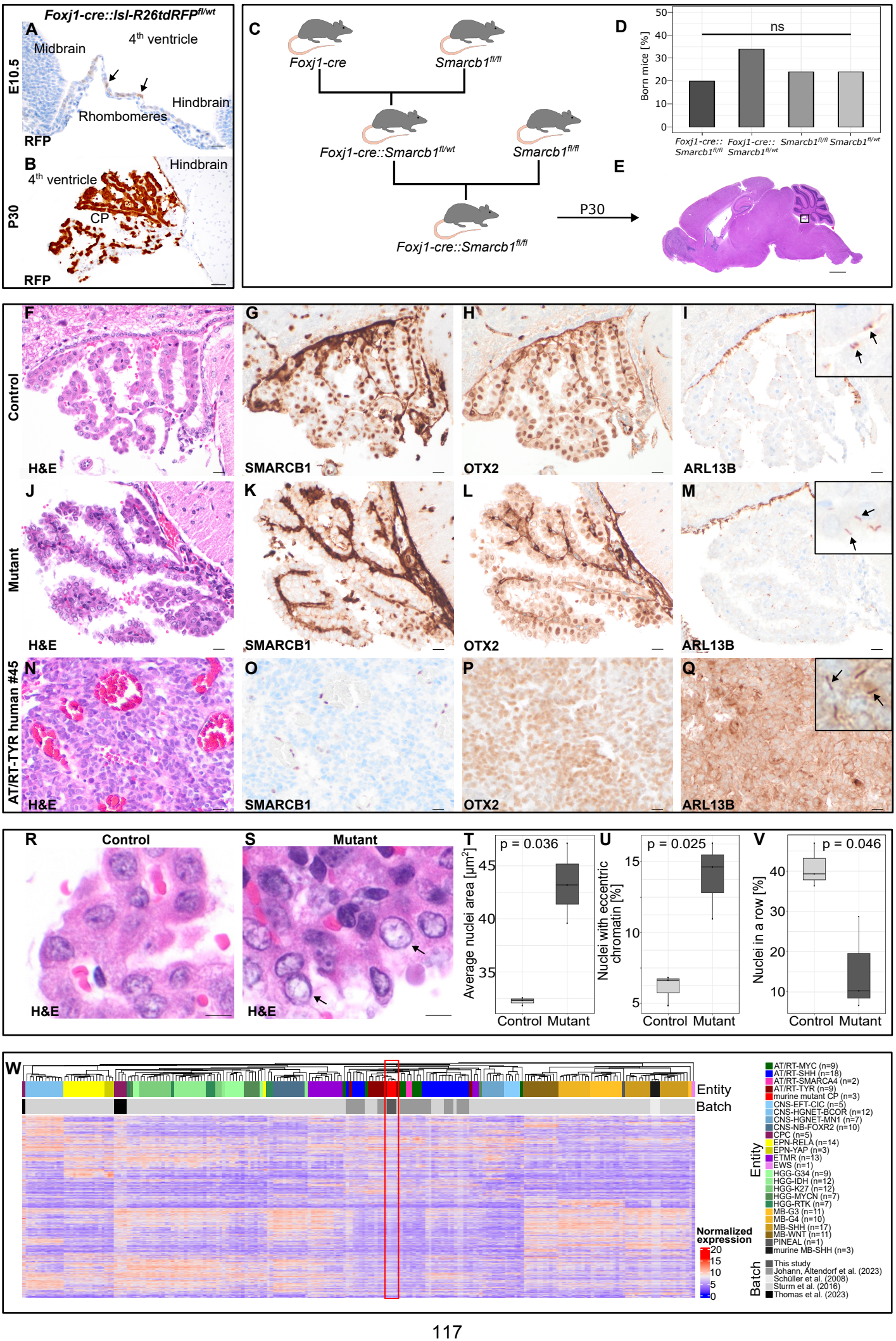
Foxj1-cre::Isl-R26tdRFP^fl/wt
A
E10.5
Midbrain
4th ventricle
Hindbrain
Rhombomeres
RFP
B
P30
4th ventricle
Hindbrain
CP
RFP
C
Foxj1-cre
Smarcb1^fl/fl
Foxj1-cre::Smarcb1^fl/wt
Smarcb1^fl/fl
Foxj1-cre::Smarcb1^fl/fl
P30
D
Born mice [%]
ns
Foxj1-cre:: Smarcb1^fl/fl
Foxj1-cre:: Smarcb1^fl/wt
Smarcb1^fl/fl
Smarcb1^fl/wt
E
F
G
H
I
Control
H&E
SMARCB1
OTX2
ARL13B
J
K
L
M
Mutant
H&E
SMARCB1
OTX2
ARL13B
N
O
P
Q
AT/RT-TYR human #45
H&E
SMARCB1
OTX2
ARL13B
R
Control
S
Mutant
H&E
H&E
T
p = 0.036
Average nuclei area [µm²]
Control
Mutant
U
p = 0.025
Nuclei with eccentric chromatin [%]
Control
Mutant
V
p = 0.046
Nuclei in a row [%]
Control
Mutant
W
Entity
Batch
Normalized expression
Entity
AT/RT-MYC (n=9)
AT/RT-SHH (n=18)
AT/RT-SMARCA4 (n=2)
AT/RT-TYR (n=9)
murine mutant CP (n=3)
CNS-EFT-CIC (n=5)
CNS-HGNET-BCOR (n=12)
CNS-HGNET-MN1 (n=7)
CNS-NB-FOXR2 (n=10)
CPC (n=5)
EPN-RELA (n=14)
EPN-YAP (n=3)
ETMR (n=13)
EWS (n=1)
HGG-G34 (n=9)
HGG-IDH (n=12)
HGG-K27 (n=12)
HGG-MYCN (n=7)
HGG-RTK (n=7)
MB-G3 (n=11)
MB-G4 (n=10)
MB-SHH (n=17)
MB-WNT (n=11)
PINEAL (n=1)
murine MB-SHH (n=3)
Batch
This study
Johann, Altendorf et al. (2023)
Schüller et al. (2008)
Sturm et al. (2016)
Thomas et al. (2023)

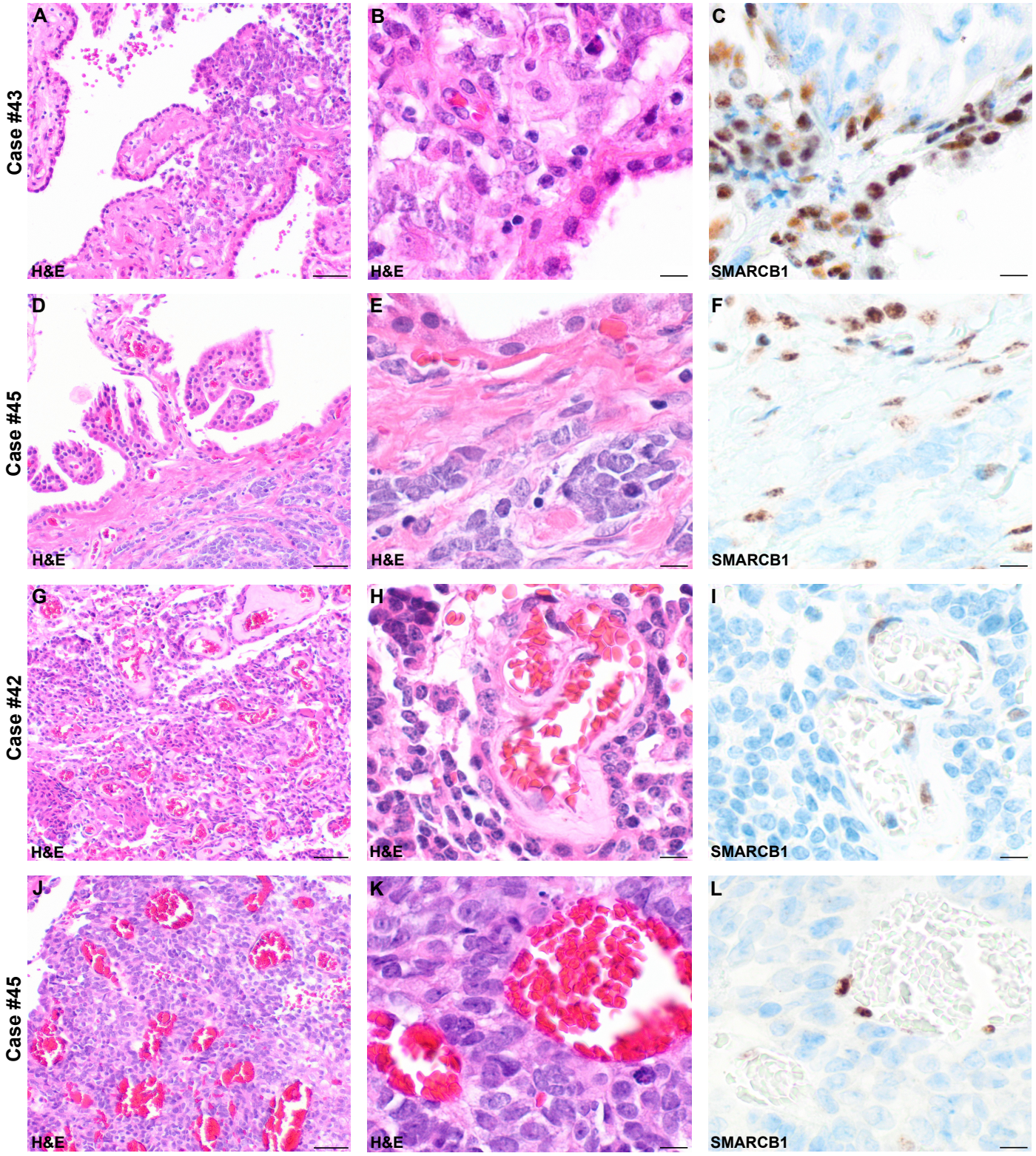

Suppl. Fig. 1: Histological examination of CP signatures in human AT/RT-TYR biopsies. A-F: Exemplary H&E (A, B, D, E) and SMARCB1 (C, F) stainings of AT/RT-TYR showing the transistion from healthy CP tissue to tumor. Scale bars in A and D indicate 50 µm and scale bars in B, C, E, and F indicate 10 µm. **G-L:** Exemplary H&E (G, H, J, K) and SMARCB1 (I, L) stainings of AT/RT-TYR showing papillary structures in the tumor areas. Scale bars in G and J indicate 50 µm and scale bars in H, I, K, and L indicate 10 µm.

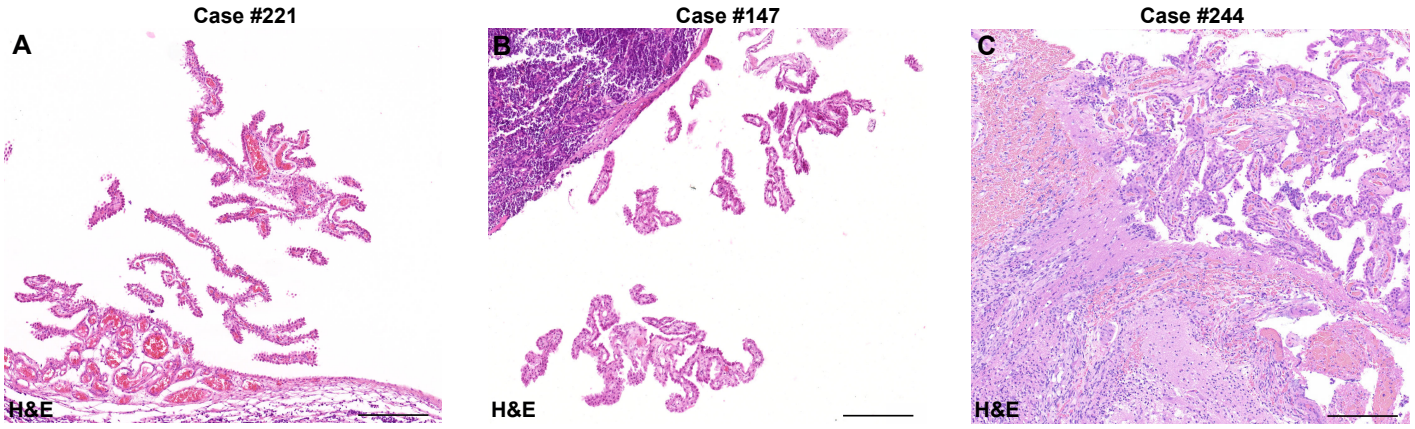

Suppl. Fig. 2: Histological examination of CP occurence at MB biopsies. A: Exemplary H&E staining of CP tissue of a MB-G4 tumor biopsy (Case #221). Scale bar indicates 250 µm. **B:** Exemplary H&E staining of CP tissue of a MB-WNT tumor biopsy (Case #147). Scale bar indicates 250 µm. **C:** Exemplary H&E staining of CP tissue of a MB-G3 tumor biopsy (Case #244). Scale bar indicates 250 µm.

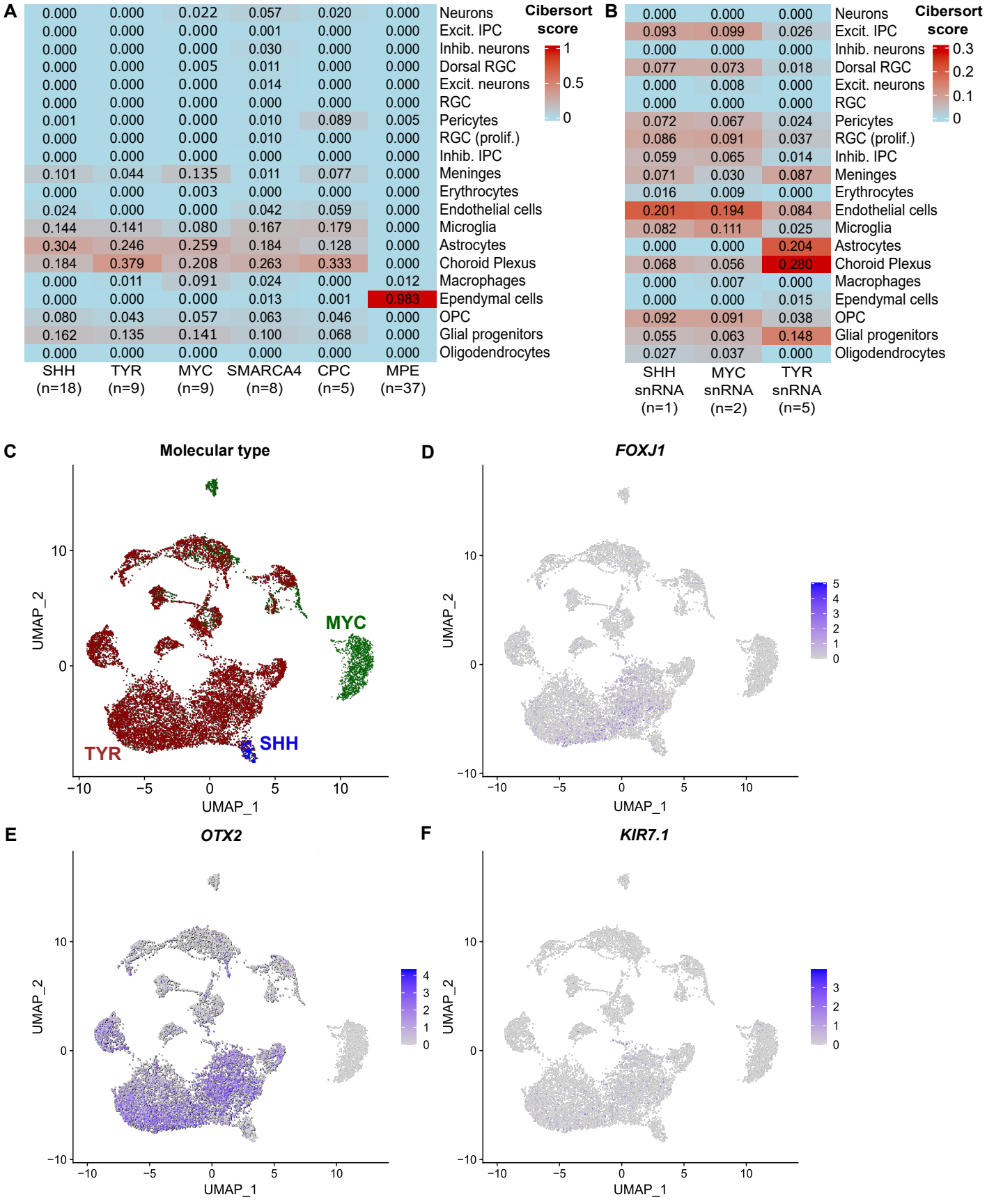

Suppl. Fig. 3: Identification and characterization of CP features in transcriptomic data of human AT/RT. A: *CIBERSORT* analysis for bulk RNAseq data of AT/RT-TYR (n = 9), AT/RT-SHH (n = 18), AT/RT-MYC (n = 9), CPC (n = 5), and MPE (n = 37). Cerebellar cell types of Jessa et al. (2019) were used as scRNAseq reference. The highest scores of AT/RT-TYR and CPC were calculated for CP, of MPE for ependymal cells, and for AT/RT-SHH and AT/RT-MYC no clear match was observed. Excit.: Excitatory; Inhib.: Inhibitory; IPC: Induced pluripotent stem cells; RGC: Radial glial cells; OPC: Oligodendrocyte progenitor cells. **B:** *CIBERSORT* analysis for snRNAseq data of AT/RT-SHH (n = 1), AT/RT-MYC (n = 2), and AT/RT-TYR (n = 5). Only tumor cells were used to generate pseudobulk data. Cerebellar cell types of Jessa et al. (2019) were used as scRNAseq reference. The highest score of AT/RT-TYR was calculated for CP, and for AT/RT-SHH and AT/RT-MYC no clear match was observed. **C:** UMAP using 10 neighboring points of SCT-normalized counts of all cells (n = 14,759), annotated by DNA methylation subtypes. **D:** FeaturePlot of all cells (n = 14,759), showing CP marker gene *FOXJ1* expression. *FOXJ1* was highly expressed in AT/RT-TYR tumor cells and the CP cluster. **E:** FeaturePlot of all cells (n = 14,759), showing CP marker gene *OTX2* expression. *OTX2* was highly expressed in AT/RT-TYR tumor cells and the CP cluster. **F:** FeaturePlot of all cells (n = 14,759), showing CP marker gene *KIR7.1* expression. *KIR7.1* was highly expressed in AT/RT-TYR tumor cells and the CP cluster.

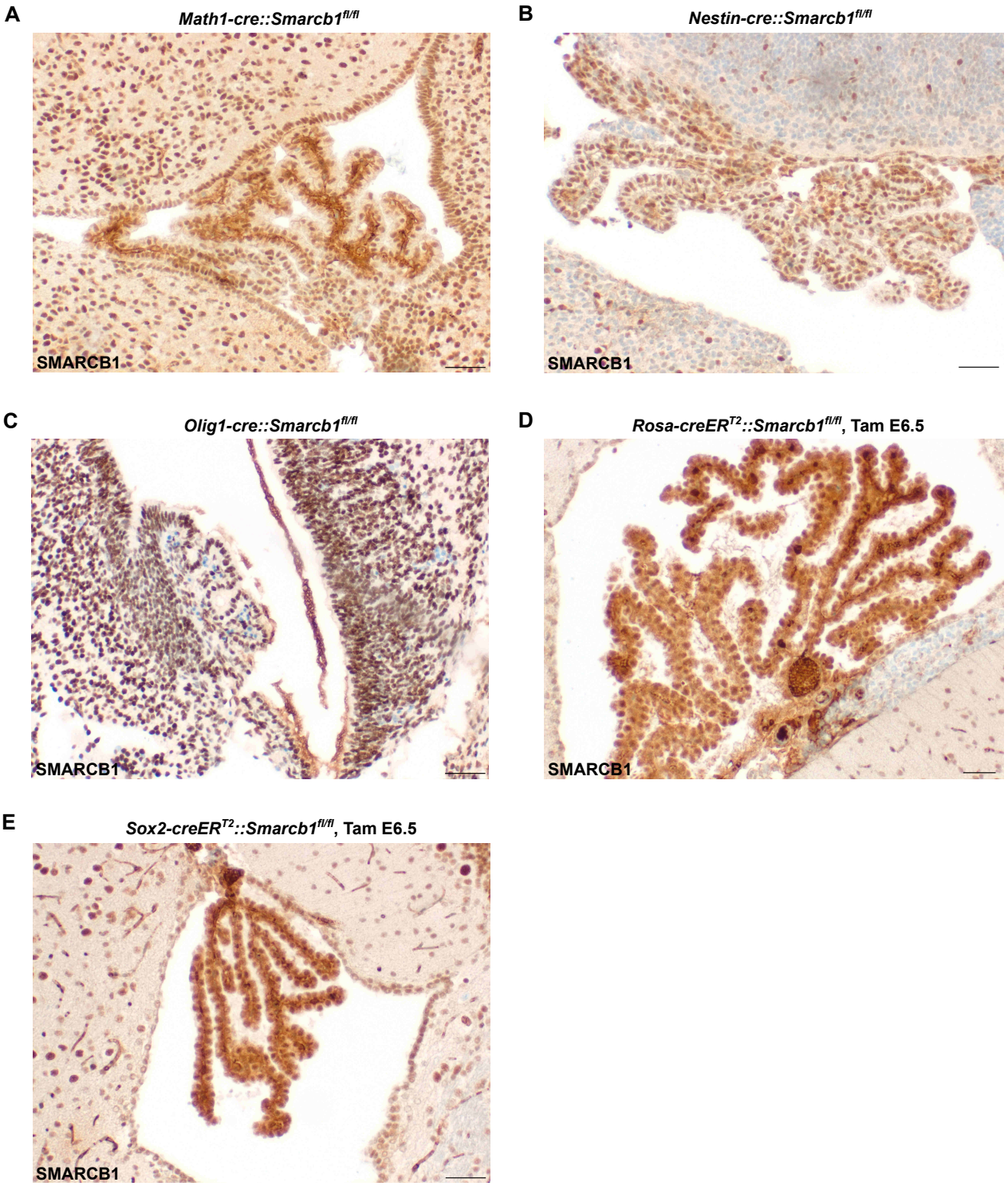

Suppl. Fig. 4: Histological examination of the fourth ventricle CP of previous mouse models. A: SMARCB1 IHC of the fourth ventricle CP of *Math1-cre::Smarcb1*$^{fl/fl}$ mice. Scale bar indicates 50 µm. **B:** SMARCB1 IHC of the fourth ventricle CP of *Nestin-cre::Smarcb1*$^{fl/fl}$ mice. Scale bar indicates 50 µm. **C:** SMARCB1 IHC of the fourth ventricle CP of *Olig1-cre::Smarcb1*$^{fl/fl}$ mice. Scale bar indicates 50 µm. **D:** SMARCB1 IHC of the fourth ventricle CP of *Rosa-creER*^{T2}*::Smarcb1*$^{fl/fl}$ mice, tamoxifen (Tam)-induced at E6.5. Scale bar indicates 100 µm. **E:** SMARCB1 IHC of the fourth ventricle CP of *Sox2-creER*^{T2}*::Smarcb1*$^{fl/fl}$ mice, tamoxifen (Tam)-induced at E6.5. Scale bar indicates 50 µm.

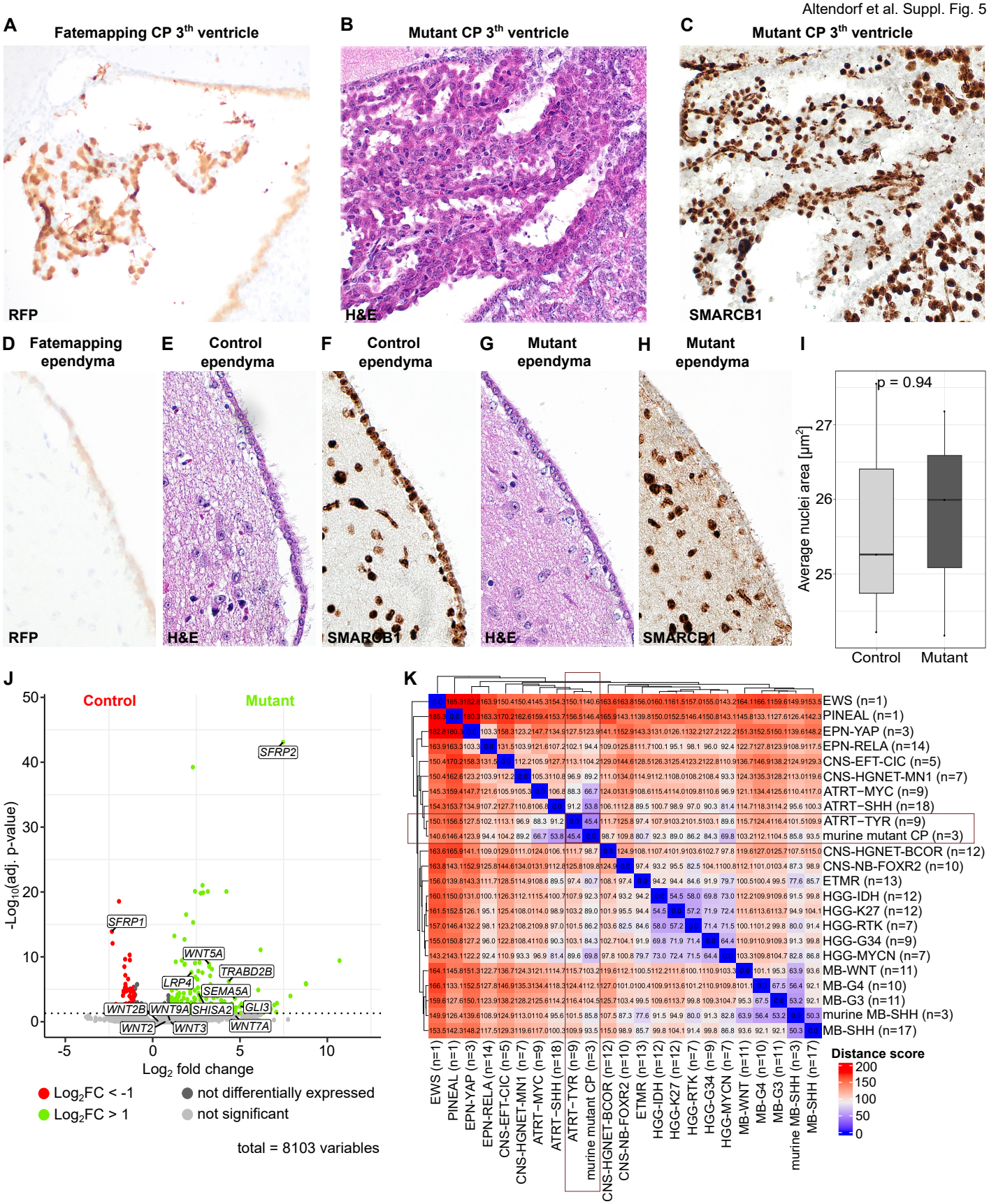

Suppl. Fig. 5: Additional analyses of the *Foxj1-cre::Smarcb*$^{fl/fl}$ mice CP at P30. A: Exemplary RFP staining of the third ventricle CP of a *Foxj1-cre::lsl-R26tdRFP*$^{fl/wt}$ (Fatemapping) mouse at P30. Scale bar indicates 50 µm. **B:** Exemplary H&E staining the third ventricle CP of a *Foxj1-cre::Smarcb1*$^{fl/fl}$ (mutant) mouse at P30. Scale bar indicates 50 µm. **C:** Exemplary SMARCB1 staining of the third ventricle CP of a *Foxj1-cre::Smarcb1*$^{fl/fl}$ (mutant) mouse at P30. Scale bar indicates 50 µm. **D:** Exemplary RFP staining of the ependyma of a Fatemapping mouse. Scale bar indicates 20 µm. **E:** Exemplary H&E staining of the ependyma of a control mouse. Scale bar indicates 20 µm. **F:** Exemplary SMARCB1 staining of the ependyma of a control mouse. Scale bar indicates 20 µm. **G:** Exemplary H&E staining of the ependyma of a mutant mouse. Scale bar indicates 20 µm. **H:** Exemplary SMARCB1 staining of the ependyma of a mutant mouse. Scale bar indicates 20 µm. **I:** Box plot showing the average ependyma nuclei area for control (n = 3) and *Foxj1-cre::Smarcb1*$^{fl/fl}$ (mutant) mice (n = 3), resulting in no significant difference (p = 0.94). **J:** Volcano Plot showing differentially expressed genes between control (n = 3) and *Foxj1-cre::Smarcb1*$^{fl/fl}$ mice (n = 3). Genes of the Wnt signaling pathway are annotated. **K:** Distance Plot based on the 1,000 most variable genes resulting from bulk RNAseq data of the CP from *Foxj1-cre::Smarcb1*$^{fl/fl}$ (mutant) mice (murine mutant CP, n = 3), murine MB-SHH from *Math1-cre::Smo*$^{fl/wt}$ mice (murine MB-SHH, n=3), and a variety of human CNS tumors derived from Sturm et al. (2016), Johann, Altendorf at al. (2023), and Thomas et al. (2023). Murine mutant CP was least distant from human AT/RT-TYR (distance score = 45.4).

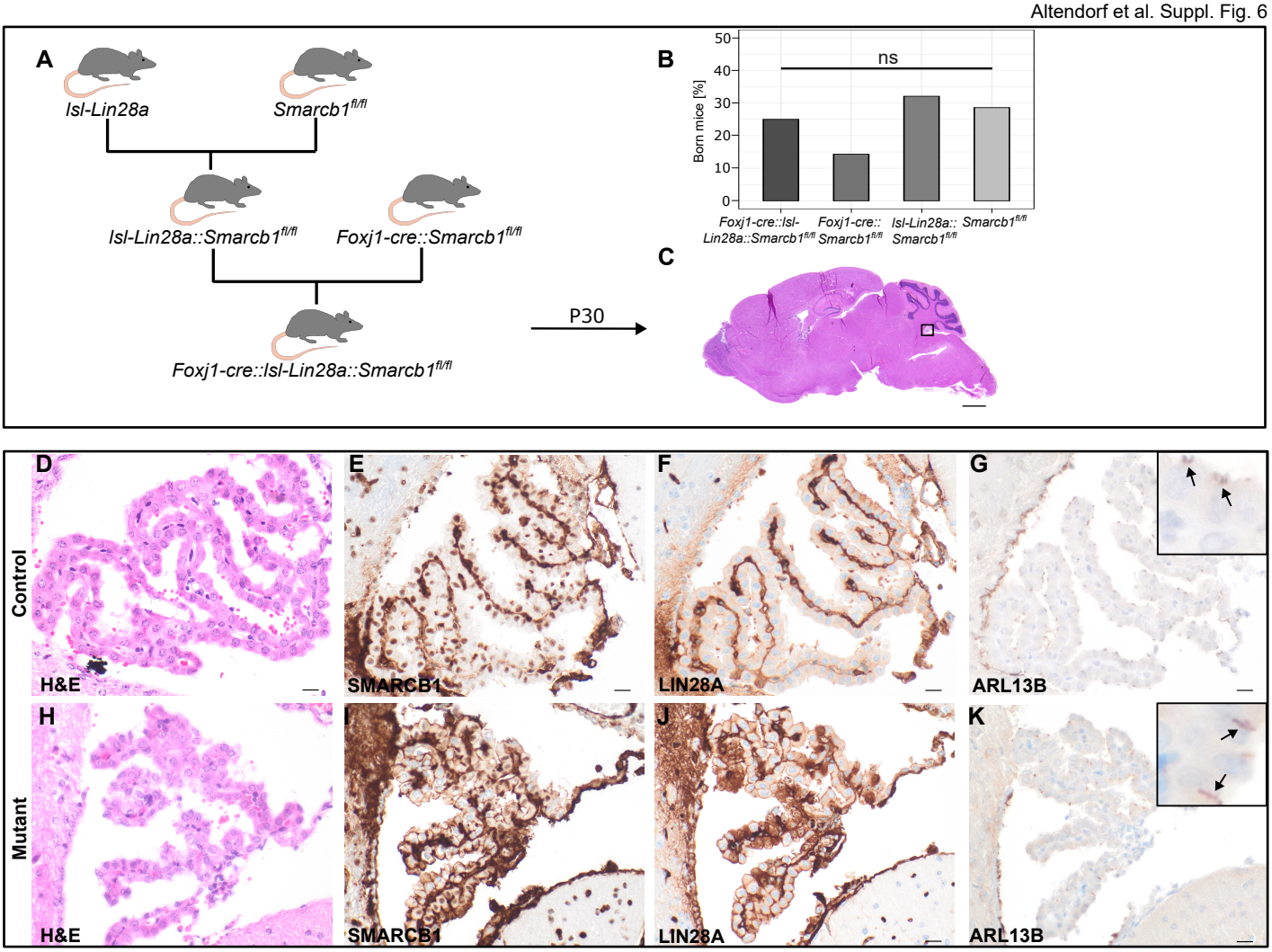

Suppl. Fig. 6: Histological examination of murine *Foxj1-cre::Isl-Lin28a::Smarcb1$^{fl/fl}$* CP at P30. A: Breeding scheme of crossing *Foxj1-cre::Smarcb1$^{fl/fl}$* and *Isl-Lin28a::Smarcb1$^{fl/fl}$* mice for the generation of *Foxj1-cre::Isl-Lin28a::Smarcb1$^{fl/fl}$* mice. **B:** Bar plot showing the proportion of born mice for each genotype. 25% were expected for each genotype according to the Mendelian ratio. **C:** H&E of a sagittal brain section of a *Foxj1-cre::Isl-Lin28a::Smarcb1$^{fl/fl}$* mouse at P30. Scale bar indicates 2 µm. **D-G:** Exemplary H&E (D), SMARCB1 (E), LIN28A (F), and ARL13B (G) stainings of a fourth ventricle CP of a control mouse at P30. Scale bars indicate 20 µm. **H-K:** Exemplary H&E (H), SMARCB1 (I), LIN28A (J), and ARL13B (K) stainings of a fourth ventricle CP of a *Foxj1-cre::Isl-Lin28a::Smarcb1$^{fl/fl}$* mouse at P30. Scale bars indicate 20 µm.

6. Discussion

This study demonstrates a thorough characterization of AT/RT, regarding their development and mechanisms of recurrence.
We identified histological and molecular differences between paired primary and recurrent AT/RT. These include alterations in DNA methylation and gene expression profiles as well as CNVs during recurrence. We further characterized the intratumoral heterogeneity of AT/RT-MYC by assigning each cell of AT/RT primary-recurrence pairs to a cancer cell state. snRNAseq also revealed therapy-resistant cells. These were characterized by differential gene expression analysis, and our findings were validated *in vitro* by performing treatment of AT/RT-MYC cell lines.
The identification of the cellular origins and developmental timepoints of AT/RT remains challenging. We confirmed that *Smarca4* plays an important role in developmental processes. A *Smarca4* loss in the murine neural crest led to neuromuscular symptoms and ubiquitously expressed germline mutations to embryonal death. For AT/RT-TYR, we made great progress regarding the identification of their cellular origin. We identified cell type signatures on the histological and gene expression level, and we developed a mouse model that has not developed any tumors but whose abnormalities showed a similar gene expression profile compared to AT/RT-TYR.

At first, we aimed to identify molecular and histological differences of a large cohort of paired AT/RT primary-recurrence pairs, which was described in publication 1 (Johann, Altendorf et al. 2023). The majority of AT/RT progresses or recurs after a short time. Patients suffering from recurrences have an even poorer prognosis, with only a few patients being alive five years after the diagnosis of a recurrence. One reason for tumor progression is the lack of targeted therapies. Therefore, it is important to identify the mechanisms regarding AT/RT tumor progression and recurrence. Ultimately, the insights gained should contribute to the development of novel therapies, preventing the emergence of recurrences, but also targeted therapies combating already present recurrences.

We collected tumor material from 26 patients who suffered from AT/RT primary tumors and recurrences for DNA methylation analysis. This is a comparatively large cohort as AT/RT are rare, and biopsies of the recurrences are performed even more rarely. This is because recurrences are assumed to be similar to primary tumors and receive the same treatment. However, in this work we showed that there are crucial differences which should not be neglected. To start with the analogies of primary and recurrent AT/RT, we identified similar DNA methylation profiles. Subtype changes from primary tumor to recurrence were only observed for three out of 26 tumors. As mentioned in publication 1, this was similar to findings in other

central nervous system (CNS) tumor entities, like, for instance, in ependymoma (Zhao et al. 2022). Overall, local tumor recurrences and primary progressing tumors were hard to distinguish as it was not always clear whether cells persisted after therapy, which could explain similar DNA methylation profiles. Another option is that the here described recurrences, which changed their subtype, were synchronous or metachronous tumors that arose as secondary malignancies due to the underlying RTPS1 (Sredni and Tomita 2015; Thomas et al. 2019). Nevertheless, all primary-recurrence pairs were included in further analyses because similar DNA methylation profiles were known from other entities, and we indeed observed differences on other levels. Using histology, increased proliferation of recurrences was identified. Additionally, we observed increased CNVs in AT/RT recurrences, especially in AT/RT-SHH. These tumors demonstrated an enhanced chromosome 1q gain and chromosome 10 loss. Both were associated with an inferior prognosis in other CNS tumor entities, like ependymoma (Araki et al. 2016; Gojo et al. 2017). In addition, we observed differences in gene expression, distinct for the DNA methylation subtypes. Due to small sample sizes of AT/RT-TYR and AT/RT-MYC, we focused on AT/RT-SHH. Relatively few genes were differentially expressed between AT/RT-SHH primary tumors and recurrences, which probably resulted from the heterogeneity within this subtype. Five genes were upregulated in recurrences of AT/RT-SHH-1A, -1B, and -2: *CA4, KAT2A, RGL2, NPIPA5, and TMEM259*. *CA4* encodes the Carbonic Anhydrase 4, which already serves as a biomarker for outcomes in, for instance, low-grade glioma (Xu et al. 2020). *KAT2A* is the gene encoding the Lysine Acetyltransferase 2A, which is a histone acetyltransferase (HAT) functioning as a transcriptional regulator. It is also involved in the regulation of cell proliferation and apoptosis (Wang et al. 2017b). The Ral Guanine Nucleotide Dissociation Stimulator Like 2 (*RGL2*) drives metastatic progression in colorectal cancer (Sun et al. 2021), which could possibly have a similar function in brain tumors. Overall, there were a number of cancer-associated genes that were differentially expressed in AT/RT-SHH recurrences compared to primary tumors.

Overall, the identified differentially expressed genes, as well as genes affected by CNVs, might serve as novel therapeutic targets. But further validation of our findings is required. At first, we aimed to investigate the role of the differentially expressed genes *in vitro*. For this purpose, we established the cell culture of the AT/RT-SHH cell lines CHLA-02 (ATCC, CRL-3020; Xu et al. 2015) and CHLA-05 (ATCC, CRL-3037; Erdreich-Epstein et al. 2014; Xu et al. 2015). These are patient-derived cell lines of AT/RT-SHH primary tumors. To investigate the influence of the identified alterations, a matching recurrent cell line is required. In a first approach, we treated the cells with a combination of doxorubicin, etoposide, and vincristine, according to the EU-RHAB registry (Benesch et al. 2014; Seeringer et al. 2014; Frühwald et al. 2016). We tested different concentrations of each inhibitor to determine the concentration which nearly killed all cells (IC0-5). We were expecting the cells to grow back as recurrent-like cells. So far, the cells

did not grow again after treatment because probably the concentrations were too high. This is why we tried another approach, which aims at a slow habituation of the cells to the inhibitor. We started to incubate the cells with low concentrations of the inhibitors, and as soon as they showed normal proliferation again, we increased the concentration. This is still ongoing because only small concentrations increases are feasible, showing again that recurrence is a highly complex process.

In addition to the above-described *in vitro* validation, we planned to further investigate paired AT/RT primary tumors and recurrences on a single-cell level to get insights into the intratumoral heterogeneity of these tumors. Moreover, the TME could be examined in more detail after no significant differences in the immune cell infiltration were observed using DNA methylation and bulk RNAseq data. These analyses and findings were described in the unpublished manuscript 1.

We investigated eight AT/RT primary recurrence pairs using snRNAseq data, and tumor cells and TME were analysed separately. The TME of AT/RT recurrences was characterized by an enrichment of *CD1A*$^{+}$ *CD207*$^{+}$ DCs. These cells, which were differentiated similarly to Langerhans cells, were previously undescribed in the CNS, they are only known to occur in the skin (Liu et al. 2021). Further cell-cell communication analyses revealed that these cells might be activated by TGF-β signaling (Kel et al. 2010), which was previously demonstrated *in vitro* (Yasmin et al. 2013; Abagnale et al. 2025). Overall, TGF-β signaling seems to play a crucial role in therapy resistance in diverse ways, and this was previously shown for other tumor entities (Gooden et al. 2011; Gulubova et al. 2013; Minesaki et al. 2021). Regarding the *CD1A*$^{+}$ *CD207*$^{+}$ DCs, we observed significantly worse survival of AT/RT patients presenting these cells in recurrences.

Afterwards, the tumor cells were further characterized for each DNA methylation subtype separately. Due to small sample and cell numbers for AT/RT-SHH and AT/RT-TYR, we focused on AT/RT-MYC. As recurrences in general are mainly supposed to arise from dormant cells, we hypothesized that AT/RT also arise from such dormant cells (Phan and Croucher 2020; Damen et al. 2021). We assume that these are cells in a quiescent state that persist after therapy and develop into recurrences. Therefore, it is necessary to identify and characterize these cells in AT/RT because it would be efficient to target these cells using novel therapies. We identified respective cells for AT/RT-MYC, which were present in all AT/RT-MYC primary tumors and showed high similarity to recurrences. The hypothesis is that these cells were dormant cells, like so-called CSCs, which exhibit latent metabolism and therapy resistance, which could be achieved due to immune escape, among others (Esmatabadi et al. 2016; Tufail et al. 2025). One of the top upregulated pathways in these cells was an altered ECM organization. By acting as a biomechanical barrier, which protects the tumor from anticancer agents, it supports tumor progression in diverse tumor entities (Winkler et al. 2020; Yuan et al.

2023; Prakash and Shaked 2024). ECM remodeling is known to be therapy-induced. The ECM is also known to play a role in the induction as well as in the reactivation of dormant tumor cells. On the one hand, the ECM can promote tumor cell dormancy by regulating the availability of growth factors and nutrients due to regulation of its density. On the other hand, the ECM can interact with the tumor cells via integrins, which might activate signaling pathways that induce cell cycle arrest and dormancy (Tufail et al. 2025). ECM alterations, like increased stiffness, can lead to the reactivation and proliferation of dormant tumor cells (Tufail et al. 2025). Increased stiffness was previously associated with therapy resistance in glioblastoma. For glioblastoma, the ECM stiffness differs between the tumor core and the tumor border (Mahaffey et al. 2024), which shows that the localization of therapy-resistant cells should also be investigated, which will be described in the following sections. As one major component of the ECM, type I collagen (*COL1A1*) was upregulated in probably therapy-resistant AT/RT-MYC tumor cells. *COL1A1* overexpression was previously associated with inferior survival and also refers to the epithelial-mesenchymal transition (EMT) as an EMT marker gene (Barkan et al. 2010; Li et al. 2022; Comba et al. 2022). Increased partial EMT (pEMT) was observed in AT/RT-MYC recurrences, and therefore, it was identified as an additional feature of therapy resistance in AT/RT-MYC. We aimed to validate this finding *in vitro* by using the AT/RT-MYC cell lines CHLA-266 (Xu et al. 2015) and BT16 (D'cunja et al. 2007). Therapy resistance was achieved due to treatment and regrowth of the cells, as described above for the AT/RT-SHH cell lines. Opposed to the AT/RT-SHH cell lines, it was successful to regrow the AT/RT-MYC cells following treatment with a combination of doxorubicin, etoposide, and vincristine. After regrowth, we observed altered cell morphology with mesenchymal-like cells that were attached to each other with loose cell-cell contacts (Sacco and Gomez 2024). Additionally, the expression of epithelial marker genes, investigated using IHC, was decreased. pEMT marker genes were also upregulated in bulk RNAseq data after treatment. EMT is also known in the context of CSCs. It is probable that CSCs undergo EMT, which allows them to survive treatment (Tufail et al. 2025). CSCs display an EMT phenotype with loose cell-cell junctions, which might lead to increased migration potential, in association with the development of metastases (Tanabe 2022). EMT and CSCs share different signaling pathways that are related to drug resistance, more precisely by expressing transporters for shifting the drugs from inside to outside the cells. These include the TGF-β and Wnt signaling pathways, among others (Savage 2016; Tanabe et al. 2020). Therefore, signaling pathways of EMT and CSCs are promising targets for novel therapies, as these will probably target the therapy-resistant cancer cell states. Particularly, TGF-β signaling seems to play a major role in AT/RT-MYC therapy resistance, as it was found to induce *CD1A*$^{+}$ *CD207*$^{+}$ DCs (Kel et al. 2010), ECM remodeling (Chakravarthy et al. 2018), and EMT (Xu et al. 2009). Overall, we demonstrated that the TGF-β signaling is a promising target in the context of therapy resistance in AT/RT-MYC.

Additionally, we identified specific genes of the TGF-β signaling pathway that were upregulated in probably therapy-resistant AT/RT-MYC cells and whose overexpression correlated with a worse survival of AT/RT-MYC patients. One of these genes was *ETS1*, whose expression is regulated by TGF-β signaling (Dittmer 2015). Previous studies revealed a crucial role in invasiveness, EMT, ECM, and therapy resistance (Sakamoto et al. 2021). This was similar for the lysosomal transmembrane protein 5 (*LAPTM5;* Seimiya et al. 2003; Sun et al. 2024). For the establishment of these genes or the associated TGF-β signaling pathway, further validation is required. Potential next steps, including this validation, will be described in the following sections. The overall aim is to perform similar analyses for the other DNA methylation subtypes by collecting and sequencing additional samples.

For AT/RT-MYC, the next step will be to get insights into the spatial localization of the therapy-resistant cells. As previously described, we observed altered ECM remodeling in the context of such cells. This is why we assume a distinct spatial localization of respective cells with an altered ECM. As mentioned before, ECM stiffness differs between the tumor border and core in glioblastoma, and increased stiffness was associated with therapy resistance (Mahaffey et al. 2024). Therefore, the localization of the therapy-resistant cells is of utmost importance because it might have an impact on the treatment, for instance, on the degree of surgical resection of AT/RT-MYC tumors. We aim to characterize the spatial localization of such cells using spatial transcriptomics by Xenium analysis from 10x Genomics. This is an image- and panel-based approach with single-cell resolution, which requires a formalin-fixed paraffin-embedded (FFPE) section as input. This approach allows us to achieve single-cell transcriptomic data of 5000 genes from a Human Brain Gene Expression Panel (#1000599, 10x Genomics). It is possible to add up to 100 custom genes. This allows to include our therapy resistance-associated genes of AT/RT-MYC to identify the localization of these cells. This will also help to analyse interactions with neighbouring cells, like those of the ECM. In addition, it is possible to perform an overlay of the Xenium results and the H&E staining of the respective section, which facilitates further morphological characterization of the therapy-resistant cells.
After that, *in vitro* validation of the identified overexpressed genes and pathways in probably therapy-resistant AT/RT-MYC cells is required. We plan to overexpress respective genes, using a lentiviral approach, in AT/RT-MYC cell lines to investigate whether they induce therapy resistance. Therefore, we will treat the transfected and not-transfected cells and perform cell viability and proliferation assays. We expect an increased survival and proliferation after treatment of cells overexpressing *ETS1*, *LAPTM5*, or other TGF-β signaling-associated genes because such genes might lead to enhanced therapy resistance.
Finally, we aim to investigate the effect of the expression of therapy resistance-associated genes in different model organisms to analyse whether silencing of therapy-resistance-associated genes improves therapy response *in vitro* and *in vivo*. We will use therapy-resistant

AT/RT-MYC cell lines that arise after regrowth following treatment and knockout the identified genes, again using a lentiviral approach, with subsequent investigation of the therapy response. To additionally investigate changes in the ECM, AT/RT tumoroids (Paassen et al. 2023) grown in Matrigel to mimic the interaction with the ECM, could be used. Among others, the invasion of the tumor cells into the ECM will be investigated using Matrigel drop invasion and degradation assays (Aslan et al. 2021). This will be compared between different conditions: With and without silencing of the identified genes, and before and after treatment. In addition, the role of the identified potentially therapy-resistant genes in AT/RT-MYC could be further examined using patient-derived orthotopic xenograft (PDOX) models and investigation of the therapy response to standard-of-care chemotherapy. AT/RT-MYC xenografts will be transfected, resulting in a knockout of respective genes. Transfected and not-transfected xenografts will then be transplanted into NOD-SCID gamma (NSG) mice, and treatment will be performed as soon as the tumor is visible in In Vivo Imaging Systems (IVIS). At the end of the experiments, tumor size, proliferation, and survival of the mice will be compared. Overall, we assume that AT/RT-MYC cell lines and tumoroids will display an enhanced therapy response after silencing the overexpressed genes of therapy-resistant cells. Tumoroids will additionally differ in their interaction with the ECM. We hypothesize less ECM remodeling, including invasion of the tumor cells into the ECM, and degradation of the ECM after silencing of respective genes. Furthermore, knockout mice are supposed to survive longer by suffering from tumors with decreased size and proliferation.

The second aim was to investigate the cellular origins of AT/RT-SMARCA4 and AT/RT-TYR. As previously described, the knowledge of the cellular origin is important for a better understanding of the tumor development, the generation of a genetically modified mouse model, and the design of targeted therapies, which in turn need to be tested in an adequate mouse model. As opposed to AT/RT-SHH and AT/RT-MYC, where at least hypotheses exist, the cellular origin is completely unknown for AT/RT-SMARCA4 and AT/RT-TYR. The results for the cellular origin of AT/RT-SMARCA4 were summarized in publication 2 (Neyazi, Altendorf et al. 2022), and for AT/RT-TYR in the unpublished manuscript 2.

AT/RT-SMARAC4 are tumors that arise the earliest compared to the other DNA methylation subtypes (Holdhof et al. 2020a), and therefore, we assume that these tumors emerge very early during embryonal development. They are mostly located supratentorially, but about one-third arise infratentorially (Holdhof et al. 2020a), which makes drawing conclusions from the localization regarding the cellular origin difficult. Therefore, we aimed for a *Smarca4* knockout in mice, induced by promoter-driven *Cre* lines, which previously led to tumor development in *Smarcb1*-deficient mice. *P0-cre::Smarcb1*$^{fl/fl}$ of Vitte et al., which suffered from a *Smarcb1* knockout at E9.5 in the neural crest, developed cranial nerve tumors, as well as tumors arising from the meninges or the spinal nerve roots. The tumor penetrance was 65%, and the median

OS was 3.2 months. These tumors demonstrated RT-like features on the histological and gene expression level, but a clear assignment to a DNA methylation subtype was not possible (Vitte et al. 2017). We generated *P0-Cre::Smarac4$^{fl/fl}$* mice, which have not developed any tumors but displayed neuromuscular symptoms, including paralysis of the limbs. These mice had a median overall OS of nine weeks. Additionally, an approach that mimics the human situation by using the germline mutation *Smarca4-p.R1189** did not result in murine tumor development (Schneppenheim et al. 2010). Heterozygous mice have not shown any symptoms, and homozygous mice were not viable. Not even the crossing of *Smarca-p.R1189*$^{+/-}$* and *P0-Cre::Smarca4$^{fl/wt}$* mice, which mimics the occurrence of a constitutive germline mutation and a conditional mutation in the neural crest, similar to patients suffering from RTPS2, resulted in tumor development. These mice demonstrated similar neuromuscular symptoms. We successfully explained this neuromuscular phenotype by an impaired myelinization of the peripheral nerves, as *P0-Cre* was also shown to target the peripheral myelin (Feltri et al. 1999; Fröb and Wegner 2020). Myelinization describes the process of Schwann cells forming myelin around the peripheral nerves, which enables a rapid conduction of action potential along the axons. Myelin is a lipid-containing biomembrane that isolates the peripheral nerves (Glenn and Talbot 2013). We confirmed this by histopathological examination using toluidine blue (TBO) stainings, which revealed thinner and impaired myelin sheaths surrounding axons of sciatic nerves, and further histological investigation revealed a neurogenic image of muscle tissue with angular atrophic myocytes in muscles that were innervated by impaired sciatic nerves.

The failure of tumor development is still under investigation. As previously described, it seems like we used a *P0-Cre* line that starts to be expressed at E13.5 (Feltri et al. 1999) and not at E9.5, which is in line with the observation that we couldn't recapitulate the tumors of Vitte et al. using *P0-Cre::Smarcb1$^{fl/fl}$* mice. This is why we tested the *P0-CreC* line, which expresses *Cre* in the neural crest starting at E9.5. We investigated 30 *P0-CreC::Smarca4$^{fl/fl}$* mice that were born with an expected Mendelian ratio over one year, but these mice have not developed any tumors either. In addition, they only suffered from mild neuromuscular symptoms. The conclusion is that either a *Smarca4* loss at E9.5 is still too late for tumor development, or that a completely different cell type is the cell of origin. Therefore, we tested another promoter-driven *Cre* line, *Dppa3-Cre*. This promoter targets pluripotent germ cells (PGCs) starting at E7.5 because other studies showed that PGCs could also be the cellular origin. Graf et al. successfully generated *Dppa3-Cre::Smarcb1$^{fl/wt}$* mice, which developed intracranial and extracranial RT-like tumors, whereas homozygous mice showed embryonic lethality. These tumors showed similar gene expression profiles compared to AT/RT-MYC (Graf et al. 2022). We monitored 22 *Dppa3-Cre::Smarca4$^{fl/wt}$* mice over one year. Homozygous mice displayed embryonic lethality as previously shown for *Dppa3-Cre::Smarcb1$^{fl/fl}$* mice. Heterozygous mice did not develop any tumors or neurological symptoms within one year. In conclusion, our

findings demonstrate that *Smarca4* plays a major role in embryonic development because a homozygous loss mostly resulted in embryonic lethality or neuromuscular disorders. We hypothesize that an early homozygous *Smarca4* knockout is required for tumor development in human but is lethal in mice. In addition, it is still possible that AT/RT-SMARCA4 arise from a different cell type or require a *Smarca4* inactivation earlier than at E7.5.

This is why we need to investigate a *Smarca4* loss in different cell types and at different timepoints in numerous combinations. Therefore, the *Cre/loxP* system is not appropriate, as this will result in a huge number of mice, and it will be very time-consuming.

To enclose the timepoint of *Smarca4* loss, which does not result in embryonic lethality, we plan to perform *in vitro* studies. The cultivation of murine embryo cells of *Smarca4*$^{fl/fl}$ mice at early timepoints, like E3.5-E9.5, is one possibility. By using a *Cre* virus, it is possible to induce a *Smarca4* knockout in these cells. Afterwards, cell viability assays will be performed to define the timepoint of highest viability of the embryonic cells. It is most likely that a homozygous *Smarca4* knockout at the identified timepoint does not result in embryonic lethality.

Another approach to test a variety of different timepoints and cell types is *in utero* electroporation. Using this method, a single-guide RNA (sgRNA) against *Smarca4* will be injected into the desired cell type at the desired timepoint *in utero*, and following electroporation, the sgRNA will be integrated, resulting in a *Smarca4* knockout (Kittock and Pilaz 2023). This is how a high number of cell type-timepoint combinations can be tested more efficiently compared to the *Cre/loxP* system. The *Smarca4* knockout will be performed by a *CRISPR/Cas9*-mediated system (Shinmyo et al. 2016). Therefore, we plan to cross *Rosa26-Cas9* mice (The Jackson Laboratory, #026179), which express the recombinase Cas9 ubiquitously, with *Smarca4-R.1189**$^{+/-}$ mice to achieve a mouse model that has a constitutive *Smarca4* germline mutation and that expresses the recombinase Cas9, which is required for *CRISPR/Cas9*-mediated *Smarca4* knockout. The resulting *Rosa26-Cas9::Smarca4-p.R1189**$^{+/-}$ mice will be further crossed with *Rosa26-Cas9* mice, and their embryos will be used for *in utero* electroporation. A sgRNA against *Smarca4* will be injected, and due to the ubiquitous expression of the Cas9 recombinase, a knockout of *Smarca4* can occur. This approach demonstrates a highly efficient method to test different combinations of cell types and timepoints for a *Smarca4* knockout, which will help to figure out the cellular origin of AT/RT-SMARCA4.

For the identification of the cellular origin of AT/RT-TYR, we used a different approach. As these tumors are mainly localized infratentorially, more precisely in the fourth ventricle with proximity to the CP, we hypothesized that precursors of the fourth ventricle CP could be the cellular origin of AT/RT-TYR. The overall goal was again to generate a mouse model, but at first, we wanted to perform histological and molecular analyses to strengthen our hypothesis.

At first, we want to underpin our hypothesis of precursors of the fourth ventricle CP being the cellular origin of AT/RT-TYR by some characteristics of cribriform neuroepithelial tumors (CRINETs). These are rare non-rhabdoid brain tumors that are characterized by a *SMARCB1* loss and cribriform growth patterns, which describes a sieve-shaped arrangement of cells (Hasselblatt et al. 2009). On DNA methylation level, they are highly similar to AT/RT-TYR. Interestingly, these tumors can be located supratentorially or infratentorially, but for both, almost all investigated tumors occurred in the ventricles with proximity to the CP. This is why the majority of these tumors were neuroradiologically considered as CP tumors (Johann et al. 2017). In addition, the cribriform growth pattern showed similarities to the cobblestone-like arrangement of the CP. These are all indications for CRINETS probably arising from the CP of all ventricles. The similarity to AT/RT-TYR strengthens our hypothesis that AT/RT-TYR also arise from the CP.

At the beginning, we examined 104 AT/RT biopsies of all DNA methylation subtypes, of which 53 were localized infratentorially. We scanned H&E stainings of these infratentorial biopsies for intermingled CP, which was predominantly detected in AT/RT-TYR (35%). In most of the cases, we observed a transition from healthy CP to tumor tissue, and it seemed like the tumors arose from the CP. In addition, the majority of examined AT/RT-TYR expressed CP markers using IHC, as opposed to the other subtypes. Furthermore, these tumors demonstrated an upregulation of CP marker genes on bulk RNAseq level compared to the other AT/RT DNA methylation subtypes and other CNS tumor entities. *CIBERSORT* analysis was performed to investigate transcriptomic similarities of AT/RT-TYR to the different cell types of the developing cerebellum. This resulted in the highest similarity to the fourth ventricle CP. SnRNAseq analyses revealed a cluster of cells of mixed AT/RT-TYR samples that expressed marker genes of the healthy CP (*TTR* and *FOLR1*) and that were not characterized by a chromosome 22 loss, identifying them as healthy CP cells. These cells clustered in direct proximity to the AT/RT-TYR tumor cells, which confirmed the similarity on the gene expression level. A *Foxj1-cre::Smarcb1*$^{fl/fl}$ mouse model was generated to specifically target CP cells and cells of the ependyma. *Foxj1* expression probably starts at E7.5 in fourth ventricle CP precursors. In the third and lateral ventricles, the expression is supposed to start later and only very patchily. These mice have not developed any tumors but were characterized by large, atypical fourth ventricle CP cells that demonstrated eccentric chromatin and a loss of characteristic cobblestone-like arrangement. These cells were monociliary, like human AT/RT-TYR, and showed high similarity to these tumors on gene expression level.

Overall, the finding that AT/RT-TYR tumors were histologically intermingled with CP tissue was exclusive to these tumors compared to other infratentorial tumors like MB. We also detected CP tissue at biopsies of the MB subtypes MB-WNT, MB-G3, and MB-G4, but the tumor was never intermingled with CP tissue. A major indication of precursors of the fourth ventricle CP

being the cellular origin of AT/RT-TYR, was the result of the *CIBERSORT* analysis, next to the CP marker expression on histological and transcriptomic level. This revealed a clear match of choroid plexus carcinoma (CPC) to the CP and of myxopapillary ependymoma (MPE) to ependymal cells, which are known to be their cellular origins, and therefore, they served as a technical control. For AT/RT-TYR, the highest similarity to the CP was calculated, which confirmed our hypothesis. Analysis for AT/RT-SHH and AT/RT-MYC has not resulted in a clear match. As described before, PGCs or the neural crest are assumed to be the cellular origins for AT/RT-MYC (Vitte et al. 2017; Custers et al. 2021; Graf et al. 2022), and AT/RT-SHH are supposed to arise from neural progenitors, more precisely from the midbrain-hindbrain boundary or the ganglionic eminence, depending on the localization of the tumor (Graf et al. 2022; Lobón-Iglesias et al. 2023). These cell types were not included in the reference data set of the developing human cerebellum (Aldinger et al. 2021). In addition, only a minority of AT/RT-SHH and AT/RT-MYC arises in the cerebellum (Johann et al. 2016; Holdhof et al. 2020a; Ho et al. 2020). Previous *Smarcb1*-deficient mouse models have not developed AT/RT-TYR-like tumors. We hypothesized that this is due to the fact that the fourth ventricle CP was not targeted by previous mouse models, and therefore, the *Smarcb1* loss did not occur in the AT/RT-TYR cell of origin. We investigated SMARCB1 IHC of the fourth ventricle CP of *Math1-cre::Smarcb1*$^{fl/fl}$, *Nestin-cre::Smarcb1*$^{fl/fl}$, *Rosa-cre*^{ERT2}*::Smarcb1*$^{fl/fl}$, *Sox2-cre*^{ERT2}*::Smarcb1*$^{fl/fl}$, and *Olig1-cre::Smarcb1*$^{fl/fl}$ mice. Only the latter demonstrated a *Smarcb1* loss in a few cells, which was in line with the fact that *Olig1* is only patchily expressed in the fourth ventricle CP, according to the Allen Developing Mouse Brain Atlas (https://developingmouse.brain-map.org). Additionally, its expression is starting later, around E13.5, which is probably too late, as we assume that these tumors arise very early during embryonic development because AT/RT-TYR arise in the youngest patients next to AT/RT-SMARCA4 (Holdhof et al. 2020a). Although *Foxj1-cre::Smarcb1*$^{fl/fl}$ mice have not developed tumors, we are convinced that this promoter is of importance, as it is the first one that targets the fourth ventricle CP precursors very early. Therefore, something else is missing for tumor development, and we hypothesize that this is a second genetic alteration. Previous studies have shown that a second genetic alteration was required for the generation of mouse models of different tumor entities, although this is not required for human tumors (Zhu et al. 2005). This was even previously shown for two RT mouse models. Ng et al. generated *GFAP-cre::Smarcb1*$^{fl/fl}$*::p53*$^{fl/fl}$ mice, although *TP53* mutations only rarely occur in human AT/RT. Nevertheless, these mice developed AT/RT-like tumors, which arose from the cerebellum starting after five months of life (Ng et al. 2015). In addition, *Smarcb1*$^{+/-}$*::p53*$^{+/-}$ mice developed malignant rhabdoid tumors (MRT; DelBove et al. 2009). Therefore, we aimed to introduce a second genetic alteration in our *Foxj1-cre::Smarcb1*$^{fl/fl}$ mice. As mentioned before, there are no further frequent recurrent mutations than *SMARCB1* and *SMARCA4* mutations in AT/RT (Hasselblatt et al. 2013), but some cases

demonstrated a *LIN28A* overexpression. LIN28A is a stem cell factor that is critically involved in developmental processes (Weingart et al. 2015). Although it was associated with driver functions of proliferation in glioblastoma (Mao et al. 2013) and with overexpression in embryonal tumors with multilayered rosettes (ETMR), its entire function in brain development remains unknown, and it is not known to play an overall role in tumor induction in the CNS (Middelkamp et al. 2021). By generating *Foxj1-cre::lsl-Lin28a::Smarcb1*$^{fl/fl}$ mice, we demonstrated that an additional *Lin28a* overexpression was not sufficient to generate murine tumors. Although we see *LIN28A* overexpression in human AT/RT, it was not described that LIN28A has driver functions in these tumors. Therefore, we plan to induce a *TP53* knockout as second genetic alteration because it was previously associated with CNS tumor driver functions. In addition, we identified at least some AT/RT cases with *TP53* mutations. We investigated whole genome/exome sequencing data of 86 AT/RT belonging to different DNA methylation subtypes, which resulted in at least 8% (n = 7/86; 4× AT/RT-SHH, 1× AT/RT-TYR, 2× unknown) of the cases exhibiting *TP53* mutations (Lee et al. 2012; Johann et al. 2016; Hasselblatt et al. 2022; Sturm et al. 2023). Furthermore, Ng et al. and Del Bove et al. successfully generated murine RT-like tumors with a combination of *Smarcb1* and *p53* knockouts (DelBove et al. 2009; Ng et al. 2015), and therefore, we plan to target this in the fourth ventricle CP by generating *Foxj1-cre::Smarcb1*$^{fl/fl}$*::p53*$^{fl/fl}$ mice. We hypothesize that these two genetic alterations will induce the development of RT-like tumors arising from the fourth ventricle CP. Despite our mouse model not having developed tumors, an interesting observation was that CP cells of the fourth ventricle were monociliary, whereas control CP cells were multiciliary. This was, as well as the complete morphological phenotype, exclusive for the fourth ventricle CP because *Foxj1* expression in the forebrain CP starts later by only displaying patchy expression (Lobas et al. 2012). Monocila were already characterized in the context of human AT/RT, which were enriched in AT/RT-TYR and associated with enhanced aggressiveness (Johann et al. 2016; Blümel et al. 2022). Next to the similar gene expression profiles of the fourth ventricle CP of *Foxj1-cre::Smarcb1*$^{fl/fl}$ mice and human AT/RT, the occurrence of monocilia confirmed the similarity on an additional level. As mentioned above, we observed further morphological changes in the murine CP cells. The chromatin was not distributed equally and was displayed as eccentric chromatin. This structure was previously characterized for the open chromatin state, called euchromatin. This state allows accessibility of the DNA, which therefore enables active transcription (Morrison and Thakur 2021). The *Smarcb1* loss likely affected the normal function of the SWI/SNF chromatin remodeling complex, leading to an altered chromatin accessibility. We assume that the Wnt signaling pathway additionally influenced these chromatin changes. Upregulation of the Wnt signaling pathway was previously reported (Johann et al. 2016), and we demonstrated that Wnt signaling pathway genes were upregulated in our mouse model. Wnt signaling was previously

associated with euchromatic structures, which strengthens our hypothesis (Matoba et al. 2023; Pagella et al. 2023; Nordin et al. 2024).

Overall, we aim to further characterize the chromatin changes in our mouse model compared to human AT/RT-TYR, as chromatin changes are crucially involved in numerous human cancers. At first, we plan to perform additional comparisons of the morphology using IHC, like screening for prominent nucleoli, which are characteristic for rhabdoid cells (Biswas et al. 2016; Louis et al. 2021). Secondly, we plan to perform an Assay for Transposase-Accessible Chromatin (ATAC) sequencing. This method includes sequencing of the accessible DNA regions. We aim to investigate similarities to human AT/RT-TYR and differences to control mice. This can provide insights into the exact mechanism underlying the chromatin changes, and in addition, it will potentially help to identify the missing factor for tumor development.
Furthermore, we plan to thoroughly investigate the monocilia, as they are a unique feature in both human AT/RT and the fourth ventricle CP of *Foxj1-cre::Smarcb1*$^{fl/fl}$ mice. At first, we want to investigate a larger cohort of CNS tumors for the occurrence of monocilia, after they were also detected in CPC and ependymoma. We aim to figure out whether this is a feature exclusive to tumors arising from ciliated cells, which would also strengthen our hypothesis that AT/RT-TYR arise from the CP. We will investigate biopsies of all DNA methylation subtypes of ependymoma, MB, and pineoblastoma by using ARL13B stainings.
Finally, we hypothesize that an additional alteration of a gene that was previously associated with the induction of CNS tumors will lead to tumor development in mice. Therefore, we are currently generating *Foxj1-cre::Smarcb1*$^{fl/fl}$*::p53*$^{fl/fl}$ mice to target a loss of both *Smarcb1* and *p53* in the CP of the fourth ventricle.

In summary, this work gives meaningful insights into the cellular origins of AT/RT and the mechanisms regarding tumor progression, therapy resistance, and recurrence. But these should not be considered only as separate projects, it is known that the cellular origins of a tumor fundamentally shape the developmental trajectory of a tumor (Azzarelli et al. 2018). The cell of origin leads to the first decisions regarding tumor development due to specific genetic and epigenetic characteristics. This development not only includes the emergence of a primary tumor, but it might also affect tumor progression, including therapy resistance and the development of recurrences (Johnson et al. 2014; Azzarelli et al. 2018; Bhat et al. 2024; Zhang et al. 2024). This was previously shown in different tumor entities, which will be discussed in the following sections.
Overall, it has been shown that the cell of origin highly influences features of CSCs, which are known to play a crucial role in therapy resistance, tumor progression, and recurrence. This potentially includes tumorigenicity, differentiation, and therapy response (Bamodu et al. 2024). It is assumed that the characteristics of a cell of origin are transmitted to the developing tumor cells, including CSCs (Gupta et al. 2019).

For different glioblastoma subtypes, different cellular origins are known. Those that originate from neural stem cells displayed aggressive, infiltrative tumors, whereas those arising from neural progenitors demonstrated less aggressive behavior (Chen et al. 2012). Another subtype that potentially arises from mesenchymal stem cells is also associated with increased invasiveness, therapy resistance, and inferior prognosis (Hossain et al. 2015; Jiménez et al. 2018). This is not exclusive to CNS tumors. In colorectal cancer, the tumors arising from intestinal stem cells were characterized by increased metastatic potential, whereas those arising from differentiated cell types were associated with a better prognosis (Barker et al. 2009). Distinct influences of the cell of origin on the tumor behavior were also described for prostate cancer (Goldstein et al. 2010), breast cancer (Chauhan et al. 2023), and melanoma (Scaini et al. 2024), among others. In addition, it is assumed that different signaling pathways are involved in the formation of CSCs, and the respective pathways are dependent on the cell of origin. For instance, SHH signaling is supposed to drive CSC properties in cerebellar stem cells that give rise to MB (Lee et al. 2013). In glioblastoma, EGFR signaling is assumed to induce CSC formation from neural stem cells (Verhaak et al. 2010).
The chromatin status is also supposed to be involved in the CSC formation (Kim et al. 2014). This is interesting for the findings in AT/RT-TYR, as a Smarcb1 loss in murine fourth ventricle CP resulted in an euchromatic structure, which is an open chromatin state. Open chromatin regions were previously associated with CSC formation and tumor heterogeneity (Kim et al. 2014).
Furthermore, EMT, which we identified in the context of therapy resistance in AT/RT, plays a crucial role in the formation of CSCs. This process is supposed to be influenced by the cell of origin (Turner and Kohandel 2010).

The overall aim is to develop targeted therapies for AT/RT by addressing therapy-resistant CSCs or the cell of origin. Current therapies mostly result in AT/RT tumor progression and recurrence and have severe cytotoxic side effects. Therefore, targeted therapies are urgently needed. The already existing approaches for targeting CSCs in various tumor entities will be discussed in the following sections.
Standard-of-care chemotherapy mainly targets proliferating cells, and therefore, dormant CSCs are not affected. One approach is to target CSC surface marker genes, like *CD44* or *CD133*, or intracellular markers like *ALDH1* or *SOX2* (Chu et al. 2024). For instance, *CD133* silencing in glioblastoma neurospheres has been shown to inhibit self-renewal and tumorigenic potential (Brescia et al. 2013). Another, in our case more promising, approach is targeting pathways that induce CSCs. Here, we identified the TGF-β signaling pathway in the context of therapy resistance in AT/RT. Previously, an inhibitor called Celastrus orbiculatus was found to target the TGF-β signaling in gastric CSCs by inhibition of *Smad3/4* (Ni et al. 2024). Further targets of the TGF-β signaling could be *TGF-β1-3*. As already mentioned, TGF-β signaling can

also induce EMT. This is why TGF-β signaling blockage is also considered for the inhibition of EMT. For this purpose, mainly TGF-β receptor (TGF-βR) inhibitors are currently being tested in clinical trials (Jonckheere et al. 2022). For solid cancers, these are phase 1 clinical trials of LY-3022859 (Tolcher et al. 2017) and SHR-1701 (Feng et al. 2022), which both block the TGF-βR2, and YL-13027 (Li et al. 2021), which blocks the TGF-βR1. Other CSC-associated pathways, like the Wnt signaling pathway, were previously targeted by the Wnt pathway inhibitor ICG-001, which eliminated the stemness phenotype in colorectal cancer (Choi et al. 2021). An additional promising target is the ECM (Huang et al. 2021a). As described above, altered ECM organization was associated with therapy resistance and the formation and maintenance of CSCs. *In vitro* experiments demonstrated that the ECM binds to cytokines like TGF-β, BMP, FGF, HGF, and VGF (Casazza et al. 2014), and changes in the ECM could promote the cytokine signaling, which then leads to increased expression of CSC marker genes like *CD44* and *CD133* (Yang et al. 2020). For therapeutic approaches targeting the ECM, again, TGF-β signaling is a promising candidate. TGF-β signaling is involved in collagen synthesis, which is a major component of the ECM. Multiple inhibitors, which reduce collagen synthesis, are currently being tested in clinical trials (Huang et al. 2021b). Among others, the monoclonal antibody fresolimumab is under investigation (Morris et al. 2014), and the inhibitor halofuginone reduced the collagen synthesis *in vitro* and in animal models of diverse tumor entities (Zion et al. 2009; Juárez et al. 2012; Lin et al. 2015; Juárez et al. 2017). To decrease the stiffness of the matrix, a feature also associated with therapy resistance, collagenases are an additional approach to reduce the collagen synthesis (Dolor and Szoka 2018). Additionally, integrin is a promising target to reduce the ECM stiffness. This was previously shown in clinical trials for different tumor entities by using the monoclonal antibodies Vitaxin or Volociximab (Gutheil et al. 2000; Figlin et al. 2006; Evans et al. 2007; Ricart et al. 2008; Bell-McGuinn et al. 2011). In summary, a variety of inhibitors, which target the ECM, are currently being investigated *in vitro*, *in vivo* in animal models, and in clinical trials. These approaches focus on collagen degradation and reduction of cross-linking, TGF-β signaling silencing, integrin binding inhibition, and many more (Huang et al. 2021b).

In conclusion, the development of AT/RT was thoroughly characterized in this study. Therefore, we performed histopathological and molecular analyses in order to identify the cellular origins and developmental timepoints of AT/RT, as well as to characterize therapy resistance, tumor progression, and recurrence.

We generated different *Smarca4*-deficient mouse models to investigate the development of AT/RT-SMARCA4. These mouse models have not developed tumors, but those that were not embryonally lethal displayed striking neuromuscular deficiencies, which confirmed the importance of *Smarca4* in embryonal development. Therefore, the cellular origins of AT/RT-SMARCA4 remain unknown, and different combinations of target cells and timepoints of

Smarca4 knockout should be tested *in vitro* and by using *in utero* electroporation in the next steps.

For AT/RT-TYR, we identified signatures of the CP on histopathological and gene expression level. Because these tumors are mostly located in the fourth ventricle, we assumed that CP precursors of the fourth ventricle could be a potential cellular origin of AT/RT-TYR. CP marker expression was predominant for AT/RT-TYR compared to the other subtypes and CNS tumor entities. *CIBERSORT* analysis confirmed the high similarity of AT/RT-TYR to the CP, and healthy CP cells were found in snRNAseq data of AT/RT-TYR biopsies, which clustered in proximity to the tumor cells. We generated *Foxj1-cre::Smarcb1*$^{fl/fl}$ mice that have not developed tumors but demonstrated a Smarcb1 loss exclusively in the fourth ventricle CP and ependyma. CP cells were characterized by large, atypical nuclei with an open chromatin state. In addition, CP cells were monociliary like human AT/RT-TYR tumor cells. Furthermore, these murine CP cells showed highly similar transcriptomic profiles compared to AT/RT-TYR. The next steps will include the introduction of a second genetic alteration, like a *p53* loss.

Regarding the mechanisms of tumor progression and recurrence, we collected 26 AT/RT primary-recurrence pairs, for which we investigated the DNA methylation profiles, including CNVs, and partially the gene expression profiles. This revealed that primary tumors and paired recurrences were highly similar on the DNA methylation level, but CNVs were increased in AT/RT-SHH recurrences. We observed an enhanced chromosome 1q gain and chromosome 10 loss. Differentially expressed cancer-associated genes were identified, which could be used, in addition to genes affected by the CNVs, as novel therapeutic targets. In the next steps, a larger cohort for AT/RT-MYC and ATRT-TYR is required to identify molecular alterations for these subtypes. Furthermore, our findings should be validated *in vitro*, and therefore, the generation of a recurrent AT/RT-SHH cell line would be useful.

In addition, we were interested in the mechanisms behind the development of those recurrences, and we assumed that therapy resistance might play a role, because this is the major cause of tumor progression and recurrence in other entities. We generated snRNAseq data of eight paired primary and recurrent AT/RT to identify therapy-resistant cells and to get insights into the intratumoral heterogeneity, as well as into the interaction with the TME. We identified such therapy-resistant cells in AT/RT-MYC primary tumors, which were characterized by increased ECM remodeling and cytokine signaling, among others. For AT/RT-MYC recurrences, the number of cells undergoing pEMT was significantly increased, which was confirmed *in vitro*, and *CD1A*$^{+}$ *CD207*$^{+}$ DCs were enriched in recurrences. These findings were previously associated with therapy resistance and tumor progression in other CNS tumor entities, and TGF-β signaling was found to be involved in all these changes. Overexpression of genes identified in therapy-resistant cells, as well as the occurrence of *CD1A*$^{+}$ *CD207*$^{+}$ DCs in recurrences, correlated with an inferior survival of AT/RT patients. The next steps should

include the identification of the spatial localization of therapy-resistant cells, *in vitro* validation, including interactions with the ECM, and *in vivo* experiments using PDOX models.

Overall, our findings should not only be considered separately, it was previously demonstrated that the cellular origins affect the development of a tumor, also including a possible progression or recurrence. Therefore, the cell of origin is also critically involved in the development of therapy resistance, which was previously shown in other tumor entities. In conclusion, our findings regarding the cellular origin and development of therapy resistance and recurrence serve as meaningful approaches to develop novel therapeutic strategies.

7. Abstract

Atypical teratoid/rhabdoid tumors (AT/RT) are rare embryonal tumors of the central nervous system that affect very young children and have a poor prognosis. Based on DNA methylation profiles, the different subtypes AT/RT-SHH, AT/RT-TYR, AT/RT-MYC, and AT/RT-SMARCA4 were identified. Although the genetics of these tumors are known, targeted therapies are lacking. Therefore, we aimed to identify the cellular origins of AT/RT and to characterize the mechanisms of tumor progression and recurrence, including therapy resistance. Both should help to develop novel therapeutic approaches.

In the first part of the project, we investigated paired primary and recurrent AT/RT using DNA methylation profiling and bulk RNA sequencing, which revealed an increased chromosome 1q gain and chromosome 10 loss in recurrences and differential expression of cancer-associated genes. Single-nucleus RNA sequencing revealed an enrichment of *CD1A*$^{+}$ *CD207*$^{+}$ dendritic cells (DCs) in recurrences and a high number of AT/RT-MYC tumor cells undergoing partial epithelial-mesenchymal transition. Potentially therapy-resistant cells were identified in AT/RT-MYC, which were characterized by increased extracellular matrix remodeling, among others. Overexpression of respective genes and occurrence of *CD1A*$^{+}$ *CD207*$^{+}$ DCs correlated with an inferior survival of AT/RT patients. All findings were associated with TGF-β signaling – a novel, promising therapeutic target.

The second part of this work deals with the identification of the cellular origins of AT/RT-SMARCA4 and AT/RT-TYR, because these are completely unknown and mouse models are lacking. We generated different *Smarca4*-deficient mouse models that targeted distinct cell types at specific timepoints. These mice did not develop tumors, but an important role of *Smarca4* in the embryonic development was demonstrated, because *Smarca4* loss either resulted in embryonic lethality or neuromuscular disorders. For AT/RT-TYR, we revealed that precursors of the choroid plexus (CP) of the fourth ventricle are potentially the cellular origin. A high proportion of AT/RT-TYR biopsies was intermingled with CP tissue, and immunohistochemistry and RNA sequencing showed that CP marker genes were predominantly expressed in AT/RT-TYR. Deconvolution analyses demonstrated the highest similarity of AT/RT-TYR to the CP. Finally, *Foxj1-cre::Smarcb1*$^{fl/fl}$ mice displayed a Smarcb1 loss in the CP, resulting in large, atypical, monociliary CP cells. These mice did not develop tumors but demonstrated high similarity to human AT/RT-TYR on gene expression level.

In conclusion, our work demonstrated insights into the development of AT/RT, as well as mechanisms of progression and recurrence, which both revealed novel potential therapeutic targets.

8. Zusammenfassung

Atypische teratoide/rhabdoide Tumore (AT/RT) sind seltene embryonale Tumore des zentralen Nervensystems, die hauptsächlich bei sehr jungen Kindern auftreten und mit einer schlechten Prognose assoziiert werden. Basierend auf den DNA-Methylierungsprofilen wurden die verschiedenen Subtypen AT/RT-SHH, AT/RT-TYR, AT/RT-MYC und AT/RT-SMARCA4 identifiziert. Obwohl die genetischen Ursachen bekannt sind, gibt es keine zielgerichteten Therapien. Deswegen ist das Ziel, die zellulären Ursprünge von AT/RT zu identifizieren und die Mechanismen der Tumorprogression und Rezidiventstehung, einschließlich der Therapieresistenz, zu charakterisieren. Beides soll dabei helfen, neue therapeutische Ansätze zu entwickeln.

Im ersten Teil des Projektes haben wir gepaarte AT/RT-Primärtumore und -Rezidive mithilfe von DNA-Methylierungsprofilen und bulk-RNA-Sequenzierungen untersucht, was sowohl in einem erhöhten Chromosom-1q-Gewinn und Chromosom-10-Verlust resultierte als auch in einer differentiellen Expression von Krebs-assoziierten Genen. Einzelkern-RNA-Sequenzierungsanalysen zeigten eine Anreicherung von *CD1A*$^{+}$ *CD207*$^{+}$ dendritischen Zellen (DZ) in Rezidiven sowie eine Vielzahl an AT/RT-MYC Tumorzellen, die sich einem einseitigen epithelialen-mesenchymalen Übergang unterziehen. Potenziell therapieresistente ATRT-MYC-Zellen wurden identifiziert, welche unter anderem durch verstärkten Umbau der extrazellulären Matrix charakterisiert wurden. Die Überexpression beteiligter Gene und das Vorhandensein von *CD1A*$^{+}$ *CD207*$^{+}$ DZ konnten mit einem verschlechterten Überleben von AT/RT-Patient/innen korreliert werden. Alle Ergebnisse konnten mit dem TGF-β-Signalweg in Verbindung gebracht werden – ein neuer, vielversprechender therapeutischer Angriffspunkt.

Der zweite Teil dieser Arbeit beschäftigt sich mit der Identifizierung der zellulären Ursprünge von AT/RT-SMARCA4 und AT/RT-TYR, da diese bisher komplett unbekannt sind und es keine Mausmodelle gibt. Wir haben verschiedene *Smarca4*-defiziente Mausmodelle generiert, die auf verschiedene Zelltypen zu bestimmten Zeitpunkten abzielten. Diese Mäuse haben keine Tumore entwickelt, aber es wurde eine wichtige Rolle von *Smarca4* in der Embryonalentwicklung gezeigt, da ein *Smarca4*-Verlust entweder in embryonaler Letalität oder neuromuskulären Störungen resultierte. Für AT/RT-TYR haben wir Choroid Plexus (CP) Vorläufer des vierten Ventrikels als potenziellen Ursprung identifiziert. Eine Vielzahl an AT/RT-TYR-Biopsien war mit CP-Gewebe vermischt und Immunhistochemie und RNA-Sequenzierungen zeigten eine verstärkte CP-Markergenexpression in AT/RT-TYR. Dekonvolutionsanalysen ergaben die größte Ähnlichkeit von AT/RT TYR zum CP. Letztendlich zeigten *Foxj1-cre::Smarcb1*$^{fl/fl}$ Mäuse einen Smarcb1-Verlust im CP, welcher in großen,

atypischen, monoziliären CP-Zellen resultierte. Diese Mäuse haben keine Tumore entwickelt, zeigten aber eine große Ähnlichkeit zu humanen AT/RT-TYR auf Genexpressionsebene.

Schlussendlich hat unsere Arbeit Einblicke in die Entstehung von AT/RT sowie in die Mechanismen der Progression und des Rezidivierens gewährt. Beides zeigte neue mögliche therapeutische Angriffspunkte.

9. Abbreviations

ATAC	Assay for Transposase-Accessible Chromatin
AT/RT	atypical teratoid/rhabdoid tumor
BH	Benjamini-Hochberg
CBTC	Canadian Paediatric Brain Tumor Consortium
CNS	central nervous system
CNV	copy-number variation
COL1A1	type I collagen
CP	choroid plexus
CPC	choroid plexus carcinoma
CRINET	cribriform neuroepithelial tumor
CSC	cancer stem cell
DC	dendritic cell
DEG	differential gene expression
DFCI	Dana Farber Cancer Institute
DOX	doxorubicin
E	embryonal day
ECM	extracellular matrix
eCN	excitatory cerebellar interneuron
EMA	epithelial membrane antigen
eMRT	extracranial malignant rhabdoid tumor
EMT	epithelial-mesenchymal transition
esBAF	embryonic-stem-cell-BAF
ETMR	embryonal tumor with multilayered rosettes
EU-RHAB	European Rhabdoid Registry
excit.	excitatory
FFPE	formalin-fixed paraffin-embedded
fl	*floxed = flanked by loxP*
GABA	Gamma-Aminobutyric Acid
GCP	granule cell precursor
GEO	Gene Expression Omnibus

GLM	generalized linear model
H&E	Hematoxylin and Eosin
HAT	histon acetyltransferase
HPF	high power field
ICE	ifosfamide, carboplatinum, etoposide
IHC	immunohistochemistry
inh.	inhibitory
IPC	induced pluripotent stem cell
IVIS	In Vivo Imaging System
JSD	Jensen-Shannon divergence
LAPTM5	lysosomal transmembrane protein 5
LHC	Langerhans cell
MB	medulloblastoma
mol.	molecular
MPE	myxopapillary ependymoma
MPZ	myelin protein zero
MRT	malignant rhabdoid tumor
MS	median survival
MTX	methotrexate
nBAF	neuronal BAF
npBAF	neural progenitor BAF
NSG	NOD-SCID gamma
OPC	oligodendrocyte progenitor cell
OS	overall survival
P	postnatal day
P0	myelin protein zero
PCA	principal component analysis
PDOX	patient-derived orthotopic xenograft
pEMT	partial epithelial-mesenchymal transition
PFS	progression-free survival
PGC	pluripotent germ cell
prog.	progenitor
r	rhombomere

RGC	radial glial cell
RGL2	Ral Guanine Nucleotide Dissociation Stimulator Like 2
RNAseq	RNA sequencing
RT	rhabdoid tumor
RTK	rhabdoid tumor of the kidney
RTPS	rhabdoid tumor predisposition syndrome
RTX	radiotherapy
sFDR	spatial false discovery rate
sgRNA	single-guide RNA
SHH	sonic hedgehog
snn	shared nearest neighbor
scRNAseq	single-cell RNA sequencing
snRNAseq	single-nucleus RNA sequencing
SWI/SNF	switch/sucrose non-fermentable
Tam	tamoxifen
TGF-βR	TGF-β receptor
TBO	toluidine blue
TF	transcription factor
TIL	tumor-infiltrating lymphocyte
TME	tumor microenvironment
Treg	regulatory T-cell
t-SNE	*t*-stochastic neighbor embedding
UBC	unipolar brush cell
UMAP	uniform manifold approximation and projection
URL	upper rhombic lip
VCA	vincristine, cyclophosphamide, actinomycin-D
VST	variance stabilized transformation
VZ	ventricular zone
wt	wildtype

10. References

Abagnale G, Schwentner R, Ben Soussia-Weiss P, van Midden W, Sturtzel C, Pötschger U, Rados M, Taschner-Mandl S, Simonitsch-Klupp I, Hafemeister C, Halbritter F, Distel M, Eder SK, Hutter C (2025) BRAFV600E induces key features of LCH in iPSCs with cell type–specific phenotypes and drug responses. Blood 145(8):850–865. https://doi.org/10.1182/blood.2024026066

Aldinger KA, Thomson Z, Phelps IG, Haldipur P, Deng M, Timms AE, Hirano M, Santpere G, Roco C, Rosenberg AB, Lorente-Galdos B, Gulden FO, O'Day D, Overman LM, Lisgo SN, Alexandre P, Sestan N, Doherty D, Dobyns WB, Seelig G, Glass IA, Millen KJ (2021) Spatial and cell type transcriptional landscape of human cerebellar development. Nat Neurosci 24(8):1163–1175. https://doi.org/10.1038/s41593-021-00872-y

Araki A, Chocholous M, Gojo J, Dorfer C, Czech T, Heinzl H, Dieckmann K, Ambros IM, Ambros PF, Slavc I, Haberler C (2016) Chromosome 1q gain and tenascin-C expression are candidate markers to define different risk groups in pediatric posterior fossa ependymoma. Acta Neuropathol Commun 4(1):88. https://doi.org/10.1186/s40478-016-0349-9

Arnhold V, Oyen F, Schneppenheim R, Haberl H, Koch A, Frühwald MC, Hernáiz Driever P (2016) Long-term survival of an infant with an atypical teratoid/rhabdoid tumor following subtotal resection and low-cumulative dose chemotherapy: a case report. Child's Nervous System 32(6):1157–1161. https://doi.org/10.1007/s00381-015-2999-5

Aslan M, Hsu E-C, Liu S, Stoyanova T (2021) Quantifying the invasion and migration ability of cancer cells with a 3D Matrigel drop invasion assay. Biol Methods Protoc 6(1). https://doi.org/10.1093/biomethods/bpab014

Azzarelli R, Simons BD, Philpott A (2018) The developmental origin of brain tumours: a cellular and molecular framework. Development 145(10). https://doi.org/10.1242/dev.162693

Bamodu OA, Chung C-C, Pisanic TR, Wu ATH (2024) The intricate interplay between cancer stem cells and cell-of-origin of cancer: implications for therapeutic strategies. Front Oncol 14. https://doi.org/10.3389/fonc.2024.1404628

Barkan D, Green JE, Chambers AF (2010) Extracellular matrix: A gatekeeper in the transition from dormancy to metastatic growth. Eur J Cancer 46(7):1181–1188. https://doi.org/10.1016/j.ejca.2010.02.027

Barker N, Ridgway RA, van Es JH, van de Wetering M, Begthel H, van den Born M, Danenberg E, Clarke AR, Sansom OJ, Clevers H (2009) Crypt stem cells as the cells-of-origin of intestinal cancer. Nature 457(7229):608–611. https://doi.org/10.1038/nature07602

Bell-McGuinn KM, Matthews CM, Ho SN, Barve M, Gilbert L, Penson RT, Lengyel E, Palaparthy R, Gilder K, Vassos A, McAuliffe W, Weymer S, Barton J, Schilder RJ (2011) A phase II, single-arm study of the anti-α5β1 integrin antibody volociximab as monotherapy in patients with platinum-resistant advanced epithelial ovarian or primary peritoneal cancer. Gynecol Oncol 121(2):273–279. https://doi.org/10.1016/j.ygyno.2010.12.362

Benesch M, Bartelheim K, Fleischhack G, Gruhn B, Schlegel PG, Witt O, Stachel KD, Hauch H, Urban C, Quehenberger F, Massimino M, Pietsch T, Hasselblatt M, Giangaspero F, Kordes U, Schneppenheim R, Hauser P, Klingebiel T, Frühwald MC (2014) High-dose

chemotherapy (HDCT) with auto-SCT in children with atypical teratoid/rhabdoid tumors (AT/RT): a report from the European Rhabdoid Registry (EU-RHAB). Bone Marrow Transplant 49(3):370–375. https://doi.org/10.1038/bmt.2013.208

Bhat GR, Sethi I, Sadida HQ, Rah B, Mir R, Algehainy N, Albalawi IA, Masoodi T, Subbaraj GK, Jamal F, Singh M, Kumar R, Macha MA, Uddin S, Akil ASA-S, Haris M, Bhat AA (2024) Cancer cell plasticity: from cellular, molecular, and genetic mechanisms to tumor heterogeneity and drug resistance. Cancer and Metastasis Reviews 43(1):197–228. https://doi.org/10.1007/s10555-024-10172-z

Biegel JA, Zhou JY, Rorke LB, Stenstrom C, Wainwright LM, Fogelgren B (1999) Germ-line and acquired mutations of INI1 in atypical teratoid and rhabdoid tumors. Cancer Res 59(1):74–79

Biswas A, Kashyap L, Kakkar A, Sarkar C, Julka PK (2016) Atypical teratoid/rhabdoid tumors: challenges and search for solutions. Cancer Manag Res 8:115–125. https://doi.org/10.2147/CMAR.S83472

Blümel L, Qin N, Berlandi J, Paisana E, Cascão R, Custódia C, Pauck D, Picard D, Langini M, Stühler K, Meyer F-D, Göbbels S, Malzkorn B, Liebau MC, Barata JT, Jeibmann A, Kerl K, Erkek S, Kool M, Pfister SM, Johann PD, Frühwald MC, Borkhardt A, Reifenberger G, Faria CC, Fischer U, Hasselblatt M, Bartl J, Remke M (2022) Primary cilia contribute to the aggressiveness of atypical teratoid/rhabdoid tumors. Cell Death Dis 13(9):806. https://doi.org/10.1038/s41419-022-05243-4

Bögershausen N, Wollnik B (2018) Mutational Landscapes and Phenotypic Spectrum of SWI/SNF-Related Intellectual Disability Disorders. Front Mol Neurosci 11. https://doi.org/10.3389/fnmol.2018.00252

Bookhout C, Bouldin TW, Ellison DW (2018) Atypical teratoid/rhabdoid tumor with retained INI1 (SMARCB1) expression and loss of BRG1 (SMARCA4). Neuropathology 38(3):305–308. https://doi.org/10.1111/neup.12452

Braun SMG, Petrova R, Tang J, Krokhotin A, Miller EL, Tang Y, Panagiotakos G, Crabtree GR (2021) BAF subunit switching regulates chromatin accessibility to control cell cycle exit in the developing mammalian cortex. Genes Dev 35(5–6):335–353. https://doi.org/10.1101/gad.342345.120

Brescia P, Ortensi B, Fornasari L, Levi D, Broggi G, Pelicci G (2013) CD133 Is Essential for Glioblastoma Stem Cell Maintenance. Stem Cells 31(5):857–869. https://doi.org/10.1002/stem.1317

Bruschi M, Grill J, Guerrini-Rousseau L (2021) Pediatric brain tumors as a developmental disease. Curr Opin Oncol 33(6):608–614. https://doi.org/10.1097/CCO.0000000000000782

Bultman S, Gebuhr T, Yee D, La Mantia C, Nicholson J, Gilliam A, Randazzo F, Metzger D, Chambon P, Crabtree G, Magnuson T (2000) A Brg1 Null Mutation in the Mouse Reveals Functional Differences among Mammalian SWI/SNF Complexes. Mol Cell 6:1287–1295

Burger PC, Yu IT, Tihan T, Friedman HS, Strother DR, Kepner JL, Duffner PK, Kun LE, Perlman EJ (1998) Atypical teratoid/rhabdoid tumor of the central nervous system: a highly malignant tumor of infancy and childhood frequently mistaken for medulloblastoma: a Pediatric Oncology Group study. Am J Surg Pathol 22(9):1083–92. https://doi.org/10.1097/00000478-199809000-00007

Carey SS, Huang J, Myers JR, Mostafavi R, Orr B, Michalik LH, Klimo P, Boop F, Nichols KE, Merchant T, Ellison DW, Robinson GW, Onar-Thomas A, Gajjar A (2022) Outcomes for children with recurrent atypical teratoid rhabdoid tumor: A single institution study with updated molecular and germline analysis. Neuro Oncol 24(Supplement_1):i8. https://doi.org/https://doi.org/10.1093/neuonc/noac079.021

Casazza A, Di Conza G, Wenes M, Finisguerra V, Deschoemaeker S, Mazzone M (2014) Tumor stroma: a complexity dictated by the hypoxic tumor microenvironment. Oncogene 33(14):1743–1754. https://doi.org/10.1038/onc.2013.121

Cavalcanti IDL, Soares JCS (2021) Conventional Chemotherapy Versus Targeted Therapy. In: Advances in Cancer Treatment. Springer International Publishing, Cham, pp 79–89

Chakravarthy A, Khan L, Bensler NP, Bose P, De Carvalho DD (2018) TGF-β-associated extracellular matrix genes link cancer-associated fibroblasts to immune evasion and immunotherapy failure. Nat Commun 9(1):4692. https://doi.org/10.1038/s41467-018-06654-8

Chauhan A, Agarwal S, Masih M, Gautam PK (2023) The Multifunction Role of Tumor-Associated Mesenchymal Stem Cells and Their Interaction with Immune Cells in Breast Cancer. Immunol Invest 52(7):856–878. https://doi.org/10.1080/08820139.2023.2249025

Chen J, Li Y, Yu T-S, McKay RM, Burns DK, Kernie SG, Parada LF (2012) A restricted cell population propagates glioblastoma growth after chemotherapy. Nature 488(7412):522–526. https://doi.org/10.1038/nature11287

Cheng FY, Huang X, Sarangi A, Ketova T, Cooper MK, Litingtung Y, Chiang C (2012) Widespread Contribution of Gdf7 Lineage to Cerebellar Cell Types and Implications for Hedgehog-Driven Medulloblastoma Formation. PLoS One 7(4):e35541. https://doi.org/10.1371/journal.pone.0035541

Choi J-H, Jang T-Y, Jeon S-E, Kim J-H, Lee C-J, Yun H-J, Jung J-Y, Park S-Y, Nam J-S (2021) The Small-Molecule Wnt Inhibitor ICG-001 Efficiently Inhibits Colorectal Cancer Stemness and Metastasis by Suppressing MEIS1 Expression. Int J Mol Sci 22(24):13413. https://doi.org/10.3390/ijms222413413

Chu X, Tian W, Ning J, Xiao G, Zhou Y, Wang Z, Zhai Z, Tanzhu G, Yang J, Zhou R (2024) Cancer stem cells: advances in knowledge and implications for cancer therapy. Signal Transduct Target Ther 9(1):170. https://doi.org/10.1038/s41392-024-01851-y

Clapier CR, Iwasa J, Cairns BR, Peterson CL (2017) Mechanisms of action and regulation of ATP-dependent chromatin-remodelling complexes. Nat Rev Mol Cell Biol 18(7):407–422. https://doi.org/10.1038/nrm.2017.26

Comba A, Faisal SM, Dunn PJ, Argento AE, Hollon TC, Al-Holou WN, Varela ML, Zamler DB, Quass GL, Apostolides PF, Abel C, Brown CE, Kish PE, Kahana A, Kleer CG, Motsch S, Castro MG, Lowenstein PR (2022) Spatiotemporal analysis of glioma heterogeneity reveals COL1A1 as an actionable target to disrupt tumor progression. Nat Commun 13(1). https://doi.org/10.1038/s41467-022-31340-1

Consalez GG, Goldowitz D, Casoni F, Hawkes R (2021) Origins, Development, and Compartmentation of the Granule Cells of the Cerebellum. Front Neural Circuits 14. https://doi.org/10.3389/fncir.2020.611841

Cui K, Tailor P, Liu H, Chen X, Ozato K, Zhao K (2004) The Chromatin-Remodeling BAF Complex Mediates Cellular Antiviral Activities by Promoter Priming. Mol Cell Biol 24(10):4476–4486. https://doi.org/10.1128/MCB.24.10.4476-4486.2004

Custers L, Khabirova E, Coorens THH, Oliver TRW, Calandrini C, Young MD, Vieira Braga FA, Ellis P, Mamanova L, Segers H, Maat A, Kool M, Hoving EW, van den Heuvel-Eibrink MM, Nicholson J, Straathof K, Hook L, de Krijger RR, Trayers C, Allinson K, Behjati S, Drost J (2021) Somatic mutations and single-cell transcriptomes reveal the root of malignant rhabdoid tumours. Nat Commun 12(1):1–11. https://doi.org/10.1038/s41467-021-21675-6

Damen MPF, van Rheenen J, Scheele CLGJ (2021) Targeting dormant tumor cells to prevent cancer recurrence. FEBS J 288:6286–6303

Dani N, Herbst RH, McCabe C, Green GS, Kaiser K, Head JP, Cui J, Shipley FB, Jang A, Dionne D, Nguyen L, Rodman C, Riesenfeld SJ, Prochazka J, Prochazkova M, Sedlacek R, Zhang F, Bryja V, Rozenblatt-Rosen O, Habib N, Regev A, Lehtinen MK (2021) A cellular and spatial map of the choroid plexus across brain ventricles and ages. Cell 184(11):3056-3074.e21. https://doi.org/10.1016/j.cell.2021.04.003

D'cunja J, Shalaby T, Rivera P, von Büren A, Patti R, Heppner FL, Arcaro A, Rorke-Adams LB, Phillips PC, Grotzer MA (2007) Antisense treatment of IGF-IR induces apoptosis and enhances chemosensitivity in central nervous system atypical teratoid/rhabdoid tumours cells. Eur J Cancer 43(10):1581–1589. https://doi.org/10.1016/j.ejca.2007.03.003

DelBove J, Kuwahara Y, Mora-Blanco EL, Godfrey V, Funkhouser WK, Fletcher CDM, Van Dyke T, Roberts CWM, Weissman BE (2009) Inactivation of SNF5 cooperates with p53 loss to accelerate tumor formation in Snf5(+/-);p53(+/-) mice. Mol Carcinog 48(12):1139–48. https://doi.org/10.1002/mc.20568

Dittmer J (2015) The role of the transcription factor Ets1 in carcinoma. Semin Cancer Biol 35:20–38. https:://doi.org/10.1016/j.semcancer.2015.09.010

Dolor A, Szoka FC (2018) Digesting a Path Forward: The Utility of Collagenase Tumor Treatment for Improved Drug Delivery. Mol Pharm 15(6):2069–2083. https://doi.org/10.1021/acs.molpharmaceut.8b00319

Eilbert JL (2014) The Vertebrate Strategy for Brain Evolution. Procedia Comput Sci 41:233–242. https://doi.org/10.1016/j.procs.2014.11.108

Encha-Razavi F, Sonigo P (2003) Features of the developing brain. Child's Nervous System 19(7–8):426–428. https://doi.org/10.1007/s00381-003-0765-6

Erdreich-Epstein A, Robison N, Ren X, Zhou H, Xu J, Davidson TB, Schur M, Gilles FH, Ji L, Malvar J, Shackleford GM, Margol AS, Krieger MD, Judkins AR, Jones DTW, Pfister SM, Kool M, Sposto R, Asgharazadeh S (2014) PID1 (NYGGF4), a New Growth-Inhibitory Gene in Embryonal Brain Tumors and Gliomas. Clinical Cancer Research 20(4):827–836. https://doi.org/10.1158/1078-0432.CCR-13-2053

Esmatabadi MJD, Bakhshinejad B, Motlagh FM, Babashah S, Sadeghizadeh M (2016) Therapeutic resistance and cancer recurrence mechanisms: Unfolding the story of tumour coming back. J Biosci 41(3):497–506. https://doi.org/10.1007/s12038-016-9624-y

Evans T, Ramanathan RK, Yazji S, Glynne-Jones R, Anthoney A, Berlin J, Valle JW (2007) Final results from cohort 1 of a phase II study of volociximab, an anti-α5β1 integrin antibody, in combination with gemcitabine (GEM) in patients (pts) with metastatic pancreatic cancer (MPC). Journal of Clinical Oncology 25(18_suppl):4549–4549. https://doi.org/10.1200/jco.2007.25.18_suppl.4549

Federico A, Thomas C, Miskiewicz K, Woltering N, Zin F, Nemes K, Bison B, Johann PD, Hawes D, Bens S, Kordes U, Albrecht S, Dohmen H, Hauser P, Keyvani K, van

Landeghem FKH, Lund EL, Scheie D, Mawrin C, Monoranu CM, Parm Ulhøi B, Pietsch T, Reinhard H, Riemenschneider MJ, Sehested A, Sumerauer D, Siebert R, Paulus W, Frühwald MC, Kool M, Hasselblatt M (2022) ATRT–SHH comprises three molecular subgroups with characteristic clinical and histopathological features and prognostic significance. Acta Neuropathol 143(6):697–711. https://doi.org/10.1007/s00401-022-02424-5

Feil S, Valtcheva N, Feil R (2009) Inducible Cre Mice. Gene Knockout Protocols, Springer Protocols pp 343–363. https://doi.org/10.1007/978-1-59745-471-1_18

Feltri ML, D'Antonio M, Previtali S, Fasolini M, Messing A, Wrabetz L (1999) P0-Cre transgenic mice for inactivation of adhesion molecules in Schwann cells. Ann N Y Acad Sci Vol. 883:116–123

Feng J, Tang D, Wang J, Zhou Q, Peng J, Lou H, Sun Y, Cai Y, Chen H, Yang J, Liu P, Wang L, Zou J (2022) SHR-1701, a Bifunctional Fusion Protein Targeting PD-L1 and TGFβ, for Recurrent or Metastatic Cervical Cancer: A Clinical Expansion Cohort of a Phase I Study. Clinical Cancer Research 28(24):5297–5305. https://doi.org/10.1158/1078-0432.CCR-22-0346

Figlin RA, Kondagunta G V., Yazji S, Motzer RJ, Bukowski RM (2006) Phase II study of volociximab (M200), an α5β1 anti-integrin antibody in refractory metastatic clear cell renal cell cancer (RCC). Journal of Clinical Oncology 24(18_suppl):4535–4535. https://doi.org/10.1200/jco.2006.24.18_suppl.4535

Foulkes WD, Kamihara J, Evans DGR, Brugières L, Bourdeaut F, Molenaar JJ, Walsh MF, Brodeur GM, Diller L (2017) Cancer surveillance in Gorlin syndrome and rhabdoid tumor predisposition syndrome. Clin Cancer Res 23(12):e62–e67. https://doi.org/10.1158/1078-0432.CCR-17-0595

Fröb F, Wegner M (2020) The role of chromatin remodeling complexes in Schwann cell development. Glia 68(8):1596–1603. https://doi.org/10.1002/glia.23766

Frühwald MC, Biegel JA, Bourdeaut F, Roberts CWM, Chi SN (2016) Atypical teratoid/rhabdoid tumors - Current concepts, advances in biology, and potential future therapies. Neuro Oncol 18(6):764–778. https://doi.org/10.1093/neuonc/nov264

Frühwald MC, Hasselblatt M, Nemes K, Bens S, Steinbügl M, Johann PD, Kerl K, Hauser P, Quiroga E, Solano Paez P, Biassoni V, Gil-da-Costa MJ, Perek Polnik M, Van De Wetering M, Sumerauer D, Pears J, Stabell N, Holm S, Hengartner H, Gerber NU, Grotzer M, Boos J, Ebinger M, Tippelt S, Paulus W, Furtwängler R, Hernaíz Driever P, Reinhard H, Rutkowski S, Schlegel P-G, Schmid I, Kortmann R-D, Timmermann B, Warmuth Metz M, Kordes U, Gerss J, Nysom K, Schneppenheim R, Siebert R, Kool M, Graf N (2020) Age and DNA methylation subgroup as potential independent risk factors for treatment stratification in children with atypical teratoid/rhabdoid tumors. Neuro Oncol 22(7):1006–1017. https://doi.org/10.1093/neuonc/noz244

Gastberger K, Fincke VE, Mucha M, Siebert R, Hasselblatt M, Frühwald MC (2023) Current Molecular and Clinical Landscape of ATRT – The Link to Future Therapies. Cancer Manag Res 15:1369–1393. https://doi.org/10.2147/CMAR.S379451

Ginn KF, Gajjar A (2012) Atypical teratoid rhabdoid tumor: Current therapy and future directions. Front Oncol 2(9):1–13. https://doi.org/10.3389/fonc.2012.00114

Glenn TD, Talbot WS (2013) Signals regulating myelination in peripheral nerves and the Schwann cell response to injury. Curr Opin Neurobiol 23(6):1041–1048. https://doi.org/10.1016/j.conb.2013.06.010

Gojo J, Lötsch D, Spiegl-Kreinecker S, Pajtler KW, Neumayer K, Korbel P, Araki A, Brandstetter A, Mohr T, Hovestadt V, Chavez L, Kirchhofer D, Ricken G, Stefanits H, Korshunov A, Pfister SM, Dieckmann K, Azizi AA, Czech T, Filipits M, Kool M, Peyrl A, Slavc I, Berger W, Haberler C (2017) Telomerase activation in posterior fossa group A ependymomas is associated with dismal prognosis and chromosome 1q gain. Neuro Oncol 19(9):1183–1194. https://doi.org/10.1093/neuonc/nox027

Goldstein AS, Huang J, Guo C, Garraway IP, Witte ON (2010) Identification of a Cell of Origin for Human Prostate Cancer. Science (1979) 329(5991):568–571. https://doi.org/10.1126/science.1189992

Gooden MJM, De Bock GH, Leffers N, Daemen T, Nijman HW (2011) The prognostic influence of tumour-infiltrating lymphocytes in cancer: A systematic review with meta-analysis. Br J Cancer 105:93–103

Graf M, Interlandi M, Moreno N, Holdhof D, Göbel C, Melcher V, Mertins J, Albert TK, Kastrati D, Alfert A, Holsten T, de Faria F, Meisterernst M, Rossig C, Warmuth-Metz M, Nowak J, Meyer zu Hörste G, Mayère C, Nef S, Johann P, Frühwald MC, Dugas M, Schüller U, Kerl K (2022) Single-cell transcriptomics identifies potential cells of origin of MYC rhabdoid tumors. Nat Commun 13(1). https://doi.org/10.1038/s41467-022-29152-4

Gulubova M, Manolova I, Ananiev J, Kjurkchiev D, Julianov A, Altunkova I (2013) Relationship of TGF-β1 and Smad7 expression with decreased dendritic cell infiltration in liver gastrointestinal cancer metastasis. APMIS 121(10):967–975. https://doi.org/10.1111/apm.12096

Gupta PB, Pastushenko I, Skibinski A, Blanpain C, Kuperwasser C (2019) Phenotypic Plasticity: Driver of Cancer Initiation, Progression, and Therapy Resistance. Cell Stem Cell 24(1):65–78. https://doi.org/10.1016/j.stem.2018.11.011

Gutheil JC, Campbell TN, Pierce PR, Watkins JD, Huse WD, Bodkin DJ, Cheresh DA (2000) Targeted antiangiogenic therapy for cancer using Vitaxin: a humanized monoclonal antibody to the integrin alphavbeta3. Clin Cancer Res 6(8):3056–61

Guthrie S, Lumsden A (1991) Formation and regeneration of rhombomere boundaries in the developing chick hindbrain. Development 112(1):221–229. https://doi.org/10.1242/dev.112.1.221

Haas JE, Palmer NF, Weinberg AG, Beckwith JB (1981) Ultrastructure of malignant rhabdoid tumor of the kidney. Hum Pathol 12(7):646–657. https://doi.org/10.1016/S0046-8177(81)80050-0

Hah N, Kolkman A, Ruhl DD, Pijnappel WWMP, Heck AJR, Timmers HThM, Kraus WL (2010) A Role for BAF57 in Cell Cycle–Dependent Transcriptional Regulation by the SWI/SNF Chromatin Remodeling Complex. Cancer Res 70(11):4402–4411. https://doi.org/10.1158/0008-5472.CAN-09-2767

Han ZY, Richer W, Fréneaux P, Chauvin C, Lucchesi C, Guillemot D, Grison C, Lequin D, Pierron G, Masliah-Planchon J, Nicolas A, Ranchère-Vince D, Varlet P, Puget S, Janoueix-Lerosey I, Ayrault O, Surdez D, Delattre O, Bourdeaut F (2016) The occurrence of intracranial rhabdoid tumours in mice depends on temporal control of Smarcb1 inactivation. Nat Commun 7. https://doi.org/10.1038/ncomms10421

Hasselblatt M, Gesk S, Oyen F, Rossi S, Viscardi E, Giangaspero F, Giannini C, Judkins AR, Frühwald MC, Obser T, Schneppenheim R, Siebert R, Paulus W (2011) Nonsense Mutation and Inactivation of SMARCA4 (BRG1) in an Atypical Teratoid/Rhabdoid Tumor Showing Retained SMARCB1 (INI1) Expression. American Journal of Surgical Pathology 35(6):933–935. https://doi.org/10.1097/PAS.0b013e3182196a39

Hasselblatt M, Isken S, Linge A, Eikmeier K, Jeibmann A, Oyen F, Nagel I, Richter J, Bartelheim K, Kordes U, Schneppenheim R, Frühwald M, Siebert R, Paulus W (2013) High-resolution genomic analysis suggests the absence of recurrent genomic alterations other than SMARCB1 aberrations in atypical teratoid/rhabdoid tumors. Genes Chromosomes Cancer 52(2):185–190. https://doi.org/10.1002/gcc.22018

Hasselblatt M, Nagel I, Oyen F, Bartelheim K, Russell RB, Schüller U, Junckerstorff R, Rosenblum M, Alassiri AH, Rossi S, Schmid I, Gottardo NG, Toledano H, Viscardi E, Balbin M, Witkowski L, Lu Q, Betts MJ, Foulkes WD, Siebert R, Frühwald MC, Schneppenheim R (2014) SMARCA4-mutated atypical teratoid/rhabdoid tumors are associated with inherited germline alterations and poor prognosis. Acta Neuropathol 128(3):453–456. https://doi.org/10.1007/s00401-014-1323-x

Hasselblatt M, Oyen F, Gesk S, Kordes U, Wrede B, Bergmann M, Schmid H, Frühwald MC, Schneppenheim R, Siebert R, Paulus W (2009) Cribriform Neuroepithelial Tumor (CRINET): A Nonrhabdoid Ventricular Tumor With INI1 Loss and Relatively Favorable Prognosis. J Neuropathol Exp Neurol 68(12):1249–1255. https://doi.org/10.1097/NEN.0b013e3181c06a51

Hasselblatt M, Thomas C, Federico A, Nemes K, Johann PD, Bison B, Bens S, Dahlum S, Kordes U, Redlich A, Lessel L, Pajtler KW, Mawrin C, Schüller U, Nolte K, Kramm CM, Hinz F, Sahm F, Giannini C, Penkert J, Kratz CP, Pfister SM, Siebert R, Paulus W, Kool M, Frühwald MC (2022) SMARCB1-deficient and SMARCA4-deficient Malignant Brain Tumors With Complex Copy Number Alterations and TP53 Mutations May Represent the First Clinical Manifestation of Li-Fraumeni Syndrome. American Journal of Surgical Pathology 46(9):1277–1283. https://doi.org/10.1097/PAS.0000000000001905

Ho B, Johann PD, Grabovska Y, De Dieu Andrianteranagna MJ, Yao F, Frühwald M, Hasselblatt M, Bourdeaut F, Williamson D, Huang A, Kool M (2020) Molecular subgrouping of atypical teratoid/rhabdoid tumors - A reinvestigation and current consensus. Neuro Oncol 22:613–624

Ho L, Miller EL, Ronan JL, Ho WQ, Jothi R, Crabtree GR (2011) esBAF facilitates pluripotency by conditioning the genome for LIF/STAT3 signalling and by regulating polycomb function. Nat Cell Biol 13(8):903–913. https://doi.org/10.1038/ncb2285

Holdhof D, Johann PD, Spohn M, Bockmayr M, Safaei S, Joshi P, Masliah-Planchon J, Ho B, Andrianteranagna M, Bourdeaut F, Huang A, Kool M, Upadhyaya SA, Bendel AE, Indenbirken D, Foulkes WD, Bush JW, Creytens D, Kordes U, Frühwald MC, Hasselblatt M, Schüller U (2020a) Atypical teratoid/rhabdoid tumors (ATRTs) with SMARCA4 mutation are molecularly distinct from SMARCB1-deficient cases. Acta Neuropathol 141(2):291–301. https://doi.org/10.1007/s00401-020-02250-7

Holdhof D, On JH, Schoof M, Göbel C, Schüller U (2021a) Simultaneous Brg1 Knockout and MYCN Overexpression in Cerebellar Granule Neuron Precursors Is Insufficient to Drive Tumor Formation but Temporarily Enhances their Proliferation and Delays their Migration. Cerebellum 20(3):410–419. https://doi.org/10.1007/s12311-020-01219-2

Holdhof D, Schoof M, Al-Kershi S, Spohn M, Kresbach C, Göbel C, Hellwig M, Indenbirken D, Moreno N, Kerl K, Schüller U (2021b) Brahma-related gene 1 has time-specific roles

during brain and eye development. Development (Cambridge) 148(10). https://doi.org/10.1242/DEV.196147

Holdhof D, Schoof M, Hellwig M, Holdhof NH, Niesen J, Schüller U (2020b) HGFAP-Positive Stem Cells Depend on Brg1 for Proper Formation of Cerebral and Cerebellar Structures. Cerebral Cortex 30(3):1382–1392. https://doi.org/10.1093/cercor/bhz173

Holmberg KO, Borgenvik A, Zhao M, Giraud G, Swartling FJ (2024) Drivers Underlying Metastasis and Relapse in Medulloblastoma and Targeting Strategies. Cancers (Basel) 16(9):1752. https://doi.org/10.3390/cancers16091752

Hossain A, Gumin J, Gao F, Figueroa J, Shinojima N, Takezaki T, Priebe W, Villarreal D, Kang S-G, Joyce C, Sulman E, Wang Q, Marini FC, Andreeff M, Colman H, Lang FF (2015) Mesenchymal Stem Cells Isolated From Human Gliomas Increase Proliferation and Maintain Stemness of Glioma Stem Cells Through the IL-6/gp130/STAT3 Pathway. Stem Cells 33(8):2400–2415. https://doi.org/10.1002/stem.2053

Huang J, Zhang L, Wan D, Zhou L, Zheng S, Lin S, Qiao Y (2021a) Extracellular matrix and its therapeutic potential for cancer treatment. Signal Transduct Target Ther 6(1):153. https://doi.org/10.1038/s41392-021-00544-0

Huang J, Zhang L, Wan D, Zhou L, Zheng S, Lin S, Qiao Y (2021b) Extracellular matrix and its therapeutic potential for cancer treatment. Signal Transduct Target Ther 6(1):153. https://doi.org/10.1038/s41392-021-00544-0

Huang Q, Li F, Liu X, Li W, Shi W, Liu F-F, O'Sullivan B, He Z, Peng Y, Tan A-C, Zhou L, Shen J, Han G, Wang X-J, Thorburn J, Thorburn A, Jimeno A, Raben D, Bedford JS, Li C-Y (2011) Caspase 3–mediated stimulation of tumor cell repopulation during cancer radiotherapy. Nat Med 17(7):860–866. https://doi.org/10.1038/nm.2385

Jessa S, Blanchet-Cohen A, Krug B, Vladoiu M, Coutelier M, Faury D, Poreau B, De Jay N, Hébert S, Monlong J, Farmer WT, Donovan LK, Hu Y, McConechy MK, Cavalli FMG, Mikael LG, Ellezam B, Richer M, Allaire A, Weil AG, Atkinson J, Farmer JP, Dudley RWR, Larouche V, Crevier L, Albrecht S, Filbin MG, Sartelet H, Lutz PE, Nagy C, Turecki G, Costantino S, Dirks PB, Murai KK, Bourque G, Ragoussis J, Garzia L, Taylor MD, Jabado N, Kleinman CL (2019) Stalled developmental programs at the root of pediatric brain tumors. Nat Genet 51(12):1702–1713. https://doi.org/10.1038/s41588-019-0531-7

Jiménez G, Hackenberg M, Catalina P, Boulaiz H, Griñán-Lisón C, García MÁ, Perán M, López-Ruiz E, Ramírez A, Morata-Tarifa C, Carrasco E, Aguilera M, Marchal JA (2018) Mesenchymal stem cell's secretome promotes selective enrichment of cancer stem-like cells with specific cytogenetic profile. Cancer Lett 429:78–88. https://doi.org/10.1016/j.canlet.2018.04.042

Johann PD, Altendorf L, Efremova EM, Holsten T, Steinbügl M, Nemes K, Eckhardt A, Kresbach C, Bockmayr M, Koch A, Haberler C, Antonelli M, DeSisto J, Schuhmann MU, Hauser P, Siebert R, Bens S, Kool M, Green AL, Hasselblatt M, Frühwald MC, Schüller U (2023) Recurrent atypical teratoid/rhabdoid tumors (AT/RT) reveal discrete features of progression on histology, epigenetics, copy number profiling, and transcriptomics. Acta Neuropathol 146(3):527–541. https://doi.org/10.1007/s00401-023-02608-7

Johann PD, Erkek S, Zapatka M, Kerl K, Buchhalter I, Hovestadt V, Jones DTW, Sturm D, Hermann C, Segura Wang M, Korshunov A, Rhyzova M, Gröbner S, Brabetz S, Chavez L, Bens S, Gröschel S, Kratochwil F, Wittmann A, Sieber L, Geörg C, Wolf S, Beck K, Oyen F, Capper D, van Sluis P, Volckmann R, Koster J, Versteeg R, von Deimling A, Milde T, Witt O, Kulozik AE, Ebinger M, Shalaby T, Grotzer M, Sumerauer D, Zamecnik J, Mora

J, Jabado N, Taylor MD, Huang A, Aronica E, Bertoni A, Radlwimmer B, Pietsch T, Schüller U, Schneppenheim R, Northcott PA, Korbel JO, Siebert R, Frühwald MC, Lichter P, Eils R, Gajjar A, Hasselblatt M, Pfister SM, Kool M (2016) Atypical Teratoid/Rhabdoid Tumors Are Comprised of Three Epigenetic Subgroups with Distinct Enhancer Landscapes. Cancer Cell 29(3):379–393. https://doi.org/10.1016/j.ccell.2016.02.001

Johann PD, Hovestadt V, Thomas C, Jeibmann A, Heß K, Bens S, Oyen F, Hawkins C, Pierson CR, Aldape K, Kim S, Widing E, Sumerauer D, Hauser P, van Landeghem F, Ryzhova M, Korshunov A, Capper D, Jones DTW, Pfister SM, Schneppenheim R, Siebert R, Paulus W, Frühwald MC, Kool M, Hasselblatt M (2017) Cribriform neuroepithelial tumor: molecular characterization of a SMARCB1-deficient non-rhabdoid tumor with favorable long-term outcome. Brain Pathology 27(4):411–418. https://doi.org/10.1111/bpa.12413

Johnson BE, Mazor T, Hong C, Barnes M, Aihara K, McLean CY, Fouse SD, Yamamoto S, Ueda H, Tatsuno K, Asthana S, Jalbert LE, Nelson SJ, Bollen AW, Gustafson WC, Charron E, Weiss WA, Smirnov I V., Song JS, Olshen AB, Cha S, Zhao Y, Moore RA, Mungall AJ, Jones SJM, Hirst M, Marra MA, Saito N, Aburatani H, Mukasa A, Berger MS, Chang SM, Taylor BS, Costello JF (2014) Mutational Analysis Reveals the Origin and Therapy-Driven Evolution of Recurrent Glioma. Science (1979) 343(6167):189–193. https://doi.org/10.1126/science.1239947

Jonckheere S, Adams J, De Groote D, Campbell K, Berx G, Goossens S (2022) Epithelial-Mesenchymal Transition (EMT) as a Therapeutic Target. Cells Tissues Organs 211(2):157–182. https://doi.org/10.1159/000512218

Juárez P, Fournier PGJ, Mohammad KS, McKenna RC, Davis HW, Peng XH, Niewolna M, Mauviel A, Chirgwin JM, Guise TA (2017) Halofuginone inhibits TGF-β/BMP signaling and in combination with zoledronic acid enhances inhibition of breast cancer bone metastasis. Oncotarget 8(49):86447–86462. https://doi.org/10.18632/oncotarget.21200

Juárez P, Mohammad KS, Yin JJ, Fournier PGJ, McKenna RC, Davis HW, Peng XH, Niewolna M, Javelaud D, Chirgwin JM, Mauviel A, Guise TA (2012) Halofuginone Inhibits the Establishment and Progression of Melanoma Bone Metastases. Cancer Res 72(23):6247–6256. https://doi.org/10.1158/0008-5472.CAN-12-1444

Judkins AR, Mauger J, Ht A, Rorke LB, Biegel JA (2004) Immunohistochemical Analysis of hSNF5/INI1 in Pediatric CNS Neoplasms. Am J Surg Pathol 28(5):644–650. https://doi.org/10.1097/00000478-200405000-00013

Kadoch C, Hargreaves DC, Hodges C, Elias L, Ho L, Ranish J, Crabtree GR (2013) Proteomic and bioinformatic analysis of mammalian SWI/SNF complexes identifies extensive roles in human malignancy. Nat Genet 45(6):592–601. https://doi.org/10.1038/ng.2628

Kaiser K, Jang A, Kompanikova P, Lun MP, Prochazka J, Machon O, Dani N, Prochazkova M, Laurent B, Gyllborg D, van Amerongen R, Fame RM, Gupta S, Wu F, Barker RA, Bukova I, Sedlacek R, Kozmik Z, Arenas E, Lehtinen MK, Bryja V (2021) MEIS-WNT5A axis regulates development of fourth ventricle choroid plexus. Development 148(10). https://doi.org/10.1242/dev.192054

Kalimuthu S, Chetty R (2016) Gene of the month: SMARCB1. J Clin Pathol 69:484–489

Kamenova M, Kaneva R, Genova K, Gabrovsky N (2023) Embryonal Tumors of the Central Nervous System with Multilayered Rosettes and Atypical Teratoid/Rhabdoid Tumors. In: Human Brain and Spinal Cord Tumors: From Bench to Bedside. Adv Exp Med Biol 1405:225-252. https://doi.org/ 10.1007/978-3-031-23705-8_8

Kel JM, Girard-Madoux MJH, Reizis B, Clausen BE (2010) TGF-β Is Required To Maintain the Pool of Immature Langerhans Cells in the Epidermis. J Immunol 185(6):3248–3255. https://doi.org/10.4049/jimmunol.1000981

Kiecker C, Bates T, Bell E (2016) Molecular specification of germ layers in vertebrate embryos. Cellular and Molecular Life Sciences 73(5):923–947. https://doi.org/10.1007/s00018-015-2092-y

Kim T-H, Li F, Ferreiro-Neira I, Ho L-L, Luyten A, Nalapareddy K, Long H, Verzi M, Shivdasani RA (2014) Broadly permissive intestinal chromatin underlies lateral inhibition and cell plasticity. Nature 506(7489):511–515. https://doi.org/10.1038/nature12903

Kittock CM, Pilaz L (2023) Advances in in utero electroporation. Dev Neurobiol 83(3–4):73–90. https://doi.org/10.1002/dneu.22910

Klochendler-Yeivin A, Picarsky E, Yaniv M (2006) Increased DNA damage sensitivity and apoptosis in cells lacking the Snf5/Ini1 subunit of the SWI/SNF chromatin remodeling complex. Mol Cell Biol 26(7):2661–74. https://doi.org/10.1128/MCB.26.7.2661-2674.2006

Kompaníková P, Bryja V (2022) Regulation of choroid plexus development and its functions. Cellular and Molecular Life Sciences 79(6):304. https://doi.org/10.1007/s00018-022-04314-1

Krumlauf R, Wilkinson DG (2021) Segmentation and patterning of the vertebrate hindbrain. Development 148(15). https://doi.org/10.1242/dev.186460

Lafay-Cousin L, Dufour C (2022) High-Dose Chemotherapy in Children with Newly Diagnosed Medulloblastoma. Cancers (Basel) 14(3):837. https://doi.org/10.3390/cancers14030837

Lafay-Cousin L, Hawkins C, Carret AS, Johnston D, Zelcer S, Wilson B, Jabado N, Scheinemann K, Eisenstat D, Fryer C, Fleming A, Mpofu C, Larouche V, Strother D, Bouffet E, Huang A (2012) Central nervous system atypical teratoid rhabdoid tumours: The Canadian Paediatric Brain Tumour Consortium experience. Eur J Cancer 48(3):353–359. https://doi.org/10.1016/j.ejca.2011.09.005

Lans H, Marteijn JA, Vermeulen W (2012) ATP-dependent chromatin remodeling in the DNA-damage response. Epigenetics Chromatin 5(1):4. https://doi.org/10.1186/1756-8935-5-4

Lee RS, Stewart C, Carter SL, Ambrogio L, Cibulskis K, Sougnez C, Lawrence MS, Auclair D, Mora J, Golub TR, Biegel JA, Getz G, Roberts CWM (2012) A remarkably simple genome underlies highly malignant pediatric rhabdoid cancers. Journal of Clinical Investigation 122(8):2983–2988. https://doi.org/10.1172/JCI64400

Lee SJ, Lindsey S, Graves B, Yoo S, Olson JM, Langhans SA (2013) Sonic Hedgehog-Induced Histone Deacetylase Activation Is Required for Cerebellar Granule Precursor Hyperplasia in Medulloblastoma. PLoS One 8(8):e71455. https://doi.org/10.1371/journal.pone.0071455

Letai A, de The H (2024) Conventional chemotherapy: millions of cures, unresolved therapeutic index. Nat Rev Cancer. https://doi.org/10.1038/s41568-024-00778-4

Leto K, Arancillo M, Becker EBE, Buffo A, Chiang C, Ding B, Dobyns WB, Dusart I, Haldipur P, Hatten ME, Hoshino M, Joyner AL, Kano M, Kilpatrick DL, Koibuchi N, Marino S, Martinez S, Millen KJ, Millner TO, Miyata T, Parmigiani E, Schilling K, Sekerková G, Sillitoe R V., Sotelo C, Uesaka N, Wefers A, Wingate RJT, Hawkes R (2016) Consensus Paper: Cerebellar Development. The Cerebellum 15(6):789–828. https://doi.org/10.1007/s12311-015-0724-2

Li F, Huang Q, Chen J, Peng Y, Roop DR, Bedford JS, Li C-Y (2010) Apoptotic Cells Activate the “Phoenix Rising” Pathway to Promote Wound Healing and Tissue Regeneration. Sci Signal 3(110). https://doi.org/10.1126/scisignal.2000634

Li J, Liu T, Bao H, Xu Z, Shu Y, Zheng B (2021) A phase I study of a TGF-β receptor I kinase inhibitor YL-13027 in patients with advanced solid tumors. Journal of Clinical Oncology 39(15_suppl):3098–3098. https://doi.org/10.1200/JCO.2021.39.15_suppl.3098

Li X, Sun X, Kan C, Chen B, Qu N, Hou N, Liu Y, Han F (2022) COL1A1: A novel oncogenic gene and therapeutic target in malignancies. Pathol Res Pract 236:154013. https://doi.org/10.1016/j.prp.2022.154013

Lin R, Yi S, Gong L, Liu W, Wang P, Liu N, Zhao L, Wang P (2015) Inhibition of TGF-ß signaling with halofuginone can enhance the antitumor effect of irradiation in Lewis lung cancer. Onco Targets Ther :3549. https://doi.org/10.2147/OTT.S92518

Liu X, Zhu R, Luo Y, Wang S, Zhao Y, Qiu Z, Zhang Y, Liu X, Yao X, Li X, Li W (2021) Distinct human Langerhans cell subsets orchestrate reciprocal functions and require different developmental regulation. Immunity 54(10):2305-2320.e11. https://doi.org/10.1016/j.immuni.2021.08.012

Lobas MA, Helsper L, Vernon CG, Schreiner D, Zhang Y, Holtzman MJ, Thedens DR, Weiner JA (2012) Molecular heterogeneity in the choroid plexus epithelium: the 22-member γ-protocadherin family is differentially expressed, apically localized, and implicated in CSF regulation. J Neurochem 120(6):913–27. https://doi.org/10.1111/j.1471-4159.2011.07587.x

Lobón-Iglesias MJ, Andrianteranagna M, Han ZY, Chauvin C, Masliah-Planchon J, Manriquez V, Tauziede-Espariat A, Turczynski S, Bouarich-Bourimi R, Frah M, Dufour C, Blauwblomme T, Cardoen L, Pierron G, Maillot L, Guillemot D, Reynaud S, Bourneix C, Pouponnot C, Surdez D, Bohec M, Baulande S, Delattre O, Piaggio E, Ayrault O, Waterfall JJ, Servant N, Beccaria K, Dangouloff-Ros V, Bourdeaut F (2023) Imaging and multi-omics datasets converge to define different neural progenitor origins for ATRT-SHH subgroups. Nat Commun 14(1). https://doi.org/10.1038/s41467-023-42371-7

Louis DN, Perry A, Wesseling P, Brat DJ, Cree IA, Figarella-Branger D, Hawkins C, Ng HK, Pfister SM, Reifenberger G, Soffietti R, von Deimling A, Ellison DW (2021) The 2021 WHO Classification of Tumors of the Central Nervous System: a summary. Neuro Oncol 23(8):1231–1251. https://doi.org/10.1093/neuonc/noab106

Mahaffey BJ, Fowler ZP, Lung Z, Dang V, Lee H, Johnson AM, Munoz MA, Goodin DA, Frieboes HB, Williams BJ, Chen J (2024) The prognostic effect of mechanical, ultrastructural, and ECM signatures in glioblastoma core and rim. APL Bioeng 8(3). https://doi.org/10.1063/5.0203570

Mao S, Song R, Jin S, Pang S, Jovanovic A, Zimmerman A, Li P, Wu X, Wendland MF, Lin K, Chen WC, Choksi SP, Chen G, Holtzman MJ, Reiter JF, Wan Y, Xuan Z, Xiang YK, Xu CS, Upadhyayula S, Hess HF, He L (2025) Multicilia dynamically transduce Sonic Hedgehog signaling to regulate choroid plexus functions. Cell Rep 44(3). https://doi.org/10.1016/j.celrep.2025.115383

Mao X, Hütt-Cabezas M, Orr BA, Weingart M, Taylor I, Rajan AKD, Odia Y, Kahlert U, Maciaczyk J, Nikkhah G, Eberhart CG, Raabe EH (2013) LIN28A facilitates the transformation of human neural stem cells and promotes glioblastoma tumorigenesis through a pro-invasive genetic program. Oncotarget 4(7):1050–1064. https://doi.org/10.18632/oncotarget.1131

Matoba N, Le BD, Valone JM, Wolter JM, Mory J, Liang D, Aygün N, Broadaway KA, Bond ML, Mohlke KL, Zylka MJ, Love MI, Stein JL (2023) Wnt activity reveals context-specific genetic effects on gene regulation in neural progenitors. bioRxiv . https://doi.org/10.1101/2023.02.07.527357

Mayor R, Theveneau E (2013) The neural crest. Development 140(11):2247–2251. https://doi.org/10.1242/dev.091751

McGinty RK, Tan S (2015) Nucleosome Structure and Function. Chem Rev 115(6):2255–2273. https://doi.org/10.1021/cr500373h

Middelkamp M, Ruck L, Krisp C, Sumisławski P, Mohammadi B, Dottermusch M, Meister V, Küster L, Schlüter H, Windhorst S, Neumann JE (2021) Overexpression of Lin28A in neural progenitor cells in vivo does not lead to brain tumor formation but results in reduced spine density. Acta Neuropathol Commun 9(1):185. https://doi.org/10.1186/s40478-021-01289-1

Minesaki A, Kai K, Kuratomi Y, Aishima S (2021) Infiltration of CD1a-positive dendritic cells in advanced laryngeal cancer correlates with unfavorable outcomes post-laryngectomy. BMC Cancer 21(1):973. https://doi.org/10.1186/s12885-021-08715-6

Moreno N, Schmidt C, Ahlfeld J, Pöschl J, Dittmar S, Pfister SM, Kool M, Kerl K, Schüller U (2014) Loss of Smarc proteins impairs cerebellar development. Journal of Neuroscience 34(40):13486–13491. https://doi.org/10.1523/JNEUROSCI.2560-14.2014

Morris JC, Tan AR, Olencki TE, Shapiro GI, Dezube BJ, Reiss M, Hsu FJ, Berzofsky JA, Lawrence DP (2014) Phase I Study of GC1008 (Fresolimumab): A Human Anti-Transforming Growth Factor-Beta (TGFβ) Monoclonal Antibody in Patients with Advanced Malignant Melanoma or Renal Cell Carcinoma. PLoS One 9(3):e90353. https://doi.org/10.1371/journal.pone.0090353

Morrison O, Thakur J (2021) Molecular Complexes at Euchromatin, Heterochromatin and Centromeric Chromatin. Int J Mol Sci 22(13):6922. https://doi.org/10.3390/ijms22136922

Müller F, O'Rahilly R (1990) The human brain at stages 18-20, including the choroid plexuses and the amygdaloid and septal nuclei. Anat Embryol (Berl) 182(3). https://doi.org/10.1007/BF00185521

Narita K, Takeda S (2015) Cilia in the choroid plexus: their roles in hydrocephalus and beyond. Front Cell Neurosci 9. https://doi.org/10.3389/fncel.2015.00039

Neigeborn L, Carlson M (1984) Genes affecting the regulation of SUC2 gene expression by glucose repression in Saccharomyces cerevisiae. Genetics 108(4):845–858. https://doi.org/10.1093/genetics/108.4.845

Nemes K, Bens S, Kachanov D, Teleshova M, Hauser P, Simon T, Tippelt S, Woessmann W, Beck O, Flotho C, Grigull L, Driever PH, Schlegel P-G, Khurana C, Hering K, Kolb R, Leipold A, Abbink F, Gil-Da-Costa MJ, Benesch M, Kerl K, Lowis S, Marques CH, Graf N, Nysom K, Vokuhl C, Melchior P, Kröncke T, Schneppenheim R, Kordes U, Gerss J, Siebert R, Furtwängler R, Frühwald MC (2021) Clinical and genetic risk factors define two risk groups of extracranial malignant rhabdoid tumours (eMRT/RTK). Eur J Cancer 142:112–122. https://doi.org/10.1016/j.ejca.2020.10.004

Nemes K, Johann PD, Tüchert S, Melchior P, Vokuhl C, Siebert R, Furtwängler R, Frühwald MC (2022) Current and Emerging Therapeutic Approaches for Extracranial Malignant Rhabdoid Tumors. Cancer Manag Res Volume 14:479–498. https://doi.org/10.2147/CMAR.S289544

Neyazi S, Altendorf L, Schwetje D, Göbel C, Schoof M, Holdhof D, Schüller U (2022) Generation of new transgenic SMARCA4-deficient mouse models results in neuromuscular weakness and paralysis of limbs. Brain Pathology 33(3):e13146. https://doi.org/10.1111/bpa.13146

Ng JMY, Martinez D, Marsh ED, Zhang Z, Rappaport E, Santi M, Curran T (2015) Generation of a mouse model of atypical teratoid/rhabdoid tumor of the central nervous system through combined deletion of Snf5 and p53. Cancer Res 75(21):4629–39. https://doi.org/10.1158/0008-5472.CAN-15-0874

Ni T, Chu Z, Tao L, Zhao Y, Lv M, Zhu M, Luo Y, Sunagawa M, Wang H, Liu Y (2024) Celastrus orbiculatus extract suppresses gastric cancer stem cells through the TGF-β/Smad signaling pathway. J Nat Med 78(1):100–113. https://doi.org/10.1007/s11418-023-01748-0

Nordin A, Chakraborty C, Jonasson M, Dano O, Zambanini G, Pagella P, Remeseiro S, Cantù C (2024) Wnt signaling alters CTCF binding patterns and global chromatin structure. bioRxiv. https://doi.org/10.1101/2024.01.22.576696

Notaro S, Reimer D, Fiegl H, Schmid G, Wiedemair A, Rössler J, Marth C, Zeimet AG (2016) Evaluation of folate receptor 1 (FOLR1) mRNA expression, its specific promoter methylation and global DNA hypomethylation in type I and type II ovarian cancers. BMC Cancer 16(1). https://doi.org/10.1186/s12885-016-2637-y

Oka H, Scheithauer BW (1999) Clinicopathological Characteristics of Atypical Teratoid/Rhabdoid Tumor. Neurol Med Chir (Tokyo) 39(7):510–518. https://doi.org/10.2176/nmc.39.510

Ostrom QT, Chen Y, De Blank PM, Ondracek A, Farah P, Gittleman H, Wolinsky Y, Kruchko C, Cohen ML, Brat DJ, Barnholtz-Sloan JS (2014) The descriptive epidemiology of atypical teratoid/rhabdoid tumors in the United States, 2001-2010. Neuro Oncol 16(10):1392–1399. https://doi.org/10.1093/neuonc/nou090

Ostrom QT, Price M, Neff C, Cioffi G, Waite KA, Kruchko C, Barnholtz-Sloan JS (2022) CBTRUS Statistical Report: Primary Brain and Other Central Nervous System Tumors Diagnosed in the United States in 2015–2019. Neuro Oncol 24(Supplement_5):v1–v95. https://doi.org/10.1093/neuonc/noac202

Paassen I, Williams J, Ríos Arceo C, Ringnalda F, Mercer KS, Buhl JL, Moreno N, Federico A, Franke NE, Kranendonk M, Upadhyaya SA, Kerl K, van de Wetering M, Clevers H, Kool M, Hoving EW, Roussel MF, Drost J (2023) Atypical teratoid/rhabdoid tumoroids reveal subgroup-specific drug vulnerabilities. Oncogene 42(20):1661–1671. https://doi.org/10.1038/s41388-023-02681-y

Pagella P, Söderholm S, Nordin A, Zambanini G, Ghezzi V, Jauregi-Miguel A, Cantù C (2023) The time-resolved genomic impact of Wnt/β-catenin signaling. Cell Syst 14(7):563-581.e7. https://doi.org/10.1016/j.cels.2023.06.004

Pessoa L, Medina L, Hof PR, Desfilis E (2019) Neural architecture of the vertebrate brain: implications for the interaction between emotion and cognition. Neurosci Biobehav Rev 107:296–312. https://doi.org/10.1016/j.neubiorev.2019.09.021

Petersdorf SH, Livingston RB (1994) High dose chemotherapy for the treatment of malignant brain tumors. J Neurooncol 20(2):155–163. https://doi.org/10.1007/BF01052725

Phan TG, Croucher PI (2020) The dormant cancer cell life cycle. Nat Rev Cancer 20:398–411. https://doi.org/10.1038/s41568-020-0263-0

Phelan ML, Sif S, Narlikar GJ, Kingston RE (1999) Reconstitution of a Core Chromatin Remodeling Complex from SWI/SNF Subunits. Mol Cell 3(2):247–253. https://doi.org/10.1016/S1097-2765(00)80315-9

Prakash J, Shaked Y (2024) The Interplay between Extracellular Matrix Remodeling and Cancer Therapeutics. Cancer Discov 14:1375–1388. https://doi.org/ 10.1158/2159-8290.CD-24-0002

Rajaraman R, Guernsey DL, Rajaraman MM, Rajaraman SR (2006) Stem cells, senescence, neosis and self-renewal in cancer. Cancer Cell Int 6. https://doi.org/10.1186/1475-2867-6-25

Ray MK, Fagan SP, Brunicardi FC (2000) The Cre–loxP System: A Versatile Tool for Targeting Genes in a Cell- and Stage-Specific Manner. Cell Transplant 9(6):805–815. https://doi.org/10.1177/096368970000900607

Ricart AD, Tolcher AW, Liu G, Holen K, Schwartz G, Albertini M, Weiss G, Yazji S, Ng C, Wilding G (2008) Volociximab, a Chimeric Monoclonal Antibody that Specifically Binds α5β1 Integrin: A Phase I, Pharmacokinetic, and Biological Correlative Study. Clinical Cancer Research 14(23):7924–7929. https://doi.org/10.1158/1078-0432.CCR-08-0378

Richardson EA, Ho B, Huang A (2018) Atypical Teratoid Rhabdoid Tumour : From Tumours to Therapies. J Korean Neurosurg Soc 61(3):302–311. https://doi.org/10.3340/jkns.2018.0061

Roberts CWM, Leroux MM, Fleming MD, Orkin SH (2002) Highly penetrant, rapid tumorigenesis through conditional inversion of the tumor suppressor gene Snf5. Cancer Cell 2(5):415–425. https://doi.org/10.1016/S1535-6108(02)00185-X

Rorke LB, Packer RJ, Biegel JA (1996) Central nervous system atypical teratoid/rhabdoid tumors of infancy and childhood: definition of an entity. J Neurosurg 85(1):56–65. https://doi.org/10.3171/jns.1996.85.1.0056

Rusu P, Shao C, Neuerburg A, Acikgöz AA, Wu Y, Zou P, Phapale P, Shankar TS, Döring K, Dettling S, Körkel-Qu H, Bekki G, Costa B, Guo T, Friesen O, Schlotter M, Heikenwalder M, Tschaharganeh DF, Bukau B, Kramer G, Angel P, Herold-Mende C, Radlwimmer B, Liu HK (2019) GPD1 Specifically Marks Dormant Glioma Stem Cells with a Distinct Metabolic Profile. Cell Stem Cell 25(2):241-257.e8. https://doi.org/10.1016/j.stem.2019.06.004

Sacco JL, Gomez EW (2024) Epithelial–Mesenchymal Plasticity and Epigenetic Heterogeneity in Cancer. Cancers (Basel) 16(19):3289. https://doi.org/10.3390/cancers16193289

Sadler TW (2005) Embryology of neural tube development. Am J Med Genet C Semin Med Genet 135C(1):2–8. https://doi.org/10.1002/ajmg.c.30049

Sakamoto K, Endo K, Sakamoto K, Kayamori K, Ehata S, Ichikawa J, Ando T, Nakamura R, Kimura Y, Yoshizawa K, Masuyama K, Kawataki T, Miyake K, Ishii H, Kawasaki T, Miyazawa K, Saitoh M (2021) EHF suppresses cancer progression by inhibiting ETS1-mediated ZEB expression. Oncogenesis 10(3). https://doi.org/10.1038/s41389-021-00313-2

Savage P (2016) Chemotherapy curable malignancies and cancer stem cells: a biological review and hypothesis. BMC Cancer 16(1):906. https://doi.org/10.1186/s12885-016-2956-z

Scaini MC, Catoni C, Poggiana C, Pigozzo J, Piccin L, Leone K, Scarabello I, Facchinetti A, Menin C, Elefanti L, Pellegrini S, Aleotti V, Vidotto R, Schiavi F, Fabozzi A, Chiarion-Sileni V, Rosato A (2024) A multiparameter liquid biopsy approach allows to track melanoma dynamics and identify early treatment resistance. NPJ Precis Oncol 8(1):78. https://doi.org/10.1038/s41698-024-00567-0

Schneppenheim R, Frühwald MC, Gesk S, Hasselblatt M, Jeibmann A, Kordes U, Kreuz M, Leuschner I, Subero JIM, Obser T, Oyen F, Vater I, Siebert R (2010) Germline Nonsense Mutation and Somatic Inactivation of SMARCA4/BRG1 in a Family with Rhabdoid Tumor Predisposition Syndrome. Am J Hum Genet 86(2):279–284. https://doi.org/10.1016/j.ajhg.2010.01.013

Seeringer A, Bartelheim K, Kerl K, Hasselblatt M, Leuschner I, Rutkowski S, Timmermann B, Kortmann R-D, Koscielniak E, Schneppenheim R, Warmuth-Metz M, Gerß J, Siebert R, Graf N, Boos J, Frühwald M (2014) Feasibility of Intensive Multimodal Therapy in Infants Affected by Rhabdoid Tumors – Experience of the EU-RHAB registry. Klin Padiatr 226(03):143–148. https://doi.org/10.1055/s-0034-1368719

Seimiya M, O-Wang J, Bahar R, Kawamura K, Wang Y, Saisho H, Tagawa M (2003) Stage-specific expression of Clast6/E3/LAPTM5 during B cell differentiation: elevated expression in human B lymphomas. Int J Oncol. https://doi.org/10.3892/ijo.22.2.301

Shahbazi MN (2020) Mechanisms of human embryo development: from cell fate to tissue shape and back. Development 147(14). https://doi.org/10.1242/dev.190629

Shinmyo Y, Tanaka S, Tsunoda S, Hosomichi K, Tajima A, Kawasaki H (2016) CRISPR/Cas9-mediated gene knockout in the mouse brain using in utero electroporation. Sci Rep 6(1):20611. https://doi.org/10.1038/srep20611

Singh AP, Foley JF, Rubino M, Boyle MC, Tandon A, Shah R, Archer TK (2016) Brg1 Enables Rapid Growth of the Early Embryo by Suppressing Genes That Regulate Apoptosis and Cell Growth Arrest. Mol Cell Biol 36(15):1990–2010. https://doi.org/10.1128/MCB.01101-15

Sive JI, Feber A, Smith D, Quinn J, Beck S, Yong K (2016) Global hypomethylation in myeloma is associated with poor prognosis. Br J Haematol 172(3):473–475. https://doi.org/10.1111/bjh.13506

Sredni ST, Tomita T (2015) Rhabdoid tumor predisposition syndrome. Pediatr Dev Pathol 18(1):49–58. https://doi.org/10.2350/14-07-1531-MISC.1

Staahl BT, Tang J, Wu W, Sun A, Gitler AD, Yoo AS, Crabtree GR (2013) Kinetic Analysis of npBAF to nBAF Switching Reveals Exchange of SS18 with CREST and Integration with Neural Developmental Pathways. Journal of Neuroscience 33(25):10348–10361. https://doi.org/10.1523/JNEUROSCI.1258-13.2013

Steinbügl M, Nemes K, Gruhle M, Johann PD, Joao Gil-da-Costa M, Ebinger M, Sehested A, Hauser P, Reinhard H, Hettmer S, Jakob M, Rutkowski S, Hernáiz Driever P, Fleischhack G, Kerl K, Witt O, Gerss J, Siebert R, Schüller U, Hasselblatt M, Frühwald MC (2022) Outcome and Therapeutic Interventions in Relapsed and Refractory ATRT - The EU-RHAB Perspective. Neuro Oncol 24 Suppl 1(Suppl 1):4–4. https://doi.org/https://doi.org/10.1093/neuonc/noac079.008

Stern M, Jensen R, Herskowitz I (1984) Five SWI genes are required for expression of the HO gene in yeast. J Mol Biol 178(4):853–868. https://doi.org/10.1016/0022-2836(84)90315-2

Stiles J, Jernigan TL (2010) The Basics of Brain Development. Neuropsychol Rev 20(4):327–348. https://doi.org/10.1007/s11065-010-9148-4

Sturm D, Capper D, Andreiuolo F, Gessi M, Kölsche C, Reinhardt A, Sievers P, Wefers AK, Ebrahimi A, Suwala AK, Gielen GH, Sill M, Schrimpf D, Stichel D, Hovestadt V, Daenekas B, Rode A, Hamelmann S, Previti C, Jäger N, Buchhalter I, Blattner-Johnson M, Jones BC, Warmuth-Metz M, Bison B, Grund K, Sutter C, Hirsch S, Dikow N, Hasselblatt M, Schüller U, Koch A, Gerber NU, White CL, Buntine MK, Kinross K, Algar EM, Hansford JR, Gottardo NG, Schuhmann MU, Thomale UW, Hernáiz Driever P, Gnekow A, Witt O, Müller HL, Calaminus G, Fleischhack G, Kordes U, Mynarek M, Rutkowski S, Frühwald MC, Kramm CM, von Deimling A, Pietsch T, Sahm F, Pfister SM, Jones DavidTW (2023) Multiomic neuropathology improves diagnostic accuracy in pediatric neuro-oncology. Nat Med 29(4):917–926. https://doi.org/10.1038/s41591-023-02255-1

Sun MS, Yuan LT, Kuei CH, Lin HY, Chen YL, Chiu HW, Lin YF (2021) Rgl2 drives the metastatic progression of colorectal cancer via preventing the protein degradation of β-catenin and kras. Cancers (Basel) 13(8). https://doi.org/10.3390/cancers13081763

Sun PP, Liao SX, Sang P, Liu MM, Yang J Bin (2024) Lysosomal transmembrane protein 5: Impact on immune cell function and implications for immune-related deficiencies. Heliyon 10(17):e36705. https://doi.org/10.1016/j.heliyon.2024.e36705

Tanabe S (2022) Epithelial–Mesenchymal Transition and Cancer Stem Cells. Adv Exp Med Biol 1393:1-49. https://doi.org/10.1007/978-3-031-12974-2_1

Tanabe S, Quader S, Cabral H, Ono R (2020) Interplay of EMT and CSC in Cancer and the Potential Therapeutic Strategies. Front Pharmacol 11. https://doi.org/10.3389/fphar.2020.00904

Thomas C, Knerlich-Lukoschus F, Reinhard H, Johann PD, Sturm D, Sahm F, Bens S, Vogt J, Nemes K, Oyen F, Kordes U, Siebert R, Schneppenheim R, Messing-Jünger M, Pietsch T, von Deimling A, Paulus W, Pfister SM, Kool M, Frühwald MC, Hasselblatt M (2019) Two molecularly distinct atypical teratoid/rhabdoid tumors (or tumor components) occurring in an infant with rhabdoid tumor predisposition syndrome 1. Acta Neuropathol 137:847–850. https://doi.org/10.1007/s00401-019-02001-3

Tolcher AW, Berlin JD, Cosaert J, Kauh J, Chan E, Piha-Paul SA, Amaya A, Tang S, Driscoll K, Kimbung R, Kambhampati SRP, Gueorguieva I, Hong DS (2017) A phase 1 study of anti-TGFβ receptor type-II monoclonal antibody LY3022859 in patients with advanced solid tumors. Cancer Chemother Pharmacol 79(4):673–680. https://doi.org/10.1007/s00280-017-3245-5

Torchia J, Golbourn B, Feng S, Ho KC, Sin-Chan P, Vasiljevic A, Norman JD, Guilhamon P, Garzia L, Agamez NR, Lu M, Chan TS, Picard D, de Antonellis P, Khuong-Quang DA, Planello AC, Zeller C, Barsyte-Lovejoy D, Lafay-Cousin L, Letourneau L, Bourgey M, Yu M, Gendoo DMA, Dzamba M, Barszczyk M, Medina T, Riemenschneider AN, Morrissy AS, Ra YS, Ramaswamy V, Remke M, Dunham CP, Yip S, Ng H keung, Lu JQ, Mehta V, Albrecht S, Pimentel J, Chan JA, Somers GR, Faria CC, Roque L, Fouladi M, Hoffman LM, Moore AS, Wang Y, Choi SA, Hansford JR, Catchpoole D, Birks DK, Foreman NK, Strother D, Klekner A, Bognár L, Garami M, Hauser P, Hortobágyi T, Wilson B, Hukin J, Carret AS, Van Meter TE, Hwang EI, Gajjar A, Chiou SH, Nakamura H, Toledano H, Fried I, Fults D, Wataya T, Fryer C, Eisenstat DD, Scheinemann K, Fleming AJ, Johnston DL, Michaud J, Zelcer S, Hammond R, Afzal S, Ramsay DA, Sirachainan N, Hongeng S, Larbcharoensub N, Grundy RG, Lulla RR, Fangusaro JR, Druker H, Bartels U, Grant R, Malkin D, McGlade CJ, Nicolaides T, Tihan T, Phillips J, Majewski J, Montpetit A, Bourque

G, Bader GD, Reddy AT, Gillespie GY, Warmuth-Metz M, Rutkowski S, Tabori U, Lupien M, Brudno M, Schüller U, Pietsch T, Judkins AR, Hawkins CE, Bouffet E, Kim SK, Dirks PB, Taylor MD, Erdreich-Epstein A, Arrowsmith CH, De Carvalho DD, Rutka JT, Jabado N, Huang A (2016) Integrated (epi)-Genomic Analyses Identify Subgroup-Specific Therapeutic Targets in CNS Rhabdoid Tumors. Cancer Cell 30(6):891–908. https://doi.org/10.1016/j.ccell.2016.11.003

Tsuneyoshi M, Daimaru Y, Hashimoto H, Enjoji M (1985) Malignant soft tissue neoplasms with the histologic features of renal rhabdoid tumors: An ultrastructural and immunohistochemical study. Hum Pathol 16(12):1235–1242. https://doi.org/10.1016/S0046-8177(85)80036-8

Tufail M, Jiang CH, Li N (2025) Tumor dormancy and relapse: understanding the molecular mechanisms of cancer recurrence. Mil Med Res 12(1):7. https://doi.org/10.1186/s40779-025-00595-2

Tulla M, Berthold F, Graf N, Rutkowski S, von Schweinitz D, Spix C, Kaatsch P (2015) Incidence, Trends, and Survival of Children With Embryonal Tumors. Pediatrics 136(3):e623–e632. https://doi.org/10.1542/peds.2015-0224

Tuoc T, Dere E, Radyushkin K, Pham L, Nguyen H, Tonchev AB, Sun G, Ronnenberg A, Shi Y, Staiger JF, Ehrenreich H, Stoykova A (2017) Ablation of BAF170 in Developing and Postnatal Dentate Gyrus Affects Neural Stem Cell Proliferation, Differentiation, and Learning. Mol Neurobiol 54(6):4618–4635. https://doi.org/10.1007/s12035-016-9948-5

Turner C, Kohandel M (2010) Investigating the link between epithelial–mesenchymal transition and the cancer stem cell phenotype: A mathematical approach. J Theor Biol 265(3):329–335. https://doi.org/10.1016/j.jtbi.2010.05.024

Upadhyaya SA, Robinson GW, Onar-Thomas A, Orr BA, Johann P, Wu G, Billups CA, Tatevossian RG, Dhanda SK, Srinivasan A, Broniscer A, Qaddoumi I, Vinitsky A, Armstrong GT, Bendel AE, Hassall T, Partap S, Fisher PG, Crawford JR, Chintagumpala M, Bouffet E, Gururangan S, Mostafavi R, Sanders RP, Klimo P, Patay Z, Indelicato DJ, Nichols KE, Boop FA, Merchant TE, Kool M, Ellison DW, Gajjar A (2021) Relevance of molecular groups in children with newly diagnosed atypical teratoid rhabdoid tumor: Results from prospective St. Jude multi-institutional trials. Clin Cancer Res 27(10):2879–2889. https://doi.org/10.1158/1078-0432.CCR-20-4731

van Essen MJ, Nayler S, Becker EBE, Jacob J (2020) Deconstructing cerebellar development cell by cell. PLoS Genet 16(4):e1008630. https://doi.org/10.1371/journal.pgen.1008630

Verhaak RGW, Hoadley KA, Purdom E, Wang V, Qi Y, Wilkerson MD, Miller CR, Ding L, Golub T, Mesirov JP, Alexe G, Lawrence M, O'Kelly M, Tamayo P, Weir BA, Gabriel S, Winckler W, Gupta S, Jakkula L, Feiler HS, Hodgson JG, James CD, Sarkaria JN, Brennan C, Kahn A, Spellman PT, Wilson RK, Speed TP, Gray JW, Meyerson M, Getz G, Perou CM, Hayes DN (2010) Integrated Genomic Analysis Identifies Clinically Relevant Subtypes of Glioblastoma Characterized by Abnormalities in PDGFRA, IDH1, EGFR, and NF1. Cancer Cell 17(1):98–110. https://doi.org/10.1016/j.ccr.2009.12.020

Visvader JE (2011) Cells of origin in cancer. Nature 469(7330):314–322. https://doi.org/10.1038/nature09781

Vitte J, Gao F, Coppola G, Judkins AR, Giovannini M (2017) Timing of Smarcb1 and Nf2 inactivation determines schwannoma versus rhabdoid tumor development. Nat Commun 8(1):1–12. https://doi.org/10.1038/s41467-017-00346-5

Wang W, Côté J, Xue Y, Zhou S, Khavari PA, Biggar SR, Muchardt C, Kalpana G V, Goff SP, Yaniv M, Workman JL, Crabtree GR (1996) Purification and biochemical heterogeneity of the mammalian SWI-SNF complex. EMBO J 15(19):5370–82

Wang X, Lee RS, Alver BH, Haswell JR, Wang S, Mieczkowski J, Drier Y, Gillespie SM, Archer TC, Wu JN, Tzvetkov EP, Troisi EC, Pomeroy SL, Biegel JA, Tolstorukov MY, Bernstein BE, Park PJ, Roberts CWM (2017a) SMARCB1-mediated SWI/SNF complex function is essential for enhancer regulation. Nat Genet 49(2):289–295. https://doi.org/10.1038/ng.3746

Wang Y, Guo YR, Liu K, Yin Z, Liu R, Xia Y, Tan L, Yang P, Lee JH, Li XJ, Hawke D, Zheng Y, Qian X, Lyu J, He J, Xing D, Tao YJ, Lu Z (2017b) KAT2A coupled with the α-KGDH complex acts as a histone H3 succinyltransferase. Nature 552(7684):273–277. https://doi.org/10.1038/nature25003

Wang Y, Wang L, Wei Y, Wei C, Yang H, Chen Q, Zhang R, Shen H (2024) Advances in the molecular regulation mechanism of tumor dormancy and its therapeutic strategy. Disc Oncol 15(1):184. https://doi.org/10.1007/s12672-024-01049-2

Weingart MF, Roth JJ, Hutt-Cabezas M, Busse TM, Kaur H, Price A, Maynard R, Rubens J, Taylor I, Mao X, Xu J, Kuwahara Y, Allen SJ, Erdreich-Epstein A, Weissman BE, Orr BA, Eberhart CG, Biegel JA, Raabe EH (2015) Disrupting LIN28 in atypical teratoid rhabdoid tumors reveals the importance of the mitogen activated protein kinase pathway as a therapeutic target. Oncotarget 6(5):3165–3177. https://doi.org/10.18632/oncotarget.3078

Wilson BG, Roberts CWM (2011) SWI/SNF nucleosome remodellers and cancer. Nat Rev Cancer 11(7):481–492. https://doi.org/10.1038/nrc3068

Winkler J, Abisoye-Ogunniyan A, Metcalf KJ, Werb Z (2020) Concepts of extracellular matrix remodelling in tumour progression and metastasis. Nat Commun 11(1):5120. https://doi.org/10.1038/s41467-020-18794-x

Xu J, Lamouille S, Derynck R (2009) TGF-β-induced epithelial to mesenchymal transition. Cell Res 19(2):156–172. https://doi.org/10.1038/cr.2009.5

Xu J, Margol A, Asgharzadeh S, Erdreich-Epstein A (2015) Pediatric Brain Tumor Cell Lines. J Cell Biochem 116(2):218–224. https://doi.org/10.1002/jcb.24976

Xu Y, Xu WH, Shi SN, Yang XL, Ren YR, Zhuang XY, Qu YY, Zhang HL, Zhang XF (2020) Carbonic Anhydrase 4 serves as a Clinicopathological Biomarker for Outcomes and Immune Infiltration in Renal Cell Carcinoma, Lower Grade Glioma, Lung Adenocarcinoma and Uveal Melanoma. J Cancer 11(20):6101–6113. https://doi.org/10.7150/jca.46902

Yang L, Shi P, Zhao G, Xu J, Peng W, Zhang J, Zhang G, Wang X, Dong Z, Chen F, Cui H (2020) Targeting cancer stem cell pathways for cancer therapy. Signal Transduct Target Ther 5(1):8. https://doi.org/10.1038/s41392-020-0110-5

Yasmin N, Konradi S, Eisenwort G, Schichl YM, Seyerl M, Bauer T, Stöckl J, Strobl H (2013) β-Catenin Promotes the Differentiation of Epidermal Langerhans Dendritic Cells. J Investig Dermatol 133(5):1250–1259. https://doi.org/10.1038/jid.2012.481

Yuan Z, Li Y, Zhang S, Wang X, Dou H, Yu X, Zhang Z, Yang S, Xiao M (2023) Extracellular matrix remodeling in tumor progression and immune escape: from mechanisms to treatments. Mol Cancer 22(1):48. https://doi.org/ 10.1186/s12943-023-01744-8

Zhang S, Xiao X, Yi Y, Wang X, Zhu L, Shen Y, Lin D, Wu C (2024) Tumor initiation and early tumorigenesis: molecular mechanisms and interventional targets. Signal Transduct Target Ther 9(1):149. https://doi.org/10.1038/s41392-024-01848-7

Zhao S, Li J, Zhang H, Qi L, Du Y, Kogiso M, Braun FK, Xiao S, Huang Y, Li J, Teo WY, Lindsay H, Baxter P, Su JMF, Adesina A, Laczik M, Genevini P, Veillard AC, Schvartzman S, Berguet G, Ding SR, Du L, Stephan C, Yang J, Davies PJA, Lu X, Chintagumpala M, Parsons DW, Perlaky L, Xia YF, Man TK, Huang Y, Sun D, Li XN (2022) Epigenetic Alterations of Repeated Relapses in Patient-matched Childhood Ependymomas. Nat Commun 13(1). https://doi.org/10.1038/s41467-022-34514-z

Zhu Y, Guignard F, Zhao D, Liu L, Burns DK, Mason RP, Messing A, Parada LF (2005) Early inactivation of p53 tumor suppressor gene cooperating with NF1 loss induces malignant astrocytoma. Cancer Cell 8(2):119–30. https://doi.org/10.1016/j.ccr.2005.07.004

Zin F, Cotter JA, Haberler C, Dottermusch M, Neumann J, Schüller U, Schweizer L, Thomas C, Nemes K, Johann PD, Kool M, Frühwald MC, Paulus W, Judkins A, Hasselblatt M (2021) Histopathological patterns in atypical teratoid/rhabdoid tumors are related to molecular subgroup. Brain Pathology 31(5). https://doi.org/10.1111/bpa.12967

Zion O, Genin O, Kawada N, Yoshizato K, Roffe S, Nagler A, Iovanna JL, Halevy O, Pines M (2009) Inhibition of Transforming Growth Factor β Signaling by Halofuginone as a Modality for Pancreas Fibrosis Prevention. Pancreas 38(4):427–435. https://doi.org/10.1097/MPA.0b013e3181967670

Zohn IE, Sarkar AA (2008) Modeling Neural Tube Defects in the Mouse. Curr Top Dev Biol 84:1–35. https://doi.org/10.1016/S0070-2153(08)00601-7

11. List of publications

11.1 First-authorships

Neyazi S*, **Altendorf L***, Schwetje D, Göbel C, Schoof M, Holdhof D, Schüller U. Generation of new transgenic SMARCA4-deficient mouse models results in neuromuscular weakness and paralysis of limbs. Brain Pathol. 2023 May;33(3):e13146. doi: 10.1111/bpa.13146. Epub 2022 Dec 29. PMID: 36582072; PMCID: PMC10154361.

Johann PD*, **Altendorf L***, Efremova EM, Holsten T, Steinbügl M, Nemes K, Eckhardt A, Kresbach C, Bockmayr M, Koch A, Haberler C, Antonelli M, DeSisto J, Schuhmann MU, Hauser P, Siebert R, Bens S, Kool M, Green AL, Hasselblatt M, Frühwald MC*, Schüller U*. Recurrent atypical teratoid/rhabdoid tumors (AT/RT) reveal discrete features of progression on histology, epigenetics, copy number profiling, and transcriptomics. Acta Neuropathol. 2023 Sep;146(3):527-541. doi: 10.1007/s00401-023-02608-7. Epub 2023 Jul 14. PMID: 37450044; PMCID: PMC10412492.

11.2 Co-authorships

Kresbach C, Dottermusch M, Eckhardt A, Ristow I, Paplomatas P, **Altendorf L**, Wefers AK, Bockmayr M, Belakhoua S, Tran I, Pohl L, Neyazi S, Bode H, Farschtschi S, Well L, Friedrich RE, Reuss D, Snuderl M, Hagel C, Mautner VF, Schüller U. Atypical neurofibromas reveal distinct epigenetic features with proximity to benign peripheral nerve sheath tumor entities. Neuro Oncol. 2023 Sep 5;25(9):1644-1655. doi: 10.1093/neuonc/noad053. PMID: 36866403; PMCID: PMC10479771.

Gödicke S, Kresbach C, Ehlert M, Obrecht D, **Altendorf L**, Hack K, von Hoff K, Carén H, Melcher V, Kerl K, Englinger B, Filbin M, Pajtler KW, Gojo J, Pietsch T, Rutkowski S, Schüller U. Clinically relevant molecular hallmarks of PFA ependymomas display intratumoral heterogeneity and correlate with tumor morphology. Acta Neuropathol. 2024 Jan 24;147(1):23. doi: 10.1007/s00401-023-02682-x. PMID: 38265527; PMCID: PMC10808473.

Sönksen M, Obrecht-Sturm D, Hernáiz Driever P, Sauerbrey A, Graf N, Kontny U, Reimann C, Langhein M, Kordes UR, Schwarz R, Obser T, Boschann F, Schüller U, **Altendorf L**, Goschzik T, Pietsch T, Mynarek M, Rutkowski S. Medulloblastoma in children with Fanconi anemia: Association with FA-D1/FA-N, SHH type and poor survival independent of treatment strategies. Neuro Oncol. 2024 Nov 4;26(11):2125-2139. doi: 10.1093/neuonc/noae111. PMID: 38919026; PMCID: PMC11534319.

Potthoff TE, Walter C, Jeising D, Münter D, Verma A, Suero Molina E, Stummer W, Dugas M, Hartmann W, Dottermusch M, **Altendorf L**, Schüller U, Scheuermann S, Seitz C, Albert TK, Kerl K. Single-cell transcriptomics link gene expression signatures to clinicopathological features of gonadotroph and lactotroph PitNET. J Transl Med. 2024 Nov 15;22(1):1027. doi: 10.1186/s12967-024-05821-4. PMID: 39548496; PMCID: PMC11566263.

De Faria FW, Riedel NC, Interlandi M, Göbel C, Melcher V, **Altendorf L**, Thomas C, Roy R, Schoof M, Münter D, Bedzhov I, Moreno N, Graf M, Hotfilder M, Holdhof D, Hartmann W, Bruns AK, Brentrup A, Liesche-Starnecker F, Maerkl B, Sandmann S, Varghese J, Dugas M, Pinto P, Balbach S, Rössig C, Ebinger M, Schuhmann M, Canak A, Schittenhelm J, Frühwald M, Schüller U, Albert T, Walter C, Bruder J, Richter M, Soehnlein O, Lu IN, Kerl K. Nat Commun. 2025 Jun 25;16:5394. doi: 10.1038/s41467-025-60442-9. PMID: 40562749; PMCID: PMC12198369.

11.3 Submitted manuscripts

Altendorf L, Althammer A, Roy R, Hack K, De Faria FW, Koch A, Thaden V, Schoof M, Schuhmann MU, Hauser P, Johann PD, Hasselblatt M, Frühwald MC, Kerl K, Schüller U. Therapy-resistance in AT/RT is driven by epithelial-mesenchymal transition, extracellular matrix changes, and enrichment of *CD1A*$^{+}$ *CD207*$^{+}$ dendritic cells. Under review at Neuro-Oncology, 20th June 2025

Schoof M*, Zheng T*, Sill M, Imle R, Cais A, Hofmann N, Ernst K, Vonficht D, Chun-Ho Chan K, Holland-Letz T, Postlmayr A, Shiraishi R, Wang W, Morcavallo A, Spohn M, **Altendorf L**, Göbel C, Niesen J, Peter LS, Eckhardt A, Bourdeaut F, Han ZY, Pei Y, Murad N, Swartling FJ, Taylor J, Yadav M, Gibson GR, Gilbertson RJ, Dottermusch M, Roy R, Kerl K, Glass R, Cheng J, Horstmann MA, Wolters-Eisfeld IG, Zhao H, Sturm D, Yadav VN, Chesler L, Haas S, Weiss WA, Northcott PA, Kutscher LM, Stucklin AG, Ayrault O, Neumann JE, Kawauchi D, Jones DTW, Pajtler K, Banito A, Pfister SM, Schüller U*, Zuckermann M*. Highly recurrent, human syntenic CNVs characterize pediatric cancer models. Revised version submitted to Nature Genetics, 14th June 2025

Schüftan E, Lu I, De Faria FW, Singla CI, Rössig C, Bothe J, Tippelt S, Monoranu C, **Altendorf L**, Spille D, Bruns AK, Brentrup A, Stummer W, Gorodezki D, Ebinger M, Schittenhelm J, Thomas C, Albert TK, Schüller U, Kerl K. Integrated dual-omics analysis elucidates transcriptional heterogeneity and hypoxia-driven spatial organisation in supratentorial ependymoma. Submitted to Cancer Research, 25th June 2025

Riedel NC, Walter C, De Faria FW, **Altendorf L**, Aust P, Göbel C, Verma A, Ballast A, Bedhzov I, Roy R, Münter D, Albert TK, Rössig C, Johann P, von Zezschwitz B, Sandmann S, Varghese

J, Thomas C, Schüller U, Bruder JM, Kerl K. In Vivo Intratumoral Heterogeneity in a Dish: Scalable Forebrain Organoid Models of Embryonal Brain Tumors for High-Throughput Personalized Drug Discovery. Revised version submitted to Cancer Communications, 30th June 2025

Peter LS, **Altendorf L**, Hack K, Thaden V, Göbel C, Krebs C, Jauch-Speer SL, Kordes UR, Obrecht-Sturm D, Thomas C, Schüller U, Schoof M. Overactivation of SHH signaling during embryonic choroid plexus development induces a cascade of dedifferentiation and carcinoma formation. Revised version submitted to Neuro-Oncology, 9th July 2025

11.4 Manuscript drafts

Altendorf L, Peter LS, Hack K, Dottermusch M, Tonn S, Roy R, Holtzman MJ, Kerl K, Schoof M, Hasselblatt M, Schüller U. Molecular and histological analyses of AT/RT-TYR suggest the choroid plexus of the fourth ventricle as cellular origin.

*These authors contributed equally.

12. Danksagung

An erster Stelle möchte ich mich herzlich bei Ulrich für die ausgezeichnete Betreuung bedanken. Danke, dass du wirklich jederzeit für Diskussionen zur Verfügung standest und mir immer mit neuen Ideen und Anregungen weitergeholfen hast. Ohne dich wäre diese Doktorarbeit nicht möglich gewesen. Vielen Dank auch an meinen Gutachter Wolfgang Streit, besonders für deine Zeit und dafür, dass ich mich nie ganz von der Mibi trennen musste.

Außerdem möchte ich mich von ganzem Herzen bei Burkhard Meyer für die Unterstützung bedanken. Ich habe mich sehr darüber gefreut, dass Sie so interessiert an meiner Arbeit waren und immer an mich geglaubt haben.

Ein ganz besonderer Dank gilt natürlich allen aktuellen und ehemaligen Mitgliedern der AG Schüller. Vor allem die gemeinsamen Mensa-Ausflüge, Kaffeepausen und Sekti-Abende haben mich immer wieder motiviert. Ihr seid alle toll, leider reicht der Platz nicht, um euch allen einzeln zu danken. Ich bin unendlich glücklich, nicht nur Kolleg*innen, sondern auch Freund*innen gewonnen zu haben. Ganz besonders möchte ich mich natürlich bei Karo bedanken. Ich bin sehr glücklich darüber, dass wir diese Zeit von Anfang an zusammen verbringen konnten und viel zusammen erlebt haben. Danke, dass du immer ein offenes Ohr für mich hattest. Außerdem möchte ich mich bei Melanie bedanken. Danke, dass du immer für mich da warst und mich aufgefangen hast, wenn ich nicht weiterwusste. Ein riesiges Dankeschön an meine Laborheldinnen Vany und Jacky, ohne euch wäre ich verloren gewesen. Ich möchte mich auch bei allen anderen Mitgliedern des Kinderkrebs-Zentrums bedanken. Ich habe die Zeit auf Retreats, aber auch beim Bingo und Pubquiz, mit euch sehr genossen.

Ein herzliches Dankeschön geht an alle Mitarbeiter*innen des Tierstalls des LIV. Danke, dass ihr euch immer um das Wohl meiner Mausis gesorgt habt, auch wenn sie besonders viel Dreck gemacht haben. Ich bin euch sehr dankbar für eure Unterstützung. Außerdem möchte ich mich bei allen Mitarbeiter*innen der Neuropathologie bedanken. Ein riesiger Dank geht vor allem an das Histo- und Molpatho-Labor und natürlich Kristin. Ohne euch würden meine Abbildungen nicht halb so gut aussehen.

Zu guter Letzt möchte ich mich bei meiner Familie, Hendrik und meinen Freund*innen bedanken. Ein besonderer Dank gilt Mama, Papa und Oma dafür, dass ihr mich seit Tag 1 begeistert unterstützt habt und immer ein offenes Ohr für mich hattet. Auch bei Hendrik, der alle guten und weniger guten Phasen miterlebt hat, möchte ich mich für seine Unterstützung bedanken. Danke, dass du immer Verständnis für mich aufgebracht hast. Ein riesiges Dankeschön gilt Marie und Bine. Es hat mir sehr geholfen, die Zeit mit euch zusammen durchzustehen und Erholung in unseren Rentnerurlauben zu finden.

13. Eidesstattliche Versicherung

Hiermit versichere ich an Eides statt, die vorliegende Dissertationsschrift selbst verfasst und keine anderen als die angegebenen Hilfsmittel und Quellen benutzt zu haben. Sofern im Zuge der Erstellung der vorliegenden Dissertationsschrift generative Künstliche Intelligenz (gKI) basierte elektronische Hilfsmittel verwendet wurden, versichere ich, dass meine eigene Leistung im Vordergrund stand und dass eine vollständige Dokumentation aller verwendeten Hilfsmittel gemäß der Guten wissenschaftlichen Praxis vorliegt. Ich trage die Verantwortung für eventuell durch die gKI generierte fehlerhafte oder verzerrte Inhalte, fehlerhafte Referenzen, Verstöße gegen das Datenschutz- und Urheberrecht oder Plagiate.

Hamburg, den 15.07.2025 Unterschrift

Ich versichere, dass dieses gebundene Exemplar der Dissertation und das in elektronischer Form eingereichte Dissertationsexemplar (über den Docata-Upload) und das bei der Fakultät (zuständiges Studienbüro bzw. Promotionsbüro Physik) zur Archivierung eingereichte gedruckte gebundene Exemplar der Dissertationsschrift identisch sind.

Hamburg, den 15.07.2025 Unterschrift